



MONASH University

**Iron isotope geochemistry and crystal chemistry of
jarosite in acidic, sulfate-rich environments**

by

Anne Jane Whitworth

A thesis submitted for the degree of Doctor of Philosophy at

Monash University, Faculty of Science

2020

COPYRIGHT NOTICE

© Anne J. Whitworth (2020).

I certify that I have made all reasonable efforts to secure copyright permissions for third-party content included in this thesis and have not knowingly added copyright content to my work without the owner's permission.

ABSTRACT

Jarosite ($\text{KFe}_3(\text{SO}_4)_2(\text{OH})_6$) is a yellow–brown mineral that forms in acidic, oxidizing, and sulfate–rich environments. It is a member of the alunite supergroup of minerals ($\text{DG}_3(\text{TO}_4)_2(\text{OH})_6$), with jarosite and related subgroup members being characterised by Fe and S in the G and T sites, respectively. Jarosite is a store of acidity and can incorporate a wide range of ions in its crystal structure, resulting in jarosite playing a critical role in the regulation of acidity and the mobility of trace elements and potential contaminants in acidic, sulfate–rich environments such as acid sulfate soils (ASS) and acid mine drainage (AMD). Management of this complex behaviour requires a thorough understanding of jarosite formation, recrystallisation, and interactions in these environments, and the research presented here aims to shed light on these processes.

Extensive jarosite–bearing outcrops occur in sulfur-rich sediments in Victoria, Australia, presenting an opportunity to better understand jarosite formation, recrystallisation and behaviour in an acidic, sulfate–rich environment. Samples were collected from two coastal sites and analysed using iron isotope geochemistry, inductively coupled plasma–mass spectrometry (ICP–MS), and synchrotron powder X–ray diffraction (PXRD). Synchrotron PXRD and ICP–MS shows that the samples are comprised predominantly of natrojarosite ($\text{NaFe}_3(\text{SO}_4)_2(\text{OH})_6$), often with minor to substantial K substitution. Rietveld refinement of the PXRD patterns shows that most of the samples are a solid solution of Na–K jarosite, differing from previous observations that (near–)end–member mixing predominantly occurs in nature. PXRD, together with electron backscatter diffraction (EBSD), also shows that one natrojarosite sample has monoclinic symmetry. This is the first time that monoclinic symmetry has been identified in a natural jarosite, with all other documented occurrences of natural jarosite having a rhombohedral symmetry. It is likely that natural monoclinic jarosites have unique formation conditions and properties compared to natural rhombohedral jarosites.

Iron isotope analysis shows that the natural jarosites have a wide range of $\delta^{56}\text{Fe}$ values (–1.91 and +1.24 ‰), with the values partially overlapping with the $\delta^{56}\text{Fe}$ values of the sulfidic sediment precursor (–0.54 to +1.30 ‰). The iron isotope composition of the jarosite also appears to be related to the D site (i.e., alkali) content. The large range in $\delta^{56}\text{Fe}$ values likely result from a combination of the variable $\delta^{56}\text{Fe}$ values of the precursor sulfides, thermodynamic differences between the Fe–O bonds in Na– versus K–bearing jarosite, and an open–system Rayleigh distillation during jarosite formation. Three–isotope experiments examining iron isotope exchange and fractionation between (natro)jarosite and $\text{Fe(II)}_{\text{aq}}$ show that during jarosite recrystallisation in the presence of Fe(II) , jarosite is expected to become isotopically heavier as lighter isotopes are fractionated into Fe(II) . Thus, iron isotope fractionation during jarosite recrystallisation in Fe(II) can also help explain the wide range of $\delta^{56}\text{Fe}$ values.

Jarosite formation in acid–sulfate environments involves an interplay of processes that, together with jarosite recrystallisation and environmental interactions, results in jarosite having chemical and structural complexity. Characterisation of jarosites in acid–sulfate environments is therefore crucial to manage them in these environments successfully.

PUBLICATIONS DURING ENROLMENT

Whitworth, A.J., Brand, H.E.A., Frierdich, A.J., 2020. Iron isotope exchange and fractionation between jarosite and aqueous Fe(II). *Chemical Geology*, 554: 119802.

Whitworth, A.J., Brand, H.E.A., Wilson, S.A., Frierdich, A.J., 2020. Iron isotope geochemistry and mineralogy of jarosite in sulfur-rich sediments. *Geochimica et Cosmochimica Acta*, 270: 282–295

THESIS INCLUDING PUBLISHED WORKS DECLARATION

I hereby declare that this thesis contains no material which has been accepted for the award of any other degree or diploma at any university or equivalent institution and that, to the best of my knowledge and belief, this thesis contains no material previously published or written by another person, except where due reference is made in the text of the thesis.

This thesis includes two original papers published in peer reviewed journals and one chapter formatted as a paper but that has not been submitted for publication. The core theme of the thesis is to investigate the formation, recrystallisation and interactions of jarosite in acidic, sulfate-rich environments using iron isotope geochemistry and X-ray diffraction. The ideas, development and writing up of all the papers in the thesis were the principal responsibility of myself, the student, working within the Faculty of Science under the supervision of Andrew J. Frierdich, Helen E. A. Brand, and Siobhan A. Wilson.

(The inclusion of co-authors reflects the fact that the work came from active collaboration between researchers and acknowledges input into team-based research.)

In the case of *Chapters 4, 5 and 6* my contribution to the work involved the following:

Thesis Chapter	Publication Title	Status (published, in press, accepted or returned for revision, submitted)	Nature and % of student contribution	Co-author name(s) Nature and % of Co-author's contribution*	Co-author(s), Monash student Y/N*
4	Iron isotope geochemistry and mineralogy of jarosite in sulfur-rich sediments	Published	92%. Concept, data collection, data analysis, manuscript synthesis	1) Andrew J Frierdich (4%): concept, data collection and analysis, manuscript feedback 2) Helen E.A. Brand (3%): data collection and analysis, manuscript feedback 3) Siobhan A Wilson (1%): manuscript feedback	N N N
5	Iron isotope exchange and fractionation between	Published	94%. Concept, data collection, data analysis,	1) Andrew J Frierdich (4%): concept, data collection and analysis, manuscript feedback	N

“All our dreams can come true; if we have the courage to pursue them”

Walt Disney

“Just keep swimming”

Dori, Finding Nemo

ACKNOWLEDGEMENTS

Firstly, I would like to thank Monash University for providing me with a Faculty of Science Dean's Postgraduate Research Award to undertake this research. I would also like to thank AINSE Limited for providing financial assistance (Award – PGRA) to enable work on this research. Part of this research was done on the Powder Diffraction beamline at the Australian Synchrotron and facilities within the Monash X-ray Platform and Monash Isotopia Facility.

I would like to thank the Bunurong Land Council Aboriginal Corporation Registered Aboriginal Party and Mornington Peninsula Shire for allowing sampling to take place at the Fossil Beach Geological Reserve.

This work would not have been possible without my supervisors, Dr Andrew J. Friedrich, Dr Helen E.A. Brand, and Dr Siobhan (Sasha) A. Wilson. Thank you for your unwavering support and guidance, unending red pen, never telling me my questions were stupid (and lets face it, some were), and for helping me haul a heap of rocks up a very steep hill.

I would like to thank Massimo Raveggi and Rachelle Pierson for assistance with ICP–OES measurements at Monash University, Dr Natasha R Stephen of the Plymouth Electron Microscopy Centre for SEM measurements, and Dr Ian Grey and Yesim Gozukara of CSIRO for TGA/DTA measurements. I would also like to thank the EAE administration and office staff for all their assistance in navigating my PhD.

To my beloved office mates, Jen, Amrei, and Al: thank you for all the laughs, girls nights, wine, more wine, vents, and unending encouragement. To my DnD group, Dangles, Jen, Alice, Harry, and Scott, thank you for our Tuesday night shenanigans. Stay nerdy. To my partner Scott, thank you for being my rock, always being there to give me a hug on a bad day, and helping me to not go insane during lockdown 1.0 and 2.0.

Lastly, to my mum Clare, whose unending love, support, and guidance have made me the person I am today, and to my inspirational grandparents, Don and Diane: I dedicate this to you.

CONTENTS

Copywrite Notice.....	2
Abstract.....	3
Publications During Enrolment.....	5
Thesis Including Published Works Declaration	6
Acknowledgements	9
List of Figures.....	13
List of Tables	15
Chapter 1. Introduction to Jarosite: The “Garbage Can” of Minerals	17
1.1 Introduction.....	18
1.2 Jarosite formation and occurrence	19
1.2.1 Supergene jarosite.....	19
1.2.2 Hypogene jarosite	21
1.2.3 Sedimentary jarosite.....	22
1.2.4 Jarosite formed during mineral processing	22
1.2.5 Martian jarosite	23
1.3 Jarosite crystal structure.....	24
1.4 Jarosite crystal chemistry.....	26
1.5 Jarosite isotope geochemistry	27
1.5.1 H, O and S stable isotopes	27
1.5.2 K/Ar and ⁴⁰ Ar/ ³⁹ Ar isotopes.....	28
1.5.3 Fe stable isotopes	29
1.6 Jarosite dissolution and decomposition and the implications for jarosite recrystallisation.....	29
1.7 Thesis aim and structure	33
Chapter 2. Introduction to Iron Isotope Geochemistry.....	35
2.1 Introduction to stable iron isotope geochemistry	36
2.2 Iron isotope geochemistry nomenclature	38
2.3 Sample preparation and purification	38
2.4 Analytical methods	39
2.4.1 MC–ICP–MS	39
2.4.1.1 Thermo–Fisher Neptune Plus MC–ICP–MS	41
2.4.2 Other methods.....	42
2.5 Iron isotope fractionation.....	42
2.5.1 Fractionation factors	43
2.5.1.1 Calculated fractionation factors	44
2.5.1.2 Experimental fractionation factors.....	44

Chapter 3. Introduction to X-ray Diffraction.....	47
3.1 Introduction to diffraction.....	48
3.2 X-rays and their sources	50
3.2.1 Laboratory X-rays	50
3.2.1.1 Bruker D8 Advance Eco	51
3.2.2 Synchrotron X-rays	51
3.2.2.1 The powder diffraction (PD) beamline, Australian Synchrotron.....	53
3.3 Powder XRD	54
3.3.1 PXRD data	55
3.3.2 Qualitative phase analysis.....	56
3.3.3 Rietveld refinement.....	56
 Chapter 4. Iron Isotope Geochemistry and Mineralogy of Jarosite in Sulfur-Rich Sediments ..	 61
4.1 Introduction.....	62
4.2 Site Description.....	63
4.3 Sampling and analytical methodology	64
4.3.1 Outcrop morphology, sample collection and preparation.....	64
4.3.2 Analytical methodology	67
4.3.2.1 PXRD.....	67
4.3.2.2 ICP-MS	68
4.3.2.3 MC-ICP-MS	68
4.4 Results.....	70
4.4.1 PXRD results	70
4.4.2 ICP-MS results	72
4.4.3 MC-ICP-MS results.....	74
4.5 Discussion	77
4.5.1 Site comparison.....	77
4.5.2 Jarosite subgroup composition.....	79
4.5.3 Iron isotope geochemistry of jarosite and implication for recrystallisation.....	80
4.6 Conclusions.....	82
 Chapter 5. Iron Isotope Exchange and Fractionation Between Jarosite and Aqueous Fe(II).....	 85
5.1 Introduction.....	86
5.2 Methodology	88
5.2.1 Jarosite collection, synthesis and characterisation.....	88
5.2.2 Three-isotope method and reversal approach to equilibrium	89
5.2.3 Exchange experiments	91
5.2.4 Isotope analysis.....	93
5.3 Results.....	94
5.3.1 Reactor pH and K release	94

5.3.2 Iron concentration and tracer isotope dynamics	95
5.3.3 Mass-dependent Fe isotope fractionation.....	97
5.3.4 PXRD results	100
5.4 Discussion	100
5.4.1 Jarosite recrystallisation in the presence of Fe(II) _{aq}	100
5.4.2 Acidity release during jarosite recrystallisation.....	102
5.4.3 Equilibrium iron isotope fraction factors and application to acid-sulfate environments ..	104
5.4 Conclusions.....	105
Chapter 6. The First Occurrence of Monoclinic Jarosite in a Natural Environment.....	107
6.1 Introduction.....	108
6.2 Experimental methodology	110
6.2.1 Room temperature PXRD	110
6.2.1.1 Rietveld refinement.....	111
6.2.2 In-situ PXRD heating experiments	111
6.2.2.1 Inductively coupled plasma-optical emission spectrometry (ICP-OES) of Js-SB-35A	112
6.2.2.2 Rietveld refinement of heating datasets	112
6.2.3 Thermogravimetric analysis.....	113
6.2.4 Electron backscatter diffraction and backscatter-electron imaging.....	113
6.3 Results.....	113
6.3.1 Room temperature PXRD	113
6.3.2 In-situ heating PXRD	115
6.3.3 Thermogravimetric Analysis	119
6.3.4 Electron backscatter diffraction and backscatter-electron imaging	120
6.4 Discussion	123
6.4.1 Structural heterogeneity in Js-SB-35	123
6.4.2 Structure and properties of natural monoclinic natrojarosite.....	123
6.4.3 Formation of natural monoclinic natrojarosite.....	125
6.5 Conclusions.....	126
Chapter 7. Summary, Implications of Results and Future Work	129
7.1 Summary and discussion of main findings	130
7.1.1 Jarosite formation and recrystallisation in acidic, sulfate-rich environments	130
7.1.2 Comparison of jarosite and sediment $\delta^{56}\text{Fe}$ values with existing data	132
7.2 Implications of findings for jarosite management in low temperature, acidic and sulfate-rich environments.....	133
7.3 Future research.....	134
References.....	137

Appendices

Appendix 1. Iron Isotope Geochemistry and Mineralogy of Jarosite in Sulphur–Rich Sediments: Supplementary Information	I
Appendix 2. Iron Isotope Exchange and Fractionation Between Jarosite and Aqueous Fe(II): Supplementary Information	XXXI
Appendix 3. The First Occurrence of Monoclinic Jarosite in a Natural Environment: Supplementary Information	XLIX

List of Figures

Chapter 1

Figure 1.1. Photograph of jarosite outcrop at Southside Beach, Victoria, Australia	18
Figure 1.2. Photograph of jarosite boulder at Southside Beach, Victoria, Australia	20
Figure 1.3. Illustration of the crystal structure of jarosite.....	24
Figure 1.4. Rietveld–fitted synchrotron diffraction pattern of monoclinic natrojarosite and rhombohedral jarosite	25
Figure 1.5. Plot of powder XRD against temperature for the thermal decomposition of jarosite ...	26
Figure 1.6. Plot of δD versus $\delta^{18}O_{SO_4}$ for jarosite samples	28
Figure 1.7. Ball and stick schematic of the jarosite T–O–T structure	30
Figure 1.8. Atomic force microscopy height image of jarosite showing thin surface overlayers....	32

Chapter 2

Figure 2.1. Plot of Fe isotope composition of various rocks and minerals.....	37
Figure 2.2. Photograph from anion–exchange chromatography.....	39
Figure 2.3. Schematic set up of a MC–ICP–MS.....	40
Figure 2.4. Schematic plot of ion intensity vs mass for two iron isotopes measured using MC–ICP–MS.....	41
Figure 2.5. Image of a Thermo Fisher Scientific Neptune Plus MC–ICP–MS.....	42
Figure 2.6. Illustration of the three–isotope method and reversal approach to equilibrium	46

Chapter 3

Figure 3.1. Illustration of the geometric conditions for diffraction	49
Figure 3.2. Illustration of a crystal lattice	50
Figure 3.3. Schematic plot of wavelength distribution vs counts of the X–ray radiation produced by a sealed tube.....	51
Figure 3.4. XRD plots measured using copper and cobalt radiation	52
Figure 3.5. Schematic of the layout at the Australian Synchrotron	53
Figure 3.6. Schematic overview of the PD beamline at the Australian Synchrotron.....	54
Figure 3.7. Diagrammatical layout of the primary end station at the PD beamline.....	54

Figure 3.8. Partial XRD patterns of jarosite collected using synchrotron and laboratory X-ray sources	55
Figure 3.9. Two-dimensional diffraction image and diffraction cone from powder diffraction	56
Figure 3.10. Schematic of a PXRD pattern.....	57
Figure 3.11. Schematic of a Gaussian and Lorentzian function peak profile	58

Chapter 4

Figure 4.1. Geological map with Fossil Beach and Southside Beach sampling locations.....	65
Figure 4.2. Photographs of the different jarosite morphologies	66
Figure 4.3. Plot of unit cell parameters a vs. c of the jarosite samples in this study	71
Figure 4.4. Representative XRD patterns of jarosite showing asymmetrical peak broadening.....	72
Figure 4.5. Plot of Fe concentration vs Na + K concentration for the jarosite samples	73
Figure 4.6. Box and whisker plots comparing the $\delta^{56}\text{Fe}$ composition of the jarosite and sediment samples	75
Figure 4.7. Comparison of the $\delta^{56}\text{Fe}$ value of the different jarosite morphologies.....	76
Figure 4.8. Plot of the alkali ratio against $\delta^{56}\text{Fe}$ for the jarosite samples	77

Chapter 5

Figure 5.1. Illustration of the three-isotope method and reversal approach to equilibrium	90
Figure 5.2. Temporal variations in pH and K for jarosite and natrojarosite reactors	94
Figure 5.3. Temporal variations in $\delta^{57/56}\text{Fe}$ values for $\text{Fe(II)}_{\text{aq}}$ during reaction with jarosite and natrojarosite in $\text{Fe(II)}_{\text{aq}}$ solutions	96
Figure 5.4. Plot of pH against $\delta^{57/56}\text{Fe}$ values for $\text{Fe(II)}_{\text{aq}}$ during reaction with jarosite and natrojarosite in $\text{Fe(II)}_{\text{aq}}$ solutions	97
Figure 5.5. Temporal variation in $\delta^{56}\text{Fe}$ values of $\text{Fe(II)}_{\text{aq}}$ during reaction with jarosite and natrojarosite in $\text{Fe(II)}_{\text{aq}}$ solutions	98
Figure 5.6. Progression of $\delta^{56}\text{Fe}$ values of $\text{Fe(II)}_{\text{aq}}$ with the fractional approach to isotopic mass balance	99

Chapter 6

Figure 6.1. Representative PXRD pattern showing characteristic peak shouldering associated with monoclinic jarosite symmetry.....	114
Figure 6.2. Partial PXRD pattern of Js-SB-35A as a function of temperature	115
Figure 6.3. Partial PXRD pattern of Js-SB-35A natrojarosite transformation as a function of temperature	118
Figure 6.4. Plot of unit cell volume against temperature for Js-SB-35A PXRD data	119
Figure 6.5. Plot of Fe site occupancy against temperature	119
Figure 6.6. Partial PXRD patterns of Js-SB-35A showing the loss of peak shouldering in the natrojarosite during heating	120
Figure 6.7. TGA and DTA curves for Js-SB-35A	120
Figure 6.8. Large field view of Js-SB-35 thin section using BSE imaging.....	121

Figure 6.9. BSE images from across the thin section of Js–SB–35	122
Figure 6.10. Indexed EBSD image of Js–SB–35A	122
 Chapter 7	
Figure 7.1. Plot of $\delta^{56}\text{Fe}$ values of jarosite and sediment samples from this work and various rocks and minerals	133
 List of Tables	
Chapter 5	
Table 5.1. Extrapolated Fe isotope composition of $\text{Fe(II)}_{\text{aq}}$ and calculated equilibrium Fe isotope fractionation factors	92
 Chapter 6	
Table 6.1. Rietveld refinement results for the room temperature PXRD samples.....	116
Table 6.2. Pseudohexagonal lattice parameters for the room temperature PXRD samples.....	118

Chapter 1

Introduction to Jarosite: The “Garbage Can” of Minerals

This thesis describes an investigation into the iron isotope geochemistry, and crystal chemistry and structure of jarosite; it includes the examination of natural jarosite samples, collected from sulfur-rich sediments in Victoria, Australia, and experiments using natural and synthetic jarosites to better understand how this mineral forms and recrystallizes in acidic and sulfate-rich environments.

This work begins with an introductory chapter on the mineral jarosite and is laid out as follows: Section 1.1 gives a brief overview of jarosite; Section 1.2 explores jarosite formation and where it occurs; Section 1.3 describes the crystal structure of jarosite; Sections 1.4 and 1.5 describe the crystal chemistry and isotope geochemistry of jarosite, respectively; Section 1.6 explores jarosite dissolution and decomposition and what these processes suggest about jarosite recrystallization. Lastly, the aims and the structure of this thesis are outlined.

1.1 INTRODUCTION

Jarosite [$\text{KFe}_3(\text{SO}_4)_2(\text{OH})_6$] is a yellowish-brown mineral (Figure 1.1) that was first identified in 1852 by German mineralogist August Breithaupt in the “Jaroso Ravine”, part of the “Jaroso Hydrothermal System”, in Sierra Almagrera, Spain (Martínez-Frías et al., 2004; Swayze et al., 2008). It has since been reported in numerous environments including (but not limited to) the weathered region of sulfide-bearing ore deposits, acid sulfate soils, acid mine drainage, in acid-hypersaline lakes and playas, and in epithermal environments and hot springs (e.g. Alpers et al., 1989, 1992; Desborough et al., 2010; Jones and Renaut, 2007; Lueth et al., 2005; Welch et al., 2007). It has also been identified at several locations on Mars (e.g. Farrand et al., 2009; Klingelhöfer et al., 2004; Milliken et al., 2008) and is a by-



Figure 1.1. Photograph of a pale-yellow jarosite outcrop on light- to dark-brown cliff sediments at Southside Beach, Victoria, Australia.

product in several mineral processing industries (Dutrizac and Jambor, 2000). Jarosite is consequently a mineral of high importance in environmental and planetary research, as well as mineral processing.

Jarosite is a member of the alunite supergroup of minerals which have a general formula of $DG_3(TO_4)_2(OH)_6$. Members of the jarosite subgroup are characterised by the predominance of Fe(III) and S in the G and T sites, respectively, and contain either monovalent, divalent, trivalent, or tetravalent cations or a partial vacancy in the D site (Bayliss et al., 2010; Spratt et al., 2013; Welch et al., 2007). Jarosite can incorporate a wide range of ions in the D, G and T sites, earning it the nickname the “garbage can” mineral (Swayze et al., 2008), and there are several end-member variants of jarosite including natrojarosite $[NaFe_3(SO_4)_2(OH)_6]$, hydronium jarosite $[(H_3O)Fe_3(SO_4)_2(OH)_6]$, and ammoniojarosite $[NH_4Fe_3(SO_4)_2(OH)_6]$, just to name a few. Jarosite and related subgroup minerals can be divided into five main types, primarily based on their process of formation: supergene jarosite, hypogene jarosite, sedimentary jarosite, jarosite formed during mineral processing, and Martian jarosite.

1.2 JAROSITE FORMATION AND OCCURRENCE

Jarosite formation requires an environment that is highly acidic, oxidising and rich in sulfate and iron (Elwood Madden et al., 2012; Lueth et al., 2005; Papike et al., 2006). These conditions, and therefore often jarosite formation, often occur in the vadose zone (i.e. above the water table) in soils and sediments, or within sediment profiles where fluids can obtain high fO_2 and low pH values (Rye and Alpers, 1997). Jarosite has been reported as the most common jarosite subgroup phase in continental environments containing both K and Na (van Breemen, 1988; Zahrai et al., 2013), and this has been attributed to formation kinetics favouring jarosite over natrojarosite (Öborn and Berggren, 1995). It is also worth noting that pure hydronium jarosite is uncommon in nature due to it being unstable over geological timescales (Desborough et al., 2010; Swayze et al., 2008).

1.2.1 Supergene jarosite

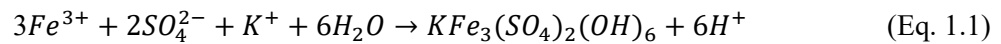
Supergene jarosite forms through the oxidation of sulfide-rich minerals in low (<100 °C) temperature environments (Desborough et al., 2010; Papike et al., 2006). It is typically very fine grained and commonly intermixed with hypogene phases such as clay minerals and quartz (Figure 1.2). The small grain size and admixture of other minerals with supergene jarosite can be prohibitive to its preparation and chemical analysis (Desborough et al., 2010; Lueth, 2006).

Supergene jarosite is commonly associated with acidic drainages, particularly acid mine drainage (AMD) and acid sulfate soils (ASS). AMD is formed through the aqueous oxidation of sulfide-rich ore minerals, commonly pyrite, resulting in the generation of acidic fluids (Desborough et al., 2010), and



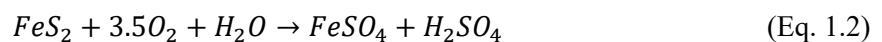
Figure 1.2. Photograph of an intermixed sediment–jarosite–iron oxide boulder at Southside Beach, Victoria, Australia.

jarosite formation because of AMD has been documented worldwide. For example, jarosite formation from AMD has been documented at Iron Mountain, a massive sulfide ore deposit in California, where jarosite precipitated from mining waters rich in iron and sulfate (Alpers et al., 1989; Jamieson et al., 2005; Nordstrom et al., 2000) according to Equation 1.1 (Nordstrom et al., 2000):

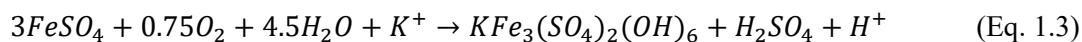


In the Tinto–Odiel Basin, Spain, oxidation of sulfide-bearing mine tailings occur as a consequence of mining in the Iberian Pyrite Belt and results in AMD and subsequent formation of jarosite (Egal et al., 2008). At the Mt Bischoff mine site, a tin deposit in Tasmania, Australia, weathering of open-pit sulfide exposures produced AMD that discharged from the main underground adit, with jarosite precipitation occurring downstream of the adit mouth (Gault et al., 2005). Jarosite has also been observed precipitating from acidic drainages formed through disturbed permafrosted sandstone bedrock overlying pyritic black shales (Lacelle and Léveillé, 2010).

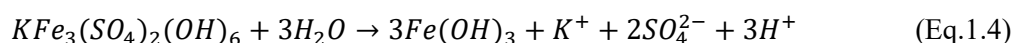
ASS form through the oxidation of soils and sediments containing iron-bearing sulfides, generating acid that surpasses the neutralising capacity of the soils and sediments (Dent, 1986; Fanning and Burch, 1997; Karimian et al., 2018b). Oxidation of the soils and sediments results in the generation of sulfuric acid and ferrous sulfate [FeSO_4] according to Equation 1.2 (Fanning and Burch, 1997):



Ferrous sulfate then undergoes oxidation and hydrolysis to form Fe(III)–bearing minerals (e.g. goethite, jarosite) according to Equation 1.3 (Fanning and Burch, 1997):



Jarosite is a major source of acidity in coastal acid sulfate soils (CASS; Beavis et al., 2005; Welch et al., 2008) as reactions involving jarosite in water can release acidity according to Equation 1.4 (Langmuir, 1997; Pritchett et al., 2012; White et al., 1997):



Over 17 million ha of ASS have been identified globally (Ljung et al., 2009). Jarosite–bearing soils have been described in (but not limited to) the US (Jennings and Driese, 2014; Wessel et al., 2017), Scandinavia (Öborn and Berggren, 1995), Thailand (Sukitprapanon et al., 2020), Vietnam (Husson et al., 2000), Antarctica (Lopes et al., 2019; Simas et al., 2006), and Australia. Australia has 3 million ha of ASS (Ljung et al., 2009), with inland and coastal occurrences being found to negatively impact land and water quality (Mosley et al., 2014b), as well as aquatic ecosystems (Glaspie et al., 2018). Consequently, the dissolution of jarosite in ASS conditions continues to be an area of active research in developing the best remediation strategies for ASS containing jarosite (Trueman et al., 2020).

Supergene jarosite has also been identified in the weathered regions of ore deposits, and on the upper flanks and summits of stratovolcanoes. For example, Scott (1987) examined jarosite in gossans derived from the weathering of Pb–Zn mineralisation in the Mount Isa region, Queensland, Australia. Cunningham et al. (2005) examined supergene destruction of a hypogene alunite deposit that resulted in the formation of supergene jarosite primarily through the oxidation of pyrite at Big Rock Candy Mountain in Utah. Zimbelman et al. (2005) identified fine–grained jarosite associated with smectite in slightly altered volcanic rocks from active stratovolcanoes in the eastern Trans–Mexican Belt and Cascade Range, North America. This jarosite was formed from sulfuric acid produced by oxidation of pyrite above the water table.

1.2.2. Hypogene jarosite

Hypogene (or steam–heated) jarosite forms through the oxidation of H₂S in near–surface environments commonly associated with volcanism (Papike et al., 2006). The temperature of these environments is typically 100–300°C, and the jarosite crystals, compared to supergene jarosite, are larger in size, well–formed and often chemically zoned. Impurities (e.g. gangue minerals) can also be present in steam–heated jarosite (Desborough et al., 2010; Lueth, 2006). Hypogene jarosite has been documented in

several hydrothermal environments. For example, Lueth et al. (2005) analysed jarosite formed from the oxidation of “sour gas” H_2S , which was derived from the thermochemical reduction of sulfate in an organic-rich sedimentary basin, in Rio Grande Rift-type (RGR) deposits in northern Mexico and New Mexico. Ebert and Rye (1997) reported coarsely crystalline steam-heated jarosite in the Crofoot–Lewis hot spring gold–silver deposit, north-western Nevada, attributing it to a late-stage alteration. Jones and Renaut (2007) documented jarosite precipitation from water discharging from a set of hot springs known as “Orange Spring”, in the Waiotapu geothermal area, New Zealand. Zimbelman et al. (2005) identified coarse ($>5\ \mu\text{m}$) jarosite associated with alunite and silica on active stratovolcanoes in the eastern Trans-Mexican Belt and Cascade Range, USA. This jarosite was identified in addition to the aforementioned supergene fine-grained jarosite, and its formation was attributed to oxidation of H_2S in volcanic gases.

1.2.3. Sedimentary jarosite

Sedimentary jarosite forms from aqueous sulfate that is either: (1) formed through the oxidation of pyrite minerals and is transported by groundwater; or (2) formed from wind-blown sulfate-rich seawater aerosols (Alpers et al., 1992), and it precipitates in sediments through the evaporation of water (Long et al., 1992). Sedimentary jarosite has not been documented as extensively as supergene and steam-heated jarosite, with most (if not all) occurrences being documented in the pore-fillings and near-surface playa sediments of acid-hypersaline lakes in southern Australia (Alpers et al., 1992; Bird et al., 1989; Long et al., 1992; Lyons et al., 1992).

1.2.4. Jarosite formed during mineral processing

Jarosite formed during mineral processing falls into two categories: (1) deliberately precipitated jarosite to control unwanted iron, sulfate, alkali elements and other impurities during mineral processing, and (2) unwanted jarosite precipitation. A classic example of deliberate jarosite precipitation is the ‘jarosite process’, used extensively in the zinc industry to remove the high (5 to 12 wt%) concentrations of Fe in Zn-sulfide concentrates. In the process, the Zn-sulfide concentrates are oxidised through roasting of the concentrate in air, primarily producing calcine containing zinc oxide. Between 5 and 15% of the zinc also combines with available Fe, forming zinc ferrite $[\text{ZnFe}_2\text{O}_4]$. Next, the calcine undergoes a “neutral-leach step” whereby dilute sulfuric acid is used to dissolve the zinc oxide, forming a ZnSO_4 -rich and almost Fe-free solution that can be purified and electrolysed. However, the zinc ferrite does not dissolve in this process, so this residue is then dissolved in hot, concentrated sulfuric acid to liberate the Zn. This dissolution also liberates the Fe, which needs to be removed so that the Zn can be recovered through recycling of the Zn and residual acids. Jarosite minerals are deliberately precipitated in the presence of alkali D site ions, typically Na^+ or NH_4^+ , to remove the unwanted Fe (Arregui et al., 1980; Dutrizac and Jambor, 2000; Graydon and Kirk, 1987; Leclerc et al., 2003).

An example of unwanted jarosite precipitation during mineral processing is the precipitation of jarosite during the bioleaching of chalcopyrite [CuFeS₂]. In this process, the oxidation of chalcopyrite results in the formation of elemental S. Microbial S oxidation typically produces SO₄²⁻_{aq}, Fe(III)_{aq} and Cu(II)_{aq}. Under low pH conditions and in the presence of monovalent alkali cations, jarosite precipitation occurs, coating the surface of the chalcopyrite (Li et al., 2013). This surficial jarosite has been implicated in chalcopyrite passivation during (bio)leaching (e.g. Sandström et al., 2005; Stott et al., 2000).

1.2.5. Martian jarosite

The existence of jarosite (and other ferric sulfate minerals) on the surface of Mars was first postulated based on evidence collected from the Viking landers (Burns, 1987). This speculation was then confirmed in 2004 by the MER rover Opportunity, which identified jarosite at Meridiani Planum using Mössbauer spectrometry (Klingelhöfer et al., 2004; Squyres et al., 2004). The jarosite discovered at Meridiani Planum was: (1) found to be Na-rich, with possible Al³⁺ substitution for Fe(III); (2) occurred as outcrop and in soil profiles; and (3) was found with hematite-rich outcrop and regolith, olivine-bearing regolith, and a pyroxene-bearing basaltic rock (known as Bounce rock; Klingelhöfer et al., 2004). Jarosite has since been identified at Valles Marineris (Milliken et al., 2008), Mawrth Vallis (Farrand et al., 2009), Ophir Chasma (Wendt et al., 2011), Noctis Labyrinthus (Thollot et al., 2012; Weitz et al., 2011), NE Syrtis Major (Ehlmann and Mustard, 2012), Gale Crater (Léveillé et al., 2015; Rampe et al., 2017) and Melas Chasma (Liu et al., 2018). Milliken et al. (2008) and Wendt et al. (2011) suggested that the jarosite identified at Valles Marineris and Ophir Chasma, respectively, is H₃O-rich. Liu et al. (2018), on the other hand, proposed that the jarosite observed at Melas Chasma is Na-K jarosite, while Farrand et al. (2009) suggested that the jarosite observed at Mawrth Vallis is K-rich. This suggests that jarosites on Mars may be chemically diverse, much like they are on Earth.

As jarosite is hydrated and oxidised, and contains OH⁻ and SO₄²⁻, the discovery of jarosite on Mars was hailed as a breakthrough in deciphering the past Martian environment as it provided mineralogical evidence for the occurrence of aqueous processes on Mars that likely occurred under oxidising, acid-sulfate conditions (Elwood Madden et al., 2004). It is also expected that jarosite will be an important mineral in understanding the evolution of the Martian atmosphere through isotope fractionation studies (Papike et al., 2006). Thus, there has been increased interest in examining the formation, geochemistry and stability of jarosite since the discovery of jarosite on Mars, particularly at sites considered potential Mars analogues, in the hopes of relating jarosite formation mechanisms on Earth to geological processes that operated on Mars in the past (e.g. Bhattacharya et al., 2016; Lacelle and Léveillé, 2010; Navrotsky et al., 2005; Papike et al., 2007; Pritchett et al., 2012). An essential piece to unravelling what jarosite can tell us about past Martian geological processes will be future sample return missions targeting jarosite-bearing surface outcrops.

1.3. JAROSITE CRYSTAL STRUCTURE

Natural jarosites and most synthetic jarosites crystallise in the rhombohedral space group $R\bar{3}m$, and consists of a trigonal network of intersecting chains of corner sharing octahedra, forming sheets perpendicular to the c axis (Figure 1.3A; Basciano and Peterson, 2008; Grey et al., 2013). Rhombohedral jarosites have hexagonal unit cell parameters of $a_h \sim 7.3$ Å and $c_h \sim 17$ Å, three formula units per unit cell ($Z = 3$), one octahedral Fe site that is partially or fully occupied, and all atoms in the structure occupy special positions with varying degrees of specialty (Basciano and Peterson, 2007, 2008; Grey et al., 2013; Papike et al., 2006). Substitution of typically monovalent ions into the large D site mainly affect the dimension of the c axis, with natrojarosite (Na^+) having a smaller c -axis compared to jarosite (K^+), while substitutions in the smaller octahedral G site mainly affect the a axis (Stoffregen et al., 2000).

Monoclinic jarosite $C2/m$, on the other hand, has only previously been reported for synthetic jarosites (Brand et al., 2012; Gasharova, 2000; Grey et al., 2011; Grey et al., 2013; Scarlett et al., 2013; Scarlett et al., 2010). Monoclinic jarosite has two independent Fe sites, Fe(1) at $0, 0, \frac{1}{2}$ and Fe(2) at $\frac{3}{4}, \frac{1}{4}, \frac{1}{2}$, and reflects an ordering of iron–site vacancies onto the Fe(1) site (Scarlett et al., 2010). The ordering of iron–site vacancies is accompanied by a lowering of symmetry, with monoclinic jarosites consisting of domains of butlerite–like $[\text{FeSO}_4(\text{OH}) \cdot 2\text{H}_2\text{O}]$ linear chains of Fe(2)–centred octahedra connected by corner–linking SO_4 tetrahedra (Figure 1.3B). The formation of these chains results in changes to the lattice parameters, with the a and c axis parameters expanding and contracting, respectively, relative to stoichiometric jarosite (Grey et al., 2011; Grey et al., 2013). The lowering of symmetry is manifested by the splitting of several peaks [e.g. $(033)_h$ and $(0.27)_h$] with a 1:2 intensity ratio in high resolution X–ray diffraction (XRD) patterns (Figure 1.4.; Grey et al., 2011; Grey et al., 2013; Scarlett et al., 2010).

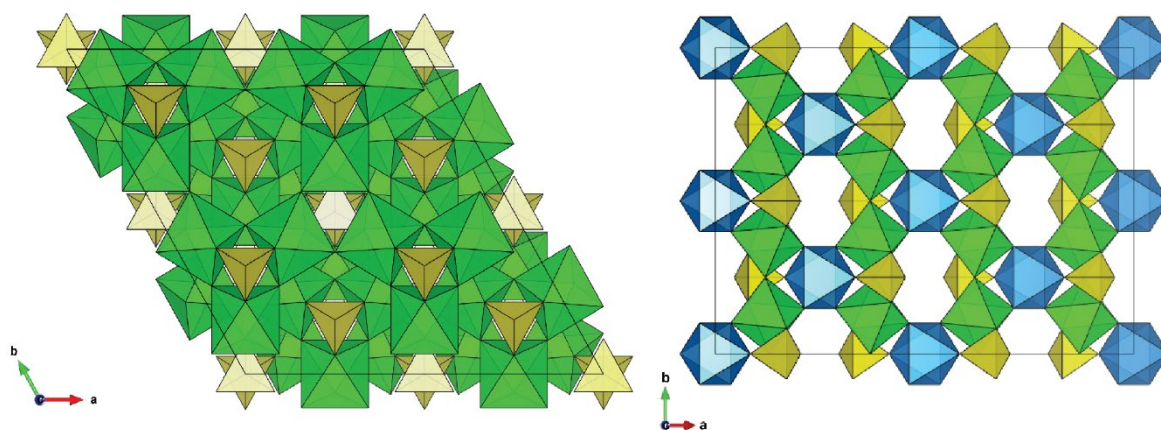


Figure 1.3. Illustration of the crystal structure of jarosite viewed along $[001]$. (A) Rhombohedral jarosite with iron octahedra (green) and sulfate tetrahedra (yellow) shown. (B) Monoclinic jarosite symmetry with the two iron octahedra sites (site one = blue, site two = green) and sulfate tetrahedra (yellow) shown. Models created using Vesta (2011) software.

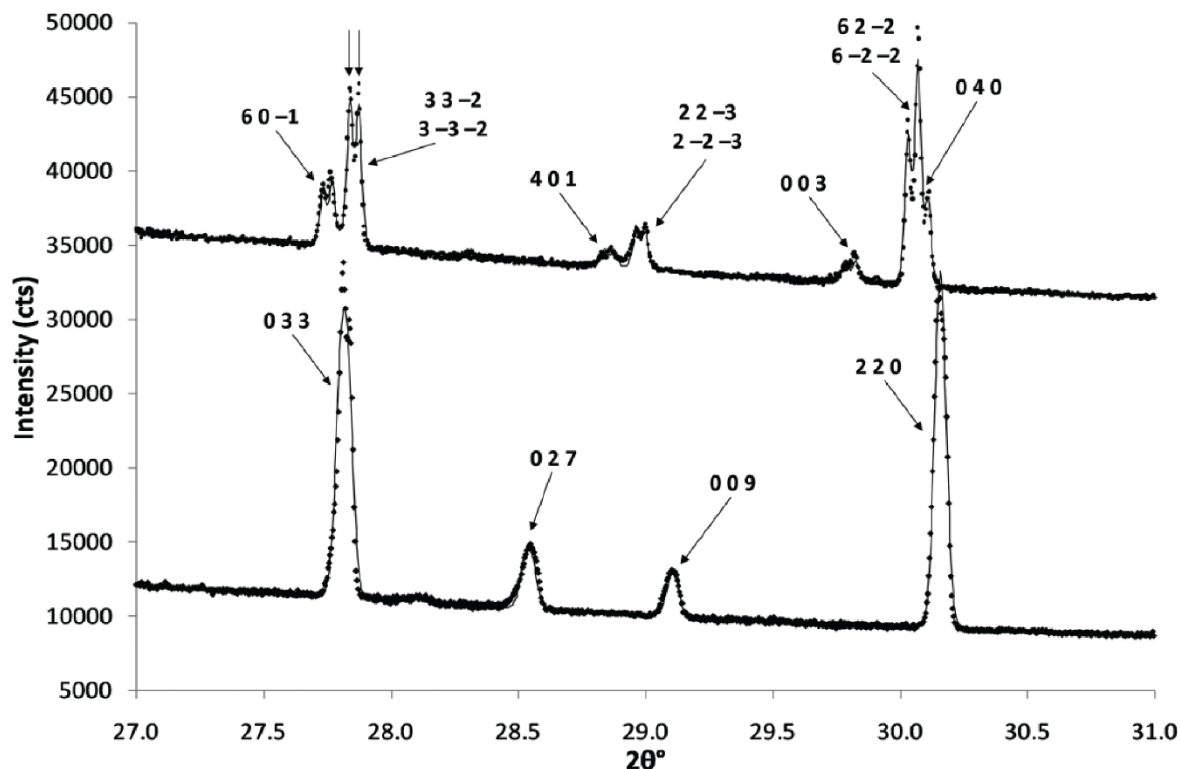


Figure 1.4. Part of a Rietveld–fitted synchrotron diffraction for monoclinic natrojarosite (top) and rhombohedral jarosite (lower) showing peak splitting associated with monoclinic symmetry. The natrojarosite and jarosite are labelled with monoclinic and hexagonal indices, respectively. The vertical arrows highlight an example of secondary peak splitting due to sample displacement across the capillary. Image from Scarlett et al. (2010).

During jarosite synthesis, stoichiometric rhombohedral jarosite formation is favoured to form at high temperatures (≥ 140 °C) and in Fe-rich fluids (Basciano and Peterson, 2007, 2008; Dutrizac, 1983) whereas non-stoichiometric rhombohedral jarosite formation is favoured in dilute solutions at typically lower temperatures (~ 100 °C or less; Drouet and Navrotsky, 2003; Kubisz, 1970; Savage et al., 2005). In contrast, monoclinic jarosite synthesis occurs at lower (80–120 °C) temperatures compared to stoichiometric rhombohedral jarosite, with the relative amount of the monoclinic phase increasing with increasing temperature. Monoclinic jarosite can be synthesized in non-acidified solutions, although jarosite synthesis is easier in acidified (i.e., ≥ 1 M H_2SO_4) solutions as lower temperatures and shorter reaction times are required (Grey et al., 2013; Scarlett et al., 2010, 2013).

There are differences in the behaviour of monoclinic and rhombohedral jarosite during heating. Monoclinic jarosite has been observed to decompose to stoichiometric rhombohedral jarosite at ~ 250 °C whereas non-stoichiometric rhombohedral jarosite has been observed to transform to stoichiometric jarosite at 170 °C (Grey et al., 2013). In both cases, the transformation of the jarosite is accompanied by the formation of FeOHSO_4 (Figure 1.5). Grey et al. (2013) attributed this difference in transformation temperature to monoclinic jarosite containing domains of a butlerite-phase, due to the ordered Fe

vacancies, that required higher energy input to dehydrate and transform compared to random Fe vacancies in the non-stoichiometric rhombohedral jarosite. During heating, both monoclinic and rhombohedral jarosite have also shown positive volume thermal expansion, although the magnitude of expansion varies between monoclinic and rhombohedral jarosite (Brand et al., 2017; Mills et al., 2013).

1.4. JAROSITE CRYSTAL CHEMISTRY

As previously mentioned, jarosite is a member of the alunite supergroup of minerals which have a general formula of $DG_3(TO_4)_2(OH)_6$ (Bayliss et al., 2010), with jarosite being able to incorporate various ions in the D, G and T sites. In the large D site, substitutions include (but are not limited to) monovalent cations Na^+ , H_3O^+ , Rb^+ , NH_4^+ , Ag^+ , divalent cations Ca^{2+} , Ba^{2+} , Pb^{2+} and Sr^{2+} , trivalent cations and REE's. Divalent cations Pb^{2+} , Zn^{2+} and Mg^{2+} and trivalent cations Al^{3+} , Cr^{3+} , V^{3+} and Ga^{3+} can substitute into the G site as well, and elements that form tetrahedral oxyanions (e.g. P, As, Cr and

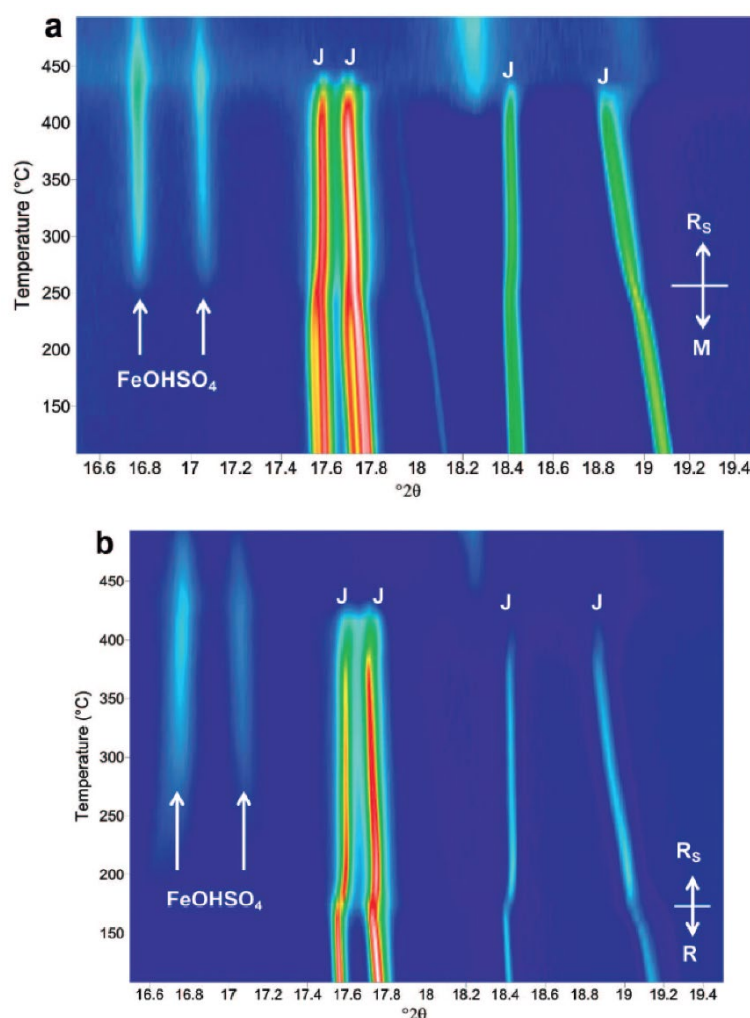


Figure 1.5. Plot of powder XRD patterns as a function of temperature for *in-situ* thermal decomposition of (a) monoclinic (M) jarosite and rhombohedral (R) jarosite. The arrows show peaks due to the presence of $FeOHSO_4$. The transformation to a stoichiometric rhombohedral jarosite phase (R_s) is indicated. Image from Grey et al. (2013).

Sb) can substitute into the T site (Papike et al., 2006; Welch et al., 2007). Non-stoichiometric occupancy of the D and G sites is common; thus, jarosite stoichiometry is typically calculated on the assumption that the T site is fully occupied (i.e. $T = 2$; Stoffregen et al., 2000). Natrojarosite $[\text{NaFe}_3(\text{SO}_4)_2(\text{OH})_6]$ is the most common naturally occurring variant of jarosite at Earth’s surface (Basciano and Peterson, 2007, 2008; Stoffregen et al., 2000), and jarosite group minerals regularly contain minor (a few %) amounts of hydronium in the D site (Drouet and Navrotsky, 2003; Ripmeester et al., 1986). The stability and reactivity of jarosite-group minerals depend on the degree of substitution into the D, G and T sites (Welch et al., 2007). Substitution of metallic and metalloid ions (e.g. As) can represent a store of toxic elements within jarosite’s structure that can be later mobilised into the environment (Karimian et al., 2017), along with acidity.

Complete solid solutions between jarosite, natrojarosite and hydronium jarosite have been observed in laboratory-synthesised samples (e.g. Basciano and Peterson, 2007, 2008; Drouet and Navrotsky, 2003; Ling et al., 2016) and have been modelled thermodynamically (Stoffregen, 1993). Natural jarosite and natrojarosite, on the other hand, have been found to have limited solid solutions. Glynn (2000) showed in a Lippmann phase diagram that at, 25 °C, natrojarosite and jarosite have different solubilities, suggesting that a solid solution is likely absent at low temperature. Papike et al. (2007) observed oscillatory Na–K zoning in their eight hypogene and three supergene natural jarosite and natrojarosite samples, suggesting physical mixing of endmember pairs occurs rather than solid solutions. Desborough et al. (2010) observed limited solid solutions and end-member mixing in 32 natural jarosite samples collected from supergene and hypogene environments, and suggested that this is due to a solvus in the jarosite–natrojarosite system below 140 °C. Furthermore, Desborough et al. (2010) suggested that for low temperature jarosite, intermediate compositions between natrojarosite and (K)jarosite likely reflect physical mixing of endmember pairs, like that seen by Papike et al. (2007), that often cannot be resolved due to the very fine-grained nature of low temperature jarosite. Thus, substantial chemical differences appear to exist between low temperature natural samples and synthesised jarosite’s, suggesting that caution should be used when applying the findings of synthetic jarosite studies to natural low temperature jarosite.

1.5. JAROSITE ISOTOPE GEOCHEMISTRY

1.5.1. H, O and S stable isotopes

As jarosite contains both sulfate and hydroxyl sites, $\delta^2\text{H}$, $\delta^{18}\text{O}_{\text{OH}}$, $\delta^{18}\text{O}_{\text{SO}_4}$ and $\delta^{34}\text{S}$ values for jarosite have been determined by several authors (Alpers et al., 1992; Chen and Li, 2014; Cunningham et al., 2005; Ebert and Rye, 1997; Lueth et al., 2005; Rye and Alpers, 1997; Zimbelman et al., 2005). Papike et al. (2006) summarises how these isotopes can be used to understand how a sample of jarosite formed. For example, Papike et al. (2006) demonstrated that low (~ -25 ‰ to $+5$ ‰) $\delta^{34}\text{S}$ values have been

recorded for jarosite samples that formed through the oxidation of pyrite or H_2S (i.e., supergene or hypogene jarosite) whereas jarosite samples that do not form from these precursors (i.e., sedimentary jarosite) have high ($\sim 22\text{‰}$) $\delta^{34}\text{S}$ values. Thus, $\delta^{34}\text{S}$ can be used to determine the sulfate source of the jarosite. Papike et al. (2006) also showed that the origin (i.e., supergene versus hypogene versus sedimentary formation) of jarosite can be determined using plots of $\delta^2\text{H}$ versus $\delta^{18}\text{O}_{\text{SO}_4}$ and $\delta^{34}\text{S}$ versus $\delta^{18}\text{O}_{\text{SO}_4}$. In both plots, sedimentary jarosite from acid–hypersaline lake deposits (“Australian lakes”; Alpers et al., 1992) is shown to plot clearly away from supergene and hypogene jarosite. However, in the plot of $\delta^2\text{H}$ versus $\delta^{18}\text{O}_{\text{SO}_4}$ (Figure 1.6), supergene samples from the Cascade Range, USA (Zimbelman et al., 2005), and hypogene samples from the RGR deposits, northern Mexico and New Mexico (Lueth et al., 2005), plotted half in and half out of the field of values suggested for supergene jarosite by Rye and Alpers (1997). Papike et al. (2006) suggested that this is due to supergene and hypogene jarosite producing similar $\delta^2\text{H}$ and $\delta^{18}\text{O}_{\text{SO}_4}$ systematics. Therefore, caution may be required when interpreting the origin of jarosite from $\delta^2\text{H}$ versus $\delta^{18}\text{O}_{\text{SO}_4}$ plots. Jarosite has also been used as a single–mineral geothermometer by calculating $\Delta\text{O}_{\text{SO}_4\text{--OH}}$ (Lueth et al., 2005; Rye and Stoffregen, 1995).

1.5.2. K/Ar and $^{40}\text{Ar}/^{39}\text{Ar}$ isotopes

Radiometric dating of jarosite using K/Ar and $^{40}\text{Ar}/^{39}\text{Ar}$ has been undertaken by several authors to constrain the age of jarosite mineralisation, as well as to better understand the geological processes responsible for the jarosite’s formation (Chen and Li, 2014; Cunningham et al., 2005; Kula and Baldwin, 2011; Lueth et al., 2005; Rye et al., 2000; Samuels–Crow et al., 2012; Vasconcelos et al., 1994). For example, Vasconcelos et al. (1994) measured the $^{40}\text{Ar}/^{39}\text{Ar}$ of supergene jarosite and alunite from Goldfield, Nevada, and used the results to infer that an extensive oxidative weathering event

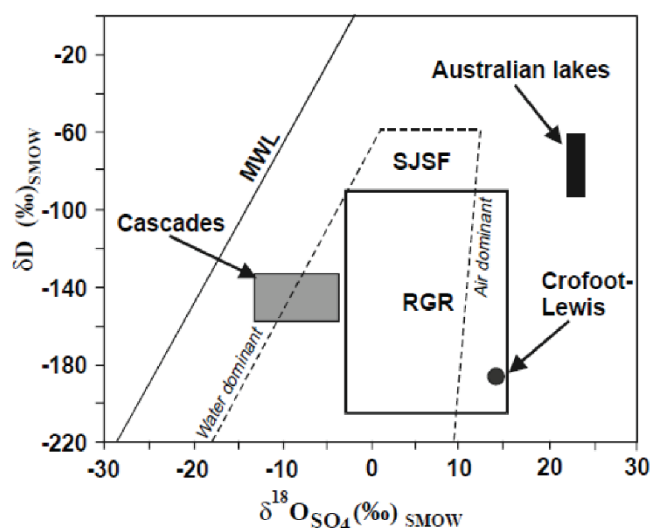


Figure 1.6. Plot of δD (an alternate expression for $\delta^2\text{H}$) versus $\delta^{18}\text{O}_{\text{SO}_4}$ values for jarosite samples from Papike et al. (2006). The supergene jarosite sulfate field (SJSF; dashed line) delineates the range of values expected for supergene jarosite (Rye and Alpers, 1997). The meteoric water line (MWL) is also shown.

occurred in the western USA during the late Miocene. Lueth et al. (2005) measured the $^{40}\text{Ar}/^{39}\text{Ar}$ of jarosite from Rio Grande Rift–type (RGR) deposits in northern Mexico and New Mexico and were able to demonstrate that the systems that produced the fluorite + barite ± sulfide + jarosite deposits were long-lived, with one deposit forming over 0.8 million years based on jarosite dating.

1.5.3. Fe stable isotopes

Iron isotope geochemistry has been shown to reflect mineral–fluid interactions and redox changes in low temperature systems allowing researchers to better understand processes such as mineral formation and recrystallization in iron-bearing minerals (Johnson et al., 2020). Despite this, only a limited number of stable Fe isotope measurements have been collected for jarosite. Dauphas and Morris (2008) examined the $\delta^{56}\text{Fe}$ of basaltic tephra from the Mauna Kea Volcano, Hawaii, that had undergone acid–sulfate alteration, forming jarosite-bearing tephra. They recorded $\delta^{56}\text{Fe}$ +0.15 ‰ for unaltered tephra and $\delta^{56}\text{Fe}$ from ~+0.11 to +0.26 ‰ for jarosite-bearing tephra. They attributed the heavy $\delta^{56}\text{Fe}$ of the jarosite-bearing tephra to Fe isotopic fractionation during basalt dissolution, partial oxidation or jarosite deposition. Egal et al. (2008) recorded $\delta^{56}\text{Fe}$ values of –0.69 ‰ (± 0.15 ‰, 2σ) and 1.14 ‰ (± 0.10 ‰, 2σ) for a jarosite and jarosite–hydronium jarosite sample from the Tinto and Odiel Basin, Spain. These values are significantly different and are outside of the range of values seen by Dauphas and Morris (2008), suggesting that jarosite can have a wide range of $\delta^{56}\text{Fe}$ values. Little is known about how iron isotopes are fractionated between jarosite and other iron-bearing minerals and dissolved iron species, making interpretation of these values challenging. However, given that limited data show jarosite can have a wide range of $\delta^{56}\text{Fe}$ values, there is the potential that the Fe isotope composition of jarosite is influenced by its formation and interactions with the environment, making this a promising avenue of research for understanding jarosite formation and behaviour over time.

1.6. JAROSITE DISSOLUTION AND DECOMPOSITION AND THE IMPLICATIONS FOR JAROSITE RECRYSTALLISATION

There have been many experimental studies examining the dissolution and decomposition of jarosite (e.g. Elwood Madden et al., 2012; Karimian et al., 2017; Karimian et al., 2018a; Welch et al., 2007, 2008; Zahrai et al., 2013) but few (if any) studies have examined jarosite recrystallisation despite the likelihood of it occurring in nature. This is a gap in the literature that should be investigated. It is, however, possible to speculate on the jarosite recrystallisation process based on existing jarosite dissolution and decomposition research.

Jarosite dissolution has been shown to be incongruent by several authors, with D site cations (i.e. Na^+ , K^+ , H_3O^+) and SO_4^{2-} being preferentially released during jarosite dissolution relative to Fe (Elwood Madden et al., 2012; Gasharova et al., 2005; Kendall et al., 2013; Smith et al., 2006b; Trueman et al.,

2020; Welch et al., 2007, 2008). Smith et al. (2006b) modelled two jarosite surfaces and found that distortion of the surfaces resulted in facilitation of the removal of K^+ , and to a lesser extent, SO_4 during jarosite dissolution relative to Fe, which was found to be located deep within the tetrahedral–octahedral–tetrahedral (T–O–T) sheet structure of jarosite (Figure 1.7). Thus, the incongruent dissolution of jarosite has been attributed to the T–O–T structure of jarosite making Fe more sterically remote and difficult to access compared to D site cations and SO_4^{2-} . This likely applies to jarosite recrystallisation as well.

Jarosite dissolution and transformation has been shown to be affected by pH, the presence of Fe(II), the composition of the jarosite and surrounding media, and whether the jarosite is synthetic or natural. Welch et al (2007) found that during the dissolution of natural jarosite, more iron was released into solution in reactors at a lower pH (3 vs 4), which was attributed to increased solubility of Fe(III) at lower pH conditions. However, at a lower pH (3 vs 4) there was a smaller release in K^+ and SO_4^{2-} into solution. In terms of dissolution rate, Elwood Madden et al (2012) and Zahrai et al (2013) observed that during the batch dissolution of synthetic jarosite and natrojarosite, respectively, dissolution rates increased with increasing pH above pH 3.5 and 3.8, respectively, but also increased with decreasing pH, forming a V-shape. Elwood Madden et al (2012) and Zahrai et al (2013) attributed this to different dissolution mechanisms occurring at low and high pH, with either increasing H^+ or OH^- concentration accelerating dissolution. Thus, jarosite appears to be most stable between a pH of 3.5 and 3.8, and this pH range may be most conducive for jarosite recrystallisation to occur.

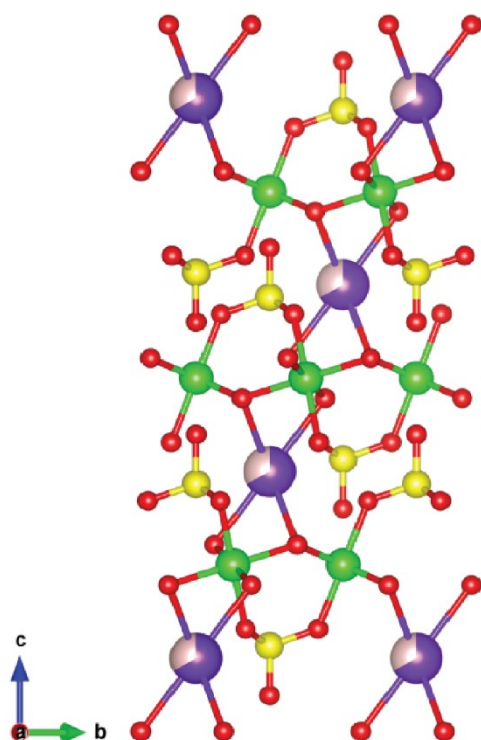


Figure 1.7. A ball and stick model of the T–O–T structure of jarosite viewed along [100]. K, Fe, S and O atoms are represented by purple, green, yellow, and red balls, respectively. Model after Smith et al. (2006) and created using Vesta (2011) software.

Jarosite transformation to more stable Fe(III)–bearing minerals is catalysed by Fe(II)_{aq} in (near–)neutral pH conditions (Jones et al., 2009; Karimian et al., 2017; Karimian et al., 2018a). Jones et al. (2009) found that synthetic jarosite completely transformed to ferrihydrite and lepidocrocite in seven days in 1 mM Fe(II)_{aq} at pH 6.5. Karimian et al (2017) found that Fe(II)_{aq} drove the transformation of synthetic As/Sb–bearing jarosite to iron oxides at neutral pH, with higher concentrations of Fe(II)_{aq} (e.g. 20 mM versus 5 mM) causing quicker transformation. However, at low pH (i.e., pH 4), Karimian et al (2018a) observed no significant transformation of synthetic As/Sb–bearing jarosite to iron oxide after the addition of 20 mM Fe(II)_{aq}. Karimian et al (2017) also noted that the addition of Fe(II)_(aq) caused the rapid release of K⁺_(aq) at all Fe(II) concentrations. This was not observed for SO₄^{2–}_(aq): at lower Fe(II) concentrations (1 and 5 mM), there was a large and rapid increase in SO₄^{2–}_(aq) whereas at higher Fe(II) concentration (10 and 20 mM), the increase in SO₄^{2–}_(aq) was smaller and slower. It is unclear if jarosite still interacts with Fe(II)_(aq) without significant transformation (i.e., during recrystallization), although it has been observed for Fe(II)_(aq) and goethite at low pH (Reddy et al., 2015), suggesting that it is possible.

Jarosite composition has been found to affect the rate of jarosite dissolution and the potential for jarosite to decompose. For example, Zahrai et al. (2013) observed that the batch dissolution rate of synthetic natrojarosite in their study was marginally faster than the batch dissolution rate of synthetic jarosite observed by Elwood Madden et al. (2012). Gasharova et al. (2005) calculated the dissolution rates for synthetic K⁺ and H₃O⁺ jarosite in deionised water and found that the substitution of H₃O⁺ for K⁺ accelerated jarosite dissolution. Kubisz (1971) and Drouet and Navrotsky (2003) observed that the dehydroxylation temperature of natrojarosite and hydronium jarosite is lower than that of jarosite. Stoffregen (1993) calculated Gibbs free energy values of –3416.3 and –3371.9 kJ/mol for jarosite and natrojarosite, respectively, suggesting that decomposition of jarosite is less likely under favourable conditions compared to natrojarosite. Thus, the presence of Na⁺ and/or H₃O⁺ in the D site rather than K⁺ has been found to increase the solubility and reactivity of jarosite. This may be the case for jarosite recrystallisation as well.

Jarosite dissolution is affected by the composition of surrounding fluids. Welch et al (2007) observed that during the dissolution of natural jarosite, the rate of jarosite dissolution was faster and more Fe, K⁺ and SO₄^{2–} was released into solution in reactors containing HCl as opposed to H₂SO₄ and this was attributed to the mineral and solution being closer to equilibrium in the sulfate reactors. Jarosite dissolution is also affected by the presence of organic material and silica. Jones et al. (2009) demonstrated that the Fe(II)–catalysed transformation of synthetic jarosite to ferrihydrite at circumneutral pH was inhibited by high concentrations of silica and natural organic matter owing to adsorption to the surface of jarosite preventing Fe(II) adsorption, and inhibiting dissolution of jarosite

and thus reprecipitation of ferrihydrite. These findings demonstrate that care will need to be taken when designing experiments to examine jarosite recrystallization in aqueous media.

Synthetic jarosite has been observed to be more reactive and more soluble than natural jarosite. Welch et al. (2008) found that the rate of dissolution of natural jarosite in their study was orders of magnitude slower than the rate of dissolution of synthetic jarosite observed by Smith et al (2006b) and Gasharova et al (2005). They attributed this to the formation of an iron-rich residuum [Fe-(OOH)] phase over time as cations in the D site and SO_4^{2-} were preferentially leached. This residuum then likely formed a passivating layer on the jarosite surface, reducing reaction rates relative to the ‘clean’ jarosite of the other studies.

The formation of a passivating layer has also been suggested by other authors as an explanation for the decrease in apparent reaction rates over time. Welch et al. (2007) observed a decrease in apparent reaction rates over time in their natural jarosite dissolution experiments and this was attributed to the formation of a diffusion-inhibiting layer on the mineral surface which was either a leached layer that formed as ions were preferentially removed or was a layer of secondary precipitates that formed from dissolution and subsequent precipitation. Gasharova et al. (2005) observed the formation of thin, overlayers on synthetic jarosite in an aqueous solution of deionized water at circumneutral pH (Figure 1.8). These layers were thought to be Fe(III) oxyhydroxides of poor crystallinity and were observed to impede jarosite dissolution. Removal of this layer through Fe(III) complexation using $\text{Na}_2\text{-EDTA}$ (and HCl to slightly acidify the solution) resulted in acceleration of the dissolution of jarosite. Kendall et al.

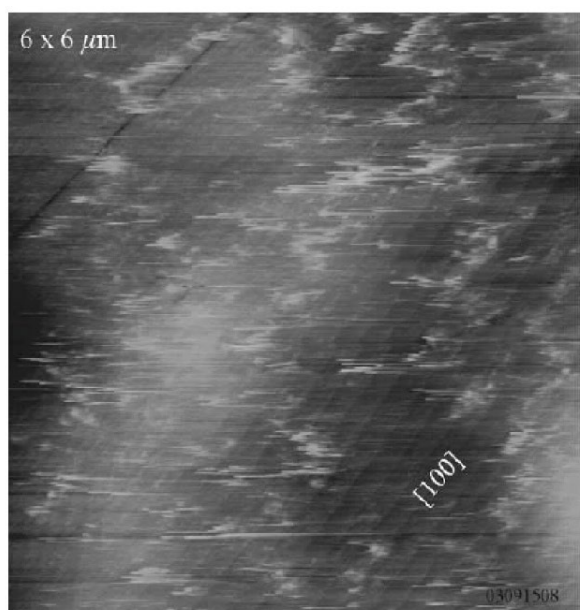


Figure 1.8. Atomic force microscopy height image of jarosite showing the formation of thin surface overlayers. Image from Gasharova et al. 2005

(2013) observed that the dissolution of synthetic As-bearing jarosites in ultrapure water decreased over time and attributed this to the formation of an enrichment of surface layer arsenate-iron complex sites, inhibiting jarosite dissolution over time. Given that the formation of a passivating layer appears to be a common occurrence during natural and synthetic jarosite dissolution, the formation of a passivating layer may occur during natural jarosite recrystallisation as well.

1.7. THESIS AIMS AND STRUCTURE

Examination of the jarosite literature shows that little is known about (1) the iron isotope composition of jarosite, despite it having the potential to shed light on jarosite formation and recrystallisation, and (2) how jarosite recrystallisation occurs over time, despite this likely being a very common process in environments such as ASS and AMD on Earth, as well as a process that could have operated on Mars in the past. To this end, the main objective of this work was to investigate jarosite formation and recrystallisation by investigating its iron isotope geochemistry. Natural jarosite samples were collected from jarosite-bearing outcrops in sulfur-rich coastal sediments in Victorian, Australia. Two sites were selected due to an abundance of jarosite outcrops and diverse jarosite morphologies at both sites creating natural laboratories to study jarosite formation and stability in the environment. Understanding how iron isotopes are fractionated between jarosite and Fe(II) is an important part of the interpretation process so experiments examining Fe isotope exchange and fractionation during jarosite recrystallisation under acid-sulfate conditions were conducted. Consequently, the jarosite recrystallisation process was also examined.

To support the investigations, the crystal chemistry and crystal structure of the natural jarosites and synthetic jarosites used in experiments were examined using powder X-ray diffraction (XRD) data collected at the Australian Synchrotron. Powder XRD data were collected at the Australian Synchrotron as high resolution data are required to resolve small changes in the jarosite unit cell and crystal structure such as the changes in the occupancy of D-site cations in the jarosite structure. During this process, a natural sample of monoclinic jarosite was identified. There have been no previous reports of natural monoclinic jarosite, so examination of the natural monoclinic jarosite sample became the third aim of this work.

This thesis is split into several chapters: Chapters 2 and 3 introduce the two main techniques utilised in this research: iron isotope geochemistry and X-ray diffraction, respectively. Chapter 4 details an investigation into the iron isotope geochemistry and mineralogy of jarosite in sulfur-rich sediments and the implications this has for jarosite formation. Chapter 5 describes the findings of laboratory experiments examining the exchange and fractionation of Fe isotopes between aqueous Fe(II) and jarosite, and the implications this has for jarosite recrystallisation in acid-sulfate environments. Chapter

6 reports on the first occurrence of monoclinic symmetry in a natural jarosite sample and the implications this has for monoclinic jarosite formation and behaviour in the natural environment. Finally, Chapter 7 summarises the results obtained throughout this research, discusses them in the context of jarosite formation and recrystallisation in acid–sulfate environments, and suggests future research directions to better understand the complex environmental behaviour of natural jarosites.

Chapter 2

Introduction to Iron Isotope Geochemistry

2.1 INTRODUCTION TO STABLE IRON ISOTOPE GEOCHEMISTRY

Stable isotope geochemistry examines the natural isotopic variability of elements containing two or more stable isotopes that occurs as a consequence of chemical and physical processes other than radioactive decay (White, 2018). Until recently, stable isotope geochemistry was restricted to light elements, primarily hydrogen, carbon, nitrogen, oxygen and sulfur, due to mass spectrometry techniques not having the sufficient sensitivity and precision to resolve the very small isotopic variations that occur in heavier elements such as magnesium and iron. With the advent of more sensitive analytical techniques, particularly multi-collector inductively coupled plasma–mass spectrometry (MC–ICP–MS), which was introduced in 1992 (Douthitt, 2008), these small variations were able to be resolved, paving the way for the study of the isotopic composition of heavier elements, particularly iron (Dauphas and Rouxel, 2006; Teng et al., 2017).

Iron is the fourth most abundant element in the Earth's crust (Beard and Johnson, 2004) and the most abundant redox-active metal on Earth and in the Solar System (Johnson et al., 2020). Located in the first transition series and group 8 of the periodic table, iron primarily behaves as a siderophile element according to Goldschmidt's (1937) classification. It can also behave as a chalcophile element in the presence of high concentrations of sulfur, and as a lithophile element in the presence of high concentrations of oxygen (Johnson et al., 2020). Iron has three oxidation states: Fe⁰ (metallic iron), Fe(II) (ferrous iron) and Fe(III) (ferric iron) (Dauphas et al., 2017), and four naturally occurring stable isotopes, ⁵⁴Fe, ⁵⁶Fe, ⁵⁷Fe and ⁵⁸Fe, with isotopic abundances of 0.058, 0.917, 0.021 and 0.0028, respectively (Meija et al., 2016). Metallic iron is primarily present in the core, ferrous iron in the mantle, and ferric iron in oxygenated surface environments. As a result, iron is an important element in core, mantle and crustal processes, and well as surficial processes, making it an element of high interest in earth and planetary science (Dauphas et al., 2017).

Iron isotope variations reflect differences in the partitioning of two or more isotopes between two phases, a process known as isotopic fractionation. The $\delta^{56}\text{Fe}$ values for natural samples vary by ~8 ‰ (Figure 2.1), with samples from high temperature environments having a small (<1 ‰) isotopic range due to high temperatures causing smaller isotopic fractionations between two phases (Johnson et al., 2020). Nevertheless, variations in iron isotopes have been used to shed light on high temperature processes including (but not limited to) planetary formation (e.g. Elardo and Shahrar, 2017; Jordan et al., 2019; Polyakov, 2009), magmatic mineral formation (e.g. Dziony et al., 2014; Liu et al., 2014; Schoenberg et al., 2009), and hydrothermal ore deposit formation (Markl et al., 2006; Wawryk and Foden, 2015; Zhu et al., 2018).

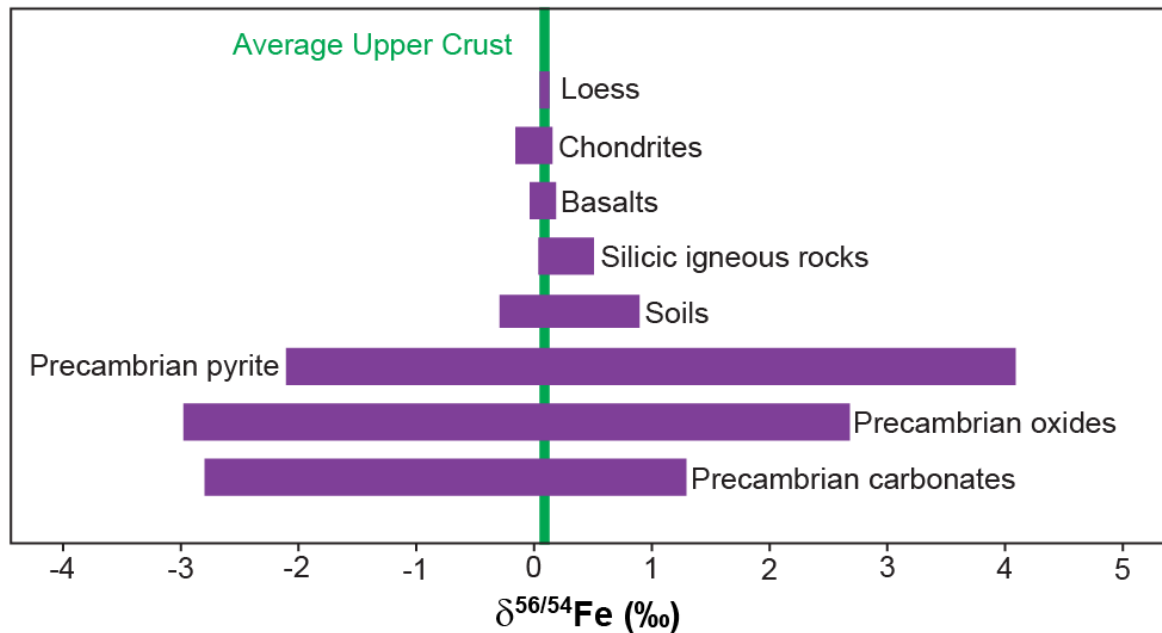


Figure 2.1. Range in Fe isotope compositions for various rocks and minerals. Isotope data reported as $\delta^{56/54}\text{Fe}$ values relative to IRMM-014. Illustration modified after Johnson et al. (2020).

Low temperature environments, on the other hand, have large Fe isotope variations reflecting mineral–fluid interactions and changes in redox causing large isotopic fractionations to occur (Johnson et al., 2020). As a result, there has been a lot of interest among researchers as to whether iron isotope fractionations can be used to better understand low temperature mineral precipitation and recrystallisation (e.g. Frierdich et al., 2019; Mansor and Fantle, 2019; Wiesli et al., 2004), biologically-mediated processes such as microbial dissimilatory iron reduction (e.g. Beard et al., 1999; Crosby et al., 2007) and microbial iron oxidation (e.g. Balci et al., 2006; Planavsky et al., 2009), and ancient processes and environmental conditions (e.g. Busigny and Dauphas, 2007; Busigny et al., 2018; Rouxel et al., 2005). Consequently, there is extensive literature on the iron isotope composition of (banded) iron formations (e.g. Busigny et al., 2018; Johnson et al., 2008; Planavsky et al., 2012), black shales and sedimentary pyrites (e.g. Duan et al., 2010; Guilbaud et al., 2011; Tahata et al., 2015), and carbonates (e.g. Craddock and Dauphas, 2011; Czaja et al., 2010; Heimann et al., 2010). However, as previously noted, few studies have investigated the iron isotope composition of iron sulfate minerals such as jarosite (e.g. Dauphas and Morris, 2008; Egal et al., 2008) and schwertmannite (Egal et al., 2008).

The remainder of this chapter provides an overview of iron isotope geochemistry relevant to the low temperature research present in this thesis. For a comprehensive overview of iron isotope research in low and high temperature environments, readers are directed to Dauphas et al. (2017) and Johnson et al. (2020).

2.2. IRON ISOTOPE GEOCHEMISTRY NOMENCLATURE

Iron is reported in the standard delta notation, which is the part per mil (‰) deviation in the ratio of $^i\text{R}/^j\text{R}$ of a sample relative to the $^i\text{R}/^j\text{R}$ of a standard according to Equation 2.1 (modified from Johnson et al., 2020):

$$\delta^i E_{\text{sample}} (\text{‰}) = [(^i\text{R}/^j\text{R})_{\text{sample}} / (^i\text{R}/^j\text{R})_{\text{standard}} - 1] \times 1000 \quad (\text{Eq. 2.1})$$

where i and j are heavy and light isotopes, respectively, of ratio R of element E . As a result, iron isotope values for a sample that are greater than zero are said to be isotopically “heavy” whereas iron isotope values less than zero are considered isotopically “light” (Anbar and Rouxel, 2007).

Iron isotope values are commonly reported as $\delta^{56}\text{Fe}$ and $\delta^{57}\text{Fe}$, which are variations in the ratios of $^{56}\text{Fe}/^{54}\text{Fe}$ and $^{57}\text{Fe}/^{54}\text{Fe}$, respectively. The $^{57}\text{Fe}/^{54}\text{Fe}$ ratio is related to $^{56}\text{Fe}/^{54}\text{Fe}$ through mass dependent fractionation (Dauphas et al., 2012). For the research presented in this thesis, iron isotope values are also presented in $\delta^{57/56}\text{Fe}$ ($^{57}\text{Fe}/^{56}\text{Fe}$). Iron isotope values were bracketed against the IRMM–524a iron standard in this research, which has an identical iron isotope composition to IRMM–014 (Craddock and Dauphas, 2010).

2.3 SAMPLE PREPARATION AND PURIFICATION

Sample preparation typically begins with powdering of rock samples so that the material to be analysed is representative of the bulk rock chemistry. A small aliquot (typically up to a few tens of milligrams) is then transferred to a Teflon beaker for digestion by acid followed by evaporation to dryness. Often there are several cycles of dissolution followed by evaporation to ensure complete dissolution of insoluble elements (e.g. fluorides) and to ensure iron is in the +3 oxidation state. The sample is then taken up in acid for anion–exchange chromatography (Dauphas et al., 2017).

Iron in rock samples is primarily purified via anion–exchange chromatography. The process used is typically modelled after that of Strelow (1980). Anion–exchange resin, the most commonly used being AG1–X8 200–400 mesh size (Dauphas et al., 2017), is loaded into a polypropylene column. The resin is then pre–cleaned typically using dilute HCl (e.g. 0.1 M HCl) or a combination of concentrated HNO_3 (e.g. 5 M HNO_3), H_2O and dilute HCl (e.g. Schoenberg and von Blanckenburg, 2005). The resin is then pre–conditioned with concentrated HCl (e.g. 6 M HCl). Next, the sample is loaded in concentrated HCl (e.g. 6 M HCl). Concentrated HCl is used during loading as it causes Fe(III) to bind strongly to the resin (by forming an FeCl anion complex), whereas matrix elements, with the exception of a few elements such as Cu and Co, do not so can be eluted from the column. The Fe(III) is then collected by loading dilute HCl (e.g. 0.1 M HCl; Strelow, 1980) or H_2O and HNO_3 (Schoenberg and von Blanckenburg,

2005) onto the column to remove the Fe(III) from the resin (by causing the Fe to come out of the FeCl anion complex). Once the Fe is fully eluted, the sample is evaporated to dryness in preparation for analysis. To achieve a high level of purification, the chromatography processes can be repeated multiple times (Dauphas et al., 2017).

In this research, sample purification involved dissolving jarosite in HCl and filtering the sample to remove insoluble organic material. The iron in the samples was purified using cation–exchange chromatography followed by anion–exchange chromatography (Figure 2.2). Cation exchange chromatography was required to remove the copious amounts of sulfate present in the samples. The exact procedure and acids using during the cation– and anion–exchange chromatography is outlined in the research chapters utilising iron isotope geochemistry.

2.4 ANALYTICAL METHODS

2.4.1 MC–ICP–MS

MC–ICP–MS was the primary method used to analyse iron isotopes in this research due to its high iron ionisation efficiency, stable instrument mass bias, high precision ($\delta^{56}\text{Fe}$ can be measured to $\pm 0.03\text{ ‰}$) and ability to analyse samples rapidly (Beard and Johnson, 2004; Dauphas et al., 2017; Johnson et al., 2020). A MC–ICP–MS is a magnetic sector multi–collector mass spectrometer with an inductively coupled plasma source. Samples are dissolved in dilute nitric acid (e.g. 2–3% HNO_3) then introduced into the machine via a desolvating nebuliser or a quartz spray chamber (Dauphas et al., 2017). The sample are then ionised by the plasma source (Figure 2.3). Following ionisation, the ions are accelerated using extraction and focusing transfer lenses and shaped to fit through the entrance slit of the mass analyser. The mass analyser consists of an electrostatic spherical analyser (ESA) and magnetic sector field. The ESA filters ion based on their kinetic energy. The ions are then separated based on their mass/charge ratios and velocity using the magnetic sector field. The ions of the different isotopes are

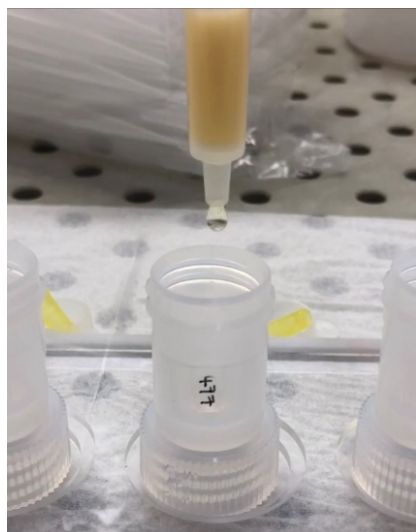


Figure 2.2. Photograph from anion–exchange chromatography showing elution of iron (yellow droplet) off a chromatography column.

then measured simultaneously using a detector consisting of a series of Faraday collectors. Alignment of the isotope beams with the Faraday collectors is crucial for accurate measurements. This is achieved by aligning the Faraday collectors to collect each isotope beam optimally, or by using quadratic zoom lenses to change the mass dispersion of the ion beams so they align with the Faraday collectors (Schönbächler, 2016). Due to the high sensitivity of the collectors, very small concentrations of iron were required in the samples (e.g. 3 ppm).

The stable instrument mass bias present in MC-ICP-MS was corrected using sample-standard bracketing (SSB) in this research following the methods of Sossi et al. (2015). In sample-standard bracketing, a sample is measured in between two standards of known isotopic compositions such that the difference in the standard measurements can be used to correct for the small instrument drift (e.g., He et al 2015, Liu et al 2014, Weyer and Schwieters 2003). This method, while simple and effective, does not mitigate against matrix elements that can influence the instrument mass bias, thus skewing the measurements. Matrix effects can be minimised by ensuring the sample and standards are matrix matched (i.e. have similar iron and acid concentrations), and by ensuring that the iron is well purified and potentially interfering elements are removed. This can be done by passing the sample through the column chemistry procedure multiple times (Dauphas et al., 2017). Alternative processes for correcting instrument mass bias including element doping and double spiking (Dideriksen et al., 2006; Gong et al., 2020; Millet et al., 2012; Schoenberg and von Blanckenburg, 2005).

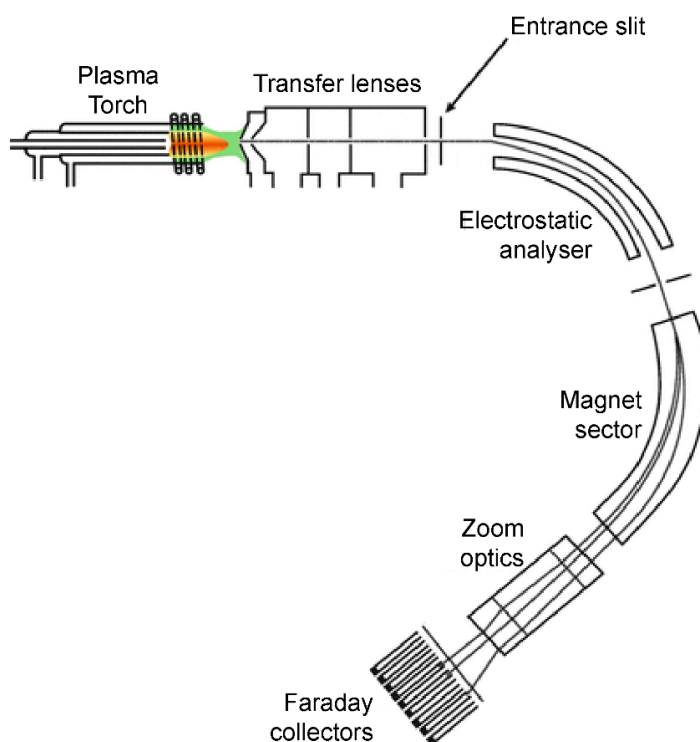


Figure 2.3. Schematic set up of a MC-ICP-MS. Images modified from Schönbächler (2016).

One challenge inherent to MC–ICP–MS analysis is polyatomic ion interference. Ionisation of argon can produce $^{40}\text{Ar}^{14}\text{N}$, $^{40}\text{Ar}^{16}\text{O}$, and $^{40}\text{Ar}^{16}\text{OH}$, which are isobaric on ^{54}Fe , ^{56}Fe and ^{57}Fe , respectively. Modern MC–ICP–MS instruments utilise “pseudo high mass resolution” to correct for these interferences. This technique works by narrowing the beam width using a narrow defining slit, which produces a flat-topped portion of the Fe isotope peak of interest that is free from argide interference (Figure 2.4). The instrument can then be configured to capture the Fe isotope signature only, either by aligning the Faraday collectors or by adjusting the quadratic zoom lenses (Johnson et al., 2020; Weyer and Schwieters, 2003). This technique does have a couple of issues. Firstly, the width of the peak-top is often narrow, so accurate measurements of the peak-top requires high instrument stability which can be difficult as the instruments are sensitive to temperature change (Dauphas et al., 2017). Secondly, when measuring in multi collection mode, simultaneous resolution of isobaric interferences is only achievable when the interference is detectable on the same side of the elements of interest (Johnson et al., 2020).

2.4.1.1 Thermo–Fisher Neptune Plus MC–ICP–MS

A Thermo Fisher Scientific Neptune Plus MC–ICP–MS (Figure 2.5) was used for iron isotope measurements conducted during this research. The Neptune Plus is a double-focusing analyser with ion optics that provide high mass resolution. This is required to separate out the argide interference present during iron isotope measurements. The Neptune Plus was operated in medium resolution mode

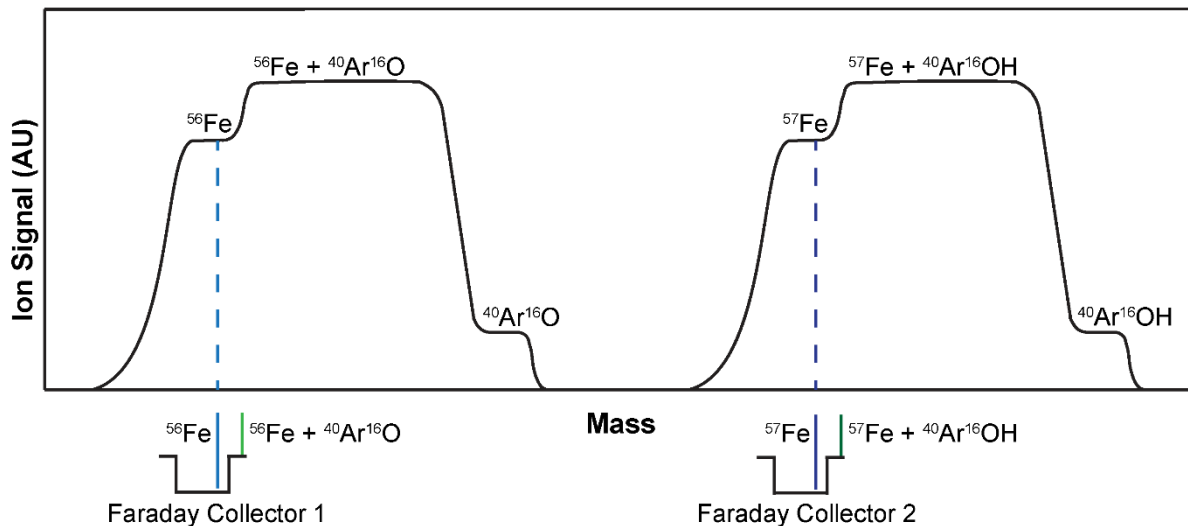


Figure 2.4. Schematic plot of ion intensity vs mass for two iron isotopes. The narrow flat-top peak associated due to collection of ^{56}Fe and ^{57}Fe signals without interference from $\text{Ar}^{40}\text{O}^{16}$ and $\text{Ar}^{40} + ^{16}\text{OH}$, respectively. This can be achieved by aligning the Faraday collector cups so that only the Fe isotope signals (in blue) are collected while the Fe + argide signal (in green) is not. The argide interference of $^{56}\text{Fe} + \text{Ar}^{40}\text{O}^{16}$ and $^{57}\text{Fe} + \text{Ar}^{40} + ^{16}\text{OH}$ occur to the right of the peaks for ^{56}Fe and ^{57}Fe , respectively, resulting in them being able to be resolved simultaneously. Image based on Weyer and Schwieters (2003) and Johnson et al. (2020).

using a wet plasma. ^{53}Cr , $^{54}(\text{Fe} + \text{Cr})$, ^{56}Fe , ^{57}Fe , ^{60}Ni and ^{61}Ni isotopes masses were collected in Faraday cups at Low 4, Low 2, Low 1, Centre, High 2 and High 4 positions, respectively. Prior to sample analysis, the machine was tuned to optimise the ion signal. This involved moving the position of the torch and adjusting the sample and auxiliary gas flow to optimise the ion signal. Samples were introduced into the machine via a desolvating nebuliser.

2.4.2 Other methods

In the 1980s and 1990s, before the advent of multiple-collector inductively coupled plasma–mass spectrometry (MC–ICP–MS), thermal ionisation mass spectrometry (TIMS) was primarily used to analyse iron isotopes. TIMS can effectively measure $\delta^{56}\text{Fe}$ to a precision of ± 0.2 ‰, however, evaporation of the sample from the filament over time results in a variable mass bias that can be challenging to correct for, it has low iron ionisation efficiency, and it takes a long time to analyse samples (4–8 hours per analysis; Beard and Johnson, 2004; Dauphas et al., 2017; Johnson et al., 2020). Iron isotopes can also be measured using two *in-situ* techniques: secondary ionisation mass spectrometry (SIMS; e.g. Kita et al., 2011; Marin–Carbonne et al., 2011) and laser–ablation multiple-collector inductively coupled plasma–mass spectrometry (LA–MC–ICP–MS; e.g. Yoshiya et al., 2012).

2.5 IRON ISOTOPE FRACTIONATION

Iron isotope fractionation examines the partitioning of two or more isotopes of iron between two phases (Dauphas et al., 2017). Iron isotope fractionation in nature is almost always mass–dependent (Johnson et al., 2020) and there are two main processes that fractionate (iron) isotopes: kinetic fractionation and equilibrium fractionation. Kinetic fractionation involves the exchange of isotopes between two phases



Figure 2.5. Image of a Thermo Fisher Scientific Neptune Plus MC–ICP–MS. Image credit: Thermo Fisher Scientific.

that are not in chemical equilibrium and is reflective of the high translational velocities of light isotopes (Johnson et al., 2020). Typically, lighter isotopes are concentrated in the reaction products and heavier isotopes, in the reactants (Schauble, 2004). There are several kinetic processes that fractionate iron isotopes including diffusion (e.g. Rodushkin et al., 2004), Soret diffusion (e.g. Richter et al., 2009), and evaporation/condensation (e.g. Wang et al., 1994).

Equilibrium fractionation, on the other hand, involves iron isotope exchange between two phases that are in chemical equilibrium and largely reflects differences in the zero-point vibrational energies of isotopically substituted species. At higher oxidation states, phases that contain covalently-bonded atoms from near the top of the periodic table, and that have lower coordination numbers, are typically associated with stronger, stiffer bond formation, and stronger bonds are typically enriched in heavier iron isotopes compared to weaker bonds. Temperature and pressure also affect bond stiffness, with higher pressures and lower temperatures increasing bond strength. Thus, equilibrium isotope fractionation between two phases is influenced by the composition of the phases, temperature and pressure present during the fractionation, and redox state (Johnson et al., 2020; Schauble, 2004; Shahar et al., 2017). Equilibrium isotope fractionation has been examined in mineral–mineral (e.g. Shahar et al., 2008; Sossi and O'Neill, 2017), mineral–metal (e.g. Elardo and Shahar, 2017; Poitrasson et al., 2009), mineral–fluid (e.g. Frierdich et al., 2019; Wiesli et al., 2004) and fluid–fluid processes (e.g. Johnson et al., 2002; Welch et al., 2003).

2.5.1. Fractionation factors

The partitioning of iron isotopes between two phases is expressed using fractionation factors (α values). The isotopic fractionation of iron between two substances, A and B, is defined by Equation 2.2:

$$\alpha_{A-B} = R_A^{i/j} / R_B^{i/j} \quad (\text{Eq. 2.2})$$

where i and j are the heavy and light isotopes, respectively (e.g. $^{56}\text{Fe}/^{54}\text{Fe}$), used in the ratio, R , of substances A and B. As such, α_{A-B} represents the contrast of the isotopic compositions of substances A and B. When applied to delta values, Equation 2.2 can be re-written as Equation 2.3:

$$\alpha_{A-B} = (1000 + \delta^i E_A) / (1000 + \delta^i E_B) \quad (\text{Eq. 2.3})$$

where $\delta^i E$ is the delta value of element E (i.e. iron) in substance A and B. Normally, α_{A-B} is very close to unity, typically on the order of 1.00X. Consequently, this equation can be modified such that the $\delta^i E$ of the two phases can simply be subtracted from each other to ascertain the fractionation factor. Utilising the relation that $X \approx 10^3 \ln(1.00X)$, Equation 2.3 can be re-written as Equation 2.4 (Johnson et al., 2020):

$$10^3 \ln \alpha_{A-B} \approx \delta^i E_A - \delta^i E_B \equiv \Delta_{A-B}^i \quad (\text{Eq. 2.4})$$

where Δ_{A-B}^i is the difference in the isotopic composition of substances A and B.

Fractionation factors can be measured directly through experiments or can be calculated by combining reduced partition coefficients.

2.5.1.1 Calculated fractionation factors

Reduced partition coefficients, also known as β -factors, reflect the differences in the vibrational frequencies between two isotopes of an element. Typically, reduced partition coefficients can be calculated using the differences in zero-point energies and a harmonic oscillator approximation according to Bigeleisen and Mayer (1947). For two phases, A and B, β -factors can be related to α -values according to Equation 2.5 (Johnson et al., 2020):

$$1000 \ln \alpha_{A-B} = 1000 \ln \beta_A - 1000 \ln \beta_B \quad (\text{Eq. 2.5})$$

where β is the reduced partition coefficient of an element in substances A and B. There are two primary methods used to calculate β -factors for iron-bearing phases: first-principle electronic structure calculations and derivation of β -factors by modelling spectroscopic data. Density functional theory (DFT; Hohenberg and Kohn, 1964; Kohn and Sham, 1965) is the most commonly used first-principle electronic structure calculation techniques, and has been used to examine isotopic fractionation in Fe-bearing aqueous and mineral phases (Anbar et al., 2005; Blanchard et al., 2009, 2015; Domagal-Goldman and Kubicki, 2008; Rustad et al., 2010; Rustad and Dixon, 2009). Infrared spectroscopy, Raman spectroscopy, Mössbauer spectroscopy and nuclear resonant inelastic X-ray scattering (NRIXS) are spectroscopic techniques that have been used to derive β -factors. Modelling data from these techniques has been used to examine isotopic fractionation in Fe-bearing minerals (Blanchard et al., 2015; Dauphas et al., 2012; Polyakov, 1997; Polyakov et al., 2007; Polyakov and Mineev, 2000; Roskosz et al., 2015; Schauble et al., 2001).

2.5.1.2 Experimental fractionation factors

Experimental determination of fractionation factors involves conducting a series of laboratory experiments to examine isotope exchange and fractionation over time. There are several methods that can be used to determine equilibrium iron isotope fractionation factors including synthesis, partial exchange, three isotope exchange, and reversal isotope exchange. For this research, the three-isotope exchange and reversal isotope exchange methods were employed to investigate iron isotope exchange and fractionation between jarosite and $\text{Fe(II)}_{\text{aq}}$ (Chapter 5). Readers are directed to Shahar et al. (2017) and Johnson et al. (2020) for descriptions of the synthesis and partial exchange methods.

The three–isotope method is a robust process that was first employed to examine oxygen isotope fractionation between quartz and water (Matsuhisa et al., 1978), and has since been used to examine iron isotope exchange and fractionation between mineral–fluid, mineral–metal and mineral–mineral phases (Beard et al., 2010; Elardo and Shaha, 2017; Frierdich et al., 2014a, 2014b, 2019; Reddy et al., 2015; Shaha et al., 2008; Wu et al., 2012). The method tracks changes in the isotopic composition of two phases by examining changes in the abundance of three stable isotopes (e.g. ^{54}Fe , ^{56}Fe and ^{57}Fe) over time. One phase is enriched in an isotope tracer, commonly ^{57}Fe , while the other has a natural abundance isotopic composition. Thus, the two samples do not plot on the same mass–dependent isotope fractionation line at the beginning of the experiment: the natural phases plots on the terrestrial fraction line (TFL) while the enriched phase plots away from the TFL.

As isotope exchange occurs between the two phases, the isotopic composition of the phases approaches a secondary fraction line (SFL) that is determined by the system mass–balance and has the same slope as the TFL. The fractionation factor is obtained by determining the difference in the isotopic values of each component after complete exchange, and if exchange is incomplete, extrapolation to the SFL to obtain the value is common. Furthermore, in experiments where the majority of iron atoms reside in the phase with the natural–abundance isotopic composition, it is common for that phases initial isotopic composition to be extrapolated to the SFL as it is unlikely to change over time (e.g. Frierdich et al., 2019).

The changes in isotopic composition are tracked on a three–isotope plot. The enriched isotopic ratio (e.g. $^{57}\text{Fe}/^{56}\text{Fe}$) is used to examine the extent of isotopic exchange while the non–enriched isotopic ratio (e.g. $^{56}\text{Fe}/^{54}\text{Fe}$) is used to examine changes in the isotope fractionation factor during the experiment. The advantage of using an enriched isotope tracer is that it can clearly show whether exchange between the two phases has occurred in a closed system, and whether equilibrium is reached (Frierdich et al., 2019; Johnson et al., 2020; Shaha et al., 2017).

Several studies (e.g. Frierdich et al., 2014a, 2014b, 2019) have combined the three–isotope method with the reversal method to examine isotope exchange and fractionation. The reversal method, also known as the multi–directional approach, involves running two isotope exchange experiments simultaneously. Both experiments contain one isotopically identical component (e.g. $^{57}\text{Fe}/^{56}\text{Fe}$) while the second components (e.g. $^{56}\text{Fe}/^{54}\text{Fe}$) isotopic composition varies: one has an initial isotopic composition above the predicted equilibrium value; the other has an initial isotopic composition below the predicted equilibrium value. Thus, equilibrium is approached from two directions, allowing for a more precise calculation of the equilibrium isotope fractionation factor (Figure 2.6A). Similarity in the final fractionation factor for the two experiments provides confidence that the results are not due to laboratory induced kinetic affects (Johnson et al., 2020; Shaha et al., 2017).

One challenge inherent to the three–isotope method is that there can be small mass balance differences across a series of experiment reactors due to minute variations in the reactor set–up (e.g. minor variations in the amount the two phases added to each reactor). To correct for this, Frierdich et al. (2019) plotted the ratio of $^{56}\text{Fe}/^{54}\text{Fe}$ against F , the fractional approach of ^{57}Fe towards the system mass balance, according to Equation 2.6 (modified from Frierdich et al., 2019):

$$F = (\delta^{57/56}\text{Fe}_t - \delta^{57/56}\text{Fe}_i) / (\delta^{57/56}\text{Fe}_{\text{sys}} - \delta^{57/56}\text{Fe}_i) \quad (\text{Eq. 2.6})$$

where $\delta^{57/56}\text{Fe}_t$ is the $^{57}\text{Fe}/^{56}\text{Fe}$ composition of one reacting component at time t , $\delta^{57/56}\text{Fe}_i$ is the initial $^{57}\text{Fe}/^{56}\text{Fe}$ composition of that component, and $\delta^{57/56}\text{Fe}_{\text{sys}}$ is the $^{57}\text{Fe}/^{56}\text{Fe}$ composition of the entire system (i.e. system mass balance). Plotting $^{56}\text{Fe}/^{54}\text{Fe}$ against F normalises out the small mass balance differences, and the equilibrium fractionation factor is still determined by calculating the difference in the isotopic composition of each component at equilibrium ($F = 1$) or extrapolation to equilibrium (Figure 2.6B).

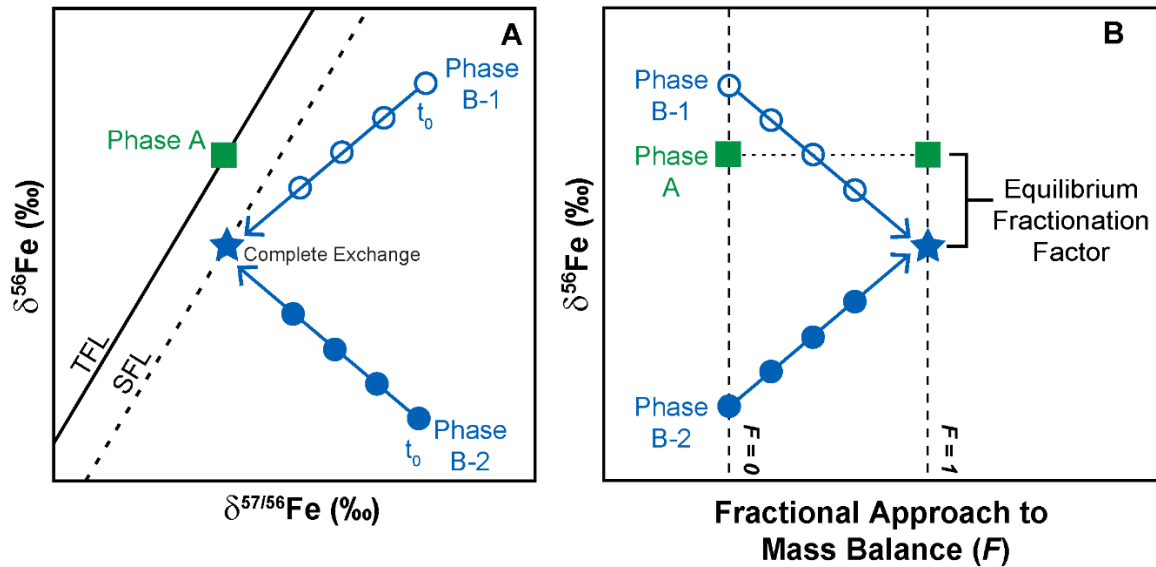


Figure 2.6. Illustration of the three–isotope method and reversal approach to equilibrium. (A) Phase A with a natural–abundance isotopic composition plots along the terrestrial fractionation line (TFL) while the enriched phases, Phase B–1 and Phase B–2, are off–set from the TFL. Phase B–1 and Phase B–2 have $\delta^{56}\text{Fe}$ ratios above and below the predicted equilibrium value, respectively. Thus, equilibrium is approached from two directions. As isotopic exchange occurs between the sample and enriched phases, the isotopic composition of the enriched phases approaches a secondary fractionation line (SFL), determined by the system mass balance, until exchange is complete. (B) Plot of $\delta^{56}\text{Fe}$ against F , the fractionation approach of ^{57}Fe towards the system mass balance. The difference in the $\delta^{56}\text{Fe}$ of Phase B and Phase A after complete exchange ($F = 1$) represents the equilibrium fractionation factor. Illustration modified after Frierdich et al (2019).

Chapter 3

Introduction to X-ray Diffraction

3.1 INTRODUCTION TO DIFFRACTION

Diffraction is the process whereby waves scattered from periodically repeating objects interact with one another. It can be visualised simplistically as the bending of waves when the wave encounters a slit in a material. This bending results in the generation of a secondary wave, which radiates away from the slit. To generate the second wave, the wavelength of the initial wave needs to be similar to the aperture of the slit. When a material contains a regularly spaced set of slits or “diffraction grating”, there will be numerous secondary waves generated, with waves in some directions interacting constructively while other waves interact destructively. Quantum mechanical wave–particle duality demonstrates that matter can undergo wave–like processes and thus diffraction.

Crystalline solids can be viewed as 3–dimensional diffraction gratings as they are comprised of regularly spaced planes of atoms. Diffraction of a crystalline solid occurs when incoming radiation with a wavelength similar to that of the distance between planes of atoms is scattered. The angle at which the radiation is coherently scattered is described by Bragg’s Law (Bragg 1913):

$$n\lambda = 2d\sin\theta \quad (\text{Eq. 3.1})$$

where λ is the wavelength of the incoming radiation, d is the spacing of planes of atoms in the crystal structure, θ is the angle of incidence (which equals the angle of scattering), and n (an integer) is the order of reflection. Bragg’s law essentially constrains the angles at which constructive interference can occur in a crystalline solid: the incoming radiation of wavelength λ is effectively reflected by the planes of atoms, described by d , in the crystalline solid at measurable angle θ . Consequently, the angle between the incoming and diffracted radiation is 2θ (Figure 3.1). Diffraction patterns therefore represent a set of intensity peaks at 2θ values which correspond to the interplanar spacings, d , in a crystal. Interplanar spacings are described using Miller indices (hkl).

The structure of a crystalline solid is made up of a set of repeating “unit cells”. Unit cells are the smallest repeating motif required to fully describe the structure and are defined by three axes (a , b , c) and three inter–axis angles (α , β , γ) (Figure 3.2). Determination of the structure of a crystalline solid using diffraction involves two main steps: the calculation of unit cell vectors from the diffraction pattern, and calculation of the electron density by structure factors (Suortti, 2003). Calculation of the electron density of a crystalline solid is challenging due to the “phase problem”: the phase of the diffraction intensity cannot be extracted from the diffraction data. Fortunately, several methods have been developed to overcome this problem (e.g. the Patterson method, three–beam diffraction), and Sayre (2015) provides a good overview of these methods.

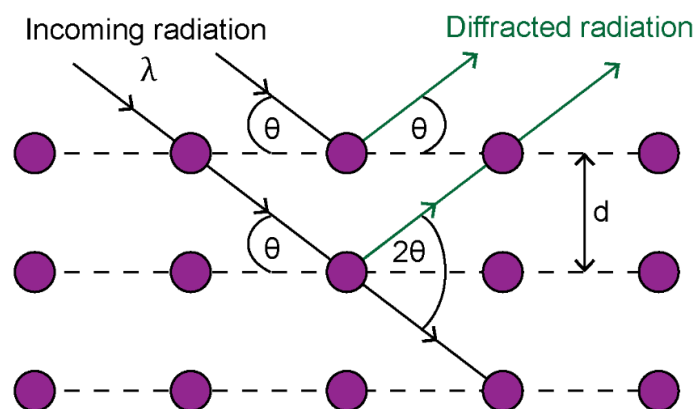


Figure 3.1. Illustration of the geometric conditions for diffraction based on Bragg's Law. The purple circles represent atoms in a crystal structure. The black dashed lines represent the planes in the crystal structure, with “d” reflecting the distance between the planes. The black and green arrows represent the incoming and diffracted radiation of wavelength λ . Illustration after Epp (2016).

There are two radiation sources commonly used to examine the structure of crystalline solids through diffraction: X-rays and neutrons. X-rays interact with the electron cloud of the crystalline material whereas neutrons interact with the atomic nuclei. The scattering of neutrons by the nucleus, rather than by electrons, means that neutrons can penetrate further into a crystalline solid whereas X-rays probe the surface layer of the solid. X-ray scattering is dependent on the electron density. This means that the scattering of X-rays is directly proportional to the atomic number of each atoms, resulting in heavier atoms dominating the scattering of X-rays whereas light elements (e.g. hydrogen) may be essentially invisible. Neutron scattering, on the other hand, is not related proportionally to atomic number; therefore, neutrons can be used to examine lighter elements in a crystalline material.

Both X-ray and neutron diffraction have been used to examine the structural properties of jarosite (e.g. Brand et al., 2017). For this study, X-ray diffraction (XRD) was selected for several reasons. Firstly, high resolution data was required for elucidating the structural features of the jarosite and XRD could achieve this more easily than neutron diffraction. Secondly, XRD can be conducted on smaller sample sizes compared to neutron diffraction. Small (~20 mg) samples were used in the exchange experiments, and many of the subsamples were <0.5 g, making neutron diffraction unsuitable for analysing the samples. The remainder of this chapter provides an overview on XRD relevant to the studies presented in this thesis. Readers are directed to Bish and Post (1989), Dittrich and Bieniok (2009) and Lavina et al. (2014) and for a comprehensive overview of X-ray diffraction.

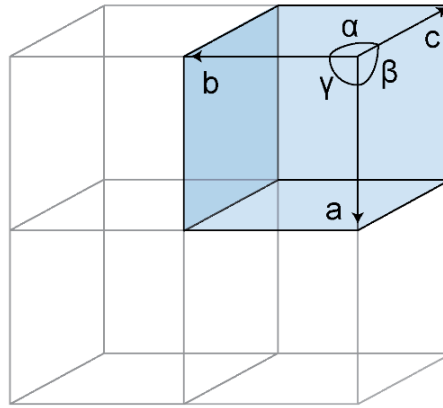


Figure 3.2. Illustration of a crystal lattice with one unit cell highlighted. The three axes and three inter-axis angles used to describe the unit cell are shown.

3.2 X-RAYS AND THEIR SOURCES

X-rays were discovered by W. C. Röntgen in 1895 and the diffraction of X-rays by a crystalline solid was first discovered by M. von Laue in cooperation with W. Friedrich and P. Knipping in 1912 (Friedrich et al., 1912). X-rays are high-energy electromagnetic radiation with a relatively short wavelength and a penetration depth ranging from microns to millimetres. The short wavelengths (0.1 to 100 Å) of X-rays, similar to inter-atomic spacings, makes them suitable for probing the structure of crystalline solids.

X-ray sources differ in their power, energy (wavelength), beam geometry and tunability. It is common to characterise an X-ray source using its brilliance according to Equation 3.2:

$$\text{brilliance} = \frac{\text{intensity}}{\text{divergence} \times \text{area} \times \text{bandwidth}} \quad (\text{Eq. 3.2})$$

There are two main sources of X-rays used for XRD: laboratory generated and synchrotron generated X-rays.

3.2.1 Laboratory X-rays

Laboratory sources commonly use sealed tubes or rotating anodes to produce X-rays. A cathode (e.g. a tungsten filament) is heated in a vacuum to generate electrons via thermionic emission. The electrons are then accelerated through a high potential field and directed at a metal anode target (e.g. copper, molybdenum), which then emits X-ray radiation. The X-ray radiation is a spectrum with strong peaks of particular wavelengths dependent on the composition of the anode (Figure 3.3). Filters or monochromators are then used to remove unwanted radiation, and slits are used to modulate the size

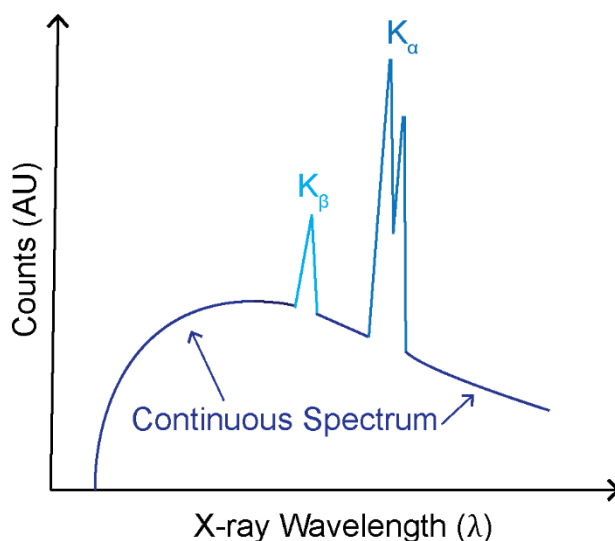


Figure 3.3. Schematic plot of wavelength distribution vs counts of the X-ray radiation produced by a sealed tube illustrating the continuous spectrum and the few strong peaks associated with K_α and K_β radiation. Illustration after Epp (2016).

and shape of the X-ray beam. The most intense radiation is typically K_α radiation, which represents electrons from the L shell falling into the inner K shell, releasing X-rays. A smaller amount of X-ray radiation known as K_β radiation is released when electrons fall from the M shell into K shell. Lastly, detectors record the diffracted X-rays, converting the intensity of X-rays into a signal that can then be analysed.

3.2.1.1 Bruker D8 Advance Eco

A small number of samples were analysed using a Bruker D8 Advance Eco X-ray diffractometer with a cobalt radiation source during this research. This diffractometer was used for phase identification and preliminary analysis. A cobalt radiation source was used to avoid iron fluorescence which would be present with a Cu tube (Cullity, 1978). Iron fluorescence results in high background level, which can lead to incorrect phase identification (Figure 3.4). The diffractometer was equipped with a high-speed line position sensitive detector, Lynxeye XE, with energy discrimination capability, and a manual divergence slit. Powdered samples were mounted dry on a zero-background holder [Si single crystal (911)] to minimise interference from the holder during diffraction.

3.2.2 Synchrotron X-rays

While the processes that generate synchrotron X-rays are on a larger scale to a traditional laboratory setup, parts of the process are familiar. Firstly, an electron gun uses thermionic emission to produce electrons from a heated metal plate. These electrons are then accelerated in a linear accelerator to an

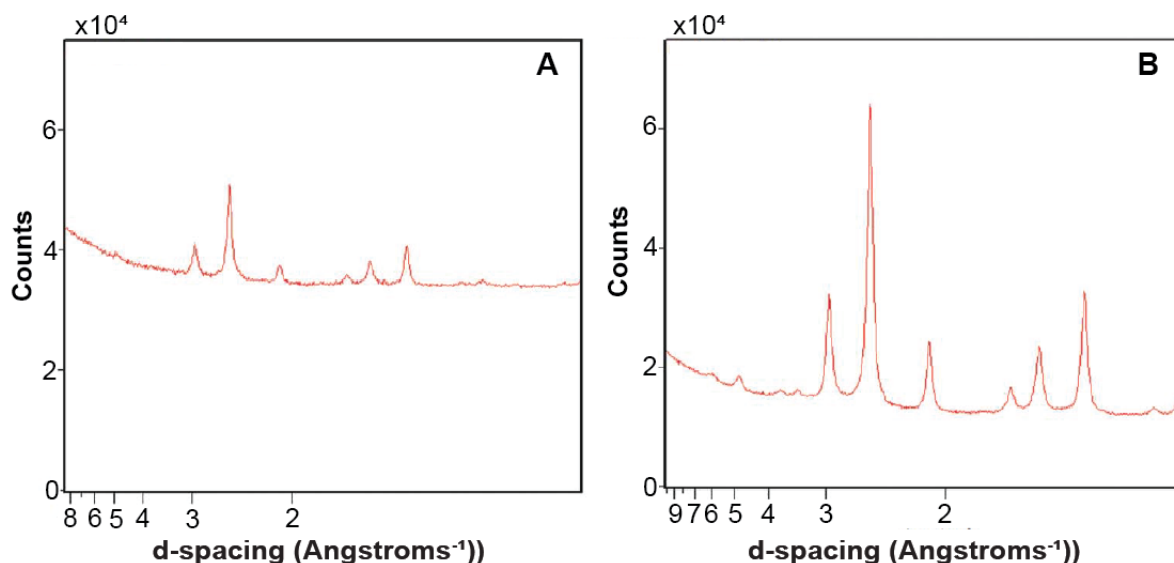


Figure 3.4. XRD pattern of maghemite samples measured using (A) copper radiation and (B) cobalt radiation. Note the elevated background of the pattern (A) due to the copper radiation causing iron fluorescence in the sample. Image modified after Mos et al. (2018).

energy of 100MeV, before being transferred to a booster ring where they are accelerated further to relativistic speeds at 3GeV. The electrons are then injected into a storage ring which is designed to hold 200mA with a lifetime of ~20 hours.

The orbit of the electrons in the system is controlled by a series of magnets and synchrotron radiation is generated when these relativistic electrons are accelerated through a magnetic field. The radiation produced via this process represents the whole electromagnetic spectrum. This radiation is directed down “beamlines” where optics (e.g. monochromators and mirrors) are used to condition the beam and select the part of the electromagnetic spectrum which is required. This radiation is then used to probe a range of samples using a range of techniques. Most beamlines at synchrotrons are designed to use X-rays.

Synchrotron X-rays are highly coherent with a higher brilliance than laboratory X-rays, typically resulting in faster data collection than using laboratory sources. The X-rays generated at synchrotrons are also more tuneable than laboratory X-rays, which are limited to fixed wavelengths. This allows selection of the most appropriate wavelength for a diffraction experiment to avoid fluorescence and absorption issues. This is important for measuring iron-bearing minerals as the use of an inappropriate wavelength can result in substantial iron fluorescence (Cullity, 1978). The higher energy of synchrotron X-rays also gives enhanced penetration meaning that more complex sample environments can be used. Diffraction beamlines at synchrotrons are often equipped with higher resolution and sensitivity detectors than laboratory sources.

However, data collection and processing procedures at synchrotrons are often less standardised, and instrument functions can be more complicated compared to laboratory X-ray sources. This must be considered during data analysis. Readers are directed to Fitch (2019), Epp (2016) and Sham and Rivers (2002) for further information on X-ray sources.

3.2.2.1 The Powder Diffraction (PD) beamline, Australian Synchrotron

The PD beamline at the Australian Synchrotron (Wallwork et al., 2007) is located on a bending magnet source. The energy is selected using a double crystal monochromator (Si(111) flat crystal pair) designed to operate over an energy range of 8–21 keV. Mirrors collimate and focus the X-ray beam to remove higher harmonic energies and maximise available flux. Figure 3.5 shows a layout of the Australian Synchrotron and Figure 3.6 shows a schematic of the PD beamline layout.

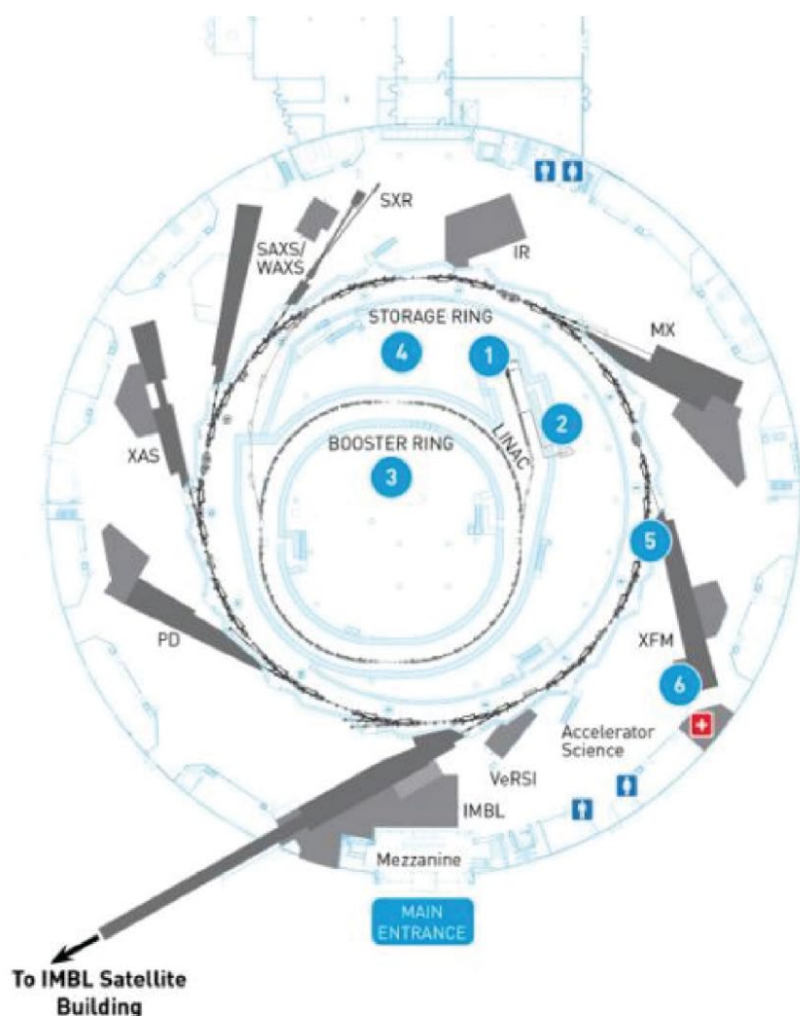


Figure 3.5. Schematic of the layout at the Australian Synchrotron. Image credit: ANSTO.

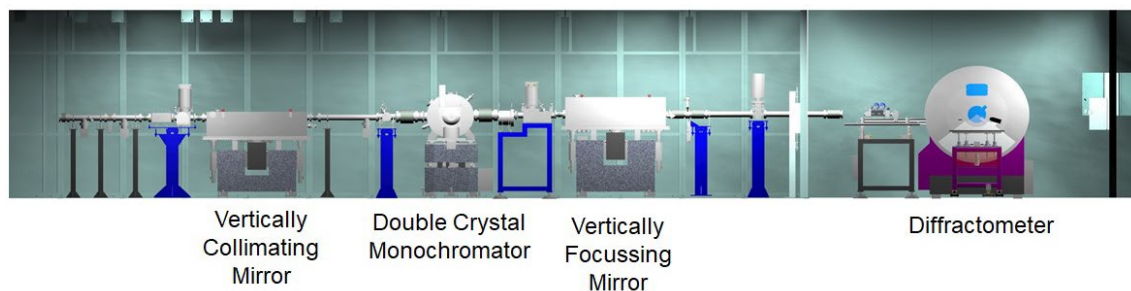


Figure 3.6. Schematic overview of the PD beamline at the Australian synchrotron showing the major optical beam conditioning components. Image credit: ANSTO.

The main experimental end station at PD is optimised for Debye–Scherrer capillary measurements under a range of sample conditions (Figure 3.7). The primary detector at the PD beamline is a Mythen II microstrip detector (Schmitt et al., 2003), a position sensitive detector which collects 80° of 2θ data simultaneously making it ideal for *in-situ* measurements. It is a high-resolution detector with a nominal resolution of 0.004° 2θ . High resolution XRD data was required in this work to resolve subtle differences in the jarosite samples due to both compositional and structural variation (Figure 3.8).

3.3. POWDER XRD

Powder XRD (or PXRD) is a bulk technique used to examine phase composition and atomic structure of polycrystalline samples. A powder sample is comprised of numerous small crystallites, with each crystallite acting as an independent single crystal. Typically, a powder sample is rotated to aid in randomising the orientation of the crystallites. Powder samples are typically loaded into capillaries or thinly packed on a flat sample holder for measurement; with capillaries being advantageous in that less sample is required for analysis. Exposure of the powders to X-rays results in a diffraction pattern representing the average condition of all the individual crystallites in the diffracting condition, and as a result, the diffracted reflections spread out as a three-dimensional cone known as a Debye cone. This cone projected onto a flat surface produces a series of rings corresponding to the diffraction reflections (Figure 3.9).

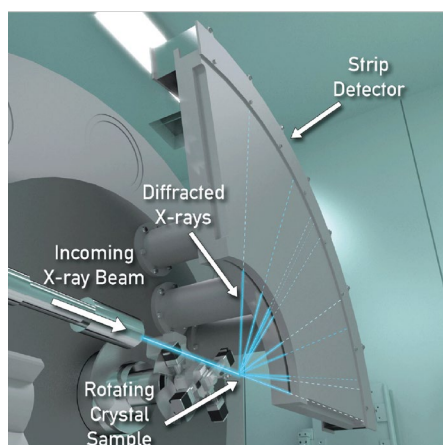


Figure 3.7. Diagrammatical layout of the primary end station at the PD beamline at the Australian synchrotron. Image credit: ANSTO.

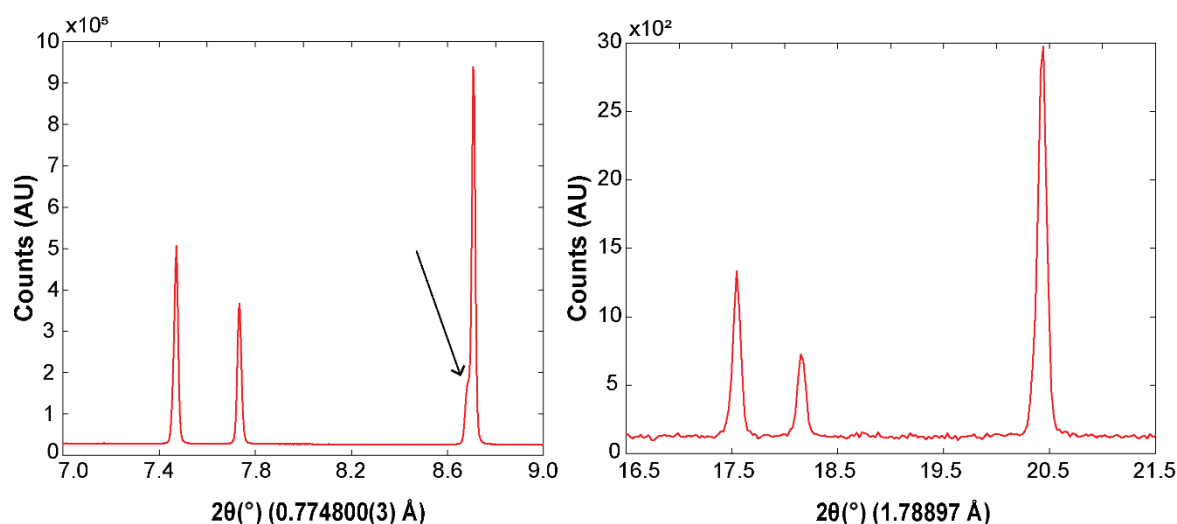


Figure 3.8. Partial XRD patterns of Js-Syn-01 (synthetic jarosite) collected using (A) the PD beamline and (B) the D8 Advance Eco X-ray diffractometer. The black arrow points to a peak shoulder visible in the synchrotron XRD data.

PXRD was used for research for several reasons. Firstly, the fine-grained nature of natural jarosite samples made separation of single crystals challenging. Secondly, because the jarosite samples contained accessory phases, PXRD was required to evaluate the mineralogy and the variability in the composition of the samples. Lastly, setting up *in-situ* PXRD heating experiments was relatively straightforward. The Mythen II microstrip detector was used as 1D data was sufficient for analysing the mineralogy and structure of the jarosite samples.

3.3.1 PXRD data

Powder diffraction experiments measure the intensity of X-rays over a range of 2θ angles. The diffraction reported here has been collected on 1-dimensional detectors which intersect the Debye cones radially. A 1D PXRD pattern is produced consisting of a series of peaks in intensity (also known as reflections) corresponding to the interplanar spacings of the crystalline phase(s) present in the sample. The peak intensity (in counts) is plotted along the y axis and the measured diffraction angle (2θ) is plotted along the x axis.

The positioning, intensity, and profile (i.e. width, shape) of the diffraction peaks, as well as the background, are indicative of the different characteristics of the crystalline material, as well as instrument contributions and the sampling environment (Figure 3.10). Peak positions reflect the unit cell parameters and space group of the sample. Peak intensity reflects the atomic arrangement and chemical composition of the sample. Textural features such as preferred orientation of the grains in a crystalline material are also reflected in the peak intensity. Peak width and shape are reflective of

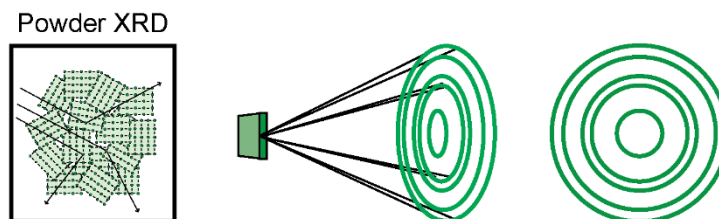


Figure 3.9. Diagrammatical representation of diffraction cones from a polycrystalline sample powder diffraction. Black arrows represent the incoming and diffracted X-rays. Figure after Dittrich and Bieniok (2009).

microstructures present in the sample such as crystallite size and strain. The diffraction background is influenced by the sampling environment (e.g. type of sample holder, air), and the presence of amorphous or poorly crystalline material. PXRD patterns contain a wealth of knowledge and there are several applications of PXRD in the characterisation of crystalline materials such as qualitative and quantitative phase analysis, and Rietveld refinement.

The instrument contribution (e.g. X-ray wavelength and zero error) to a diffraction pattern is typically determined using a reference material standard e.g. NIST LaB6 660b and then fixed during subsequent analysis. Other instruments contributions such as the divergence of the incident beam can influence the profile width and shape of the diffraction peaks.

3.3.2. Qualitative phase analysis

Minerals consist of unique combinations and arrangements of atoms. Each mineral composition will have a unique combination of peak positions and intensities in diffraction data, which can be thought of as each mineral having a unique PXRD fingerprint. This fingerprint facilitates identification of the different phases present in a mixed-phase powder sample by qualitative phase analysis. Qualitative phases analysis involves matching the peak positions and relative intensities of reference patterns to the peaks generated by a powder sample. There are several databases available for qualitative phase analysis including those provided by the International Centre for Diffraction Data (ICDD) (PDF4+), and the Crystallographic Open Database (COD; Grazulis et al., 2009). The software packages DIFFRAC. EVA and Panalytical Highscore Plus were used in combination with these databases in this work to determine the mineral phases present.

3.3.3. Rietveld refinement

The Rietveld (1967; 1969) method is a whole pattern structural refinement procedure where a calculated model is refined to fit PXRD data. It is used to determine the structure of the crystals present in a polycrystalline material and can also be used for quantitative analysis. Rietveld refinement uses a non-

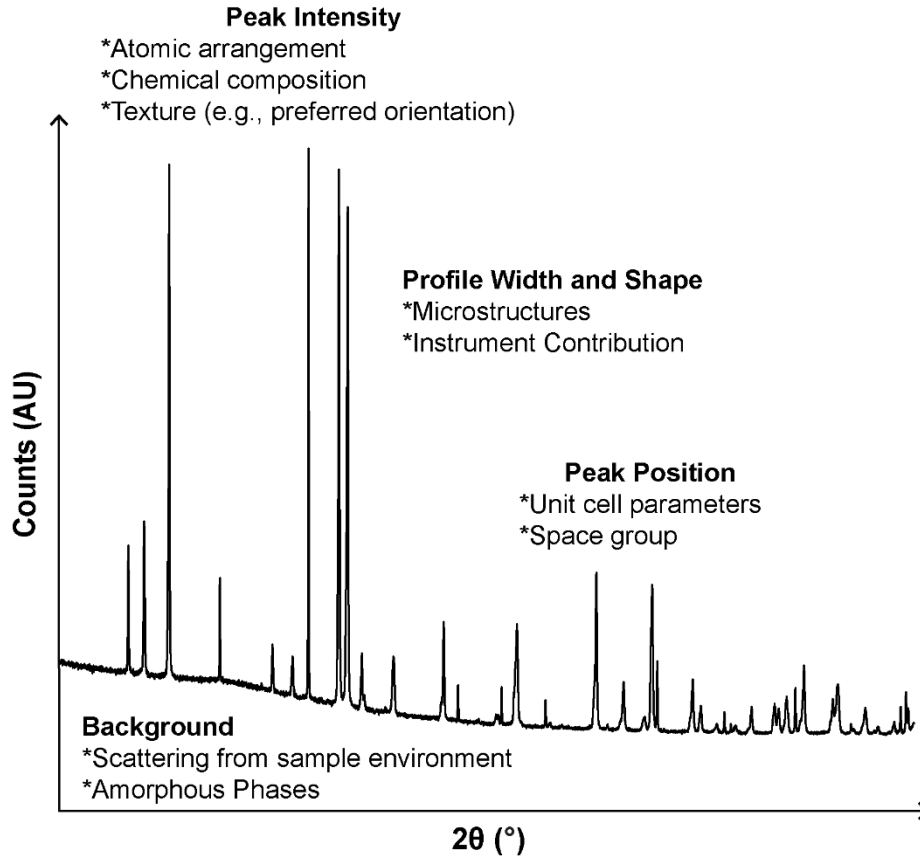


Figure 3.10. Schematic of a PXRD pattern with the information that can be extracted from the pattern highlighted.

linear least square fitting approach, and the refinement process involves minimisation of the parameter S_y , a measurement of the weighted difference between the observed data points and a calculated profile (McCusker et al., 1999) according to Equation 3.3:

$$S_y = \sum_i w_i [y_i(obs) - y_i(calc)]^2 \quad (\text{Eq. 3.3})$$

where w_i is the weight of each observation point, $y_i(obs)$ and $y_i(calc)$ are the observed and calculated peak intensities at each 2θ position i , and the sum i is over all data points. During Rietveld refinement phase parameters including atomic position, atomic site occupancies, atomic thermal parameters, unit cell parameters, space group, scale factor, and preferred orientation, as well as the peak shape functions describing the peak width and shape, can be refined. The fit to the background of the pattern can also be included in the refinement model.

Peak shape functions are used to describe the size and shape of the peaks and there are several functions used to model PXRD profiles including the Pseudo-Voigt (PV; Wertheim et al., 1974), Pearson VII

(PVII; Hall et al., 1977) and Thompson–Cox–Hasting pseudo–Voigt (TCHV; Thompson et al., 1987) functions. All three functions convolute a Gaussian and a Lorentzian function. A Gaussian function gives a peak shape with a rounded peak maximum and small peak tail, whereas a Lorentzian function gives a peak shape with a sharper peak maximum but longer peak tail (Figure 3.11). As PXRD patterns often contain a combination of peak profiles and asymmetry, refinements often involve trying the different peak shape functions to ascertain which is the best fit for the PXRD profile. Synchrotron XRD data of jarosite from the powder diffraction beamline at the Australian synchrotron of is typically best described using the TCHV profile.

Preferred orientation effects arise when the crystallites in a sample have a non-random distribution. Departure from a random distribution can occur, for example, in materials containing highly anisotropic grain shapes, frozen grain orientations and during recrystallisation experiments. Preferred orientation effects present in a powder sample often need to be accounted for during Rietveld refinement. Two preferred orientation corrections readily applied are the March–Dollase model (Dollase, 1986; March, 1932) and spherical harmonics (Von Dreele, 1997). The main difference between these corrections is that March–Dollase can be applied to preferred orientation in one or two directions, whereas spherical harmonics corrects for preferred orientations in multiple directions. Peak broadening effects often need to be accounted for during Rietveld refinement and there are several strain parameters as well as line broadening models (e.g., the Stephens (1999) strain models) that can be applied during refinement. Details of the refinement conditions used for particular samples will be described further in the appropriate chapter.

As Rietveld refinements are not linear, several cycles of refinement are often needed to achieve an acceptable level of convergence or “goodness of fit” between the observed and calculated patterns. The goodness of fit (χ^2) of a refinement is calculated according to Equation 3.4 (McCusker et al., 1999):

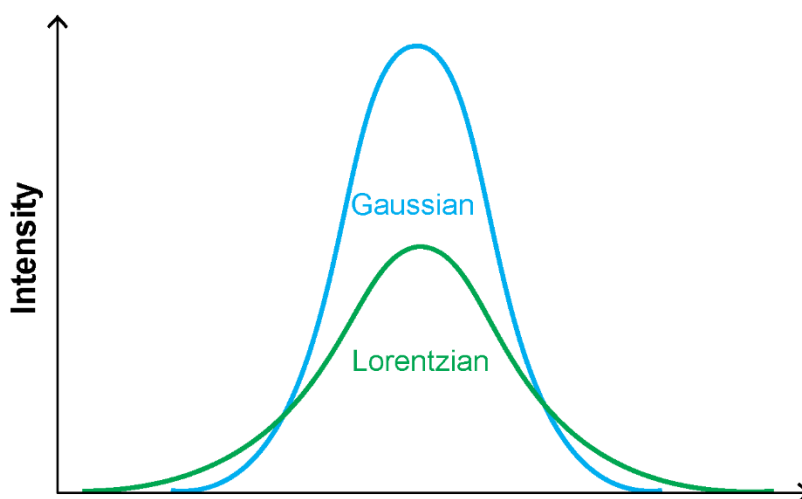


Figure 3.11. Schematic of a Gaussian (blue) and Lorentzian (green) function peak profile

$$X^2 = (R_{wp}/R_{exp})^2 \quad (\text{Eq. 3.4})$$

where R_{wp} is the Residuals weighted profile (Equation 3.5):

$$R_{wp} = \left\{ \sum_i w_i [y_i(obs) - y_i(calc)]^2 / \sum_i w_i [y_i(obs)]^2 \right\}^{1/2} \quad (\text{Eq. 3.5})$$

and R_{exp} is the minimum expected R_{wp} (Eq. 3.6):

$$R_{exp} = \left[(N - P) / \sum_i w_i y_i(obs)^2 \right]^{1/2} \quad (\text{Eq. 3.6})$$

with N being the number of experimental points and P the number of refined parameters. The R_{wp} value alone also provides a statistically meaningful indication of the quality of the refinement. Two other commonly used measures of the quality of the fit are the R-structure (R_s) and R-Bragg (R_B) factors (Eq. 3.7 and 3.8, respectively; McCusker et al., 1999)

$$R_s = \sum_{hkl} F_{hkl}(obs) - F_{hkl}(calc) / \sum_{hkl} F_{hkl}(obs) \quad (\text{Eq. 3.7})$$

$$R_B = \sum_{hkl} I_{hkl}(obs) - I_{hkl}(calc) / \sum_{hkl} I_{hkl}(obs) \quad (\text{Eq. 3.8})$$

where $F_{hkl}(obs)$ and $F_{hkl}(calc)$ are the observed and calculated structure factors, respectively, and $I_{hkl}(obs)$ and $I_{hkl}(calc)$ are the observed and calculated weighted equivalent structure factors, respectively. The R-structure gives an indication of the quality of the structure, and the R-Bragg monitors improvement in the structure model during refinement.

The structure of the jarosite present in the natural and synthetic jarosite samples at room temperature and during *in-situ* heating was examined through Rietveld refinement. The software program DIFFRAC. TOPAS 5 was used for the refinements. Input files for TOPAS 5 were edited using the text-based editor jEdit. Accessory minerals were modelled using the Rietveld method or a Le Bail fit (Le Bail et al., 1988). A Le Bail fit is simpler than a Rietveld fit in that it fits the intensity of the calculated peaks to the observed peaks without considering the structural components (i.e. the atoms) of the unit cell. Given full structural refinement of the accessory minerals was outside the scope of this work, Le

Bail fits were sufficient for modelling the accessory phases. The exact details of the Rietveld refinement procedure used in this research are outlined in each research chapter.

Readers are directed to Louër (2016), Will (2006), Epp (2016) and McCusker et al. (1999) for further information on powder diffraction and Rietveld refinement.

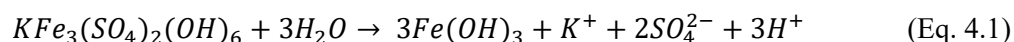
Chapter 4

Iron Isotope Geochemistry and Mineralogy of Jarosite in Sulfur-Rich Sediments

This chapter describes an investigation into the iron isotope composition and mineralogy of jarosite samples collected from sulfur-rich coastal sediments in Victoria, Australia. The work from this chapter forms a paper that was published in *Geochimica et Cosmochimica Acta* (Whitworth, A.J., Brand, H.E.A., Wilson, S.A., Friedrich, A.J., 2020b. Iron isotope geochemistry and mineralogy of jarosite in sulfur-rich sediments. *Geochimica et Cosmochimica Acta*, 270: 282–295).

4.1 INTRODUCTION

Jarosite [$KFe_3(SO_4)_2(OH)_6$] plays a critical role in regulating the acidity of aquatic systems and the mobility of trace elements and potential contaminants in the environment. Jarosite forms in highly acidic, oxidising, and sulfate- and iron-rich environments (Elwood Madden et al., 2012; Lueth et al., 2005). As a result of these conditions, jarosite occurs in the vadose zone (i.e. above the water table) in soils and sediments, or within sediment profiles where fluids can obtain high fO_2 and low pH values (Rye and Alpers, 1997). In humid, circumneutral pH environments, however, jarosite decomposes rapidly to Fe-oxyhydroxides (Langmuir, 1997; Pritchett et al., 2012) according to Equation 4.1:



Jarosite is a member of the alunite supergroup of minerals which have a general formula of $DG_3(TX_4)_2(X)_6$ (Bayliss et al., 2010). All alunite group minerals have sulfur in the T site (Bayliss et al., 2010) and members of the jarosite subgroup are characterised by the predominance of Fe^{3+} in the G site (Spratt et al., 2013; Welch et al., 2007). Jarosite has been described as a “garbage can” mineral as it can incorporate a wide range of substitutions into its crystal structure (Swayze et al., 2008). In the large D site, substitutions include (but are not limited to) monovalent cations Na^+ , H_3O^+ , Rb^+ , NH^+ , Ag^+ , divalent cations Ca^{2+} , Ba^{2+} , Pb^{2+} and Sr^{2+} , trivalent cations and REE’s. Divalent cations Pb^{2+} , Zn^{2+} and Mg^{2+} and trivalent cations Al^{3+} , Cr^{3+} , V^{3+} and Ga^{3+} can substitute into the G site as well, and elements that form tetrahedral oxyanions (e.g. P, As, Cr and Sb) can substitute into the T site (Papike et al., 2006; Welch et al., 2007). Because the jarosite subgroup can incorporate a wide range of ions in the D site there are several isostructural endmember species that are related to jarosite, the most common naturally occurring variant of jarosite being natrojarosite [$NaFe_3(SO_4)_2(OH)_6$] (Basciano and Peterson, 2007, 2008; Stoffregen et al., 2000). The stability and reactivity of jarosite-group minerals depend on the degree of substitution into the D, G and T sites (Welch et al., 2007). Substitution of metallic and metalloid ions (e.g. As) can represent a store of toxic elements within the jarosite structure that can be later mobilised into the environment (Karimian et al., 2017), along with acidity.

Jarosite is common in a variety of environments on Earth, as well as on Mars (e.g. Klingelhöfer et al., 2004), and it can be categorised as either supergene, hydrothermal, or sedimentary based on the process

of formation. Supergene jarosite forms in low-temperature environments through the oxidation of sulfide minerals, commonly pyrite (Desborough et al., 2010; Papike et al., 2006), and is typically very fine grained and commonly intermixed with hypogene phases such as clay minerals (Desborough et al., 2010; Lueth et al., 2005). Supergene jarosite is commonly associated with the weathered regions of sulfide-bearing ore deposits, acid mine drainage (AMD) and acid sulfate soils (ASS) (Desborough et al., 2010), the latter of which are prevalent throughout Australia and negatively impact land and water quality (Mosley et al., 2014a) and aquatic ecosystems (Glaspie et al., 2018). Extensive jarosite-bearing outcrops occur in coastal sediments and ecologically-sensitive coastal wetlands in Victoria, Australia, providing a unique opportunity to better understand the geochemistry of jarosite formation, transformation, and interaction with the environment. This knowledge is critical for the successful management of jarosite as a long-term sink for metals, metalloids, and acidity in coastal regions.

Previous research has shown that variations in the stable iron isotope composition of ancient rocks and minerals provide insight into the biogeochemical cycling of iron, particularly when oxidation-reduction reactions are involved (Dauphas et al., 2017). This makes stable iron isotope geochemistry a powerful tool to understand mineral formation and transformation over time. As a result, there is a growing body of research on the iron isotope composition of sedimentary rocks and minerals including banded iron formations (BIFs) (e.g. Busigny et al., 2018; Johnson et al., 2008; Li et al., 2015; Planavsky et al., 2012), black shales and sedimentary pyrites (e.g. Duan et al., 2010; Guilbaud et al., 2011; Tahata et al., 2015), and carbonates (e.g. Craddock and Dauphas, 2011; Czaja et al., 2010; Heimann et al., 2010). The iron isotope geochemistry of iron sulfate minerals, such as jarosite, is essentially unexplored, with only a few iron isotope measurements for jarosite (Egal et al., 2008). Consequently, little is known about how iron isotopes are fractionated between jarosite and other iron-bearing minerals and dissolved iron species despite the potential for such information to unlock clues into the coupled iron and sulfur cycles in modern and ancient environments. This work thus investigates the iron isotope composition and mineralogy of natural jarosite samples collected from sulfur-rich coastal sediments in Victoria, Australia. The abundance of jarosite and its diverse morphologies at these locations create a natural laboratory to study its formation and stability in the environment.

4.2 SITE DESCRIPTION

Fossil Beach and Southside Beach (Figure 4.1), located along the Victoria coastline, were selected for sample collection due to the abundance of outcrops containing diverse morphologies of jarosite. Fossil Beach is located within the Fossil Beach Geological Reserve on the Mornington Peninsula, southeast of Melbourne (Figure 4.1). The most prominent stratigraphic unit exposed is the Gellibrand Marl, previously referred to as the Balcombe Clay (VandenBerg, 2009), which is comprised of two horizons: a calcareous, fossiliferous clayey silt horizon with hard limestone concretions, and a non-calcareous,

poorly fossiliferous and leached clayey silt horizon. The Fossil Beach Fault exposes the Mt Martha Sand Beds, a littoral and near-shore sand deposit, and fluvial Harmon Rocks Sand Bed at the southern end of the beach. These units were deposited during a marine transgression in the Miocene and form part of the Port Phillip Basin. The area is heavily landslipped (Gostin, 1966; Holdgate and Gallagher, 2003).

Southside Beach is located southwest of Melbourne (Figure 4.1). The main stratigraphic units exposed are the Anglesea Formation and Addiscot Formation. The Anglesea Formation is comprised of carbonaceous and pyritic siltstones and fine sandstone. It is overlain by the Addiscot Formation, which is comprised of carbonaceous, pyritic clayey siltstones, fine sandstones and silty claystones. These units form subdivisions of the Demon's Bluff Group, a marginal marine siliciclastics and volcanic group deposited during the Eocene to Oligocene. The Demon's Bluff Group is one of several groups comprising the Torquay Basin, a predominantly offshore basin with onshore coastal exposure between Eastern View and Torquay (Holdgate and Gallagher, 2003; Holdgate et al., 2001).

4.3 SAMPLING AND ANALYTICAL METHODOLOGY

4.3.1 Outcrop morphology, sample collection and preparation

Jarosite was present in cliff outcrops that run the length of the beaches at both Fossil Beach and Southside Beach, as well as at the bases of cliffs as pebbles (4 mm – 64 mm), cobbles (64 mm – 256 mm) and boulders (>256 mm) within the intertidal zone. Jarosite was identified primarily based on its pale yellow to yellow colour. The jarosite in the cliffs occurs either as beds (Figure 4.2A) or veins (Figure 4.2B) within the sediment, or as surface coatings (Figure 4.2C) or nodules (Figure 4.2D) on the sediment. The jarosite beds vary from 1 – 6 cm in thickness, are laminar and are interbedded with sediment. The jarosite veins are typically thinner (2 mm – 1 cm) and are either laminar or meandering in morphology. The jarosite surface coatings are very thin (< 1mm – 1 cm) and either occur as a continuous, thin layer or a variably fine to coarse granular layer. The jarosite nodules are typically small (0.5 cm – 6 cm), are sub-rounded to rounded and can variably be intermixed with sediment and supergene iron oxide phases. Jarosite pebbles typically consist of only jarosite, whereas jarosite cobbles and boulders typically consist of intermingled jarosite, sediment and iron oxides (Figure 4.2E and 4.2F). The cobbles and boulders appeared to be cemented.

Eleven jarosite samples from Fossil Beach and twenty-four jarosite samples from Southside Beach were collected for X-ray powder diffraction (PXRD), elemental abundance by inductively coupled plasma-mass spectrometry (ICP-MS), and stable iron isotope analysis by multi-collector inductively coupled plasma-mass spectrometry (MC-ICP-MS). The jarosite samples were selected such that arrange of different jarosite morphologies were represented. To minimise iron oxide contamination,

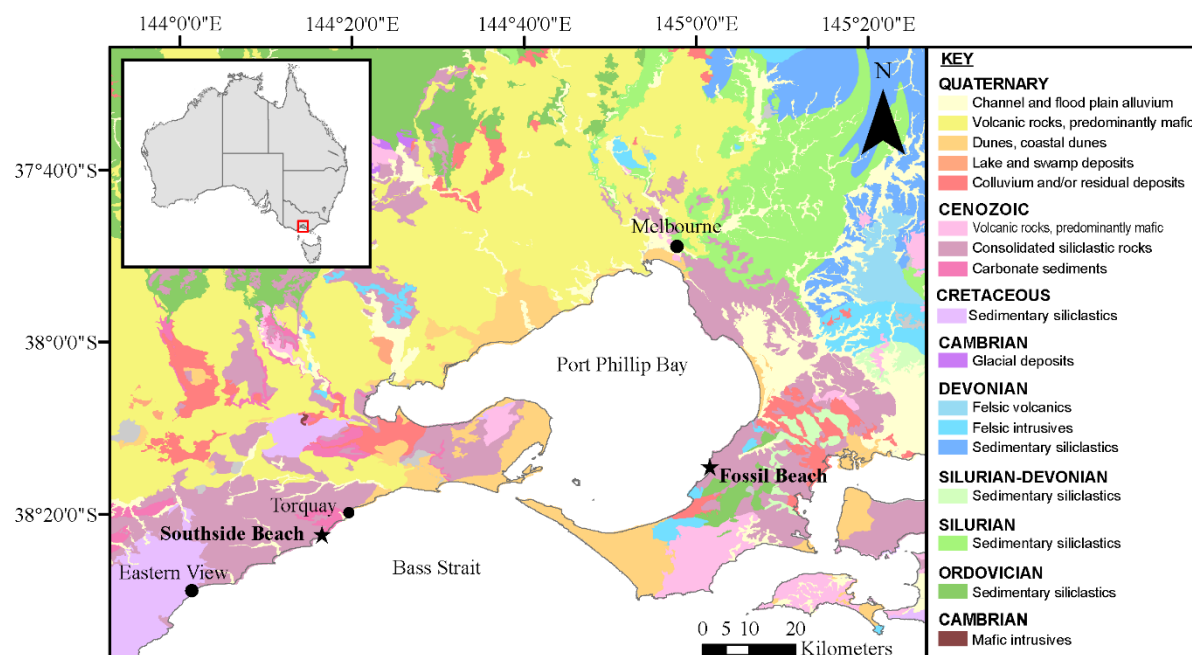


Figure 4.1. Simplified geological map with the location of Fossil Beach and Southside Beach in Victoria, Australia. The red box on the insert shows where these sites are located relative to the rest of Australia. Surface geology sourced from Geoscience Australia (Raymond et al., 2012).

samples of jarosite were collected from outcrops devoid of iron oxide mineralisation, where possible. A few grams of jarosite were collected from cliff jarosite outcrops, whereas a few grams to a few kilograms of jarosite were collected from the jarosite pebbles, cobbles and boulders. Jarosite samples vary from being friable (crushed or broken by fingernail) to rigid (required hammer to break), with the veins being the softest and the beach cobbles and boulders the hardest. Jarosite samples ranged from pale yellow (5Y 8/3; 5Y 8/4) to yellow (5Y 8/6; 5Y 8/8) in colour and appeared fine grained under a hand specimen microscope. Subsamples were collected from external versus internal regions of boulders, to identify heterogeneity in the mineralogy, trace element content, or iron isotope composition. Samples were dried at room temperature and ground using an agate mortar and pestle. Jarosite was isolated from matrix material (e.g., iron oxides, sediment, sand, and organic material such as fungal filaments) using tweezers, picks, and brushes while viewing the samples under a hand specimen microscope. Sample colour was determined using the Munsell colour system and is described using the three variables: hue, value and chroma.

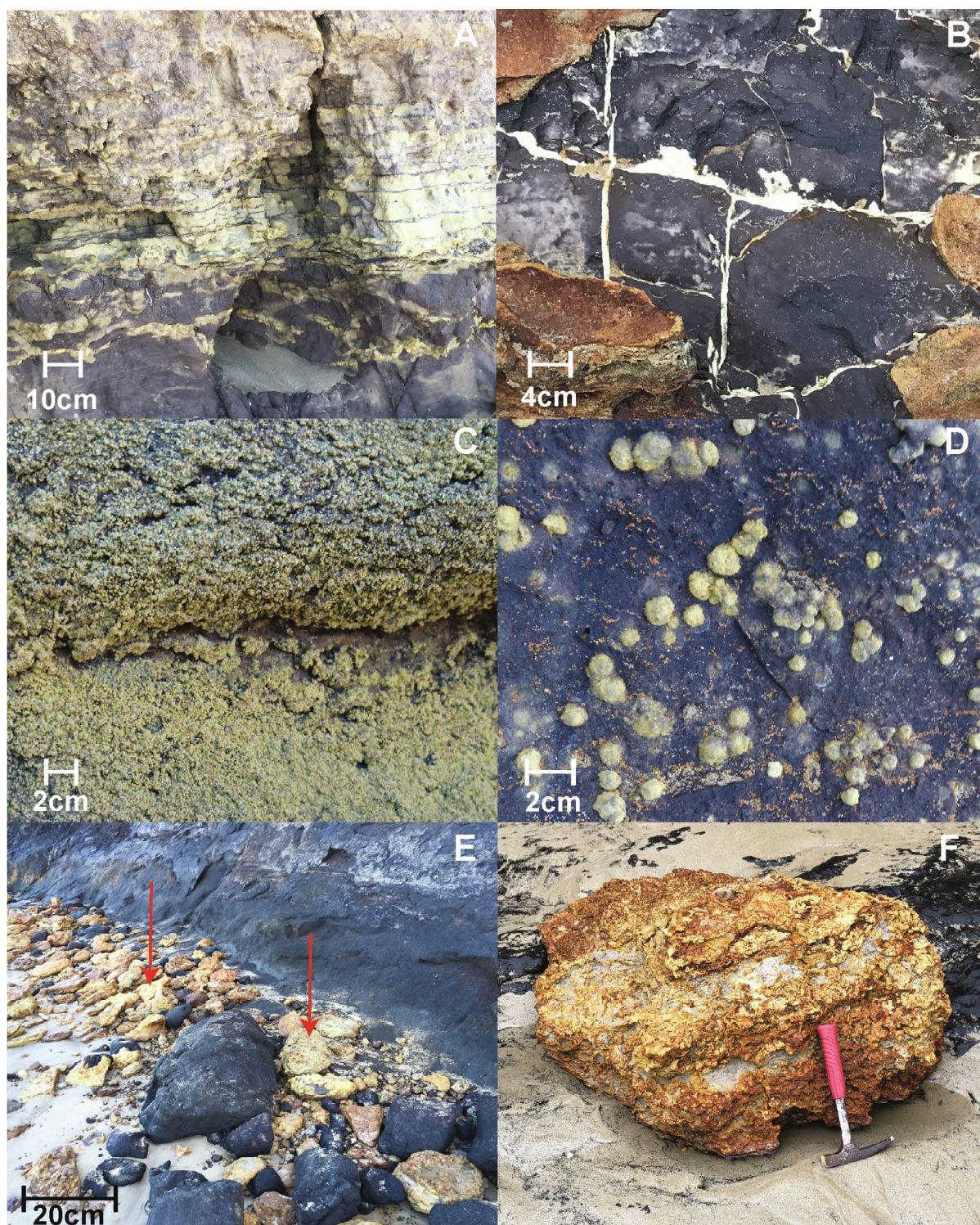


Figure 4.2 Photographs of the different jarosite morphologies. (A) Bedded jarosite; (B) jarosite veins; (C) jarosite coating on a sub-vertical cliff surface; (D) jarosite nodules embedded in a cliff surface; (E) jarosite pebbles, cobbles and boulders at the base of a cliff along with calved portions of the sediment; red arrows point to jarosite cobbles; (F) close-up of an intermingled jarosite and iron oxide boulder. Photographs were taken at Southside Beach but are also representative of morphologies seen at Fossil Beach.

To explore the relationship between the jarosite and sulfidic sediments, which presumably are the source of the iron in the jarosite, sediment samples were also collected from both sites. Sediment was identified based on its colour, ranging from light grey–brown to black, texture and presence of clay minerals. At Southside Beach there were two cliff sediment horizons: a lower horizon that was black–brown in colour, had a sulfidic smell and frequent disseminated pyrite mineralisation, and an upper lighter brown–grey sediment with little pyrite mineralisation. Jarosite mineralisation predominantly occurred at the horizon contact and in the upper horizon. As such, the two horizons are reflective of a change in redox conditions, with the upper region being relatively more oxidised than the lower region. This was not observed at Fossil Beach. At Fossil Beach the cliff sediment was a light grey–brown colour, was fossiliferous and contains sporadic pyrite mineralisation. Jarosite mineralisation occurred throughout. Six cliff sediment samples from Fossil Beach and nine cliff sediment samples from Southside Beach were collected for analysis. Sediment samples were collected such that a range of physical properties (e.g., colour, texture) were represented, and a few grams of sediment was collected from outcrops proximal to jarosite outcrops, where possible. As Fossil Beach contains fossil beds of high geological significance, sediment (and jarosite) samples from this site were collected from cliff sections that did not contain fossil beds to prevent disturbance of the fossils. The cliff samples colour ranged from light grey (10YR 7/2) and brown (7.5YR 6/4) to black (10YR 2/1) and textures ranged from a very soft, fine–grained clayey silt through to a coarser grained, sandy texture. All cliff sediment samples were consolidated. In addition to the cliff sediment samples, one sediment pebble (Js–SB–63) was collected from the base of a cliff at Southside Beach. It was consolidated, brown–black in colour and has a soft, silty texture. A sample of sediment deposited in an external cavity of a boulder containing jarosite at Southside Beach was also collected. The boulder sediment (Js–SB–59B) was consolidated, light grey in colour and has a silty–sand texture. Disseminated pyrite is visible in four of the cliff samples, as well as the sediment pebble, when viewed under a hand specimen microscope. See Appendix 1 Table SI 1 for detailed information.

A full list of the jarosite and sediment samples, including GPS coordinates and textural and colour descriptions, is presented in Appendix 1 (Table SI 1). Samples containing “FB” in the sample name were collected from Fossil Beach whereas samples containing “SB” in the sample name were collected from Southside Beach. Photographs of the sediment (and jarosite) horizons at both sites is also presented in Appendix 1 (section SI2).

4.3.2 Analytical methodology

4.3.2.1 PXRD

Hand ground samples of jarosite and sediment were loaded into 0.3 mm diameter borosilicate glass capillaries then mounted onto the Powder Diffraction (PD) beamline (Wallwork et al., 2007) at the

Australian Synchrotron. Capillaries were rotated at ~ 1 Hz during data collection to aid powder averaging. Diffraction patterns were collected with the MYTHEN-II microstrip detector (Schmitt et al., 2003). The X-ray beam wavelength was determined from refinement of NIST Standard Reference Material LaB₆ 660b (see Appendix 1 section SI 5 for further details). Two patterns, each of 300 s, were collected with the detector set 5° apart to cover the gaps between detector modules. The two patterns were then merged into a single dataset using the PDViPeR software available at the PD beamline.

Bruker DIFFRAC.EVA was used to identify the minerals present in the samples using the Crystallography Open Database (Grazulis et al., 2009) and Bruker DIFFRAC.TOPAS 5 software was used to investigate the structure of minerals present in each sample through Rietveld refinements (Rietveld, 1969).

4.3.2.2 ICP-MS

Powdered jarosite (20.0 ± 0.2 mg) was dissolved in 1 mL of 10 M HCl at 25°C for 24 hours. 9 mL of ≥ 18.2 M Ω cm water (hereon H₂O) was then added to the sample, diluting the HCl to 1 M, and the sample was then filtered ($0.22\ \mu\text{m}$) to remove insoluble organic material. Powdered sediment (20.0 ± 0.2 mg) was dissolved in a mixture of 0.5 mL 16 M HNO₃ : 0.25 mL 50% HF at 120°C for 48 hours then dried down at 80°C . Samples were then taken up in a mixture of 0.75 mL of 6 M HCl : 0.25 mL 7 M HNO₃ at 80°C for 48 hours then dried down at 80°C . Samples were then taken up in 1 mL of 10 M HCl at 25°C for 24 hours. 9 mL of H₂O was then added to the sample, diluting the HCl to 1 M, and the sample was then filtered ($0.22\ \mu\text{m}$) to remove insoluble organic material. The total iron concentration was then determined for all samples using Ferrozine following the method outlined in Stookey (1970). A small aliquot of each sample was then diluted to one tenth or one hundredth of the original concentration for analysis.

Element concentrations were measured on a Thermo iCAP-Q quadrupole ICP-MS operated in kinetic energy discrimination (KED) mode using He as a collision gas ($5\ \text{mL min}^{-1}$) to remove polyatomic interferences (e.g., $^{40}\text{Ar}^{16}\text{O}$ interference on ^{56}Fe). Elemental concentrations were quantified by conversion of counts per second to parts per million using calibration curves prepared by analysis of standard solutions containing High-Purity Standards ICP-MS-68 Solution A and ICP-MS-68 Solution B at varying concentrations.

4.3.2.3 MC-ICP-MS

Prior to measuring iron isotope ratios, all potentially interfering matrix components were separated by ion exchange chromatography in a class 350 clean room. A small aliquot of dissolved jarosite or sediment sample containing $2\ \mu\text{mol}$ ($\sim 110\ \mu\text{g}$) of iron was transferred into 8 mL PFA beakers. The open

beakers were then placed on a hotplate and evaporated to dryness. Two drops of 16 M HNO₃ were then added to each beaker to ensure oxidation to ferric iron. Samples then underwent cation–exchange chromatography in columns containing 1 mL Bio–Rad AG 50W–X8 (200 – 400 mesh size). This was critical to remove the copious amounts of sulfate. After the resin was added to the columns, it was pre–cleaned using 3 mL of 6 M HCl followed by pre–conditioning using 5 mL of 0.6 M HNO₃. Next, the samples were loaded onto the columns in 1 mL of 0.6 M HNO₃. Anions were eluted from the column using 4 mL of 0.6 M HNO₃. Iron and other non–eluted matrix elements were then rinsed from the column using 5 mL of 6 M HCl, collected in a beaker and dried down on a hotplate. Once dry, one drop of 10 M HCl was added to the beaker to remove NO₃[–] and to convert iron to a chloride form. Samples were again dried down and then underwent anion–exchange chromatography in columns containing 1 mL of Bio–Rad AG 1–X8 resin (100 – 200 mesh size) to separate out the iron from remaining matrix elements. After the resin was added to the columns for this second chromatography treatment, it was pre–cleaned using 5 mL of 0.1 M HCl then underwent pre–conditioned using 5 mL of 6 M HCl. Next, the samples were loaded in 1 mL of 6 M HCl. After loading, the remaining matrix elements were eluted from the column using 5 mL of 6 M HCl. Iron was then eluted from the column using 4 mL of 0.1 M HCl, collected in a beaker and dried down. Once dry, two drops of 16 M HNO₃ were added and evaporated to oxidise any residual organic substances and remove residual chloride. The samples were then diluted to 1.8 ppm iron in 0.1 M HNO₃ for analysis.

Iron isotope ratios (⁵⁶Fe/⁵⁴Fe) were measured on a Thermo–Fisher *Neptune Plus* in medium–resolution mode using a wet–plasma and standard–sample bracketing following previously described methods (Sossi et al., 2015). Iron isotopes were reported using standard delta notation according to Equation 4.2:

$$\delta^{56}\text{Fe} (\text{‰}) = \left[\frac{\left(\frac{{}^{56}\text{Fe}}{{}^{54}\text{Fe}} \right)_{\text{sample}}}{\left(\frac{{}^{56}\text{Fe}}{{}^{54}\text{Fe}} \right)_{\text{standard}}} - 1 \right] \times 10^3 \quad (\text{Eq. 4.2})$$

where *sample* refers to ratio of the iron isotopes in the sample, and *standard* is the ratio of IRMM–014. Iron isotope values were bracketed against the IRMM–524a iron standard which has an identical iron isotope composition to IRMM–014 (Craddock and Dauphas, 2010). The accuracy of measured $\delta^{56}\text{Fe}$ values of samples was assessed by analysing test solutions containing matrix materials (e.g. K₂SO₄, Na₂SO₄, HCl) and IRMM–524a iron in the same proportions as the sample fractions in this study after they were run through the same column chemistry process as the samples. The average measured $\delta^{56}\text{Fe}$ value of these test solutions was $0.03 \pm 0.04 \text{ ‰}$ (2σ , $n = 9$), which is close to the measured value of the pure iron solution $0.01 \pm 0.07 \text{ ‰}$ (2σ , $n = 10$) and hence indicates that iron isotope values were not significantly altered during column chemistry and sample handling. The external precision of $\delta^{56}\text{Fe}$

values was assessed by replicate analyses of samples; the average standard deviation was found to be 0.07 ‰ (2σ , $n = 19$).

4.4 RESULTS

4.4.1 PXRD results

Jarosite is present in 45 of the 49 samples collected with only Js-SB-12, Js-SB-26A, Js-SB-40A and Js-SB-47B having no detectable jarosite. The majority of the jarosite samples also contain quartz (SiO_2). Minor accessory minerals present include halite (NaCl), gypsum ($\text{CaSO}_4 \cdot 2\text{H}_2\text{O}$), kaolinite [$\text{Al}_2\text{Si}_2\text{O}_5(\text{OH})_4$], illite [$(\text{K},\text{H}_3\text{O})(\text{Al},\text{Mg},\text{Fe})_2(\text{Si},\text{Al})_4\text{O}_{10}$], alunite [$(\text{K},\text{Na})\text{Al}_3(\text{SO}_4)_2(\text{OH})_6$], goethite [$\text{FeO}(\text{OH})$] and pyrite (FeS_2).

Of the samples that do not contain detectable jarosite, sideronatrite [$\text{Na}_2\text{Fe}(\text{SO}_4)_2(\text{OH}) \cdot 3\text{H}_2\text{O}$] is present in Js-SB-26A and Js-SB-40A. Js-SB-12 is comprised of quartz and gypsum and Js-SB-47B is comprised of alunite; no iron-bearing minerals are present in Js-SB-12 and Js-SB-47B. Alunite and goethite are only present in Southside Beach samples whereas pyrite is only present in one of the Fossil Beach samples. Additionally, what appears to be a smectite mineral was identified in a small number of samples. Although we detected some characteristic peaks, we did not detect a single, narrow basal peak in the range of 10 Å to 20 Å. However, changes in relative humidity during PXRD data acquisition for smectites containing a variety of interlayer cations (e.g. Na, K, Ca, Mg) commonly results in a broad basal peak reflecting a range of $d(001)$ positions (Bish et al., 2003). The minor clay content of these samples could thus not be conclusively identified.

Although the jarosite samples represent a continuous solid solution, as a simple means of classification for descriptive purposes, the jarosite samples were classified according to subgroups determined by refining the lattice parameters using synchrotron-based PXRD data. Literature lattice parameters for endmember jarosite (a : 7.3029, c : 17.2043) and endmember natrojarosite (a : 7.3153, c : 16.5868) from Basciano and Peterson (2007) and (2008), respectively, were used as an indicative guides to the relative amount of K and Na in the D site. Figure 4.3 illustrates how the samples were classified. Samples with a c -lattice parameter > 16.8956 Å (halfway between the literature c parameters for endmember jarosite and natrojarosite) are denoted as jarosite. Those with a c -lattice parameter < 16.8956 Å are denoted as natrojarosite. Within these two categories, we then describe the level of substitution of K or Na in the D site. Samples with more than a 10% relative deviation from the literature value for pure natrojarosite (> 16.6846 Å) are described as “K-natrojarosite”. Similarly, samples with more than a 10% relative deviation from the literature value for pure jarosite (< 17.1426 Å) are described as “Na-jarosite”. No attempt is made to account for hydronium substitution. It can be seen from Figure 4.3 that the majority

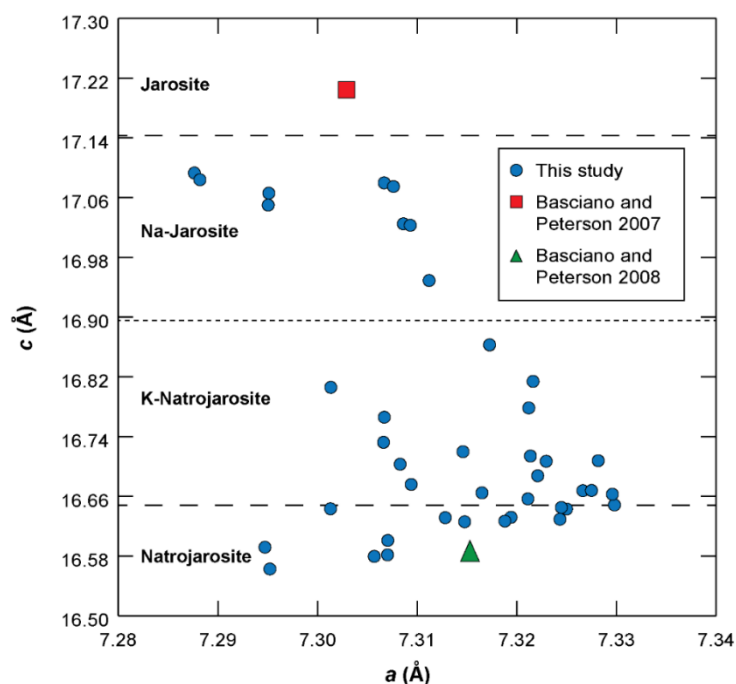


Figure 4.3. Plot of unit cell parameters a vs. c of the jarosite samples from this study. Unit cell parameters of jarosite (red square) and natrojarosite (green triangle) from Basciano and Peterson (2007) and (2008), respectively, were used as a guide to descriptively classify the type of jarosite in the jarosite samples. The horizontal dotted line represents halfway between the literature c parameters for endmember jarosite and natrojarosite. The horizontal dashed lines represent a 10% deviation away from the literature c parameters for endmember jarosite and natrojarosite. Analytical errors are approximately the same size as the data points.

of samples are K–natrojarosite, with a smaller number being natrojarosite and Na–jarosite. All Na–jarosite samples were collected from boulder samples, and predominantly from exterior regions of the boulders. No samples were classified as endmember jarosite. As such, the name ‘jarosite’ is used herein to refer to all members of the subgroup and (K)jarosite is used to refer to endmember jarosite.

Asymmetric peak–broadening was identified in the $(00l)$ peaks in most jarosite samples. Anisotropic line broadening, which appears similar to asymmetric microstrain broadening, can be the result of asymmetric compositional variation in a phase that exhibits solid solution (Leineweber and Mittemeijer, 2006). Endmember compositions within the jarosite subgroup rarely occur in nature; within the subgroup, solid solution occurs via substitution in the D site, and substitutions in the G and T sites extends solution to other species within the larger alunite supergroup. Substitutions in the D site mainly affect the dimension of the c parameter of the unit cell along $[001]$, while substitutions in the G site mainly affect the dimension of the a parameter along $[100]$ (Stoffregen et al., 2000). The peak asymmetry that is observed in the $(00l)$ peaks in the majority of jarosite samples indicates that substitution is occurring in the D site. In the samples classified as K–natrojarosite, there is an often log normal distribution toward larger d –spacings (at lower 2θ), reflecting substitution of the larger K cation

into the D site of the samples. Conversely, in the samples classified as Na-jarosite, there is an often log normal distribution toward smaller d-spacings (at higher 2θ), reflecting substitution of the smaller Na cation into the D site of the samples (Figure 4.4A). It should also be noted that in a small number of samples, two distinct (001) peaks are present, indicating that the sample is comprised of two distinct compositions of jarosite sub-group minerals. In most cases, asymmetric peak broadening is still present in one of the two peaks (Figure 4.4B).

The mineralogy of the sediment samples is similar at both sites with quartz, kaolinite and illite being the predominant minerals and pyrite, halite, gypsum, calcite [CaCO_3] and an additional unspecified clay mineral that is likely a smectite occurring in minor concentrations. Additionally, sideronatrite is present in one sample (from Southside Beach) and jarosite is present in one sample (from Fossil Beach). PXRD results for all samples are reported in Appendix 1 (Table SI 5).

4.4.3 ICP-MS results

Elemental results indicate that the majority of the jarosite samples are more enriched in Na relative to K, with jarosite samples at Southside Beach being, on average, slightly more enriched in Na relative to K (78% Na / 22% K) than Fossil Beach jarosite (72% Na / 28% K; see Table SI 3A, Appendix 1). This is consistent with the refined unit cell parameters which suggest structural Na incorporation relative to K (Figure 4.3). When the sum of the Na and K concentrations for all samples is plotted versus the Fe concentration from the jarosite dissolutions, the data follow a 1:3 line (Figure 4.5), consistent with the stoichiometry of jarosite. Small deviations above this ratio may be due to the presence of other minerals

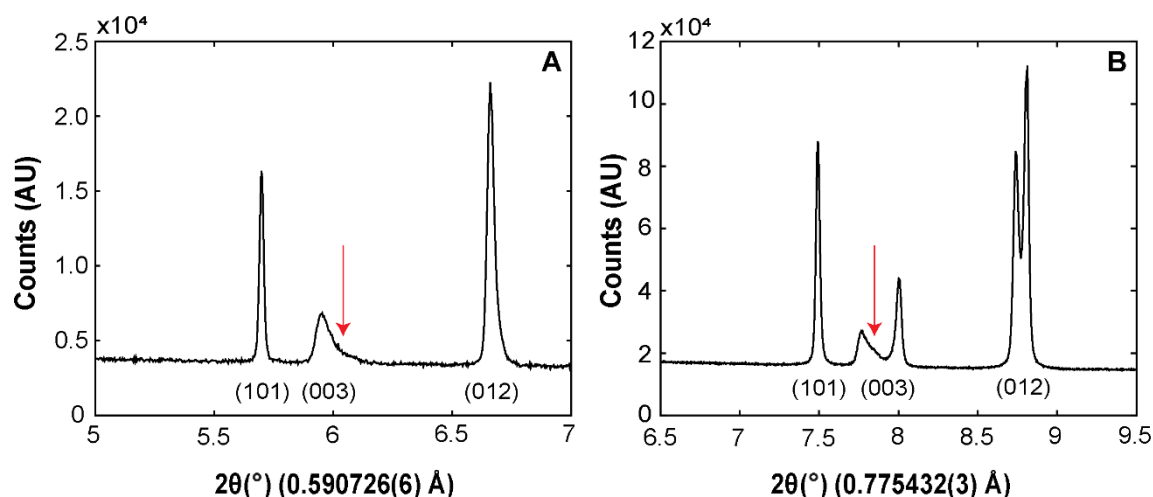


Figure 4.4. Representative PXRD patterns of jarosite samples with only the first three jarosite peaks shown. (A) Js-SB-32A, a Na-jarosite sample, with log-normal asymmetric peak broadening of the (003) peak, (B) Js-FB-21B showing two distinct (003) peaks, with the lowest angle peak exhibiting asymmetric peak broadening. The red arrows show the asymmetric peak broadening.

in the sample containing Na and/or K (e.g. halite), as well as the presence of other ions (e.g. H_3O^+) substituting into the D site. Moreover, the sideronatrite samples contain a Na:Fe ratio that is similar to the 2:1 stoichiometric ratio expected for this phase (Figure 4.5). The jarosite samples also do not contain substantial concentrations of iron oxyhydroxides (apart from the samples with known goethite incorporation based on PXRD; see Figure SI 3, Appendix 1). Other major element concentrations are similar between sites. Minor and trace elements at the highest concentrations (> 500 ppm) were As, Sr, V, Ni, La, Ce, with As, Sr and V having the highest mean concentration (mean > 150 ppm) across all samples. Minor (> 100 ppm) enrichments in B, Cr, Mn, Zn, Rb, Mo, Ba, Pb and Th are seen in some samples. Average minor and trace element concentrations are similar between sites, with the largest differences occurring for Sr (505.6 ppm at Southside Beach vs 832.3 ppm at Fossil Beach) and Ce (28.4 ppm at Southside Beach vs 199.7 ppm at Fossil Beach). Major and trace element concentrations for the jarosite samples are reported in the Appendix 1 (Table SI 3A).

The sediment samples were highly variable in chemical composition. Iron concentrations ranged from 1.3 to 37.1 wt%, with the majority (82 %) of the sediments containing < 5 wt% Fe. Aluminium

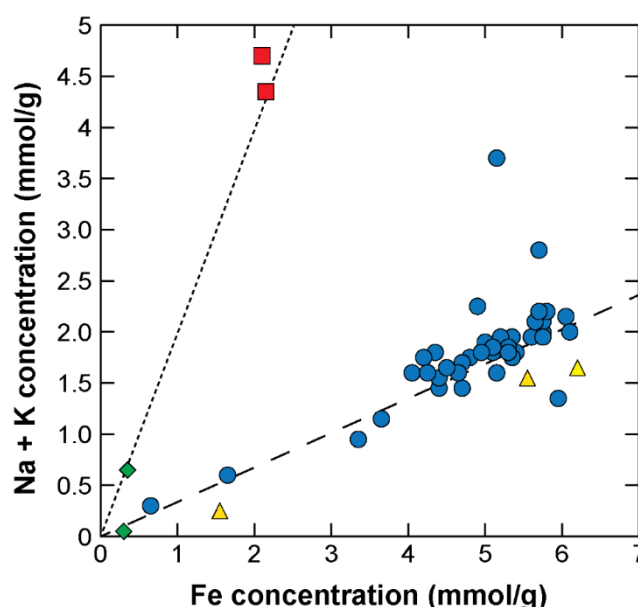


Figure 4.5. Plot of Fe concentration vs Na + K concentration for the jarosite samples after dissolution of ~20 mg of dry sample in 10 mL of 1 M HCl. Samples containing sideronatrite (and no jarosite) are shown as red squares. Samples containing jarosite and other iron-bearing minerals (goethite, pyrite) are shown as yellow triangles. Samples containing no jarosite (or other primary iron-bearing minerals) are shown as green diamonds. The dotted line represents the stoichiometric ratio of Na:Fe in sideronatrite $[\text{Na}_2\text{Fe}(\text{SO}_4)_2(\text{OH}) \cdot 3\text{H}_2\text{O}]$. The dashed line represents the stoichiometric ratio of (Na+K):Fe in the jarosite–natrojarosite solid solution $[(\text{K},\text{Na})\text{Fe}_3(\text{SO}_4)_2(\text{OH})]$. The majority of samples plot close to this line, which indicates that the D site is predominantly occupied by Na and K, with only minor amounts of hydronium or other monovalent cations.

concentrations tended to be higher than those for Fe, ranging from 0.2 to 23.9 wt% with the majority (59%) of samples containing > 5 wt% Al. Southside Beach sediments have a higher average concentrations of Na (1.9 wt%), Al (9.7 wt%) and K (2.6 wt%) compared to Fossil Beach (0.3 wt%, 3.4 wt% and 0.6 wt%, respectively). Conversely, Fossil Beach sediments have a higher average concentration of Fe (13.6 wt%) compared to Southside Beach (2.9 wt%). This can be attributed to two Fossil Beach samples having elevated Fe concentrations (37.1 and 36.2 wt%) due to a higher abundance of pyrite in the samples based on qualitative PXRD results.

Minor and trace elements at the highest concentrations across all samples were Ba, Mn, Sr, V and Zr, with a mean concentration > 180 ppm. Minor (> 100 ppm) enrichments in Li, B, Cr, Zn, As, Rb, Ce, Th and U were seen in some samples. Southside Beach sediments on average have a higher concentration of most minor and trace elements, with the largest difference in average compared to Fossil Beach occurring for Ba (649.5 ppm vs 149.0 ppm), V (271.9 ppm vs 99.4 ppm) and Zr (502.1 ppm vs 99.3 ppm). Major and trace element concentrations for the sediment samples are reported in the Appendix 1 (Table SI 3A)

4.4.4 MC–ICP–MS results

There is a large spread in $\delta^{56}\text{Fe}$ values for the jarosite and sediment samples at both sites (Figure 4.6). Excluding jarosite samples containing other Fe-bearing minerals and those containing no jarosite, as well as sediment samples containing jarosite or sideronatrite, based on PXRD, the Fossil Beach jarosite samples have $\delta^{56}\text{Fe}$ values that range from -1.91 to $+0.10$ ‰, with a mean of -0.63 ± 0.59 ‰ (1σ) whereas the sediment samples range from -0.54 to $+0.56$ ‰, with a mean of -0.11 ± 0.55 ‰ (1σ). Similarly, jarosite samples from Southside Beach have a large range of $\delta^{56}\text{Fe}$ values, -1.56 to $+1.24$ ‰, with a mean value of 0.01 ± 0.74 ‰ (1σ) and the sediment samples $\delta^{56}\text{Fe}$ values range from -0.27 to $+1.30$ ‰, with a mean of $+0.20 \pm 0.47$ ‰ (1σ).

Comparing the mean $\delta^{56}\text{Fe}$ values for jarosite and sediment samples at Fossil Beach and at Southside Beach using a Student's T-test shows that the probability of the two datasets having the same mean is high ($p = 0.127$ and $p = 0.327$, respectively), indicating that the mean jarosite and sediment iron isotope compositions at each site are not significantly different. This is also observed when the sediment $\delta^{56}\text{Fe}$ data sets from Southside Beach and Fossil Beach are compared ($p = 0.323$), indicating that there is no significant difference in mean iron isotope composition between sites. When the jarosite $\delta^{56}\text{Fe}$ data sets from Southside Beach and Fossil Beach are compared the opposite is observed ($p = 0.009$), indicating that the iron isotope composition of the jarosite is significantly different between sites. The p -values may be influenced by the small datasets for the Southside Beach sediment (11 samples) and Fossil Beach jarosite (12 samples) and sediment (6 samples).

Jarosite samples with different morphologies have similar $\delta^{56}\text{Fe}$ compositions (Figure 4.7). The boulder samples have a very large spread of both positive and negative $\delta^{56}\text{Fe}$ values (-1.91 to $+1.24$ ‰), with the two boulder samples collected from Fossil Beach having negative $\delta^{56}\text{Fe}$ values. The coating samples also have a large spread of both positive and negative $\delta^{56}\text{Fe}$ values (-1.44 to 0.23 ‰). The bedded and pebble jarosite samples all have positive $\delta^{56}\text{Fe}$ values (0.10 ‰ for the bedded sample and 0.12 ‰ and 0.47 ‰ for the pebble samples), whereas the nodule and vein samples have negative $\delta^{56}\text{Fe}$ values (-0.45 to -0.12 ‰ for the nodule samples and -0.69 to -0.06 ‰ for the vein samples; Figure 4.7). On average (excluding the samples containing other iron-bearing minerals and those containing no jarosite based on PXRD) the nodules are the most isotopically light, with an average $\delta^{56}\text{Fe}$ of -0.36 ‰, followed by the coatings (-0.34 ‰), veins (-0.29 ‰), boulders (-0.01 ‰) and pebble (0.29 ‰) jarosite samples. The boulder jarosite samples have the largest spread in values, with a standard deviation of 1.05 ‰ followed by the coating (0.47 ‰), vein (0.35 ‰), pebble (0.18 ‰) and nodule (0.14 ‰) samples. While

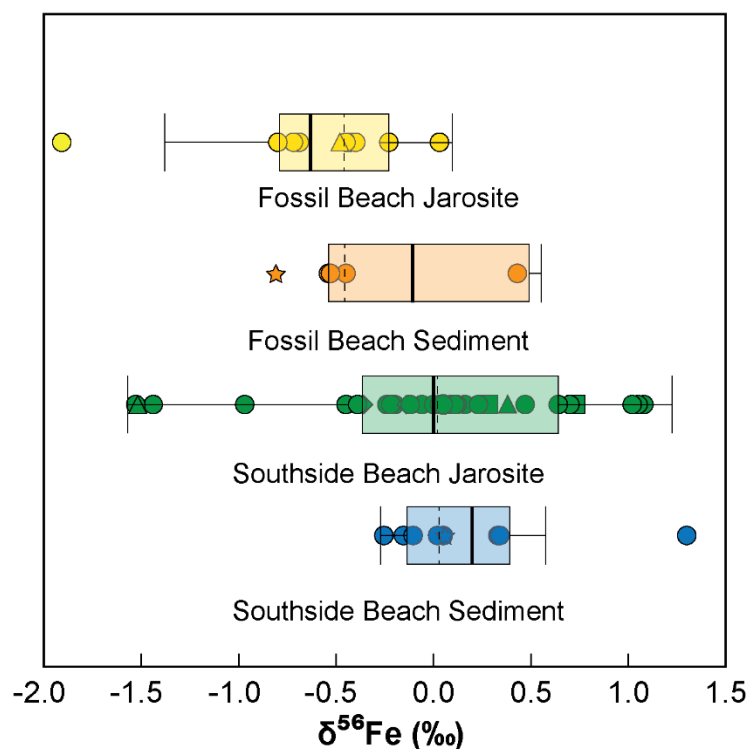


Figure 4.6. Box and whisker plots comparing of the $\delta^{56}\text{Fe}$ composition of the jarosite and sediment samples at Fossil Beach and Southside Beach. The boxes are bound by the 25th and 75th percentiles; whiskers extend to the minimum and maximum values observed. The thick black lines represent the mean. The dotted black lines represent the median. Jarosite samples containing other Fe-bearing minerals and those containing no jarosite, as well as sediment samples containing jarosite or sideronatrite, where not included in the box and whisker plot calculations but are shown for comparison with the rest of the data. Jarosite samples containing sideronatrite (and no jarosite) are shown as squares. Jarosite samples containing jarosite and other iron-bearing minerals (goethite, pyrite) are shown as triangles. Jarosite samples containing no jarosite (or other primary iron-bearing minerals) are shown as diamonds. Sediment samples containing jarosite or sideronatrite are shown as stars.

some jarosite morphologies appear to have characteristic $\delta^{56}\text{Fe}$ compositions, other morphologies do not. The nodule samples are an example of a morphology with a characteristic signature — the samples all have a negative $\delta^{56}\text{Fe}$ signature and the spread in the data is relatively small. The boulder samples, on the other hand, have both positive and negative $\delta^{56}\text{Fe}$ compositions, with an average that is very slightly negative and a very large range in values. Comparing the different morphologies using an analysis of variance (ANOVA) shows that the different morphologies are not significantly different ($p > 0.05$), indicating that the iron isotope composition of the different morphologies are similar. Thus, the variability in $\delta^{56}\text{Fe}$ values cannot be attributed to jarosite morphology.

The iron isotope composition of the jarosite samples appears to be related to alkali content. Excluding samples containing other iron-bearing minerals, those containing no jarosite based on PXRD, and outliers determined by bagplot analysis (Wessa, 2017), there is a moderately strong ($R^2 = 0.443$ and 0.689 for Southside Beach and Fossil Beach samples, respectively) negative correlation between the alkali ratio $[\text{Na}/(\text{Na}+\text{K})]$ and $\delta^{56}\text{Fe}$ value. This suggests that $\delta^{56}\text{Fe}$ values become more negative as the Na content increases (Figure 4.8). In general, phases that form strong bonds with iron become enriched in heavier iron isotopes at equilibrium compared to phases with weaker bonds (Dauphas et al., 2017).

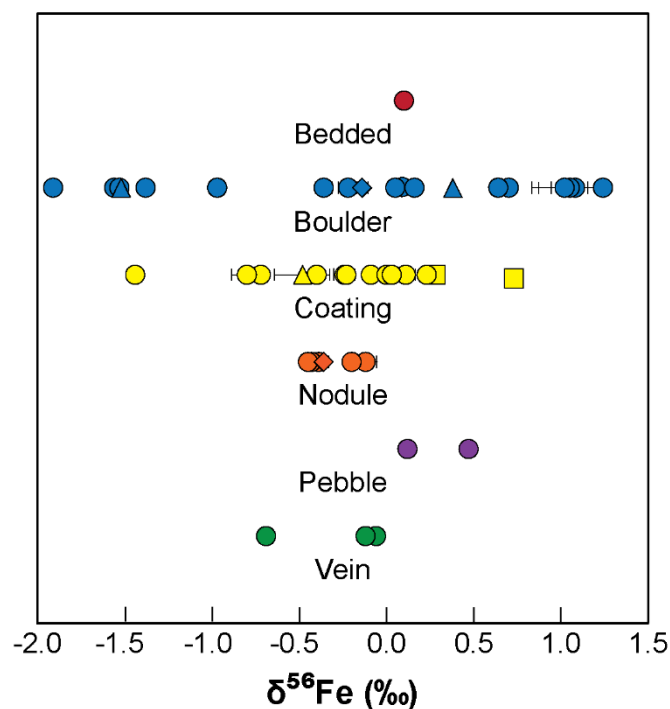


Figure 4.7. Comparison of the $\delta^{56}\text{Fe}$ value of the different jarosite morphologies at both sites. Samples containing sideronatrite (and no jarosite) are shown as squares. Samples containing jarosite and other iron-bearing minerals (goethite, pyrite) are shown as triangles. Samples containing no jarosite (or other primary iron-bearing minerals) are shown as diamonds. Error bars (reflecting 2σ values) are smaller than the symbols employed for most samples.

This suggests that iron is able to form stronger bonds in (K)jarosite, resulting in the enrichment of heavier iron isotopes. This is consistent with experimental and thermodynamic data of natrojarosite being more reactive and soluble than (K)jarosite (Drouet and Navrotsky, 2003; Stoffregen, 1993; Zahrai et al., 2013). Iron isotope results for the jarosite and sediment samples are reported in the Appendix 1 (Table SI 4)

4.5 DISCUSSION

4.5.1 Site comparison

The sediment samples at both Fossil Beach and Southside Beach have a similar mineralogy, with an abundance of quartz, illite and kaolinite at both locations. Similarly, the mean iron isotope composition is not significantly different between sites. The chemistry, on the other hand, varies across sites, with Southside Beach sediments having a higher enrichment, on average, in Na, Al, K and most minor and trace elements. This difference is likely due to the sediment samples being collected from the poorly fossiliferous, leached clayey silt horizon of the Gellibrand Marl at Fossil Beach. The presence of

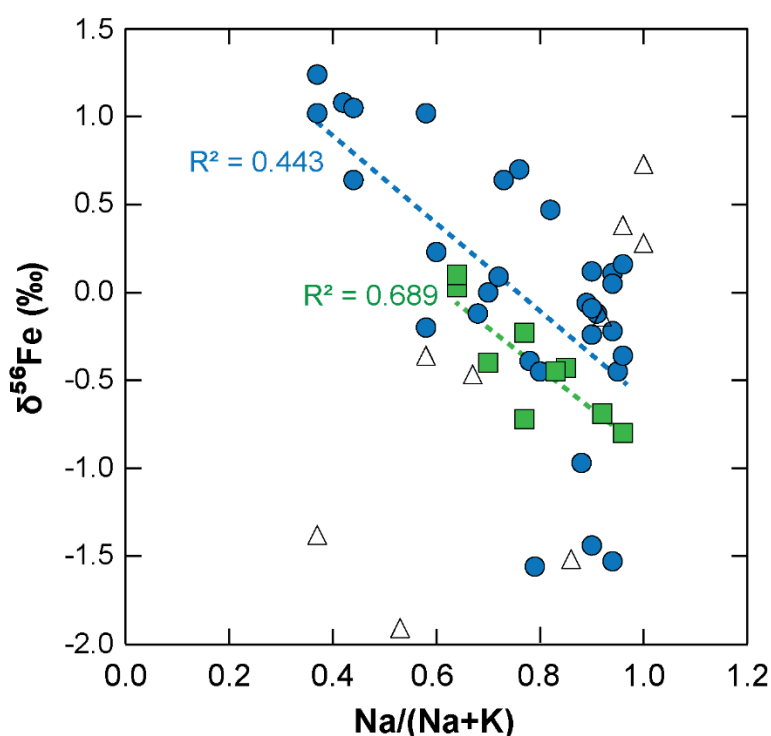


Figure 4.8. Plot of the alkali ratio ($\text{Na}/(\text{Na}+\text{K})$) against $\delta^{56}\text{Fe}$ for the jarosite samples. Fossil Beach samples are green squares. Southside Beach samples are blue circles. The dashed green and blue lines represent the line of best fit for Fossil Beach and Southside Beach samples, respectively. Samples containing other iron-bearing minerals (goethite, pyrite, sideronatriite), no jarosite (or other primary iron-bearing minerals) or are outliers were not included in the calculation of the trendlines and are shown as open triangles.

abundant clay minerals, as well as a similar iron isotope composition, at both sites suggests that similar weathering and redox processes are occurring at both sites.

At both sites, jarosite is observed occurring as veins or beds within the cliff sediment, as nodules or coatings on the cliff sediment, or as pebbles or boulders on the beach. PXRD results are similar, with most samples containing similar accessory mineral assemblages, and both asymmetrical peak broadening and multiple distinct compositions are present in samples taken from the two sites. Similarly, the jarosite at both sites is, on average, enriched more in Na than K, and there are minor enrichments in As, Sr and V. Overall, the morphology, mineralogy, jarosite crystal structure, and chemistry of the jarosite samples is similar across both sites, and this likely reflects similar weathering and redox processes acting on the jarosite during its formation, as well as over time. The iron isotope composition, on the other hand, is significantly different between sites, with jarosite at Southside Beach having, on average, more positive and a larger spread in $\delta^{56}\text{Fe}$ values. It is not clear why the iron isotope composition varies between sites despite the similarity in mineralogy, crystal structure and chemistry. One possible explanation is that the Southside Beach jarosite has a more positive $\delta^{56}\text{Fe}$ signature compared to the Fossil Beach jarosite simply because the sediment at Southside Beach has a more positive $\delta^{56}\text{Fe}$ signature compared to the Fossil Beach sediment. While the students T-test indicated that the iron isotope composition of the sediments was similar at both sites, suggesting that the difference in jarosite iron isotope composition is not due to differences in sediment iron isotope composition, this similarity could be due to the small number of sediment samples analysed (11 at Southside Beach sediment and six at Fossil Beach).

It is unusual that jarosite is present in large abundance at both Fossil Beach and Southside Beach given that the environment at both locations does not appear to be conducive to jarosite stability. For jarosite to remain stable in a humid environment, fluids in contact with the minerals must be acidic and oxidising (Brown, 1971). Elwood Madden et al. (2012) and Pritchett et al. (2012) showed that maximum jarosite stability occurs around a pH of 3.5, with the lifetime of the jarosite estimated to be on the order of 100 to 1000 years (not considering other factors such as temperature, water activity, etc). Jarosite stability was then shown to decrease with increasing pH, with the lifetime of jarosite decreasing to around the order of 10 or less years by pH 8. Continual interaction of jarosite with sea spray and inundation of the pebbles, cobbles, and boulders of jarosite by seawater during high tide suggests that it would be unstable in this environment given seawater is well buffered at ~pH 8. However, the high salinity of seawater is expected to increase the lifetime of jarosite (Pritchett et al., 2012). Furthermore, the jarosite samples appeared fine grained under a hand specimen microscope. Pritchett et al. (2012) modelled the effect of grain size (0.01 cm – 1 cm) on jarosite lifetimes and found that the finer the grain size, the shorter the

jarosite lifetime. As such, the fine-grained nature of the jarosite is also not conducive to jarosite stability.

One explanation for the large abundance of jarosite is that the transformation of jarosite to iron oxides is being slowed. All of the boulders appear to be cemented and contain quartz, causing them to be difficult to break with a rock hammer. Jones et al. (2009) demonstrated that the Fe(II)-catalysed transformation of synthetic jarosite to ferrihydrite at circumneutral pH was prevented by high concentrations of silica and natural organic matter. These compounds prevented transformation in two ways: 1) by adsorbing to the surface of jarosite, preventing Fe(II) adsorption, and 2) by inhibiting dissolution of jarosite and thus reprecipitation of ferrihydrite. As such, the presence of the cement and organic matter may be acting as a barrier between the jarosite and seawater, slowing the transformation of jarosite to iron oxides. Iron oxide cobbles and boulders are present at Southside Beach, as well as many of the jarosite cobbles and boulders contain intermingled goethite, so transformation of jarosite to iron oxide (goethite) is occurring over time, it may be that it is occurring at a rate slower than expected. However, this is not likely happening for the cliff jarosite samples as they are not cemented (and hence are quite soft). However, this is not likely happening for the cliff jarosite samples as they are not cemented (and hence are quite soft). Although the pH of seawater is not conducive to jarosite stability, its high sulfate and sodium concentrations, which are required for the formation of jarosite in low-temperature environments (Papike et al., 2006), supersede the effect of the high pH and hence sufficiently stabilise jarosite.

Another explanation is that the abundance of cliff jarosite is a result of a high rate of formation relative to decomposition and recrystallisation. Given that jarosite requires acidic conditions to form, acidic conditions must be being generated at the site, but they may be occurring in continuous, short pulses (e.g. through periodic rainfall). As such, even if the jarosite is becoming unstable shortly after formation and decomposing, the continual pulses of acidity would likely be causing more jarosite to form. As such, the apparent longevity of the jarosite may simply reflect a steady state between jarosite formation, decomposition, and recrystallisation.

4.5.2. Jarosite subgroup composition

In terrestrial continental environments containing both K and Na, such as coastal acid sulfate soils, (K)jarosite has been found to be the most common jarosite subgroup phase (van Breemen, 1988; Zahrai et al., 2013) and this has been attributed to formation kinetics favouring K-bearing jarosite over natrojarosite (Öborn and Berggren, 1995). Natrojarosite has been observed in soils (Öborn and Berggren, 1995), as well as the weathered region of ore deposits (i.e. gossan; Desborough et al., 2010) and one possible explanation is that natrojarosite formation predominantly occurs in environments

where a deficiency in K limits (K)jarosite formation (Dutrizac, 1983; Öborn and Berggren, 1995). ICP–MS analysis of the sediment samples shows that the sediments at each site contains both K and Na, and are often more enriched in K relative to Na. Furthermore, the jarosite samples regularly encounter seawater, either through sea spray or, in the case of the boulders, cobbles and pebbles, inundation during high tide, so a K–deficiency in the environment is unlikely. As such, it is unusual that the predominant jarosite subgroup phase present at both sites is natrojarosite. The likely explanation is that because the jarosite is forming in an environment in regular contact with seawater, which has a Na/K ratio of ~50, the high concentration of Na in seawater is resulting in the formation of predominantly natrojarosite..

ICP–MS results indicate that when the concentrations of Na and K are summed and compared to the concentration of iron in the jarosite samples, the samples fall close to the stoichiometric 1:3 ratio expected if the D and G sites were fully occupied by these cations. Furthermore, refinement of the jarosite subgroup PXRD peaks suggests that the majority of the samples classified as natrojarosite have K–enrichment and all of the samples classified as K-jarosite have Na–enrichment. Given that peak asymmetry is present on (00 l) in most samples, it appears that the majority of the jarosite samples fall along the solid solution between Na– and K–jarosite. Complete solid solutions between Na– and K–jarosite have been observed in laboratory–synthesised samples (e.g. Basciano and Peterson, 2008; Drouet and Navrotsky, 2003; Ling et al., 2016) and have been modelled thermodynamically (Stoffregen, 1993) whereas for natural jarosites, (near–)endmember mixing and limited solid solutions have been observed (Desborough et al., 2010; Papike et al., 2007). Furthermore, Desborough et al. (2010) suggested that for low temperature jarosite, intermediate compositions between natrojarosite and (K)jarosite likely reflect physical mixing of endmember pairs that cannot be resolved due to the very fine–grained nature of low–temperature jarosite. The observation of peak asymmetry suggests that extensive solid solution can occur between naturally occurring, low temperature Na– and K–jarosite. It should be noted that there are likely still some other ions (e.g. H₃O⁺) substituting for the Na and K in the D site of our jarosite subgroup samples. Minor substitutions may also be occurring in the T site. For example, As⁵⁺ as AsO₄^{3–} has been found to occupy the T site in jarosite (Paktunc and Dutrizac, 2003; Savage et al., 2005) and given there is a minor (> 150 ppm) enrichment of As in many of the jarosite samples the As may be substituting for the S in the T site.

4.5.3 Iron isotope geochemistry of jarosite and implications for recrystallisation

The large spread in iron isotope values of jarosite may reflect the range in $\delta^{56}\text{Fe}$ values of the precursor sulfides, differences in alkali content, and fractionation during jarosite precipitation and recrystallisation. The sulfidic sediment which hosts jarosite is isotopically heterogeneous, with each site having approximately a 1.5 ‰ range in $\delta^{56}\text{Fe}$ values. Consequently, the resulting Fe isotope composition of jarosite is expected to inherit some of this complexity.

The issue of interpreting the Fe isotope composition of jarosite is compounded by the multiple alkali compositions resulting from the Na–K jarosite solid solution. Basciano and Peterson (2008) observed that substitution of Na for K in jarosite resulted in two of the six Fe–O bonds (Fe–O₂ and Fe–O₃) in jarosite becoming longer. Longer chemical bonds are typically weaker than shorter bonds, and, as previously mentioned, phases with stronger iron bonds typically will become enriched in heavier iron isotopes at equilibrium than weaker bonds (Dauphas et al., 2017). Hence, jarosite samples predominately composed of Na are expected to be isotopically light compared to those composed predominantly of K, a presumption that is consistent with our observations (Figure 4.8). Natrojarosite is less stable than (K)jarosite (Stoffregen, 1993) and thus should slowly recrystallise via dissolution–reprecipitation in the presence of aqueous K⁺ (Putnis, 2009), resulting in the thermodynamically favoured (K)jarosite. Accordingly, jarosite becomes isotopically heavier as more K substitutes for Na over time. This does not explain the isotopically light jarosite, which exhibits $\delta^{56}\text{Fe}$ values down to about –2 ‰ and is far more negative than the precursor sediments. If jarosite is forming in the presence of sea–spray on the outcrop or during exposure to seawater in the intertidal zone, then a shift in the equilibrium due to the seawater being substantially richer in Na could favour the formation of isotopically lighter natrojarosite.

A number of chemical processes during sulfide weathering and jarosite precipitation also likely fractionates iron isotopes. Under acidic conditions, oxidative leaching of sulfide–rich rocks is known to enrich the fluid phase in heavier iron isotopes (Fernandez and Borrok, 2009). As such, isotopically heavy dissolved Fe²⁺ that completely precipitates to form jarosite will also have this heavy iron isotope composition. However, partial oxidation of Fe²⁺ and precipitation of jarosite would likely result in the residual Fe²⁺ being isotopically lighter than the solid. Open–system Rayleigh distillation would produce an iron–bearing fluid that becomes progressively lighter, along with the corresponding jarosite product. Experiments synthesising the Na–K jarosite solid solution have observed that (K)–jarosite precipitates before natrojarosite (Basciano and Peterson, 2008). Under an open–system Rayleigh distillation model, isotopically heavier K–rich jarosite would initially precipitate out of an iron–bearing fluid containing K and Na. As precipitation continued, the remaining iron–bearing fluid would progressively become isotopically lighter, as well as richer in Na, causing the corresponding jarosite product to become isotopically lighter and richer in Na. Hence, Na–rich jarosite samples are expected to be isotopically light compared to those composed predominantly of K. Thus, Rayleigh distillation is a possible explanation for the negative correlation between alkali (Na/(Na + K)) content and $\delta^{56}\text{Fe}$ values observed in Figure 4.8. It is also possible that iron cycling, through jarosite recrystallisation, could fractionate iron isotopes. However, given the large range in $\delta^{56}\text{Fe}$, as well as significant overlap of jarosite $\delta^{56}\text{Fe}$ values with the $\delta^{56}\text{Fe}$ of the sulfidic source sediments, this is difficult to decipher.

A main challenge in the interpretation of the $\delta^{56}\text{Fe}$ values of jarosite is that the equilibrium iron isotope fractionation between jarosite and other iron-bearing minerals and dissolved iron species is poorly understood. To our knowledge no experiments have directly examined how iron isotopes fractionate between jarosite and dissolved Fe(II) or Fe(III). However, Dauphas et al. (2012) employed nuclear resonant inelastic X-ray scattering (NRIXS) to determine the reduced partition function ratio, or β -factor, of potassium and hydronium jarosite. β -factors can be used to calculate the equilibrium isotopic fractionation of two phases, A and B, according to Equation 4.3:

$$\delta_A - \delta_B \simeq 1000 \times (\ln \beta_A - \ln \beta_B) \quad (\text{Eq 4.3})$$

Using the β -factor calculated for K(jarosite) and hydronium jarosite by Dauphas et al. (2012), together with the β -factor for Fe(II)_{aq} from Rustad et al. (2010), the calculated Fe(II)_{aq}–(K)jarosite and Fe(II)_{aq}–(H₃O)jarosite equilibrium fractionation factors are approximately –3.5 and –4.76 ‰, respectively, at 22 °C in $^{56}\text{Fe}/^{54}\text{Fe}$. The difference in these values shows that the substitution of different cations into jarosite likely has a significant impact on the partitioning of iron isotopes into jarosite which is observed in our samples when alkali content is compared to $\delta^{56}\text{Fe}$ values (Figure 4.8). Laboratory experiments using the three-isotope method have been successful at calibrating the iron isotope fractionation factors between Fe(II) and a number of Fe(III)-bearing minerals (Friedrich et al., 2014a; Friedrich et al., 2014b; Friedrich et al., 2019). Similar three-isotope experiments could be useful to refine the fractionation factors for jarosite and other Fe species and ultimately help constrain the iron isotope geochemistry of jarosite.

4.6 CONCLUSIONS

The jarosite samples analysed in this study are geochemically and morphologically diverse, reflecting their dynamic formation environment. At both Fossil Beach and Southside Beach morphologies include beds and veins within the sulfidic (and variably iron-rich) outcropped sediment, nodules and coatings on the outcropped sediment, and pebbles, cobbles, and boulders at the base of the outcropped sediment within the intertidal zone. Natrojarosite enriched in K was the most common phase identified at both sites, followed by near end-member natrojarosite then (K)jarosite enriched in Na. No end-member (K)-jarosite was identified at either site. The predominance of natrojarosite (with or without K-enrichment) at both sites is unusual given (K)jarosite is thermodynamically favoured, and may reflect formation of jarosite from seawater substantially richer in Na than K. The identification of an extensive solid solution between naturally occurring Na- and K-jarosite also differs from previous observations that (near-)end-member mixing predominantly occurs in natural jarosite.

The jarosite samples have an exceptionally large range of $\delta^{56}\text{Fe}$ values ($>3\text{ ‰}$), representing a spectrum nearly as large as that observed for all iron-bearing samples in the geological record. There is a moderate but significant negative relationship between alkali ($\text{Na}/(\text{Na} + \text{K})$) content and iron isotope composition, suggesting that heavier iron isotopes are preferentially partitioned into K-rich jarosite. The large spread in iron isotope values of jarosite may reflect (1) the large spread in $\delta^{56}\text{Fe}$ values (1.5 ‰) of the precursor sulfides, (2) differences in alkali content, due to the Na–K solid solution nature of the jarosite, affecting the partitioning of isotopes into jarosite during its formation and recrystallisation, and (3) fractionation of iron isotopes resulting from Rayleigh distillation during jarosite formation.

This work has demonstrated that iron isotopes are a valuable tool to decipher how jarosite forms in sulfur-rich sediments. One challenge in interpreting the iron isotope composition of jarosite is that the equilibrium iron isotope fractionation between jarosite and other iron-bearing minerals (e.g. goethite) and dissolved iron species (e.g. Fe(II)) is poorly understood. The next research chapter in this thesis aims to address this.

Chapter 5

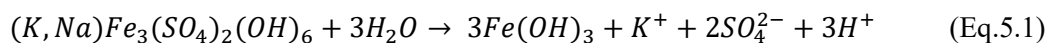
Iron Isotope Exchange and Fractionation Between Jarosite and Aqueous Fe(II)

This chapter describes an experimental investigation into iron isotope exchange and fractionation between jarosite and Fe(II)_{aq}. The results are discussed in terms of the large range in $\delta^{56}\text{Fe}$ values for the jarosite samples examined in Chapter 5. The results are also compared with calculated equilibrium iron isotope fractionation factors including those presented in Chapter 4. The work from this chapter forms a paper that was published in Chemical Geology (Whitworth, A.J., Brand, H.E.A., Frierdich, A.J., 2020a. Iron isotope exchange and fractionation between jarosite and aqueous Fe(II). Chemical Geology, 554: 119802).

5.1. INTRODUCTION

Jarosite [$\text{KFe}_3(\text{SO}_4)_2(\text{OH})_6$] is a common mineral in acid–sulfate environments such as acid sulfate soils (ASS) and acid mine drainage (AMD; e.g. Desborough et al., 2010; Jamieson et al., 2005; Murray et al., 2014; Welch et al., 2007, 2008), where its formation has the potential to buffer acidity and capture toxic metals. It is a member of the alunite supergroup of minerals, which have the general formula of $\text{DG}_3(\text{TO}_4)_2(\text{OH})_6$, and falls into the aptly–named jarosite subgroup which contain predominantly Fe and S in the G and T sites, respectively (Bayliss et al., 2010; Spratt et al., 2013; Welch et al., 2007). The most common naturally occurring variant of jarosite is natrojarosite [$\text{NaFe}_3(\text{SO}_4)_2(\text{OH})_6$] (Desborough et al., 2010; Stoffregen et al., 2000). However, jarosite subgroup minerals typically are a solid solution due to substitution of different ions into the D, G and T sites, rather than endmember compositions (Stoffregen et al., 2000; Whitworth et al., 2020b).

A wide range of metallic and metalloid ions can substitute into the jarosite crystal structure. For example, jarosite has been shown to incorporate both As and Sb in acidic and sulfate–rich conditions (Asta et al., 2009; Courtin–Nomade et al., 2012; Johnston et al., 2010). As a result, jarosite can be a scavenger of toxic metal(oids) in the environment. Conversely, captured toxic metal(oids) can also be released into the environment during jarosite decomposition (Karimian et al., 2017; Smith et al., 2006a). For jarosite to remain stable, fluids in contact with the mineral need to be acidic, otherwise jarosite will undergo hydrolysis to Fe–oxyhydroxides, releasing acidity (Brown, 1971; Langmuir, 1997; Pritchett et al., 2012) according to Equation 5.1:



Thus, jarosite is a mineral with the ability to both trap and release toxic metal(oid)s into the environment, as well as can release stored acidity during hydrolysis, resulting in the need for specific strategies to control this complex behavior. Research investigating jarosite dissolution, transformation and recrystallisation is key to this management.

Jarosite formed in acid sulfate soils is often exposed to fluctuating redox conditions (e.g. from changes in the water levels; Karimian et al., 2018b) which can cause the oxidation state of Fe to shift between Fe(III) and Fe(II) (Thompson et al., 2006) and thus expose jarosite to aqueous Fe(II) (Fe(II)_{aq}). Jarosite transformation to more stable Fe(III)–bearing minerals is catalysed by Fe(II)_{aq} in (near–)neutral pH conditions (Jones et al., 2009; Karimian et al., 2017, 2018a) but low pH jarosite transformation has not been observed (Karimian et al., 2018a). However, it is unclear if jarosite still interacts with Fe(II)_{aq} without significant transformation, similar to what has been observed for Fe(II)_{aq} and goethite at low pH (Reddy et al., 2015). Low pH recrystallisation of jarosite may affect the mineral–fluid partitioning of associated metal(oid)s or cause Fe isotope fractionation between jarosite and the dissolved Fe(II). A recent survey of the Fe isotope composition of jarosite in acidic coastal sediments found that jarosite can have a very large (>3 ‰) range of $\delta^{56}\text{Fe}$ values (Chapter 4; Whitworth et al., 2020b). However, interpretation of the $\delta^{56}\text{Fe}$ values has been challenging as the equilibrium iron isotope fractionation factors between jarosite and other iron–bearing minerals and dissolved iron species is poorly understood.

Equilibrium isotope fractionation examines the partitioning of isotopes between two phases in chemical equilibrium (Dauphas et al., 2017). This knowledge can then be used to constrain the interpretation of measured Fe isotope values for the phase of interest. Fractionation factors (α values) can be measured directly through experiments, or can be calculated by combining the reduced partition coefficients, also known as β –factors, for two phases, A and B (Johnson et al., 2020) according to Equation 5.2:

$$1000\ln\alpha_{A-B} = 1000\ln\beta_A - 1000\ln\beta_B \quad (\text{Eq. 5.2})$$

There are two primary methods used to calculate β –factors for Fe–bearing phases: first–principle electronic structure calculations and derivation of β –factors by modelling spectroscopic data. Density functional theory (DFT) is the most commonly used calculation technique and has been used to examine isotopic fractionation in Fe–bearing aqueous and mineral phases (e.g. Anbar et al., 2005; Blanchard et al., 2015, 2017; Domagal–Goldman and Kubicki, 2008; Rustad et al., 2010; Rustad and Dixon, 2009). Mössbauer spectroscopy and nuclear resonant inelastic X–ray scattering (NRIXS) are used to determine β –factors (Blanchard et al., 2015; Dauphas et al., 2012; Polyakov, 1997; Polyakov et al., 2007; Polyakov and Mineev, 2000; Roskosz et al., 2015; Schauble et al., 2001).

Using β –factors for jarosite and hydronium jarosite [(H₃O)Fe₃(SO₄)₂(OH)₆] from Dauphas et al. (2012), and the β –factor for Fe(II)_{aq} from Rustad et al. (2010), Whitworth et al. (2020b) calculated equilibrium fractionation factors for Fe(II)_{aq}–jarosite and Fe(II)_{aq}–hydronium jarosite, to be approximately –3.53 and –4.76 ‰, respectively, in $^{56}\text{Fe}/^{54}\text{Fe}$ at 22 °C. It is difficult, however, to assess the accuracy of these values as there is no experimental data on the fractionation of Fe isotopes between Fe(II)_{aq} and jarosite.

Additionally, to our knowledge, there is no β -factor for natrojarosite reported in the literature despite Na-rich jarosite being commonly found in nature (Chen et al., 2013; Cunningham et al., 2005; Desborough et al., 2010; Öborn and Berggren, 1995; Whitworth et al., 2020b). The experimental determination of the fractionation factor between $\text{Fe(II)}_{\text{aq}}$ and jarosite could hence add confidence that calculated β -factors are accurate, aid in the interpretation of the iron isotope values for jarosite in nature, and shed light on how $\text{Fe(II)}_{\text{aq}}$ and jarosite interact in low-pH, acid-sulfate environments.

Here we employ the three-isotope (^{57}Fe – ^{56}Fe – ^{54}Fe) method to experimentally measure Fe isotope exchange and fractionation between $\text{Fe(II)}_{\text{aq}}$ and synthetic jarosite and natural natrojarosite. Hydronium jarosite was not examined as pure hydronium jarosite is metastable and uncommon (Drouet and Navrotsky, 2003; Ripmeester et al., 1986; Swayze et al., 2008), although jarosite group minerals often contain minor (a few %) amounts of hydronium. Specifically, we apply a reversal-approach to equilibrium by reacting jarosite and natrojarosite with two ^{57}Fe -enriched $\text{Fe(II)}_{\text{aq}}$ solutions which have distinct $^{56}\text{Fe}/^{54}\text{Fe}$ ratios that are expected to be above and below equilibrium. We then compare our results with calculated equilibrium fractionation factors and conclude with a discussion on the mechanisms involved in jarosite recrystallisation in acid-sulfate conditions and the implications this has for jarosite management.

5.2 METHODOLOGY

5.2.1 Jarosite collection, synthesis and characterisation

The natural natrojarosite sample was acquired from Southside Beach in Victoria, Australia and is described in detail in Appendix 1 as “Js-SB-38”. In brief, Js-SB-38 was prepared by air-drying a natrojarosite pebble at room temperature, removing matrix material (e.g. sand) using tweezers and brushes while viewing the sample under a hand specimen microscope, then grinding up a subsample of material using an agate mortar and pestle. The sample consists of rhombohedral natrojarosite and minor amounts of quartz and halite based on Synchrotron powder X-ray diffraction (PXRD).

Synthetic jarosite, Js-Syn-01, was grown in a chloride-rich medium using a method modified after Basciano and Peterson (2007). This method was employed to minimise the incorporation of hydronium in the crystal structure. Ten millilitres of 1.23 M FeCl_3 followed by 1.0 g of KCl were added to 24 mL of a 10.81 M LiCl solution. Twelve grams of $\text{Fe}_2(\text{SO}_4)_3 \cdot x\text{H}_2\text{O}$ was dissolved in 25 mL $\geq 18.2 \text{ M}\Omega \text{ cm}$ water (hereon H_2O) then slowly added over one minute to the chloride solution. The final solution was mixed for five minutes using a magnetic stirrer, filtered into a Teflon-lined stainless steel pressure vessel and heated for ~48 hours at 140 °C. The sample was rinsed thoroughly with H_2O , filtered, and allowed to dry at room temperature before being further dried at 100 °C for three hours to remove any

excess water. After cooling to room temperature, the entire sample was ground to a powder using an agate mortar and pestle and characterised using PXRD.

A subsample of jarosite was loaded into a 0.5 mm diameter borosilicate glass capillary then mounted onto the powder diffraction (PD) beamline (Wallwork et al., 2007) at the Australian Synchrotron. The X-ray beam wavelength was 0.824942(4) Å based on refinement of NIST standard Reference Material LaB₆ 660b. The diffraction pattern was collected with the MYTHEN-II microstrip detector (Schmitt et al., 2003) and the capillary was rotated at ~1 Hz during data collection to aid powder averaging. Two patterns, each of 300 s, were collected with the detector set 5° apart to cover gaps between the detector modules. PDViPeR software available at the PD beamline was then used to merge the two patterns into a single dataset. Bruker DIFFRAC.EVA was used to examine the mineralogy of the sample using the Crystallography Open Database (Grazulis et al., 2009) and structural analysis of the sample through Rietveld refinement (Rietveld, 1969) was completed using Bruker DIFFRAC.TOPAS 5. The jarosite sample was found to have a rhombohedral symmetry.

The stoichiometry of both samples was determined using inductively coupled plasma–optical emission spectrometry (ICP–OES). A subsample of ground Js–SB–38 was rinsed with H₂O to remove halite, filtered and dried at room temperature. Twenty milligrams of each sample were dissolved in 1 mL of 10 M HCl at 25 °C for 24 hours, then diluted to 1 M HCl using 9 mL H₂O and filtered (0.22 µm). A small aliquot of the solution was then diluted to one tenth of the original concentration for ICP–OES analysis. Element (K, Na, Fe, S) concentrations were measured on a Thermo iCAP 7400 Duo ICP–OES in radial mode. Elemental concentrations were quantified by conversion of counts per second to ppm using calibration curves prepared by measuring standard solutions containing Fisher Chemical K, Na, Fe and S solutions for ICP–OES at known concentrations. The stoichiometry of the samples was determined based on the ratio of alkali ions and Fe to S. The SO₄ site in the jarosite and natrojarosite was assumed to be fully occupied. Thus, the alkali ions and Fe were normalised to two S atoms per chemical formula. It was also assumed that the D site was fully occupied in the samples, and any deficiency in this site was attributed to the presence of H₃O⁺. Js–Syn–01 has a stoichiometry of (K_{0.941}H₃O_{0.059})Fe_{3.040}(SO₄)₂(OH)₆ and Js–SB–38 has a stoichiometry of (Na_{0.852}K_{0.097}H₃O_{0.051})Fe_{3.195}(SO₄)₂(OH)₆. ICP–OES results are reported in Appendix 2 (Table SI 10A).

5.2.2 Three–isotope method and reversal approach to equilibrium

The three–isotope method has been described in detail by several authors (see Frierdich et al., 2019; Shahr et al., 2017), and is described in detail in Chapter 2, so is only briefly described below in the context of this study. The method tracks changes in the isotopic composition of two phases by examining changes in the abundance of three isotopes (i.e. ⁵⁴Fe, ⁵⁶Fe and ⁵⁷Fe) over time. One phase is

enriched in an isotopic tracer (i.e. ^{57}Fe) while the other has a natural abundance isotope composition. The changes in isotopic composition are tracked on a three-isotope plot (Figure 5.1A). The phase with the natural-abundance isotope composition (i.e. jarosite) plots on the terrestrial fractionation line (TFL) while the enriched phase (i.e. $\text{Fe(II)}_{\text{aq}}$) plots adjacent to the TFL. The location of the enriched phase relative to the TFL depends on the level of enrichment, as well as the isotopes that are enriched (e.g. a phase enriched in ^{54}Fe and ^{57}Fe will plot in a different location to one with ^{57}Fe enrichment only). As isotope exchange occurs between the two phases, the isotopic composition approaches a secondary fractionation line (SFL) that is determined by the system mass balance. The fractionation factor is obtained by determining the difference in the isotopic values of each component after complete exchange, and if exchange is incomplete, extrapolation to the SFL is possible. The enriched isotopic ratio (i.e. $^{57}\text{Fe}/^{56}\text{Fe}$) is used to examine the extent of isotopic exchange while the non-enriched isotopic ratio (i.e. $^{56}\text{Fe}/^{54}\text{Fe}$) is used to examine changes in the isotope fractionation factor during the experiment. With the reversal approach, two different $\text{Fe(II)}_{\text{aq}}$ solutions were used, both with near-identical ^{57}Fe enrichment but one has a small ^{54}Fe enrichment (see below) that results in $^{56}\text{Fe}/^{54}\text{Fe}$ ratios above and below the predicted equilibrium value. Consequently, the presumed isotopic equilibrium value is approached from two directions, improving accuracy in the measured value and confidence that equilibrium is attained.

One challenge inherent to the three-isotope method is that there can be small mass balance differences across a series of experiment reactors due to minute variations in the reactor set-up (e.g. there may be

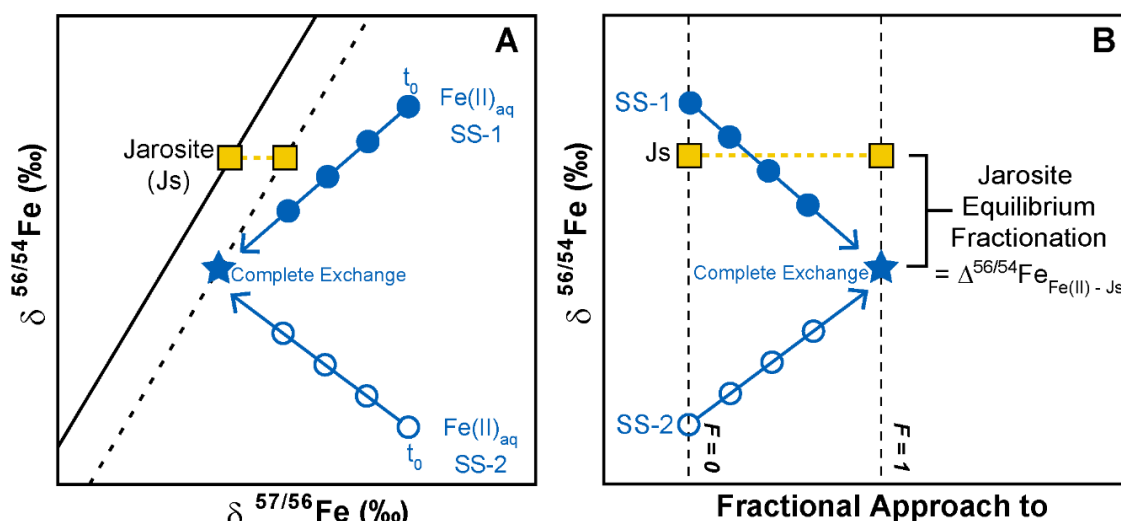


Figure 5.1. Illustration of the three-isotope method and reversal approach to equilibrium. (A) Sample (i.e., jarosite) with a natural-abundance isotopic composition plots along a terrestrial fractionation line (TFL) while the enriched phases (i.e. $\text{Fe(II)}_{\text{aq}}$ Solutions 1 and 2 at t_0) are off-set from the TFL. Solutions 1 and 2 have $^{56}\text{Fe}/^{54}\text{Fe}$ ratios above and below the predicted equilibrium value, respectively. As isotopic exchange occurs between the sample and enriched phases, the isotopic composition of the enriched phases approaches a secondary fractionation line (SFL), determined by the system mass balance, until exchange is complete. (B) Plot of $^{56}\text{Fe}/^{54}\text{Fe}$ against F , the fractional approach of ^{57}Fe towards the system mass balance. The difference in the $^{56}\text{Fe}/^{54}\text{Fe}$ ratios of $\text{Fe(II)}_{\text{aq}}$ and jarosite after complete exchange ($F = 1$) represents the equilibrium fractionation factor, Δ . Illustration modified after Frierdich et al. (2019).

minor variations in the amount of jarosite added to each reactor). To correct for this, Frierdich et al. (2019) plotted the ratio of $^{56}\text{Fe}/^{54}\text{Fe}$ against F , the fractional approach of ^{57}Fe towards the system mass balance, according to Equation 5.3 (modified from Frierdich et al., 2019):

$$F = \delta^{57/56}\text{Fe}_t - \delta^{57/56}\text{Fe}_i / \delta^{57/56}\text{Fe}_{\text{sys}} - \delta^{57/56}\text{Fe}_i \quad (\text{Eq. 5.3})$$

where $\delta^{57/56}\text{Fe}_t$ is the $^{57}\text{Fe}/^{56}\text{Fe}$ composition of one reacting component at time t , $\delta^{57/56}\text{Fe}_i$ is the initial $^{57}\text{Fe}/^{56}\text{Fe}$ composition of that component, and $\delta^{57/56}\text{Fe}_{\text{sys}}$ is the $^{57}\text{Fe}/^{56}\text{Fe}$ composition of the entire system (i.e. system mass balance). Plotting $^{56}\text{Fe}/^{54}\text{Fe}$ against F (Figure 5.1B) normalises out the small mass balance differences, and the equilibrium fractionation factor is still determined by calculating the difference in the isotopic composition of each component at equilibrium ($F = 1$), or extrapolation to equilibrium.

5.2.3 Exchange experiments

In this study, jarosite and natrojarosite samples with natural-abundance Fe isotope compositions (Table 5.1) were reacted with ^{57}Fe -enriched $\text{Fe(II)}_{\text{aq}}$ solutions under anoxic, acidic conditions (pH <4.5). Acidic conditions were required as jarosite will decompose to Fe-oxyhydroxides at circumneutral pH. Anoxic conditions were required to prevent oxidation of Fe(II) to Fe(III) by O_2 . All reactions were conducted inside an anoxic chamber (~2% H_2 , balance N_2) with an O_2 content maintained at <0 ppm by continual atmospheric circulation over Pd catalysts. All material was placed inside the anoxic chamber >48 hours prior to use. Water was deoxygenated by sparging with N_2 for 30 minutes outside the chamber. After entry into the chamber, the water was further sparged with the chamber atmosphere for 30 minutes after passing it through a secondary O_2/CO_2 trap consisting of 15% pyrogallol–50% KOH aqueous solution.

Inside the anoxic chamber, two solutions containing 5 mM H_2SO_4 , 50 mM FeSO_4 (of natural isotopic abundance) and H_2O were prepared. Each solution was enriched with ^{57}Fe by adding 250 μL of a 0.1 M $\text{Fe(II)}_{\text{aq}}$ solution consisting of ~97% ^{57}Fe (derived from dissolution of ^{57}Fe -metal in 5 M H_2SO_4 followed by dilution to 0.1 M Fe(II) and 0.5 M H_2SO_4 using H_2O). One solution was then spiked with 30 μL of 10 mM $^{54}\text{Fe(II)}_{\text{aq}}$ solution (obtained from dissolution of ^{54}Fe -metal in 5 M H_2SO_4 followed by dilution to 10 mM Fe(II) and 0.5 M H_2SO_4 using H_2O) to give it a slightly lower $^{56}\text{Fe}/^{54}\text{Fe}$ ratio). Resultantly, two 50 mM $\text{Fe(II)}_{\text{aq}}$ solutions were prepared with $^{56}\text{Fe}/^{54}\text{Fe}$ ratios presumably above and below equilibrium with jarosite: Spike Solution 1 (SS-1) that has a $\delta^{57}\text{Fe}/^{56}\text{Fe}$ value of $884.80 \pm 1.57 \text{ ‰}$ (1σ) and $\delta^{56}\text{Fe}/^{54}\text{Fe}$ value of $1.03 \pm 0.08 \text{ ‰}$ (1σ), and Spike Solution 2 (SS-2) that has a $\delta^{57}\text{Fe}/^{56}\text{Fe}$ value of $891.72 \pm 1.14 \text{ ‰}$ (1σ) and $\delta^{56}\text{Fe}/^{54}\text{Fe}$ value of $-3.49 \pm 0.04 \text{ ‰}$ (1σ).

Table 5.1 Extrapolated Fe isotope composition of Fe(II)_{aq} and calculated equilibrium Fe isotope fractionation factors.

Experiment	Solid $\delta^{56}\text{Fe}$ (‰) ^a	Fe(II) _{aq} $\delta^{56}\text{Fe}$ Final (‰) ^b	$\Delta^{56}\text{Fe}$ Fe(II) _{aq} –(Na)Js (‰)
Jarosite			
SS–1	0.30 (± 0.09) ^c	–1.96 (± 0.09)	–2.26 (± 0.19)
SS–2	0.30 (± 0.09) ^c	–1.97 (± 0.08)	–2.27 (± 0.19)
		Weighted Average	–2.26 (± 0.27)
Natrojarosite			
SS–1	0.12 (± 0.03)	–1.98 (± 0.11)	–2.10 (± 0.11)
SS–2	0.12 (± 0.03)	–2.17 (± 0.13)	–2.29 (± 0.13)
		Weighted Average	–2.19 (± 0.18)

^a The solid (i.e. Js–Syn–01 and Js–SB–38) $\delta^{56}\text{Fe}$ compositions are not expected to change during the experiments as they dominate the system Fe mass balance: ~98% of all the Fe atoms in each jarosite and natrojarosite reactor are located within the jarosite and natrojarosite structure.

^b Determined by a linear fit through all data points and extrapolation to $F=1$ (see Figure 5.4)

^c Errors reported at the 2σ level

All reactors were done in duplicate and consisted of combining pre-weighed Js–SB–38 (natrojarosite) or Js–Syn–01 (jarosite; 20 ± 0.2 mg) with 8.9 mL and 8.8 mL of H₂O, respectively, in 15 mL polypropylene centrifuge tubes. To each reactor, 1 mL of 0.1 M Na₂SO₄ was added to shift the equilibrium in favor of jarosite stability to prevent transformation according to Equation 5.1. For the jarosite reactors, K₂SO₄ was not used as it was found to be unfavourable for Fe exchange during preliminary tests, despite it being conducive for jarosite stability. Reactions were initiated by adding 0.05 mL of 50 mM ⁵⁷Fe-enriched Fe(II)_{aq} solution (pH ~2). Prior to addition of ⁵⁷Fe-enriched Fe(II)_{aq}, 60 uL and 160 uL of 0.01 M NaOH were added to the natrojarosite and jarosite reactors, respectively, so that the addition of the Fe(II)_{aq} resulted in the natrojarosite reactors having a starting pH of 4.4 ± 0.08 and the jarosite reactors, 4.4 ± 0.15 . Thus, all reactors contained 10 ml of solution. Additionally, control reactors containing (1) Fe(II)_{aq} in the absence of Js–SB–38 or Js–Syn–01, and (2) Js–SB–38 or Js–Syn–01 without the addition of ⁵⁷Fe-enriched Fe(II)_{aq}, were prepared to verify the absence of external Fe(II) oxidation and the stability of natrojarosite and jarosite in Fe(II)-free solutions, respectively, and were collected at completion of the experiment. After initialising the experiment, the reactors were wrapped in aluminium foil to prevent photo-oxidation and placed on a gyratory mixer to keep the natrojarosite and jarosite suspensions mixed.

Reactors were sampled at specific time intervals for determination of Fe concentration and isotopic composition of Fe(II)_{aq}. First, the pH of the reactors was measured. Then, 9 mL of sample was filtered (0.2 μm) into a clean tube and acidified with 1 mL of 1 M HCl. Iron concentrations were measured using the Fe(II)-selective reagent Ferrozine (Stookey, 1970). Total iron concentrations were measured following the reduction of any Fe(III) by hydroxylamine hydrochloride.

For both the jarosite and natrojarosite reactors, three solid samples from the 70-day reactors, one from a SS-1 reactor, one from a SS-2 reactor, and one from a control reactor containing no Fe(II)_{aq}, were collected to assess any structural (i.e. cation exchange) or phase transformation of the jarosite using PXRD. The solid samples were dried at room temperature, ground using an agate mortar and pestle, then analysed on the PD beamline at the Australian Synchrotron following the procedure used to characterise Js-Syn-01 (see section 5.2.1 for details). For these samples, the X-ray beam wavelength was 0.774800(3) Å based on refinement of NIST standard Reference Material LaB₆ 660b.

To examine whether ion exchange was occurring between K in the jarosite and natrojarosite solid and Na in the reactor fluid, small aliquots of the reactor fluid were collected from the experimental reactors, diluted to a tenth of the original concentration, and K concentrations were measured using either a Thermo iCAP-Q quadrupole inductively coupled plasma-mass spectrometer (ICP-MS) operated in kinetic energy discrimination (KED) mode or a Thermo iCAP 7400 Duo ICP-OES in radial mode. Potassium concentrations were quantified by conversion of counts per second to micromolar using calibration curves by analysis of standard solutions containing High-Purity ICP-MS-68 Solution A or Fisher Chemical K, Na, Fe and S solutions for ICP-OES at varying concentrations.

5.2.4 Isotope analysis

The reactor solutions were purified in a class 350 clean room using ion exchange chromatography to remove potentially interfering matrix components (e.g. SO₄²⁻) following the method in Chapter 4 (Whitworth et al., 2020b). Test solutions containing matrix elements (i.e. Na₂SO₄, K₂SO₄, HCl) and IRMM-524a in the same proportions as the reactor solutions in this study were also purified using the method in Chapter 4 (Whitworth et al., 2020b) to confirm that iron isotope fractionation did not occur during ion exchange chromatography and sample handling.

Iron isotopes ratios, ⁵⁶Fe/⁵⁴Fe and ⁵⁷Fe/⁵⁴Fe, are presented in per mil (‰) units using standard delta notation according to Equations 5.4 and 5.5:

$$\delta^{56}\text{Fe}(\text{‰}) = [({}^{56}\text{Fe}/{}^{54}\text{Fe})_{\text{sample}}/({}^{56}\text{Fe}/{}^{54}\text{Fe})_{\text{standard}} - 1] \times 1000 \quad (\text{Eq. 5.4})$$

$$\delta^{57/56}\text{Fe}(\text{‰}) = [({}^{57}\text{Fe}/{}^{56}\text{Fe})_{\text{sample}}/({}^{57}\text{Fe}/{}^{56}\text{Fe})_{\text{standard}} - 1] \times 1000 \quad (\text{Eq. 5.5})$$

where *sample* refers to the ratio of the iron isotopes in the sample, and *standard* is the ratio of the iron isotopes in IRMM-014.

Iron isotopes were measured on a Thermo–Fisher *Neptune Plus* in medium–resolution mode using a wet–plasma and standard–sample bracketing following previously described methods (Sossi et al., 2015). In this study, iron isotope values were bracketed against the IRMM–524a iron standard which has an identical iron isotope composition to IRMM–014 (Craddock and Dauphas, 2010). The measured $\delta^{56}\text{Fe}$ value of test solutions was $0.03 \pm 0.04 \text{ ‰}$ (2σ ; $n = 6$), which is close to the measured value of the pure iron standard $0.00 \pm 0.03 \text{ ‰}$ (2σ ; $n = 13$), indicating that the iron isotope values were not significantly altered during column chemistry and sample handling. Measurement precision of $\delta^{56}\text{Fe}$ and $\delta^{57/56}\text{Fe}$ was also assessed by replicate analyses of reactor and test solution samples, and the reactor average standard deviation was 0.03 ‰ and 0.04 ‰ (2σ ; $n = 30$), respectively.

5.3 RESULTS

5.3.1 Reactor pH and K release

The solution pH in both the jarosite and natrojarosite reactors decreases by a small amount (~ 0.8) over the 70 day period (Figure 5.2A), and the jarosite reactors have a lower pH than the natrojarosite reactors at all sampling intervals except 70 days. In the jarosite reactors, pH decreases rapidly during the first 24 hours ($\sim 4.5 - 4.19$) then gradually slows over time, dropping to 3.71 after 70 days. In the natrojarosite reactors, pH remains steady (between 4.4 and 4.5) for the first 24 hours before decreasing gradually to ~ 3.62 after 70 days. The rate of decrease varies over the course of the 70 days. The pH in reactors containing SS–1 and SS–2 decreases at a similar rate over time for both jarosite types, and this is

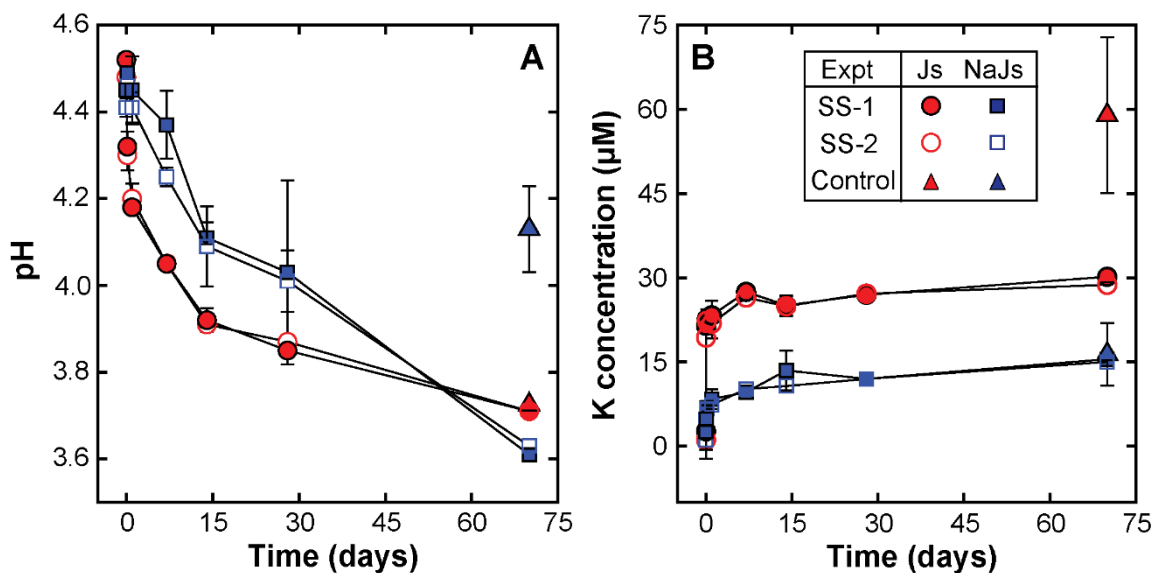


Figure 5.2. Temporal variations in (A) pH and (B) K concentration for jarosite (red circles) and natrojarosite (blue squares) reactors containing Spike Solution 1 (SS–1; closed symbol) and Spike Solution 2 (SS–2; open symbol). The 70 day pH and K values for the control reactors containing jarosite (red triangle) and natrojarosite (blue triangle) but no Fe(II) are provided for comparison. Data points for both graphs represent the mean of duplicate reactions.

expected given the solutions have a chemically identical composition (within experimental uncertainty). A difference in pH values is observed though when comparing the 70 day experiment reactors and the control reactors without Fe(II) spike. The natrojarosite reactors containing Fe(II)_{aq} have a lower (~0.5) pH value than the control reactor containing no Fe(II)_{aq}, whereas for the jarosite reactors, the pH values are nearly identical. There are a couple of different explanations for this, as well as several possible explanations for the decrease in pH over time, and these are discussed further below (see section 5.4.2). Reactor pH results are reported in Appendix 2 (Table SI 1).

The concentration of K increases over the 70 day period for all reactions with Fe(II)_{aq} (Table SI 2 in Appendix 2, Figure 5.2B). The jarosite reactors have greater amounts of K release (from ~2 μ M to ~29 μ M) than the natrojarosite reactors (~2 μ M to ~15 μ M), consistent with the low levels of K substitution (~10% of the D site) in the natrojarosite compared to the jarosite (~95% of the D site is K). The concentration of K⁺ in the 70 day Fe(II)_{aq} – free reactors are more than in the Fe(II)_{aq} reactors, with the jarosite and natrojarosite Fe(II)_{aq} – free reactors increasing from ~2 μ M to ~59 μ M and ~16 μ M, respectively. Although there are measurable amounts of K released into solution, the observed concentrations account for only 0.74% and 3.35% of the total K in the jarosite and natrojarosite, respectively (see SI 7 in Appendix 2 for calculations). The release of K from jarosite suggests that minor amounts of K-rich regions of the mineral phase are replaced by Na which is present in large excess in the fluid (~10 mM).

5.3.2 Iron concentration and tracer isotope dynamics

For all experiments, the concentration of Fe(II)_{aq} shows little (~ 0.04 mM) variation over time, with the reactors having an average initial Fe(II)_{aq} concentration of 0.21 ± 0.02 mM (2σ) and an average Fe(II)_{aq} concentration of 0.23 ± 0.02 mM (2σ) over the duration of the experiments (Table SI 3, Appendix 2). There is also no significant difference in the Fe(II)_{aq} concentration between the reactors containing SS–1 and SS–2 at each time point. This suggests that no detectable net Fe(II) sorption occurred over time, within error, and is consistent with the low tendency for cation sorption at low pH on oxygen terminated mineral surfaces (Handler et al., 2014; Jones et al., 2014; Reddy et al., 2015) and accordant with previous observation of no net Fe(II) sorption at low pH (Karimian et al., 2018a). Total Fe measurements show that little Fe(III)_{aq} is present in the experiment reactors (Table SI 3, Appendix 2), with the reactors having an average Fe(III)_{aq} concentration of 0.02 ± 0.01 mM (2σ) over the duration of the experiment. This suggests that negligible jarosite and natrojarosite dissolution occurred during the experiment. The 70 day control reactors free of Fe(II)_{aq} spike also contain negligible Fe(III)_{aq}, suggesting that jarosite and natrojarosite dissolution is not the cause of the pH decrease in these reactors.

Despite $\text{Fe(II)}_{\text{aq}}$ concentrations showing little change, $\delta^{57/56}\text{Fe}$ values decrease with time for all experiments (Figure 5.3; Table SI 4, Appendix 2). For the jarosite reactors, the $\delta^{57/56}\text{Fe}$ of $\text{Fe(II)}_{\text{aq}}$ decreases from an initial value of $884.80 \pm 1.57 \text{‰}$ to $370.76 \pm 14.85 \text{‰}$ for SS-1 and $891.72 \pm 1.14 \text{‰}$ to $396.31 \pm 17.52 \text{‰}$ for SS-2 after 70 days of reaction. For the natrojarosite reactors, the $\delta^{57/56}\text{Fe}$ of $\text{Fe(II)}_{\text{aq}}$ decreases from an initial value of $884.80 \pm 1.57 \text{‰}$ to $407.50 \pm 25.88 \text{‰}$ for SS-1 and $891.72 \pm 1.14 \text{‰}$ to $422.44 \pm 4.88 \text{‰}$ for SS-2 after 70 days of reaction. Thus, there is an average decrease in $\delta^{57/56}\text{Fe}$ of $\sim 489 \text{‰}$ over the duration of the experiments. This decrease over time demonstrates that the ^{57}Fe tracer–isotope in the fluid phase mixed with the natural–abundance Fe in the jarosite and natrojarosite over time. Although there is a large decrease in the $\delta^{57/56}\text{Fe}$ values of $\text{Fe(II)}_{\text{aq}}$ over time, both the jarosite and natrojarosite reactors do not attain their respective $\delta^{57/56}\text{Fe}$ mass balance values of $\sim 20 \text{‰}$ and $\sim 18 \text{‰}$ (Figure 5.3). This suggests that equilibrium was not reached in the reactors, although the large procession towards the mass balance suggests that they were approaching equilibrium. The rate of $\delta^{57/56}\text{Fe}$ decrease over time varies depending on the type of jarosite present in the reactor. For the jarosite reactors, the $\delta^{57/56}\text{Fe}$ value drops rapidly from $\sim 888 \text{‰}$ to $\sim 650 \text{‰}$ within the first 24 hours, then gradually slows over time. For the natrojarosite reactors, $\delta^{57/56}\text{Fe}$ only drops from $\sim 888 \text{‰}$ to $\sim 802 \text{‰}$ in the first 24 hours, whereas the most rapid decrease occurs between 30 and 70 days where $\delta^{57/56}\text{Fe}$ decreases from $\sim 647 \text{‰}$ to 415‰ . This difference in the rate of $\delta^{57/56}\text{Fe}$ decrease over time between the two types of jarosite appears to mirror the decrease observed in their respective pH values over time. When $\delta^{57/56}\text{Fe}$ values are plotted as a function of pH (Figure 5.4), a strong (average $R^2 =$

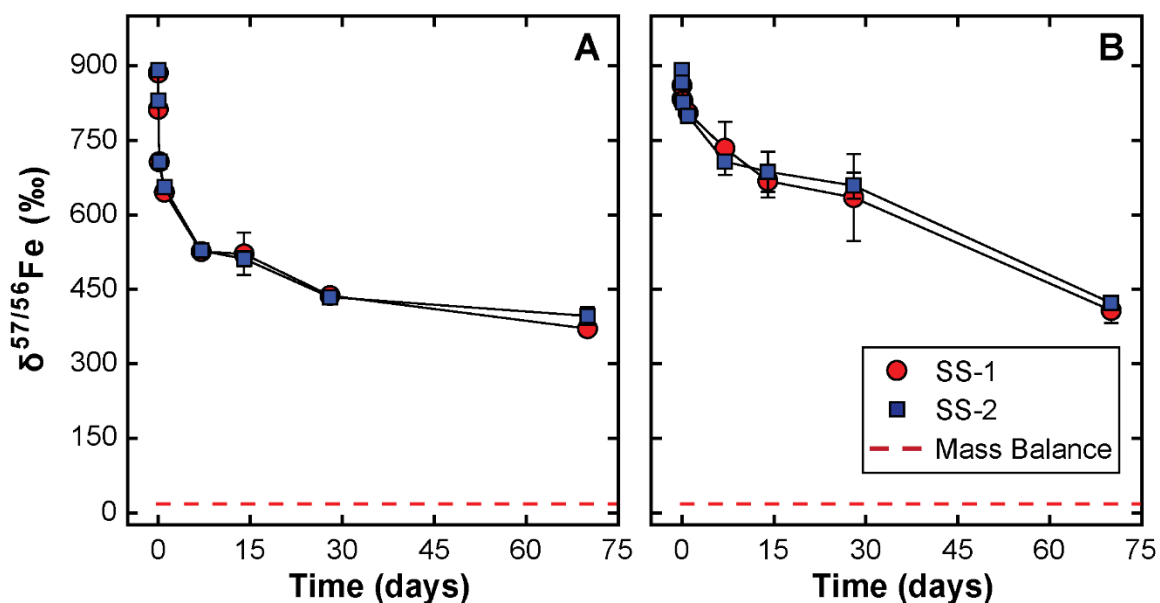


Figure 5.3. Temporal variation in $\delta^{57/56}\text{Fe}$ values for $\text{Fe(II)}_{\text{aq}}$ during reaction with (A) jarosite and (B) natrojarosite in $\text{Fe(II)}_{\text{aq}}$ solutions. Dashed horizontal line represents the isotopic mass balance value of the system ($\sim 20 \text{‰}$ and $\sim 18 \text{‰}$ for jarosite and natrojarosite, respectively). Red circles and blue squares are for experiments with Spike Solution 1 and 2, respectively. Data points represent the mean of duplicate reactions.

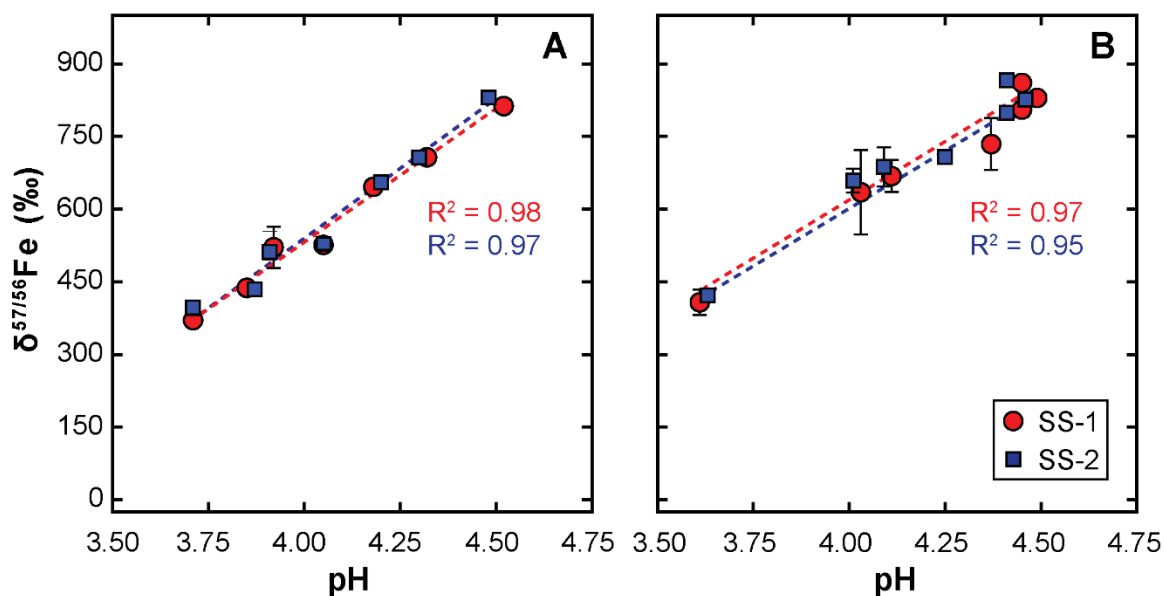


Figure 5.4. Plot of pH against $\delta^{57/56}\text{Fe}$ values for $\text{Fe(II)}_{\text{aq}}$ during reaction with (A) jarosite and (B) natrojarosite in $\text{Fe(II)}_{\text{aq}}$ solutions. Red circles and blue squares are for experiments with Spike Solution 1 and 2, respectively. The dashed red and blue lines represent the line of best fit for Spike Solution 1 and 2, respectively. Data points represent the mean of duplicate reactions.

0.97) negative correlation is observed. This correlation suggests that the exchange of Fe between $\text{Fe(II)}_{\text{aq}}$ and jarosite and natrojarosite is linked to the process responsible for the pH drop observed in the reactors (Section 5.3.1).

5.3.3 Mass-dependent Fe isotope fractionation

Measured $\delta^{56}\text{Fe}$ values for both reactor types vary over the course of the experiment, and the direction of these changes depends on the initial $^{56}\text{Fe}/^{54}\text{Fe}$ ratios of the $\text{Fe(II)}_{\text{aq}}$ relative to jarosite and natrojarosite (Figure 5.5). For the jarosite reactors, when the initial $^{56}\text{Fe}/^{54}\text{Fe}$ ratio of $\text{Fe(II)}_{\text{aq}}$ is similar to jarosite (SS-1), there is a decrease in $\delta^{56}\text{Fe}$ values of $\text{Fe(II)}_{\text{aq}}$ over time. During the first 24 hours, the rate of decrease is rapid, with $\delta^{56}\text{Fe}$ dropping from 1.03 ± 0.08 ‰ to 0.29 ± 0.00 ‰. It is then much slower for the remainder of the experiment, dropping to -0.71 ± 0.04 ‰ by 70 days. In contrast, when the $^{56}\text{Fe}/^{54}\text{Fe}$ ratio of the $\text{Fe(II)}_{\text{aq}}$ are initially lower than jarosite (SS-2), there is an increase in $\delta^{56}\text{Fe}$ values of the $\text{Fe(II)}_{\text{aq}}$ over time. The rate of increase in $\delta^{56}\text{Fe}$ values of the $\text{Fe(II)}_{\text{aq}}$ mirrors those observed in the reactors containing SS-1, with $\delta^{56}\text{Fe}$ increasing rapidly in the first 24 hours from -3.49 ± 0.04 ‰ to -3.06 ± 0.05 ‰ then more slowly to -2.61 ± 0.03 ‰ by 70 days. The overall magnitude of change in $\delta^{56}\text{Fe}$ values is less in the reactors containing SS-2 (~ 0.88 ‰) compared to SS-1 (~ 1.80 ‰), suggesting SS-1 was farther from equilibrium.

For the natrojarosite reactors, the temporal variation in the $\delta^{56}\text{Fe}$ values of the $\text{Fe(II)}_{\text{aq}}$ is similar to that of the jarosite reactors, with the $\delta^{56}\text{Fe}$ values of reactors containing SS-1 and SS-2 decreasing and

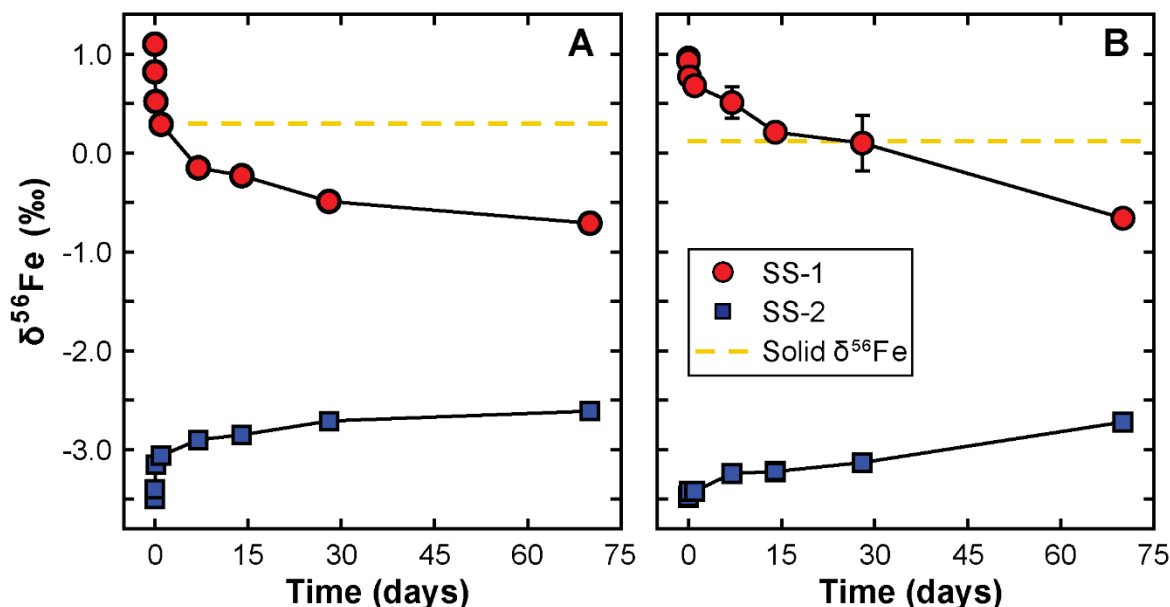


Figure 5.5. Temporal variation in $\delta^{56}\text{Fe}$ values of $\text{Fe(II)}_{\text{aq}}$ during reaction with (A) jarosite and (B) natrojarosite in $\text{Fe(II)}_{\text{aq}}$ solutions. Each jarosite and natrojarosite sample was reacted in a ^{57}Fe -enriched $\text{Fe(II)}_{\text{aq}}$ solution that either contained a $\delta^{56}\text{Fe}$ composition that was presumed to be above the isotopic equilibrium with the (natro)jarosite (SS-1; red circles) or below the isotopic equilibrium with the (natro)jarosite (SS-2; blue squares). For simplicity, the dashed yellow horizontal line represents the initial $\delta^{56}\text{Fe}$ value of (A) Js-Syn-01 and (B) Js-SB-38. Since jarosite and natrojarosite dominates the Fe mass balance ($\sim 98\%$ of all Fe atoms in each reactor reside in the jarosite), the $\delta^{56}\text{Fe}$ value does not significantly change with time. Data points represent the mean of duplicate reactions.

increasing over time, respectively. The overall magnitude of change in $\delta^{56}\text{Fe}$ values is also similar, with reactors containing SS-1 having an overall larger magnitude of change in $\delta^{56}\text{Fe}$ (~ 1.61 ‰) compared to SS-2 (~ 0.76 ‰). However, in the natrojarosite reactors, the most rapid change in $\delta^{56}\text{Fe}$ values occurs between 30 and 70 days. In the first 24 hours, SS-1 $\delta^{56}\text{Fe}$ values decrease from 1.03 ± 0.08 ‰ to 0.68 ± 0.03 ‰, whereas between 30 and 70 days, the values decrease from 0.21 ± 0.10 ‰ to -0.66 ± 0.08 ‰. For SS-2, the $\delta^{56}\text{Fe}$ values increase from -3.49 ± 0.04 ‰ to -3.42 ± 0.02 ‰ in the first 24 hours, whereas between 30 and 70 days the values increase from -3.22 ± 0.08 ‰ to -2.72 ± 0.02 ‰. The rates of change are similar to those observed in the $\delta^{57/56}\text{Fe}$ values and pH, suggesting that the drop in pH, isotopic exchange and fractionation are linked.

Comparison of the $\delta^{56}\text{Fe}$ values of $\text{Fe(II)}_{\text{aq}}$ against F , the fractional approach of the ^{57}Fe tracer-isotope to the system mass balance (Eq. 5.3), shows that there are two unique trajectories for each spike solution (Figure 5.6). For the jarosite, the $\delta^{56}\text{Fe}$ values of $\text{Fe(II)}_{\text{aq}}$ decrease linearly for SS-1 and increase linearly for SS-2. Neither spike solution approaches the isotopic value of Js-Syn-01 (0.30 ‰) suggesting that the changes in the $\delta^{56}\text{Fe}$ values of $\text{Fe(II)}_{\text{aq}}$ are not affected by net jarosite dissolution or a disequilibrium process. When these trajectories are fit with a linear regression ($R^2 = 0.99$), and the trajectories are

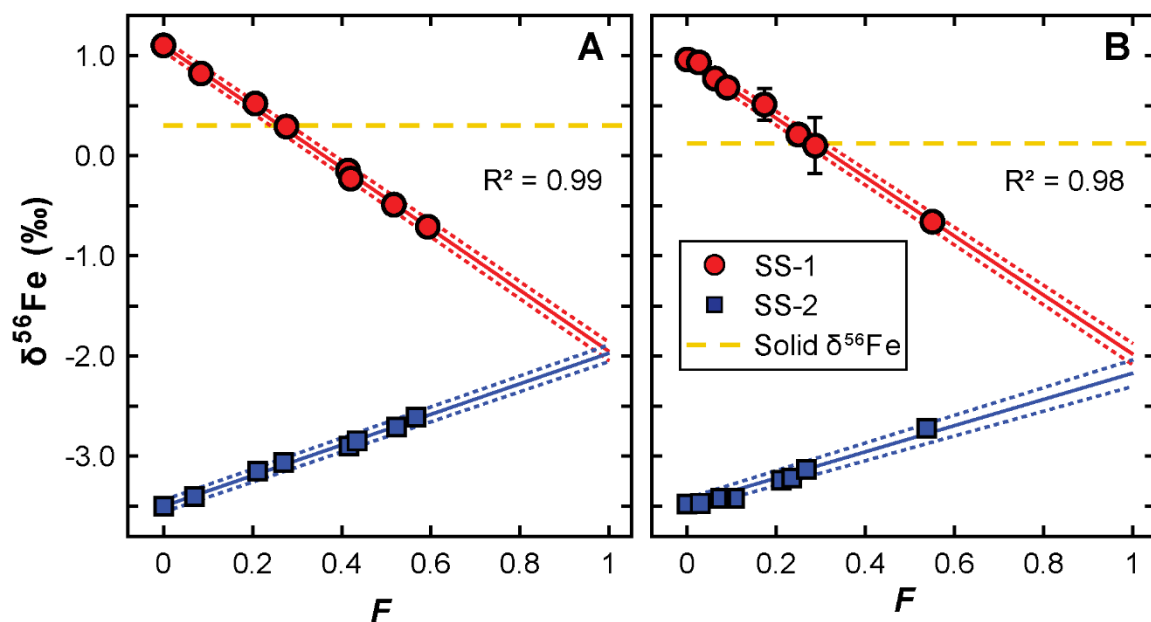


Figure 5.6 Progression of $\delta^{56}\text{Fe}$ values for $\text{Fe(II)}_{\text{aq}}$ with the fractional approach to isotopic mass balance (F), calculated (Eq. 1) from changes in the ^{57}Fe tracer, during reactions with (A) jarosite and (B) natrojarosite. Solid lines represent the linear regression of all data points. Dotted lines represent the error envelope from the fitting uncertainties (2σ) of the solid line. Each jarosite sample was reacted in a ^{57}Fe -enriched $\text{Fe(II)}_{\text{aq}}$ solution that either contained a $\delta^{56}\text{Fe}$ composition that was presumed to be above (SS-1; red circles) or below (SS-2; blue squares) the isotopic equilibrium with the (natro)jarosite. For simplicity, the dashed yellow horizontal line represents the $\delta^{56}\text{Fe}$ value of (A) Js-Syn-01 and (B) Js-SB-38 since the $\delta^{56}\text{Fe}$ value of the jarosite dominates the system Fe mass balance ($\sim 98\%$ of all Fe atoms in each reactor reside in the jarosite) and does not significantly change with time. Data points represent the mean of duplicate reactions.

extrapolated to $F = 1$ (i.e. equilibrium), the two trajectories converge, with the extrapolated $\delta^{56}\text{Fe}$ values differing by 0.01 ‰. Both experiments with the different $\text{Fe(II)}_{\text{aq}}$ solutions yield a similar equilibrium fractionation factor, and the weighted average value is $\Delta^{56}\text{Fe}_{\text{Fe(II)aq-Js}} = -2.26 \text{ ‰} (\pm 0.27 \text{ ‰}, 2\sigma)$ at 22 °C.

For the reactions with natrojarosite, the $\delta^{56}\text{Fe}$ values of $\text{Fe(II)}_{\text{aq}}$ decrease linearly for SS-1 and increase linearly for SS-2. Again, neither spike solution trajectories approach the isotopic value of Js-SB-38 (0.12 ‰). When these trajectories are fit with a linear regression ($R^2 = 0.98$), and the trajectories are extrapolated to $F = 1$, the two trajectories also converge to similar $\delta^{56}\text{Fe}$ values (differing by 0.19 ‰). A similar equilibrium fractionation factor is obtained for both experiments that have a weighted value of $\Delta^{56}\text{Fe}_{\text{Fe(II)aq-NaJs}} = -2.19 \text{ ‰} (\pm 0.18 \text{ ‰}, 2\sigma)$ at 22 °C. This value is within error of the $\text{Fe(II)}_{\text{aq}}$ -jarosite fractionation factor (Table 5.1).

5.3.4 PXRD results

PXRD analysis of solid samples collected after 70 days of reaction with Fe(II)_{aq}, or after suspension in an Fe(II)–free fluid, shows that the only iron–bearing phase present in the jarosite reactors is jarosite, and in the natrojarosite reactors, natrojarosite (Figures SI 5A and 5B, Appendix 2). This shows that no phase transformation occurred during the experiment. Lattice parameters for the two types of jarosite are identical within error and are comparable to the lattice parameters for the unreacted (natro)jarosite (Table SI 5, Appendix 2). This suggests that no significant amount of cation exchange has occurred during the suspension of jarosite or natrojarosite in the presence and absence of Fe(II)_{aq} in acidic, sulfate rich fluids. This is also consistent with the low extents of K and H⁺ release from jarosite and natrojarosite.

5.4 DISCUSSION

5.4.1 Jarosite recrystallisation in the presence of Fe(II)_{aq}

Jarosite is common in redox–dynamic environments and may be exposed to Fe(II)_{aq} in sediments. Experimental studies have shown that Fe(II)_{aq} catalyses the transformation of jarosite to more stable iron oxides at circumneutral pH (Jones et al., 2009; Karimian et al., 2017, 2018a). At low pH, however, jarosite is stable in the presence of Fe(II)_{aq} (Karimian et al., 2018a), as evidenced by the absence of any phase transformation. As observed here and reported in prior work (Karimian et al., 2018a), Fe(II) sorption to jarosite is limited at low pH and presumably limits the extent of Fe isotope exchange between Fe(II)_{aq} and structural Fe(III) in jarosite. The absence of net Fe(II) uptake by goethite and hematite in low–pH Fe(II)_{aq} solutions has also been implicated in the limited extents of mineral–fluid exchange in these systems (Friedrich et al., 2015; Handler et al., 2014; Reddy et al., 2015).

The substantial decrease in the $\delta^{57/56}\text{Fe}$ values of Fe(II)_{aq} (i.e. ~ 888 ‰ to ~ 399 ‰ after 70 days of reaction) demonstrates that Fe atoms in the solution are being replaced by those in the jarosite. To quantify the percent of the Fe atoms in jarosite that have exchanged with Fe(II)_{aq}, and thus, the amount of jarosite that has recrystallised at a given time, a recrystallisation model that accounts for how the solid interacts with the fluid is required. Two such models are the homogeneous recrystallisation model and the heterogeneous recrystallisation model (see Gorski and Fantle, 2017, for further details). In brief, the homogenous model assumes that the recrystallised portion of a mineral is re–equilibrating constantly with the fluid. Thus, the isotopic composition of the recrystallised portion of jarosite will be homogenous and equal in composition to the fluid. Using the equation for homogeneous recrystallisation (Eq. SI 9A, Appendix 2), the percentage of Fe atoms in the reactors containing jarosite that were exchanged with Fe(II)_{aq} after 70 days were 2.91 and 2.62% for SS–1 and SS–2, respectively. For the natrojarosite, the percentage of Fe atoms that were exchanged with Fe(II)_{aq} were 2.43 and 2.31% for SS–1 and SS–2, respectively, after 70 days.

The heterogeneous recrystallisation model, conversely, assumes that the recrystallised portion of jarosite does not re-exchange with the fluid and thus, the isotopic composition of jarosite will be heterogeneous. Furthermore, it assumes that structural atoms that enter the fluid emanate from the un-recrystallised portion of the solid and hence the isotopic composition of the fluid will approach the initial isotopic composition of the mineral. In three-isotope space, this mechanistic constraint, or lack thereof, can be key in identifying the reaction mechanism (more below). Using the equation for heterogeneous recrystallisation (Eq. SI 9B, Appendix 2), the percentage of Fe atoms in the reactors containing jarosite that were exchanged with Fe(II)_{aq} after 70 days were 1.82 and 1.70% for SS-1 and SS-2, respectively. For the natrojarosite reactors, the percentage of Fe atoms that were exchanged with Fe(II)_{aq} were 1.61 and 1.55% for SS-1 and SS-2, respectively, after 70 days. Although less exchange occurs with the assumption of heterogeneous recrystallisation, each model predicts relatively small amounts of jarosite and natrojarosite underwent exchange with Fe(II)_{aq}.

Even though low extents of (natro)jarosite were open to exchange with the fluid, the Fe(II)_{aq}/Fe(III)–(natro)jarosite ratio used in this study (i.e. 1:42) means that only a small percentage of the solid needs to be open to exchange for the fluid to reach, or approach, equilibrium. Importantly, however, low amounts of mineral exchange may result in equilibration of a fluid with the atoms at the mineral surface rather than the bulk crystalline solid. Bond lengths of surface atoms may be relaxed relative to the bulk. Consequently, they may exhibit unique thermodynamic properties and hence different degrees of isotopic fractionation, a phenomenon noted previously for Fe(II)_{aq} and goethite (Beard et al., 2010; Frierdich et al., 2014a). The exact nature of whether only surface atoms or perhaps, localised regions on the surface and recrystallisation fronts extending into the bulk, would require nanoscale analysis of the tracer isotopes in the solid (e.g. Frierdich et al., 2019; Taylor et al., 2019) and is beyond the scope of this study.

Further insight into the recrystallisation mechanism arises when the isotopic values are plotted on a three-isotope diagram (Figure 5.6). For homogeneous recrystallisation, because the recrystallised portion of mineral (i.e. jarosite) is continuously equilibrating with the surrounding fluid, it is expected that there will be a linear approach of the two different Fe(II)_{aq} solutions (i.e. SS-1 and SS-2) towards a new equilibrium value. Conversely, for heterogeneous recrystallisation, because the recrystallised portion of the mineral does not re-equilibrate, or exchange at all, with the surrounding fluid, the isotopic composition of the Fe(II)_{aq} solutions are expected to approach the initial value of the mineral as recrystallisation proceeds (Frierdich et al., 2019). The linear trajectories of the SS-1 and SS-2 $\delta^{56}\text{Fe}$ values towards a new equilibrium, with neither approaching the initial isotopic composition of Js–Syn–01 or Js–SB–38, indicates that both the jarosite and natrojarosite are recrystallising homogeneously, and that there appears to be no significant heterogeneous recrystallisation during the experiment. This finding differs from previous three-isotope experiments examining Fe isotope exchange and

fractionation between Fe(II)_{aq} and magnetite, goethite, and hematite (Beard et al., 2010; Frierdich et al., 2014a, 2014b, 2019). In these prior works, an inflection in the different Fe(II)_{aq} solutions' trajectories was interpreted by Frierdich et al. (2019) as a change from initially rapid heterogeneous recrystallisation involving surface exchange of Fe to slower, homogeneous recrystallisation involving the bulk mineral. Interestingly, these inflections or curvature were shown to decrease and $\delta^{56}\text{Fe}$ trajectories of Fe(II)_{aq} approached a more linear trend when Fe(II)_{aq} was reacted with goethite at low pH conditions (Reddy et al., 2015). A long distance conduction mechanism involving electron transfer between sorbed Fe(II) and hematite single crystals, and electron conduction through the mineral, resulting in reductive dissolution of spatially-distinct Fe atoms, has been used to explain exchange of Fe atoms between Fe(II) and Fe(III) oxides (Yanina and Rosso, 2008), and could explain the initial heterogeneous exchange of hematite in Frierdich et al. (2019). The results presented in this study in combination with the finding that $\delta^{56}\text{Fe}$ trajectories of Fe(II)_{aq} are more linear when Fe(II)_{aq} was reacted with goethite at low pH suggests that at low pH, where Fe(II) sorption is less favourable, long distance electron conduction may be limited. Given that only a small percentage of the jarosite recrystallised during the experiments and the lines of evidence above, Fe exchange between Fe(II) and jarosite in acidic conditions appears to be best explained by localised dissolution–reprecipitation at near–equilibrium conditions, although a long distance electron conduction recrystallisation mechanism with small amounts of undetected sorbed Fe(II) cannot be ruled out.

5.4.2 Acidity release during jarosite recrystallisation

The exchange of Fe between Fe(II)_{aq} and jarosite appears to be linked to the small decrease in pH (~0.8) observed over the 70 day period (Figure 5.4). There are three possible mechanistic reasons for this connection. Firstly, the decrease in pH and enhanced Fe exchange may occur through the decomposition of jarosite (Eq. 5.1), which may produce substantial acidity, as well as release structurally incorporated H_3O^+ that substitutes for K^+ or Na^+ . The amount of jarosite that would need to decompose to release enough acidity to cause the ~0.8 pH decrease, according to Eq. 5.1, is 1.33% and 1.62% for the reactors containing jarosite and natrojarosite, respectively (see SI 8 in Appendix 2 for calculations). However, in this process, Fe–oxyhydroxides are expected to form, and PXRD of the 70–day reactor solids showed that no Fe–oxyhydroxide phases formed during the experiment. Thus, it appears unlikely that jarosite decomposition is the cause of the decrease in pH observed in the reactors, although it cannot be ruled out completely as the formation of amorphous Fe–hydroxide phases may be difficult to resolve using PXRD. The second explanation is that simple cation exchange may be occurring through exchange of H_3O^+ for Na^+ , which is present in large excess in solution (>10 mM). Similarly, the third explanation is that exchange of H_3O^+ for Na^+ may occur during dissolution and reprecipitation of jarosite. Jarosite dissolution is incongruent, with D site cations (i.e. Na^+ , K^+ , H_3O^+) and SO_4^{2-} being preferentially released during jarosite dissolution relative to Fe (Gasharova et al., 2005; Smith et al., 2006b; Trueman

et al., 2020; Welch et al., 2007, 2008). This has been attributed to the Fe being located deep within the tetrahedral–octahedral–tetrahedral (T–O–T) sheet structure of jarosite, making it more sterically remote and difficult to remove during dissolution compared to the D–site ions and SO_4^{2-} (Smith et al., 2006b). Thus, partial jarosite dissolution appears to be essential for accessing the Fe sites within jarosite and hence, for Fe exchange between Fe(II) and jarosite to occur. Liberation of H_3O^+ during dissolution and uptake of Na^+ during reprecipitation would explain why there is a decrease in pH as Fe is exchanged between $\text{Fe(II)}_{\text{aq}}$ and jarosite. However, calculation of the amount of jarosite dissolution required to liberate enough H_3O^+ to cause the ~ 0.8 drop in pH observed here, $\sim 4.00\%$ jarosite and 4.90% natrojarosite dissolution is required (see SI 6 in Appendix 2 for calculations). Given that only $\sim 2.67\%$ and $\sim 2.31\%$ of the Fe atoms in jarosite and natrojarosite reactors, respectively, were calculated to have exchanged during recrystallisation, this suggests that exchange of H_3O^+ for Na^+ during dissolution and reprecipitation cannot fully explain the amount of pH decrease during the experiments. Thus, a combination of jarosite decomposition, simple cation exchange between surface H_3O^+ and Na^+ , and hydronium jarosite dissolution and reprecipitation of natrojarosite could explain the decrease in pH observed in the reactors.

At all time points except 70 days, the jarosite reactors have a lower pH value than the natrojarosite reactors. This is despite jarosite being more thermodynamically stable than natrojarosite (Drouet and Navrotsky, 2003; Stoffregen, 1993; Stoffregen et al., 2000). There are a couple of explanations for this pH difference. Firstly, as the natrojarosite is in a solution containing Na_2SO_4 , the solid and solution are in closer equilibrium than in the reactors containing jarosite, decreasing the reactivity of the natrojarosite and hence, slowing its recrystallisation and subsequent pH decrease. Secondly, Welch et al. (2008) observed that the rate of dissolution of natural jarosite in their dissolution study was orders of magnitude slower than the rate of dissolution of synthetic jarosite observed in the dissolution experiments of Smith et al. (2006b) and Gasharova et al. (2005). They attributed this slower rate of dissolution to the formation of an iron–rich passivating layer in the natural jarosite (as D site cations and SO_4^{2-} were preferentially leached) that reduced reaction rates relative to the clean synthetic jarosite of the other studies. Thus, the rate of reaction in the natural natrojarosite reactors may be slower compared to the synthetic jarosite reactors due to formation of a passivating layer, although no passivating layer was evident from the PXRD results. As such, one or a combination of these factors could have resulted in the natural (Na)jarosite undergoing a slower rate of dissolution and reprecipitation compared to the jarosite.

The natrojarosite experiment and Fe(II)–free 70 day reactor pH values were observed to differ by ~ 0.5 , with the Fe(II)–free reactors having a higher pH, whereas the jarosite reactors had near–identical values. Given that the reactor fluids contain substantial Na_2SO_4 , it is possible that as H_3O^+ –rich portions of the natrojarosite in the Fe(II)–free reactors dissolve and reprecipitate as natrojarosite, the natrojarosite solid

as a whole becomes closer to being in equilibrium with the reactor fluid. This in turn slows down further dissolution and reprecipitation of the natrojarosite and consequently slows the rate of pH decrease as H_3O^+ liberation is inhibited. In the natrojarosite experiment reactors containing Fe(II), it is possible that the Fe(II) is facilitating the dissolution–reprecipitation of the jarosite, causing the jarosite to continue reacting despite becoming closer to being in equilibrium with the reactor fluid. For the jarosite reactors, because the jarosite is rich in K, the dissolution of H_3O^+ –rich portions of the jarosite and reprecipitation of natrojarosite does not result in the mineral becoming close to being in equilibrium with the reactor fluid. Thus, regardless of the presence or absence of Fe(II), the jarosite continues to dissolve and reprecipitate, with pH decreasing as a result.

5.4.3 Equilibrium iron isotope fractionation factors and application to acid–sulfate environments

Based on extrapolation of the $\delta^{56}\text{Fe}$ values of the $\text{Fe(II)}_{\text{aq}}$ solutions to $F = 1$, the equilibrium Fe isotope fractionation factors for jarosite ($\Delta^{56}\text{Fe}_{\text{Fe(II)aq-Js}}$) and natrojarosite ($\Delta^{56}\text{Fe}_{\text{Fe(II)aq-NaJs}}$) are -2.26‰ and -2.19‰ , respectively, at 22 °C . The final extrapolated $\delta^{56}\text{Fe}$ values of SS–1 and SS–2 differ by 0.01‰ for jarosite (Table 5.1), providing strong evidence that the $\delta^{56}\text{Fe}$ values of $\text{Fe(II)}_{\text{aq}}$ reflects equilibrium with (K)jarosite. The final extrapolated $\delta^{56}\text{Fe}$ values of SS–1 and SS–2 for natrojarosite, on the other hand, differ by 0.19‰ which is still reasonably small. The jarosite and natrojarosite fractionation factors are both similar, suggesting the Fe isotope fractionation between Fe(II) and jarosite and natrojarosite is not strongly influenced by the type of ion occupying the D site in the jarosite structure, despite the substitution of different ions being shown to effect Fe–O bond lengths (Basciano and Peterson, 2008).

The final fractionation factor values of -2.26‰ and -2.19‰ for jarosite and natrojarosite, respectively, are markedly different to the equilibrium Fe isotope fractionation factors of -3.53 and -4.76‰ for jarosite and hydronium jarosite ($\Delta^{56}\text{Fe}_{\text{Fe(II)aq-(H}_3\text{O)Js}}$), respectively, at 22 °C , calculated in Chapter 4 (Whitworth et al., 2020b). It was suggested that the difference in values was the result of substitution of different cations into the jarosite structure, affecting the Fe–O bond lengths and thus the partitioning of iron isotopes into jarosite. As noted previously, the β –factors for the jarosite and $\text{Fe(II)}_{\text{aq}}$ used to do these calculations were taken from Dauphas et al. (2012) and Rustad et al. (2010), respectively. Blanchard et al. (2015) tried to replicate the measurements of Dauphas et al. (2012) without success, and attributed this to issues with the interpretation of the low– and high–energy ends of the NRIXS spectrum by Dauphas et al. (2012). Blanchard et al. (2015) re–analysed uncompressed sample material from Dauphas et al. (2012) using new software (SciPhon) and generated new β –factors for jarosite and hydronium jarosite. Using the β –factors for jarosite and hydronium jarosite from Blanchard et al. (2015), and the β –factor for $\text{Fe(II)}_{\text{aq}}$ from Rustad et al. (2010), the equilibrium Fe isotope fractionation factors for jarosite ($\Delta^{56}\text{Fe}_{\text{Fe(II)aq-Js}}$) and hydronium jarosite ($\Delta^{56}\text{Fe}_{\text{Fe(II)aq-(H}_3\text{O)Js}}$) are -4.11 and -3.79‰ ,

respectively, in $^{56}\text{Fe}/^{54}\text{Fe}$ at 22 °C. These calculated values are still markedly different from the values in this study, suggesting that there is another explanation for the difference in the values. One explanation is that the difference in values reflects a surface iron exchange process, which was likely in this study, versus a bulk mineral iron exchange process. As noted previously, surface atoms may exhibit unique thermodynamic properties and hence, different degrees of isotopic fractionation, due to having more relaxed bond lengths relative to the bulk of the mineral. NRIXS probes the vibrational properties of the bulk mineral, thus measurements using NRIXS data may differ from those where only surface iron exchange is measured. Given there was limited recrystallisation during the experiments, the fractionation factors calculated here may be influenced by the thermodynamic properties of surficial atoms, while Blanchard et al. (2015) β -factors reflect the bulk mineral. Further work may be required to resolve this difference.

The equilibrium Fe isotope fractionation factors between $\text{Fe(II)}_{\text{aq}}$ and jarosite and natrojarosite (-2.26 and -2.19 ‰, respectively) indicates that during jarosite recrystallisation in the presence of $\text{Fe(II)}_{\text{aq}}$, jarosite is expected to become isotopically heavier as lighter isotopes are fractionated into $\text{Fe(II)}_{\text{aq}}$ and mobilised into the environment. Thus, recrystallisation of jarosite in the environment during pyrite oxidation, for example, would result in significant fractionation of Fe isotopes between jarosite and Fe(II) . In natural systems containing jarosite it is also possible that at redox boundaries where the Fe oxidation states fluctuates between Fe(II) and Fe(III) , jarosite may interact with $\text{Fe(III)}_{\text{aq}}$ resulting in Fe isotope exchange. It is possible to investigate these interactions by summing the fractionation measured between $\text{Fe(II)}_{\text{aq}}$ and $\text{Fe(III)}_{\text{aq}}$ and the fractionation between $\text{Fe(II)}_{\text{aq}}$ and jarosite. Using the $\text{Fe(II)}_{\text{aq}} - \text{Fe(III)}_{\text{aq}}$ fractionation value from Welch et al. (2003), $\Delta^{56}\text{Fe}_{\text{Fe(II)aq-Fe(III)aq}} = -3.01$ ‰, the $\Delta^{56}\text{Fe}_{\text{Fe(III)aq-KJs}}$ and $\Delta^{56}\text{Fe}_{\text{Fe(III)aq-NaJs}}$ are 0.75 and 0.82 ‰, respectively. This suggests that lighter Fe isotopes will be fractionated into jarosite during jarosite interactions with $\text{Fe(III)}_{\text{aq}}$. Thus, at redox boundaries, there could be significant fractionation of Fe isotopes between jarosite, $\text{Fe(II)}_{\text{aq}}$ and $\text{Fe(III)}_{\text{aq}}$, and this could help explain the large (>3 ‰) variability in $\delta^{56}\text{Fe}$ observed in the natural jarosite and natrojarosite samples examined in Chapter 4 (Whitworth et al., 2020b).

5.5 CONCLUSIONS

This research demonstrates that the three-isotope method and reversal approach to equilibrium can be used to examine the Fe isotope exchange and fractionation between $\text{Fe(II)}_{\text{aq}}$ and jarosite. In acidic (<4.5 pH), sulfate rich conditions, iron isotope exchange between $\text{Fe(II)}_{\text{aq}}$ and jarosite during recrystallisation appears to be restricted to the surface of jarosite as Fe(II) sorption is limited due to the low pH. While jarosite recrystallisation may be limited in acidic conditions, recrystallisation may result in substantial liberation of acidity and D-site ions into the environment and strategies designed to manage jarosite in these conditions need to be mindful of this. The results presented here suggest that jarosite is expected to become isotopically heavier relative to $\text{Fe(II)}_{\text{aq}}$ during recrystallisation, with the type of ion

occupying the D site not strongly influencing the isotopic properties of jarosite. Discrepancy exists between the fractionation factors presented here and those based on the β -factors derived from NRIXS spectroscopy by Blanchard et al. (2015). These discrepancies may reflect surface iron exchange process in this study versus bulk mineral iron exchange processes which are reflected by the β -factors of Blanchard et al. (2015). Further work may be required to resolve these discrepancies.

Chapter 6

The First Occurrence of Monoclinic

Jarosite in a Natural Environment

Synchrotron powder X-ray diffraction (PXRD) results from Chapter 4 suggested that one of the cobbles at Southside beach contains natrojarosite with monoclinic symmetry. To date, all natural and most synthetic jarosites have been observed to have rhombohedral symmetry. Thus, this is the first observation of monoclinic symmetry in a natural jarosite sample. This chapter presents the results of an investigation of the natural monoclinic natrojarosite sample.

6.1 INTRODUCTION

Jarosite [$\text{KFe}_3(\text{SO}_4)_2(\text{OH})_6$] and related subgroup minerals are of high importance in research and mineral processing. Jarosite has been documented in acid-sulfate environments (e.g., Egal et al., 2008; Welch et al., 2007) where it can act as a contaminant sink, incorporating toxic metal(oids) such as As into its structure (Asta et al., 2009; Johnston et al., 2010), or as a contaminant source through acid and toxic metal(oid) release during decomposition (Karimian et al., 2017; Langmuir, 1997; Smith et al., 2006a). In some mineral processing industries (e.g., zinc), jarosite is deliberately precipitated to remove unwanted iron, a procedure known as the ‘jarosite process’ (Arregui et al., 1980), and maximization of Fe incorporation during jarosite precipitation is strived for. In other mineral processing industries (e.g., bioleaching of chalcopyrite), jarosite precipitation occurs as a passivation layer and is therefore unwanted (Sandström et al., 2005; Stott et al., 2000). Knowledge on jarosite formation mechanisms, stability and thermoelastic properties are therefore essential for its management and utilization in the environment and mineral processing. Jarosite has also been documented at several location on Mars including Meridiani Planum and Mawrth Vallis (Farrand et al., 2009; Klingelhöfer et al., 2004), sparking interest in its potential to shed light on geological processes acting on Mars in the past, and is of theoretical interest as a model compound for spin frustration in Kagomè–Heisenberg antiferromagnetic materials (Grohol et al., 2003; Nishiyama et al., 2003; Wills et al., 2000).

The jarosite subgroup forms a subset of the alunite supergroup, which has the general formula $\text{DG}_3(\text{TO}_4)_2(\text{OH})_6$ (Bayliss et al., 2010). In nature, Na frequently substitutes for K in the D site of jarosite, forming natrojarosite [$\text{NaFe}_3(\text{SO}_4)_2(\text{OH})_6$] (Desborough et al., 2010; Stoffregen et al., 2000). Substitution of different ions into the D, G and T sites effects the structure of jarosite (Stoffregen et al., 2000), and structural changes due to ion substitution and other processes (e.g., heating) have been found to cause changes to the volume, heat capacity, stability and reactivity of jarosite subgroup minerals (e.g., Brand et al., 2017; Grey et al., 2013; Majzlan et al., 2010; Welch et al., 2007), with implications for jarosite behaviour in the environment and mineral processing.

Most natural and synthetic jarosites crystallise in the rhombohedral space group $R\bar{3}m$. The structure consists of a trigonal network of sulfate tetrahedra and Fe-centered octahedra chains, with the octahedra corner sharing to form Kagomè layers perpendicular to the *c* axis (Basciano and Peterson, 2008; Grey

et al., 2013). During synthesis, stoichiometric rhombohedral jarosite formation is favoured at high (≥ 140 °C) temperatures and in Fe-rich fluids (Basciano and Peterson, 2007, 2008; Dutrizac, 1983) whereas non-stoichiometric rhombohedral jarosite formation is favoured in dilute solutions at typically lower (~ 100 °C or less) temperatures (Drouet and Navrotsky, 2003; Kubisz, 1970; Savage et al., 2005). Non-stoichiometric rhombohedral jarosite has been observed to transform to stoichiometric jarosite at 170 °C due to dehydration of regions to form FeOHSO_4 (Grey et al., 2013).

Monoclinic jarosite $C2/m$ has only been reported for synthetic jarosites (Brand et al., 2012; Grey et al., 2011, 2013; Scarlett et al., 2010, 2013). The monoclinic jarosite structure reflects an ordering of iron-site vacancies onto one of the two independent Fe sites, Fe(1), accompanied by a lowering of symmetry. Monoclinic jarosites consist of linear chains of Fe(2)-centred octahedra connected by corner-sharing SO_4 tetrahedra (Grey et al., 2013; Scarlett et al., 2010) and have been described as containing butlerite-like regions by Grey et al. (2011). Monoclinic jarosite synthesis is favoured at lower (80–120 °C) temperatures compared to rhombohedral jarosite, with the relative amount of monoclinic phase increasing with increasing temperature. Both monoclinic jarosite and natrojarosite can be synthesised in non-acidified solutions, although jarosite synthesis is easier in acidified (i.e. ≥ 1 M H_2SO_4) solutions (Grey et al., 2013; Scarlett et al., 2010, 2013). Monoclinic jarosite has been observed to decompose to stoichiometric rhombohedral jarosite at ~ 250 °C, a significantly higher temperature than the equivalent transition in rhombohedral jarosite (Grey et al., 2013). The volume thermal expansion of monoclinic natrojarosite during heating is of the same magnitude as rhombohedral jarosite, but is larger in value (Brand et al., 2017), with implications for weathering and stability of jarosite bearing outcrops.

X-ray diffraction (XRD) data can be used to determine the space group of a sample. There are three main structural features which will be used here to differentiate between monoclinic and rhombohedral symmetry. Firstly, the lowering of symmetry from rhombohedral to monoclinic results in the apparent “splitting” of some XRD peaks, for example, the $(012)_h$ (hexagonal indices) reflection. If the reflections are very close together, they may appear as a main peak with a smaller shoulder and may only be apparent in very high-resolution data. Secondly, refinement of the Fe site occupancies using a monoclinic space group model will result in a preferential ordering of iron site vacancies onto the Fe(I) site (Scarlett et al., 2010). Thirdly, conversion of monoclinic lattice parameters into pseudohexagonal lattice parameters can be used to examine the degree of monoclinic distortion. As the pseudohexagonal β' angle falls between the monoclinic a axis and pseudohexagonal c_{ph} axis values, deviations away from 90° are indicative of monoclinic distortion (Grey et al., 2013). XRD data collected during *in-situ* experiments can also be used to examine structural transformations. Grey et al. (2013) compared the thermal behaviours of monoclinic and rhombohedral jarosite and found subtle differences in the behaviour of these species. The thermal evolution of jarosite species has been studied here using *in-situ* XRD to give further insights into the structural behaviour of these samples.

In addition to XRD data, thermogravimetric analysis (TGA) and electron backscatter diffraction (EBSD) can be used to differentiate between monoclinic and rhombohedral symmetry. Thermal analysis of jarosite by Grey et al. (2011) showed that an endotherm below 280 °C was detected. This was attributed to the formation of FeOHSO_4 due to the dehydration of domains of butlerite-like chains present in the monoclinic jarosite. Rhombohedral symmetry was observed after complete dehydration of the butlerite-like regions. Thus, TGA can be used to elucidate the temperature of transformation from monoclinic to rhombohedral symmetry during heating. Scanning electron microscopy (SEM) and EBSD allows us to spatially access the symmetry within a sample. This is important for investigating the abundance and heterogeneity of the jarosite through the larger sample and determining how the rhombohedral and monoclinic jarosites interact and are related within the cobble.

This work reports the first occurrence of monoclinic natrojarosite in a natural environment. Synchrotron powder XRD (PXRD), TGA and EBSD were used to confirm monoclinic symmetry and examine the decomposition of monoclinic to rhombohedral natrojarosite. Backscatter-electron (BSE) imaging was also employed to examine the morphology of the jarosite crystals. The implications for jarosite formation and behaviour in natural environments are discussed.

6.2 EXPERIMENTAL METHODOLOGY

6.2.1 Room temperature PXRD

Seven subsamples of natrojarosite were collected from a natrojarosite-bearing cobble (64–256 mm) denoted Js-SB-35 located in the intertidal zone at Southside Beach in Victoria, Australia. Four of those subsamples, Js-SB-35A, -35B, -35E and -35F were part of the Chapter 4 study (Whitworth et al., 2020b). The other three subsamples denoted Js-SB-35G, -35H and -35I were obtained after the study. All subsamples were hand ground using an agate mortar and pestle, and jarosite was isolated from matrix materials (e.g., sediment, sand) using tweezers, picks and brushes while viewing the samples under a hand specimen microscope. The seven subsamples were loaded into 0.3 mm diameter borosilicate glass capillaries and mounted onto the Powder Diffraction (PD) beamline (Wallwork et al., 2007) at the Australian Synchrotron. Capillaries were rotated at ~1 Hz during data collection to aid powder averaging. Diffraction patterns were collected over two beamtime allocations with the MYTHEN-II microstrip detector (Schmitt et al., 2003) at a wavelength of 0.77448(1) Å and 0.590726(6) Å. The instrument contribution and wavelength were determined from a NIST LaB_6 660b standard reference material using the fundamental parameters approach within DIFFRAC. TOPAS 5. Two patterns, each of 300 s, were collected for each sample with the detector set 5° apart to cover the gaps between detector modules. The two patterns were then merged into a single dataset using the PDViPeR software available at the beamline. DIFFRAC. EVA was used to identify the minerals present

in the samples using the Crystallography Open Database (Grazulis et al., 2009) and Rietveld refinement as embodied in the TOPAS 5 software was used to model the structure of the minerals present.

6.2.1.1 Rietveld refinement

Rietveld refinement was started using the monoclinic jarosite structure from Scarlett et al. (2010). Natrojarosite peak shapes were modelled using a Thompson–Cox–Hasting pseudo–Voigt function (Thompson et al., 1987). The Na and K occupancy factors were initially allowed to refine unless chemical data was present for the sample, in which case, they were set accordingly. Thermal parameters were constrained for like atoms on similar/identical sites, i.e. Na and K, both Fe sites and O sites. Hydrogen positions and thermal parameters were set to values from (Grey et al., 2011) and not refined due to the insensitivity of X-rays to light elements.

Accessory mineral phase peak shapes were modelled with a Thompson–Cox–Hasting pseudo–Voigt function (Thompson et al., 1987) or a Pearson VII (PVII; Hall et al., 1977) function as most appropriate. The lattice parameters of the accessory phases were refined whereas atom positions, occupancies and thermal parameters were set to literature values. Preferred orientation effects were identified in several samples. These effects were modelled using spherical harmonics (Von Dreele, 1997).

6.2.2 In-situ PXRD heating experiments

Grey et al. (2013) observed transformation of synthetic monoclinic jarosite to rhombohedral jarosite during *in-situ* PXRD heating experiments. To test whether this would occur with the natural monoclinic natrojarosite, a subsequent beamtime was awarded to investigate the behaviour of the natrojarosite during *in-situ* heating experiments. Subsample Js–SB–35A was selected for the experiments as indicative monoclinic peak shouldering of the natrojarosite was visible (see Figure 6.1) and there was powder available to run multiple heating experiments. Subsamples were loaded in 0.7 mm silica glass capillaries, heated using a cyberstar hot air blower and rotated during measurement. A temperature calibration curve was provided for this equipment by the beamline team. The X-ray wavelength and instrument contributions were determined using NIST Lab6 660b. The wavelength was 0.774800(3) Å. The first heating experiment was a coarse heating profile from 30 – 500 °C, with a heating rate of 5 °C/minute, to give an overview of the temperature behaviour of the sample and allow targeting of phase transition points for finer measurements. The second experiment involved heating a subsample at a rate of 1 °C/minute, from 160 – 260 °C. Data was collected in 60 and 30 second contiguous pairs for the coarse and fine heating experiments, respectively. EVA was used to identify the minerals present in the samples and Rietveld refinements were carried out in TOPAS 5 to investigate the phases present.

6.2.2.1 Inductively coupled plasma–optical emission spectrometry (ICP–OES) of Js–SB–35A

To constrain the occupancy factors during refinement of Js–SB–35A, the chemistry of the sample was determined using ICP–OES. Powdered sample (20.0 ± 0.2 mg) was dissolved in 1 mL of 10 M HCl at 25 °C for 24 hours followed by 9 mL of ≥ 18.2 M Ω cm water, diluting the HCl to 1 M. The samples were then filtered (0.22 μ m) to remove insoluble organic material. A small aliquot of the solutions was then diluted to one tenth of the original concentration for ICP–OES analysis. Element (K, Na, Fe, S) concentrations were measured on a Thermo iCAP 7400 Duo ICP–OES in radial mode and elemental concentrations were quantified by conversion of counts per second to ppm using calibration curves prepared by measuring standard solutions containing Fisher Chemical K, Na, Fe and S solutions for I.C.P. at known concentrations. The stoichiometry of the samples was determined based on the ratio of alkali ions and Fe to S in natrojarosite, with the S site assumed to be fully occupied (i.e., the alkali ions and Fe were normalised to two S atoms per chemical formula). The stoichiometry of Js–SB–35A was found to be $(\text{Na}_{1.00}\text{K}_{0.05})\text{Fe}_{3.46}(\text{SO}_4)_2(\text{OH})_6$. Excess Na and Fe were attributed to the presence of halite and amorphous Fe–bearing phases (not detected by PXRD but potentially linked to the aforementioned unidentified small peaks) in the sample, respectively. Thus, normalised to the ideal formula of natrojarosite, the calculated stoichiometry of Js–SB–35A is $(\text{Na}_{0.95}\text{K}_{0.05})\text{Fe}_3(\text{SO}_4)_2(\text{OH})_6$.

6.2.2.2 Rietveld refinement of heating datasets

The room temperature natrojarosite structure for Js–SB–35A was used as the starting point for Rietveld refinement of the heating datasets. As per the room temperature samples, the natrojarosite peak shapes were modelled using a Thompson–Cox–Hasting pseudo–Voigt function (Thompson et al., 1987), the thermal parameters were constrained for like atoms on similar/identical sites, and the hydrogen positions and thermal parameters were set to values from Grey et al. (2011) and not refined.

To ensure jarosite refinements were consistent at each heating time point, the following procedure was used: Firstly, the jarosite lattice parameters (i.e., a , b , c and β) and Fe occupancy factors were refined, next, the B_{eq} values. At this point reflection dependent peak broadening became apparent and it became necessary to use the Stephens anisotropic line-shape broadening model, adapted for monoclinic symmetry (Stephens (1999)). If significant discrepancy still existed between the Rietveld refinement fit and PXRD pattern, then the atomic coordinates for S and O were refined.

Accessory mineral phase structures were modelled for the initial room temperature dataset and then only their lattice parameters were refined at non–ambient temperatures. During Rietveld refinement, several small peaks were noted in a subset of the PXRD patterns. These phases reflect sample impurities at or below detection and so were unable to be identified.

6.2.3 Thermogravimetric Analysis

Thermogravimetric analysis and differential thermal analysis (DTA) were performed using a Netzsch STA 449 F1 Jupiter Simultaneous TGA/DSC thermal analyser. Powdered Js–SB–35A (36 mg) was contained in an alumina crucible and heated to 800 °C, at a heating rate of 10 °C/minute, under ultra-high purity argon purge gas at 40 mL/minute. A blank was run prior to the samples to correct for the background.

6.2.4 Electron backscatter diffraction and backscatter–electron imaging

A portion of Js–SB–35 was mounted in epoxy resin and polished for EBSD and BSE imaging using facilities within the Plymouth Electron Microscopy Centre, University of Plymouth. BSE images were collected using a JEOL 7001F field emission SEM at 15 kV and 10nA. Data was processed in Oxford Instruments AZtec software. EBSD analysis was conducted using a Zeiss Crossbeam 550 FIB–SEM, using 15 kV and 5 nA. The EBSD detector was an Oxford Instruments Symmetry detector, with AZtec software for acquisition. A step size of 0.05 µm was used. The sample was mounted on a pre-titled sample holder held at 70°. The EBSD pattern was indexed using monoclinic natrojarosite lattice parameters from Scarlett et al. (2010) and rhombohedral natrojarosite lattice parameters from Basciano and Peterson (2008; sample P).

6.3 RESULTS

6.3.1 Room temperature PXRD

The room temperature PXRD shows that natrojarosite and quartz (SiO₂) are present in all seven of the Js–SB–35 samples. The absence of asymmetrical peak broadening and sharpness of the (00l) reflection indicates that there is only minor substitution of other elements (i.e. K) into the D site of the natrojarosite (Figure 6.1A; Basciano and Peterson, 2007; Whitworth et al., 2020b). This is consistent with the stoichiometry of Js–SB–35A, as well as the sample chemistry determined by Whitworth et al. (2020b). There are also some minor accessory phases present including gypsum (CaSO₄·2H₂O), halite [NaCl] and goethite [FeO(OH)].

In all the room temperature samples, the high-resolution of the synchrotron PXRD patterns enabled observation of peak shoulders suggestive of monoclinic symmetry. This is illustrated in Figure 6.1A, where a shoulder at ~8.8 2θ is present adjacent to the main natrojarosite peak. In comparison, the equivalent peak at ~6.7 2θ in Figure 6.1B, which is from a rhombohedral jarosite from Whitworth et al. (2020b), does not contain a peak shoulder.

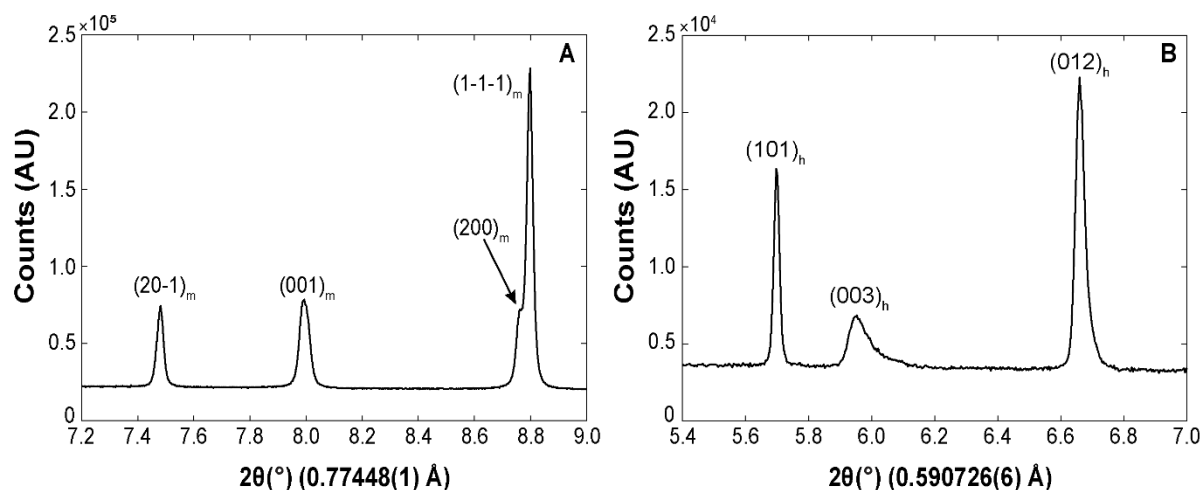


Figure 6.1. Representative PXRD patterns with only selected peaks shown. (A) Js-SB-35A, a natrojarosite sample showing a characteristic peak shoulder (indicated by a black arrow) associated with monoclinic symmetry and a sharp (001) reflection indicative of little substitution of different elements into the D-site. (B) Js-SB-32A, a rhombohedral jarosite sample from Whitworth et al. (2020b), showing an absence of peak shouldering and a wide (003) reflection resulting from substitution of different elements into the D site. Subscript m and h indicate that the indices are monoclinic and hexagonal, respectively.

To test whether monoclinic symmetry best describes the structure of the natrojarosite, and to rule out mixed phases as seen, for example, by Scarlett et al. (2013), the natrojarosite was first fitted with both rhombohedral and monoclinic structures, separately and in the same refinement, as well as with multiple rhombohedral structures to determine which gave the best fit to the observed data. Starting structures for the monoclinic and rhombohedral fits were taken from Scarlett et al. (2010) and Basciano and Peterson (2008), respectively. The best fit to the data was observed to be a monoclinic structure. For example, Js-SB-35A returned a residual weighted profile (R_{wp}) values of 4.44, with an R_{bragg} of 1.55 for the monoclinic phase itself. This is compared to R_{wp} and R_{bragg} of 9.453 and 6.076, respectively, for a single rhombohedral structure. Similarly, when two rhombohedral structures were fitted, an R_{wp} value of 7.451 was returned, with R_{braggs} of 7.336 and 5.173 for each of the two rhombohedral structures. Allowing a mixture of a monoclinic and a rhombohedral structure in the same refinement results in a relative semi-quantitative 20% rhombohedral: 80% monoclinic mixture, with an R_{wp} of 4.750. Thus, it seems that the monoclinic structure is the best fit in this case and so detailed structural analysis proceeded using a single monoclinic structure.

The natrojarosite peaks were fitted with a C-centered monoclinic cell model, space group $C2/m$, during Rietveld refinement and the results are reported in Table 6.1. In the $C2/m$ model there are two independent iron atom sites: Fe1 and Fe2 at 0, 0, $\frac{1}{2}$ and $\frac{3}{4}$, $\frac{1}{4}$, $\frac{1}{2}$, respectively. Rietveld refinement results show that iron vacancies occur preferentially in the Fe(1) site for all samples which is characteristic of monoclinic jarosite (Grey et al., 2011; Scarlett et al., 2010). To further investigate if

the fit was valid, the monoclinic unit cell was converted into a pseudohexagonal lattice using the transformations (Grey et al., 2013): $a_{ph} = \frac{1}{3}(2a/\sqrt{3} + b)$, $c_{ph} = (a^2 + 9c^2 + 6accos\beta)^{\frac{1}{2}}$ and $\beta' = \cos^{-1}[(a^2 + c_{ph}^2 - 9c^2)/2ac_{ph}]$. Table 6.2 reports the pseudohexagonal values calculated for the room temperature PXRD samples. All the samples return β' values that deviate from 90° , suggesting that a monoclinic distortion is present.

The amount of monoclinic distortion appears to vary between samples. For example, Js-SB-35A has clear peak shouldering, iron site occupancies of 0.872(3) and 0.978(2) for Fe(I) and Fe(II), respectively, and a β' value of 89.84° . In comparison, sample Js-SB-35H does not have clear peak shouldering, iron site occupancies of 0.854(8) and 0.970(4) for Fe(I) and Fe(II), respectively, and a β' value of 89.90° . These results suggest that a monoclinic model does not fit the data for Js-SB-35H as well as Js-SB-35A. This can be attributed to monoclinic distortion being less prominent in Js-SB-35H and suggests that structural heterogeneity exists within the natrojarosite of Js-SB-35. An illustration of the differences in peak shouldering between subsamples is presented in SI 1 in Appendix 3.

6.3.2 In-situ heating PXRD

The PXRD data collected during *in-situ* coarse (i.e., $5^\circ\text{C}/\text{minute}$) heating of Js-SB-35A from 30 and 500°C shows that several of the phases in Js-SB-35A undergo thermal decomposition. Between 130 – 140°C , gypsum can be observed to disappear as anhydrite appears (Figure 6.2). Halite and natrojarosite peaks disappear at ~ 360 and $\sim 400^\circ\text{C}$, respectively. Quartz reflections, however, are apparent across the whole temperature range, suggesting quartz decomposition does not occur.

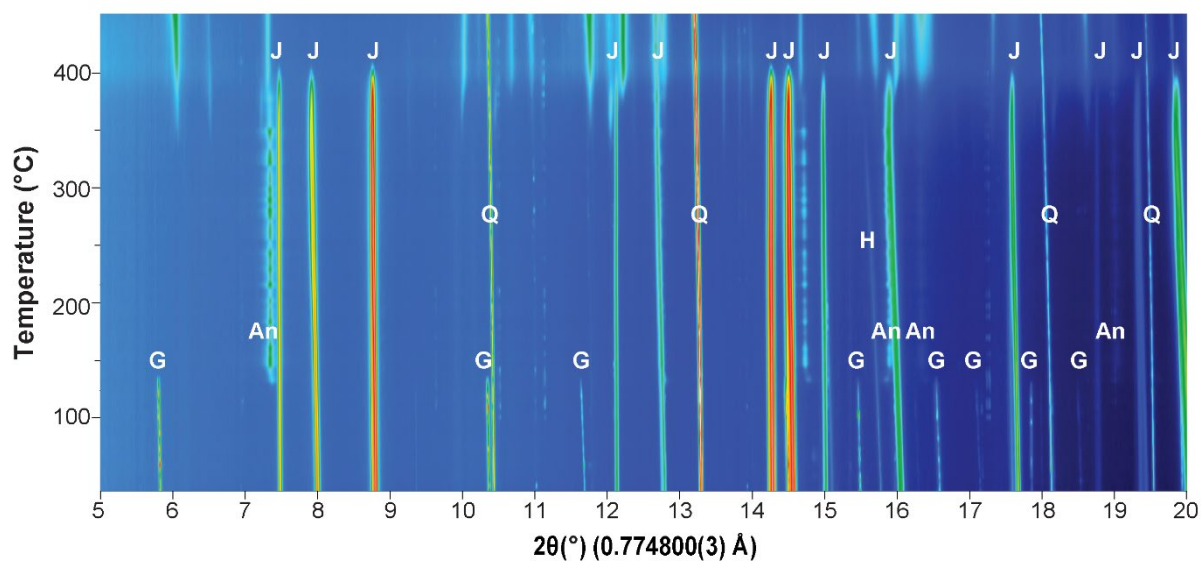


Figure 6.2. Partial PXRD pattern as a function of temperature for *in-situ* decomposition of Js-SB-35A natrojarosite (J) during coarse heating. Accessory phases present include quartz (Q), Gypsum (G), Halite (H) and Anhydrite (An).

Table 6.1. Rietveld refinement results for the room temperature PXRD samples.

Sample	Js-SB-35A	Js-SB-35B	Js-SB-35E	Js-SB-35F	Js-SB-35G	Js-SB-35H	Js-SB-35I
Mineralogy	NaJs, Qtz, Gyp, Hal	NaJs, Goe, Qtz, Gyp, Hal	NaJs, Qtz, Gyp	NaJs, Qtz	NaJs, Qtz, Gyp	NaJs, Qtz, Gyp	NaJs, Qtz, Gyp
R _{wp}	4.44	3.84	4.83	5.15	4.84	4.83	4.50
<i>Natrojarosite</i>							
Crystal system	Monoclinic	Monoclinic	Monoclinic	Monoclinic	Monoclinic	Monoclinic	Monoclinic
<i>a</i> (Å)	12.6906(1)	12.6887(2)	12.6915(2)	12.6916(2)	12.6887(2)	12.6831(2)	12.6874(2)
<i>b</i> (Å)	7.32285(6)	7.32244(7)	7.32426(9)	7.32322(9)	7.3244(1)	7.31608(8)	7.32103(8)
<i>c</i> (Å)	6.96586(5)	6.96593(6)	6.96885(8)	6.97085(8)	6.96969(9)	6.9776(1)	6.96563(7)
β (Å)	127.2287(8)	127.2327(9)	127.187(1)	127.211(1)	127.215(2)	127.197(2)	127.255(1)
Na							
Occ	0.95 ^a	0.92 ^a	0.895(8)	0.885(8)	0.919(8)	0.88(1)	0.983(7)
B (Å ²)	5.6(2)	6.1(1)	6.3(3)	6.0(1)	6.3(3)	5.0(1)	5.0(2)
K							
Occ	0.05 ^a	0.08 ^a	0.105	0.115	0.081	0.12	0.017
B (Å ²)	5.6(2)	6.1(1)	6.3(3)	6.0(1)	6.3(3)	5.01(1)	5.0(2)
Fe(1)							
Occ	0.872(3)	0.895(5)	0.851(4)	0.855(5)	0.855(5)	0.854(8)	0.834(5)
B (Å ²)	0.69(2)	0.70(2)	0.63(4)	0.62(2)	0.63(4)	0.59(3)	0.59(3)
Fe(2)							
Occ	0.978(2)	0.987(3)	0.986(3)	0.983(3)	0.987(3)	0.970(4)	1.000(3)
B (Å ²)	0.69(2)	0.70(2)	0.63(4)	0.62(2)	0.63(4)	0.59(3)	0.59(3)
S							
<i>x</i>	0.3087(3)	0.3098(4)	0.3086(4)	0.3083(4)	0.3086(4)	0.3118(7)	0.3092(4)
<i>z</i>	0.9336(3)	0.9361(4)	0.9343(3)	0.9342(3)	0.9343(3)	0.9359(5)	0.9349(3)
Occ	1	1	1	1	1	1	1
B (Å ²)	0.96(3)	0.81(3)	0.90(8)	0.76(3)	0.90(8)	0.75(5)	0.75(5)

O(1)							
<i>x</i>	3.3921(6)	0.3877(7)	0.3880(7)	0.3876(7)	0.3880(7)	0.388(1)	0.3092(4)
<i>z</i>	0.1967(6)	0.1950(8)	0.1996(7)	0.2024(7)	0.1996(7)	0.200(1)	0.1995(7)
Occ	1	1	1	1	1	1	1
B (Å ²)	1.54(3)	1.01(5)	1.01(5)	1.01(5)	1.01(5)	1.01(5)	1.01(5)
O(2)							
<i>x</i>	0.1699(8)	0.172(1)	0.1706(9)	0.1718(9)	0.1706(9)	0.170(1)	0.1721(9)
<i>z</i>	0.854(1)	0.860(2)	0.865(2)	0.867(2)	0.865(2)	0.869(3)	0.866(1)
Occ	1	1	1	1	1	1	1
B (Å ²)	1.54(3)	1.01(5)	1.01(5)	1.01(5)	1.01(5)	1.01(5)	1.01(5)
O(3)							
<i>x</i>	0.3295(5)	0.3276(6)	0.3247(6)	0.3255(6)	0.3247(6)	0.326(1)	0.3278(6)
<i>y</i>	0.1684(6)	0.16667(7)	0.1679(7)	0.1669(7)	0.1679(7)	0.165(1)	0.1656(7)
<i>z</i>	0.8407(7)	0.8355(9)	0.8304(8)	0.8315(8)	0.8304(8)	0.831(1)	0.8332(8)
Occ	1	1	1	1	1	1	1
B (Å ²)	1.54(3)	1.01(5)	1.01(5)	1.01(5)	1.01(5)	1.01(5)	1.01(5)
OH(1)							
<i>x</i>	0.2536(8)	0.255(1)	0.260(1)	0.264(1)	0.260(1)	0.266(2)	0.256(1)
<i>z</i>	0.392(1)	0.393(2)	0.400(2)	0.406(2)	0.400(2)	0.412(3)	0.394(2)
Occ	1	1	1	1	1	1	1
B (Å ²)	1.54(3)	1.01(5)	1.01(5)	1.01(5)	1.01(5)	1.01(5)	1.01(5)
OH(2)							
<i>x</i>	0.0701(4)	0.0690(6)	0.0694(6)	0.0690(6)	0.0694(6)	0.0627(9)	0.0681(6)
<i>y</i>	0.1868(7)	0.1861(9)	0.1856(9)	0.1848(8)	0.1856(9)	0.184(1)	0.1864(8)
<i>z</i>	0.4050(7)	0.4033(9)	0.404(1)	0.4017(9)	0.404(1)	0.394(2)	0.4044(9)
Occ	1	1	1	1	1	1	1
B (Å ²)	1.54(3)	1.01(5)	1.01(5)	1.01(5)	1.01(5)	1.01(5)	1.01(5)

Notes: Monoclinic H(1) and H(2) fixed at (0.2984, 0, 0.317) and (0.4887, 0.2012, 0.6742), respectively. NaJs = natrojarosite; Qtz = quartz; Gyp = gypsum; Hal = halite; Goe = goethite.

^a Site occupancy based on sample stoichiometry

Table 6.2. Pseudo-hexagonal lattice parameters for the room temperature PXRD samples.

Sample	Js-SB-35A	Js-SB-35B	Js-SB-35E	Js-SB-35F	Js-SB-35G	Js-SB-35H	Js-SB-35I
a_{ph} (Å)	7.326	7.325	7.326	7.326	7.325	7.320	7.324
c_{ph} (Å)	16.639	16.639	16.656	16.655	16.651	16.674	16.633
β' (°)	89.84	89.85	89.81	89.85	89.85	89.90	89.87

Figure 6.3 shows a close-up of how a diffraction peak assigned to natrojarosite at ~ 24.4 2θ varies with temperature. During heating, there is gradual movement of the natrojarosite reflection towards lower 2θ angles, which can be explained by thermal expansion. From 200 °C, the intensity of the reflection begins to change, and this continues until ~ 255 °C where the trajectory of the reflection suddenly changes. This change is also obvious when the volume of the monoclinic natrojarosite unit cell is displayed as a function of temperature (Figure 6.4). During heating, the unit-cell volume of the natrojarosite expands linearly until ~ 255 °C. At ~ 255 °C there is then an inflection in the data. The increase in the unit-cell volume with temperature is similar to that observed for heating experiments using synthetic monoclinic natrojarosite by Brand et al. (2017). However, Brand et al. (2017) did not report unit cell variation close to the transition from monoclinic to rhombohedral jarosite so it is unknown if there was an inflection in their data.

Rietveld refinements of the data shows that that below

160 °C, there is an ordering of iron-site vacancies on the Fe(1) site (Figure 6.5), and calculated β' values are $\leq 89.84^\circ$, suggesting that monoclinic distortion is present. Between 160 and 200 °C, a gradual decrease in peak splitting is observed (Figures 6.3 and 6.6), and the occupancy of the Fe(1) site gradually increases in value towards the value of Fe(2) site. Above 200 °C peak splitting is absent and the Fe(I) and Fe(II) sites have similar occupancies. However, the calculated β' value at 200 °C is

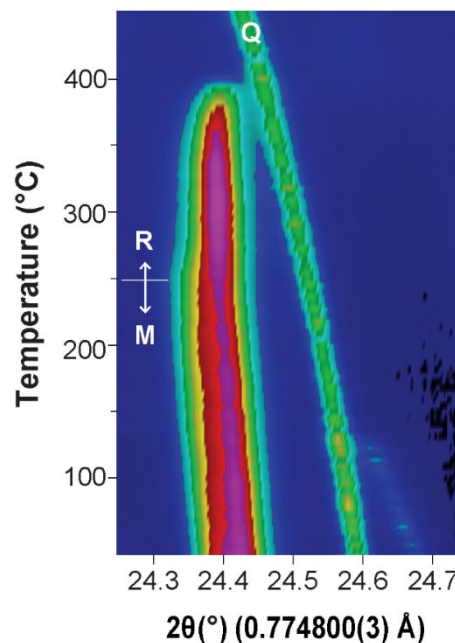


Figure 6.3. Partial PXRD pattern as a function of temperature for in situ decomposition of Js-SB-35A natrojarosite during coarse heating. The transformation from monoclinic (M) to rhombohedral (R) natrojarosite is indicated. The peak associated with quartz (Q) is noted.

~89.86 °C, suggesting that some monoclinic distortion is still present in the sample. At 255 °C the calculated β' values are ~89.9° and, together with the absence of peak splitting and iron–site ordering, this suggests that the natrojarosite can be best described using a rhombohedral crystal symmetry. This supports that at ~255 °C, the natrojarosite has transformed from monoclinic to rhombohedral symmetry.

6.3.3 Thermogravimetric Analysis

Thermogravimetric analysis of jarosite by Grey et al. (2011) showed that TGA can be used to elucidate the temperature of transformation of jarosite from monoclinic to rhombohedral symmetry during heating. TGA was employed here in the hopes of observing a similar transformation of the natrojarosite from monoclinic to rhombohedral symmetry during heating. TGA and DTA data for the natrojarosite show three main endotherms at 140, 390 and 668 °C (Figure 6.7). The first endotherm at 140 °C corresponds to water loss due to dehydration of gypsum, as indicated in the PXRD data by the transformation of gypsum to anhydrite between 130–140 °C. The endotherm at 390 °C corresponds to H₂O–loss due to dehydroxylation of the iron–centred octahedra, and this results in decomposition of jarosite at ~400 °C as seen by the absence of natrojarosite peaks in PXRD. The endotherm at 668 °C corresponds to SO₃ evolution during decomposition of sulfate (Grey et al., 2013).

Dehydroxylation of synthetic monoclinic jarosites together with water loss due to H₂O/H₃O⁺ substitution has been observed between 390 and 450 °C by several authors including Drouet and Navrotsky (2003), Grey et al. (2011, 2013) and Kubisz (1971) between 390 and 450 °C; thus, the temperature of dehydroxylation here is comparable with previous studies. The transition of the natrojarosite from monoclinic to rhombohedral symmetry was not

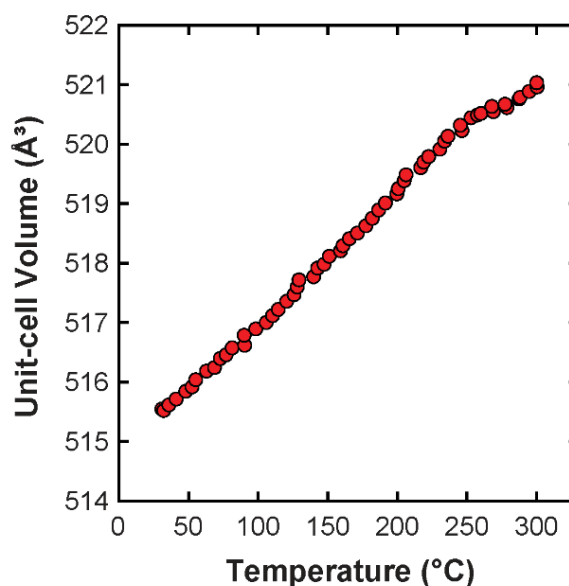


Figure 6.4. Graph of unit-cell volume determined from PXRD data as a function of temperature.

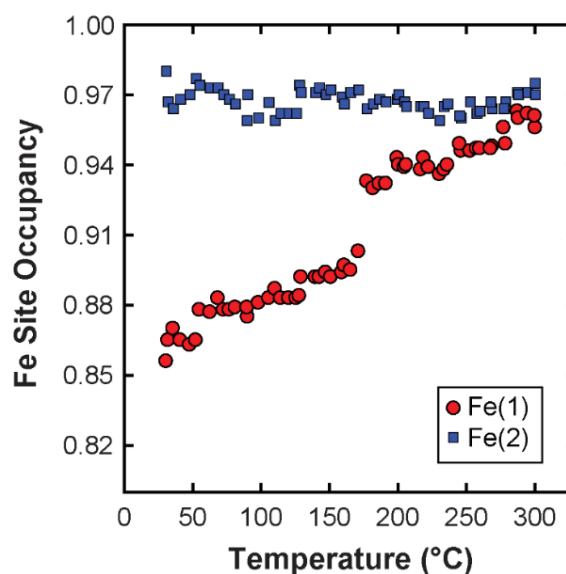


Figure 6.5. Plot of Fe site occupancy, from fitting of the coarse heating PXRD data, against temperature.

observed in the TGA data. This may be due to the heating rate employed during TGA analysis or the microstructure of the natrojarosite. The latter is discussed in more detail below (section 6.4.2).

6.3.4 Electron backscatter diffraction and backscatter–electron imaging

Powder X-ray diffraction is a bulk technique: the structure obtained from refinements of the PXRD data is an average of the natrojarosite structures present in the subsample. Room temperature PXRD has shown that variations in the structure of the natrojarosite exist between the subsamples. This is likely due to structural heterogeneity in the natrojarosite cobble. To investigate the variation in the structure of the natrojarosite spatially, a thin section was prepared for microscopic studies. Figure 6.8 shows a large field view of the thin section using BSE imaging. The very light grey areas are mostly cemented sediment, with the slightly darker grey areas that often appear speckled containing jarosite or intermingled jarosite and quartz. Figure 6.9 shows several zoomed in images from across the thin section. Figure 6.9A shows that the natrojarosite crystals present in the cobble are very small ($<2\ \mu\text{m}$ in diameter) and have octahedral faces and a cubic habit. This morphology has been observed in low temperature jarosites in acidic, sulfate-rich environments by several authors (e.g., Carson et al., 1982; Doner and Lynn, 1989; Wagner et al., 1982) and may suggest that the natrojarosite has formed pseudomorphically after cubic pyrite.

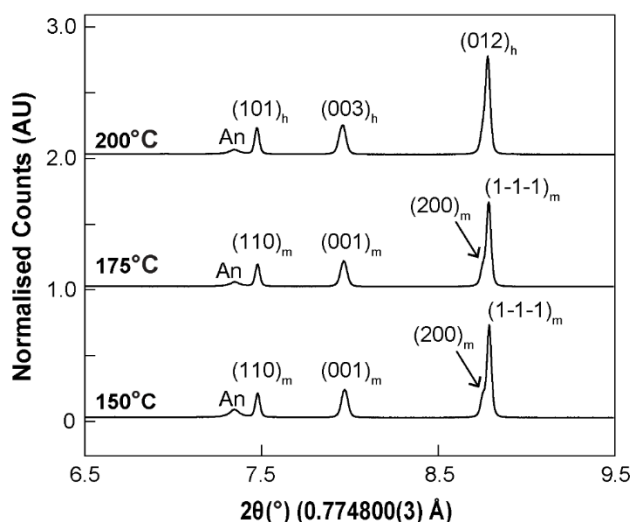


Figure 6.6. Partial XRD pattern of Js-SB-35A showing gradual loss of peak shouldering due to transformation of monoclinic jarosite to rhombohedral jarosite between 150 and 250 °C during coarse heating. (A) Peak shouldering of $(012)_h$ into $(200)_m$ and $(1-1-1)_m$ at 150 °C. (B) Peak shouldering becoming less evident at 175 °C. Loss of peak shouldering at 200 °C. Subscript m and h indicate that the indices are monoclinic and hexagonal, respectively. Black arrows point to the peak shouldering. Peak associated with anhydrite (An) noted.

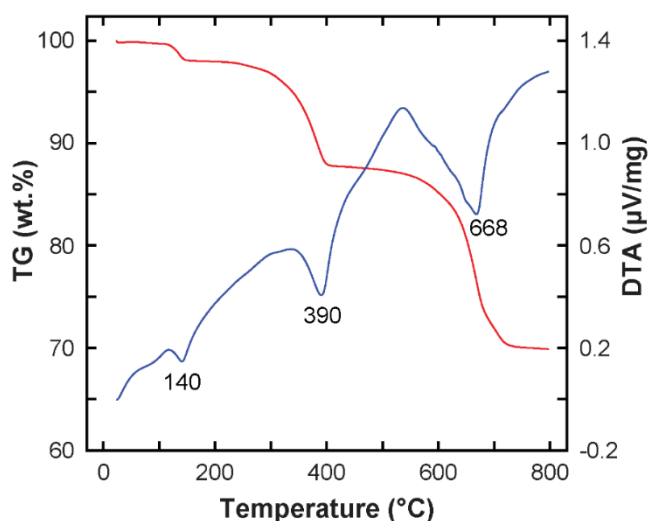


Figure 6.7. The thermogravimetric analysis (red) and differential thermal analysis (blue) curves for Js-SC-35A. The temperatures of the endothermic peak maxima are given.

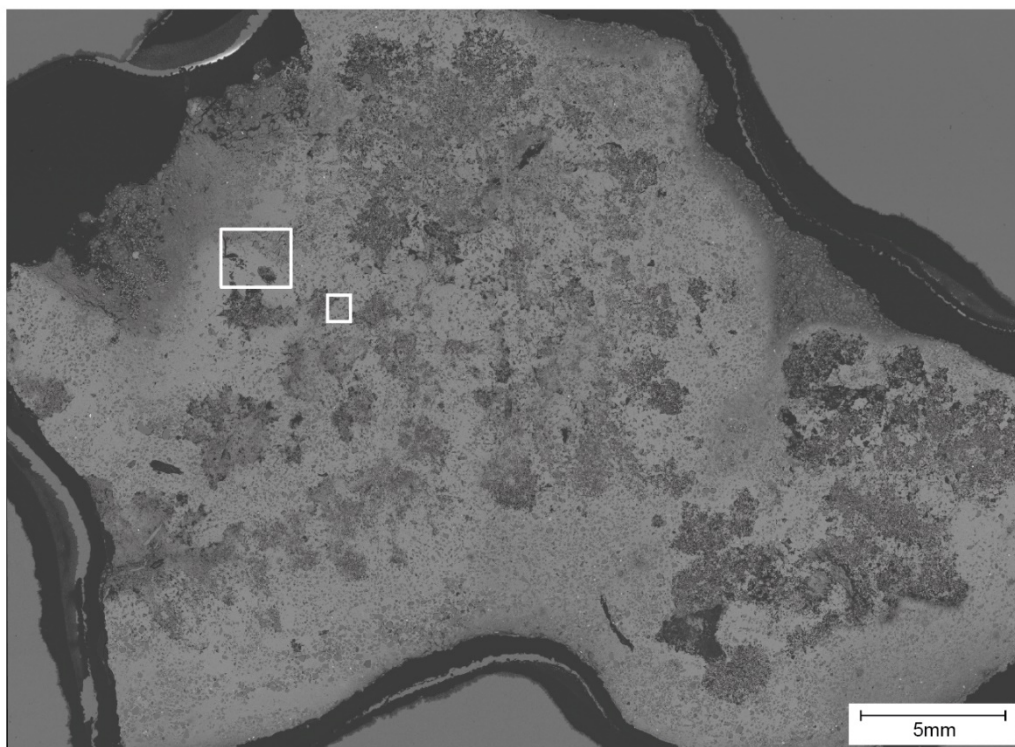


Figure 6.8. Large field view of the thin section from Js-SB-35 using BSE imaging. The white box encloses the areas that EBSD was conducted.

Figures 6.9B–D show accessory minerals that are present in Js-SB-35. In Figure 6.9B, tabular, striated gypsum crystals can be seen intermixed with the natrojarosite. Figures 6.9C and 6.9D show a zircon and phosphate mineral, possibly monazite, respectively, surrounded by jarosite crystals. These minerals were not picked up in PXRD likely for two reasons. Firstly, they occur in low abundance in the thin section. Secondly, they were not seen throughout the thin section. As a result, they may not have been present in the subsamples collected from the cobble. This demonstrates the heterogeneity present in the sample, and highlights the benefits investigating the sample spatially using microscopy.

EBSD was conducted in the two regions enclosed by white boxes in Figure 6.8, and Figure 6.10 shows one of the images collected from within the smaller region. The grains in these regions were indexed using both a monoclinic and rhombohedral natrojarosite structure (see section 6.2.4 for details). The grains that did not index represent accessory minerals and can be identified as dark regions in Figure 6.10. The natrojarosite can be indexed one of three ways: (1) as monoclinic natrojarosite (predominantly purple), (2) as rhombohedral natrojarosite (predominantly blue), and (3) as either monoclinic or rhombohedral natrojarosite (mottled purple and blue). The natrojarosite grains appeared bright in colour, indicating that they index very well against the respective natrojarosite structure. Thus, EBSD shows unambiguously that monoclinic natrojarosite grains are present in Js-SB-35 and highlights that both monoclinic and rhombohedral natrojarosite occur in the cobble.

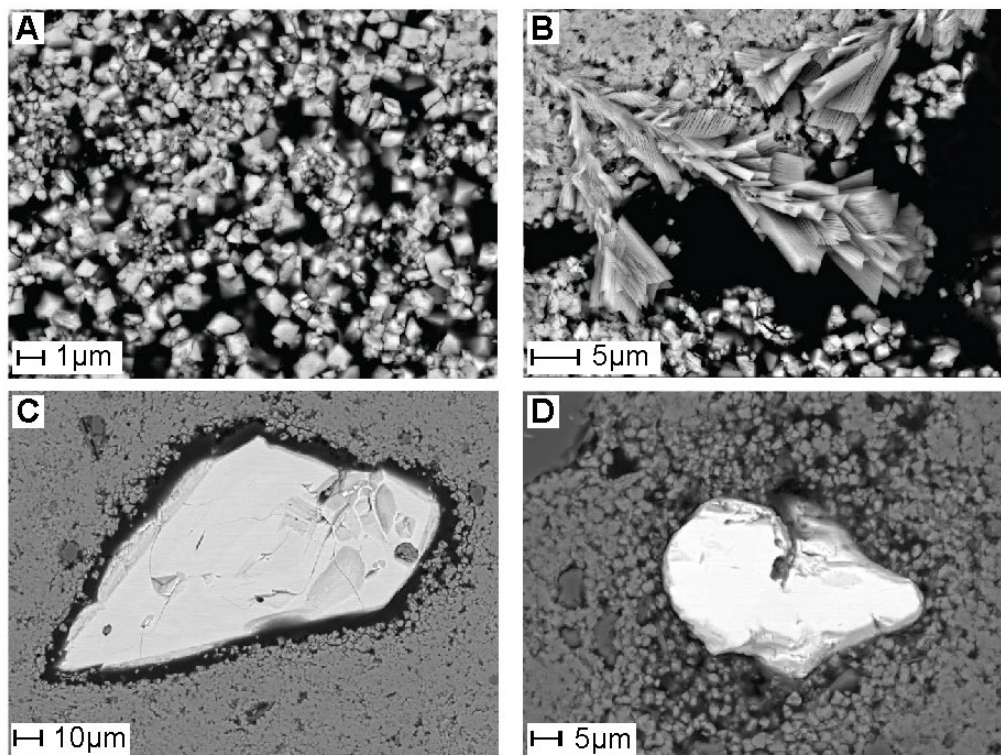


Figure 6.9. BSE images from across the thin section of Js-SB-35. (A) Pseudocubic natrojarosite crystals. (B) Tabular, striated gypsum intermixed with pseudocubic natrojarosite. (C) A rounded, bright white zircon crystal surrounded by natrojarosite (light grey) and quartz (darker grey and rounded) crystals. (D) A phosphate mineral surrounded by natrojarosite and quartz crystals.

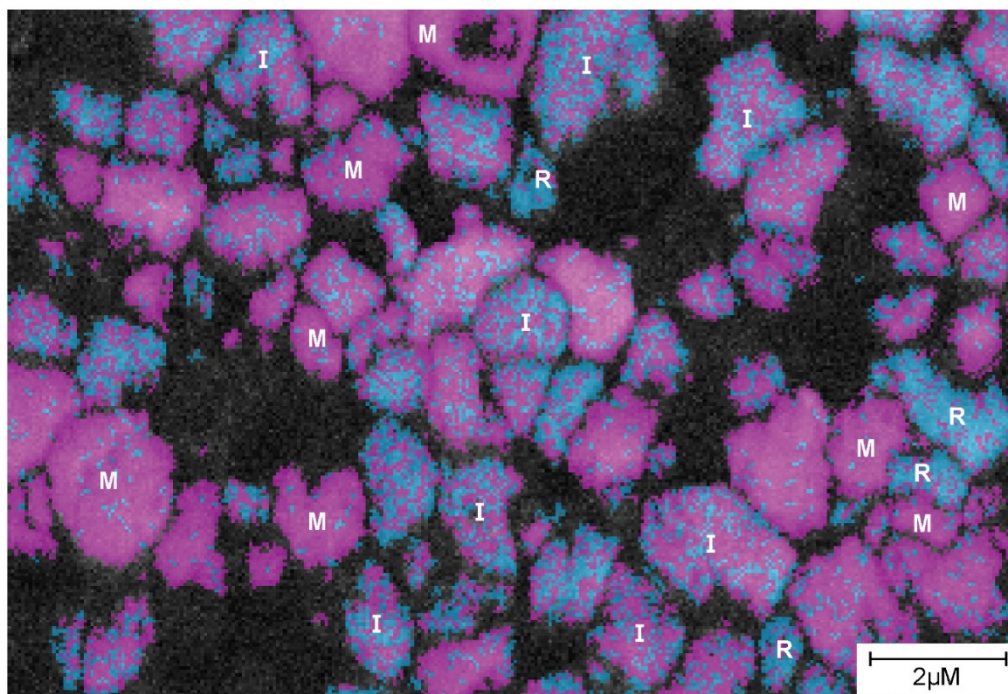


Figure 6.10. EBSD image of the thin section of Js-SB-35A highlighting regions that index as monoclinic natrojarosite (M; purple), rhombohedral natrojarosite (R; blue), or can be indexed using either a monoclinic or rhombohedral model (I; mottled blue and purple). Black regions correspond to accessory phases.

Quantitative analysis of the phases present Figure 6.10 shows that 40.1% of the phases index as monoclinic natrojarosite, 16.3% index as rhombohedral jarosite, and 43.6% do not index as monoclinic or rhombohedral natrojarosite. Quantitative analysis of this regions therefore suggests the monoclinic natrojarosite is more prevalent than rhombohedral natrojarosite, similar to what was seen in the semi-quantitative phase analysis of Js-SB-35A (see section 6.3.1 for details). Additional EBSD images are presented in SI 2 in Appendix 3.

6.4 DISCUSSION

6.4.1 Structural heterogeneity in Js-SB-35

In the room temperature PXRD data, variations in the intensity of peak shoulders, amount of ordering of iron-site vacancies onto the Fe(I) site, and degree of distortion from rhombohedral symmetry exist between the subsamples. This is likely a consequence of the subsamples being comprised of varying amounts of monoclinic and rhombohedral natrojarosite. As shown in the EBSD image (Figure 6.7), unambiguous regions of monoclinic and rhombohedral natrojarosite are present in the cobble, as well as regions that can be described using either model. This suggests that these regions are intermixed monoclinic and rhombohedral natrojarosite.

Subsamples such as Js-SB-35A, which has clear peak shouldering, well-ordered iron-site vacancies and a pseudohexagonal β angle of 89.84° , likely represent regions in the EBSD image describable only by a monoclinic model. Conversely, subsamples such as Js-SB-35H, which does not have clearly visible peak shouldering, well-ordered iron-site vacancies but a pseudohexagonal β angle of 89.9° , likely represent regions in the EBSD image that can be described using both a monoclinic and rhombohedral model reflecting that the subsample contains both monoclinic and rhombohedral natrojarosite. The PXRD data for all subsamples are still best fit with a monoclinic model, suggesting that there is more monoclinic natrojarosite in the samples than rhombohedral natrojarosite. This is supported by quantitative phase analysis of the region analysed using EBSD. Structural and chemical heterogeneity clearly exists within the natrojarosite in Js-SB-35. This highlights the importance of collecting and analysing multiple samples when investigating natural jarosites.

6.4.2 Structure and properties of natural monoclinic natrojarosite

In the study of Grey et al. (2011), structural modelling of hydrothermally synthesised natrojarosite and hydronium jarosites showed that these samples were comprised of domains of butlerite-like $[\text{Fe}_2(\text{SO}_4)_2(\text{OH})_2(\text{H}_2\text{O})_4]$ chains within the stoichiometric jarosite. Thermal analysis of these jarosites detected an endotherm below 280°C that was attributed to the formation of FeOHSO_4 due to the dehydration of domains of butlerite-like chains present. Similar endotherms have also been detected during thermal analysis of synthetic jarosites by Drouet and Navrotsky (2003), Grey et al. (2013) and

Kubisz (1971). This endotherm is not present in this study, nor is FeOHSO_4 seen in the PXRD data, suggesting that domains of butlerite-like chains may not be present in these samples and so natural monoclinic natrojarosite shows a range of structural variations. This finding also suggests that the crystallization of monoclinic jarosites in low temperature natural environments may occur differently to the synthetic monoclinic jarosites studied to date. Thus, caution should be exercised when applying the findings of synthetic monoclinic jarosites studies to a natural environment.

The presence of iron-site vacancies in the natural monoclinic natrojarosite requires a charge compensation mechanism, and two models have been proposed to account for this. The Kubisz (1970; 1971) model has each Fe(III)-site vacancy charged compensated by protonation of 3OH^- to $3\text{H}_2\text{O}$. The Nielsen et al. (2008) model, on the other hand, has each Fe(III)-site vacancy charged compensated by protonation of 4OH^- to $4\text{H}_2\text{O}$, with one proton coming from coupled deprotonation of a D-site H_3O^+ molecule. Regardless of the model, Fe(III)-site vacancy charge compensation in monoclinic jarosites results in the jarosites containing excess water, likely affecting the crystal structure and properties of jarosites. For example, we have seen that the thermal behaviour in monoclinic natrojarosite is closely related to hydrogen bonding within the structure (Brand et al., 2017). Hydrogen bonding is expected to vary between monoclinic and rhombohedral jarosites. Therefore, it can be expected that the thermal behaviours of monoclinic and rhombohedral jarosites will vary. This is seen in Brand et al. (2017) where the volume thermal expansion of monoclinic natrojarosite during heating is of the same magnitude but larger in value compared to rhombohedral jarosite. This difference in expansion could affect the behaviour of a jarosite outcrop. For example, outcrops containing monoclinic jarosite may have greater pressures between the grains when the jarosite expands compared to outcrops containing rhombohedral jarosite. As a result, monoclinic jarosite outcrops may deform differently to rhombohedral outcrops, leading to different weathering regimes.

Similarly, the presence of iron-site vacancies in monoclinic jarosites also likely effects the magnetic properties of the jarosites, a notion that has been suggested before (Scarlett et al., 2010). Rhombohedral jarosites, as previously noted, are comprised of Kagomè layers formed by corner-sharing Fe-centered octahedra, and triangular spin frustration results when unpaired spins, situated at the triangle corners of the Kagomè layers, couple through strong antiferromagnetic exchange (Frunzke et al., 2001; Grohol et al., 2003). Because monoclinic jarosites contain ordered iron-site vacancies, these vacancies likely disrupt the triangular spin frustration, effecting the magnetic behavior of the jarosites. Thus, it is expected that the magnetic properties of natural jarosites will depend on whether the samples have a monoclinic or rhombohedral symmetry.

6.4.3 Formation of natural monoclinic natrojarosite

Numerous studies (e.g., Alpers et al., 1992; Chen et al., 2013; Desborough et al., 2010; Mills et al., 2013; Whitworth et al., 2020b) have examined the crystallography of natural jarosites, reporting only rhombohedral symmetry. In contrast, the results of this study demonstrate that monoclinic natrojarosite can form in a natural environment, which raises questions as to why monoclinic symmetry has not been observed in other natural jarosite samples before.

One explanation is that the formation conditions required to produce monoclinic jarosite rarely occur in nature. Hydrothermal syntheses of monoclinic jarosites require low temperatures (80 °C to 120 °C), solutions with [Fe]/[D site] atomic ratios ≥ 1 , and relatively slow growth conditions to stabilize the monoclinic phase (Grey et al., 2011, 2013; Scarlett et al., 2010). Natural hydrothermal jarosites typically form in temperatures typically ranging from 100–300 °C (Desborough et al., 2010). Thus, hydrothermal jarosites may form at temperatures too high for monoclinic symmetry. Supergene jarosites, on the other hand, form in cooler conditions that may be more suitable for monoclinic symmetry formation, and the presence of monoclinic jarosite in the low-temperature cobble studied here supports this. Natural jarosites also often form at redox boundaries in physically dynamic environments such as intertidal zones, weathering horizons and geothermal systems (Desborough et al., 2010; Lueth et al., 2005; Whitworth et al., 2020b). These environments are likely not conducive to slow jarosite growth, favouring rhombohedral symmetry, as suggested by Grey et al. (2011). However, the jarosite analysed in this study was sampled from a cobble collected from an environment (i.e., intertidal zone) where rapid formation would be favoured. This may suggest that growth rate is not as strong a factor in monoclinic symmetry formation in jarosites as previously suggested.

Another explanation for the absence of monoclinic jarosites in natural settings is that, while monoclinic formation does occur in natural settings, it quickly decomposes to rhombohedral symmetry. Grey et al. (2013) found in their experiments that when monoclinic jarosites were exposed to temperatures ≥ 100 °C for prolonged periods they progressively converted to rhombohedral symmetry. Our experiments also show that heating monoclinic natrojarosite over short (i.e., few hours) timeframes causes gradual transformation from monoclinic to rhombohedral symmetry above 150 °C. Thus, monoclinic natural jarosites exposed to temperatures of 100 °C or greater for prolonged periods of time, or monoclinic jarosites that experience even short periods of heating above 150 °C, are likely to transform to rhombohedral symmetry. It is therefore not surprising that monoclinic symmetry has not been observed in natural hydrothermal jarosites.

Decomposition of monoclinic jarosites to rhombohedral symmetry has not been examined at low temperature, so it is difficult to speculate on whether decomposition from monoclinic to rhombohedral

symmetry would occur rapidly at low temperature. The presence of monoclinic symmetry in the low temperature cobble studied here would suggest that monoclinic symmetry can persist in low temperature jarosites.

Alternatively, it is possible that the transformation of monoclinic to rhombohedral natrojarosite is being slowed in this cobble. The work reported in Chapter 4 (Whitworth et al. (2020b) suggests that the large abundance of jarosite documented at the two beaches could be due to transformation of jarosite to iron oxide being slowed by the presence of silica in many of the samples. Silica has been shown to inhibit Fe(II)–catalysed transformation of synthetic jarosite to ferrihydrite (Jones et al., 2009). Similarly, the presence of silica in this cobble may be inhibiting the transformation from monoclinic symmetry to rhombohedral symmetry by acting as a physical barrier between the monoclinic natrojarosite and the surrounding environment. Thus, the presence of monoclinic natrojarosite documented here may be the result of a combination of conditions (i.e., low temperature, slow jarosite formation, a solution with an [Fe]/[Na] atomic ratios ≥ 1 , and physical barriers slowing the conversion of monoclinic to rhombohedral symmetry).

A third explanation for the lack of reported monoclinic symmetry could be that the resolution of the diffraction instruments used in many of the earlier studies were not sufficient to resolve the subtle peak splitting associated with monoclinic symmetry. In a number of the room temperature samples, peak splitting was almost absent. This is not the first time that the resolution of X–ray diffractometers used in crystal structure analysis has been suggested as a reason for the absence of monoclinic jarosites in the jarosite literature (see Grey et al., 2011), and further highlights the need for suitable data collection strategies when examining the crystal structure of jarosites.

6.5 CONCLUSION

This study has described the first natural occurrence of monoclinic symmetry in jarosite and suggests that natural monoclinic jarosites require specific conditions to form. It is also likely that the presence of monoclinic symmetry will result in natural monoclinic jarosites having different physical properties compared to natural rhombohedral jarosites. Further research on the formation conditions and physical (e.g., thermal, magnetic) differences between natural monoclinic and rhombohedral jarosites is therefore recommended. Understanding the complexities of natural jarosites could not only shed light on the formation conditions and environmental histories of jarosite outcrops on Earth and Mars but would be valuable knowledge for the management and utilisation of jarosites in the environment and mineral processing.

A caveat to this is that it is currently unclear how common monoclinic jarosites are in nature. High-resolution PXRD data is required to resolve the subtle peak splitting associated with monoclinic symmetry, which is not always available. This may make resolving this question using PXRD data alone challenging. However, this study has also demonstrated the EBSD is an effective technique for distinguishing between monoclinic and rhombohedral jarosite grains in intermingled samples. This may occur frequently in natural jarosites, making EBSD a good tool for investigating the prevalence of monoclinic jarosites in nature. The data set provided here will be a valuable tool in the interpretation of future studies on the crystal structure of natural jarosites.

Chapter 7

Summary, Implications of Results and Future Work

7.1 SUMMARY AND DISCUSSION OF MAIN FINDINGS

7.1.1 Jarosite formation and recrystallisation in acidic, sulfate-rich environments

The iron isotope data presented in this thesis suggests that jarosite formation and recrystallisation in acidic, sulfate-rich environments are complex processes. The results from Chapter 4 (Whitworth et al., 2020b) on the study of natural jarosites in sulphide-rich sediments from Southside Beach and Fossil Beach shows that the natural jarosites have a wide range of $\delta^{56}\text{Fe}$ values (-1.91 and $+1.24$ ‰), which partially overlap with the $\delta^{56}\text{Fe}$ values of the precursor sulfidic sediment (-0.54 to $+1.30$ ‰; Figure 4.6). A correlation also exists between iron isotope composition and alkali (i.e. D site) content, with K-rich jarosite having a heavier iron isotope composition compared to Na-rich jarosite (Figure 4.8). Several processes can explain the wide range of $\delta^{56}\text{Fe}$ values and correlation between iron isotope composition and alkali content: (1) that natural jarosites inherit some of the isotopic composition of the precursor sulphides, which have a relatively wide range of values, 2) thermodynamic differences between Na- versus K-bearing jarosite result in K-rich jarosites having a heavier iron isotope composition than Na-rich jarosites, and (3) open-system Rayleigh distillation results in K-rich jarosites, which precipitate out first from an iron-rich pool, having a heavier iron isotope composition compared to Na-rich jarosites, which precipitate out later once the pool is isotopically lighter and more enriched in Na.

The experiments in Chapter 5 examining the iron isotope exchange and fractionation between (natro)jarosite and $\text{Fe(II)}_{\text{aq}}$ in acidic, sulfate-rich conditions, show that not only does (natro)jarosite become isotopically heavier during recrystallisation in $\text{Fe(II)}_{\text{aq}}$, that the type of ion occupy the D site does not strongly influence the isotopic properties of jarosite. Thus, it is possible that thermodynamic differences between Na- versus K-bearing jarosite have less of an impact on the isotopic composition of natural jarosites than was previously thought in Chapter 4. Calculation of the iron isotope fractionation between jarosite and Fe(III) as part of the experimental study also showed that (natro)jarosite is expected to become isotopically lighter during interactions with Fe(III) , the opposite of what is seen for Fe(II) . Therefore, jarosite recrystallisation in and interaction with different iron species (e.g. Fe(II) , Fe(III)) over time could also explain some of the variation observed in the natural jarosite $\delta^{56}\text{Fe}$ values. The numerous processes that can explain the wide range in jarosite $\delta^{56}\text{Fe}$ values reflect mineral-fluid interactions and changes in redox state occurring during jarosite formation and recrystallisation in acid-sulfate conditions. It is likely that other minerals commonly found in acid-sulfate environments (e.g. schwertmannite) undergo similar mineral-fluid interactions and changes in redox state. As a result, various minerals may be interacting with the same fluids over time. The isotopic composition of minerals precipitating out from or recrystallising in these fluids would therefore be influenced by the various minerals interacting with the fluid over time. Therefore, the wide range in $\delta^{56}\text{Fe}$ values for the natural jarosite studied here may represent the various mineral-fluid interactions

and mineral redox changes occurring in acid–sulfate environments over time, and highlights the complex interplay of processes effecting not only jarosite, but other minerals present in acid–sulfate environments.

The experiments examining iron isotope exchange and fractionation between (natro)jarosite and $\text{Fe(II)}_{\text{aq}}$ in Chapter 5 (Whitworth et al., 2020a) show that iron isotope exchange between $\text{Fe(II)}_{\text{aq}}$ and jarosite during recrystallisation appears to be restricted to the surface of jarosite as Fe(II) sorption is limited due to the low pH. While recrystallisation was restricted to the surface of the jarosite, substantial liberation of acidity and minor liberation of K occurred during the experiment. This liberation was, in part, likely due to exchange of H_3O^+ and K^+ in the jarosite for Na^+ in the reactor fluid during dissolution and reprecipitation of jarosite. These results are important for two reasons. Firstly, these results demonstrate that surficial jarosite recrystallisation in acid–sulfate environment is likely an ongoing process over time. Secondly, jarosite recrystallisation has the potential to capture and/or release substantial quantities of acid (e.g. H_3O^+) and different D–site ions. These findings have implications for the management of jarosite in acid–sulfate environments, and these implications are discussed below (Section 7.2).

The synchrotron powder X–ray diffraction (PXRD) data presented in this thesis demonstrates that extensive solid solutions between jarosite and natrojarosite can occur in natural samples. This is significant as extensive solid solution in the jarosites analysed here have only been observed in synthetic jarosite samples (e.g. Basciano and Peterson, 2007, 2008; Drouet and Navrotsky, 2003). Prior studies on natural jarosites have observed (near–)end–member mixing and limited solid solutions only (Desborough et al., 2010; Papike et al., 2007). The presence of a complete solid solution in the natural jarosite samples analysed here may be in part due to two of the processes that may explain the wide range of $\delta^{56}\text{Fe}$ values of the jarosites analysed: (1) open–system Rayleigh distillation during jarosite formation, and (2) the mechanics of jarosite recrystallisation in acid–sulfate environments. As noted above, in open–system Rayleigh distillation, jarosite precipitated from a pool containing K and Na is expected to be initially enriched in K. As precipitation continues, the jarosite is expected to become progressively richer in Na as K is removed from the pool. Jarosite samples precipitated from this pool would therefore form a solid solution, with the exact composition of the jarosite depending on how much K was present in the pool at the time of precipitation. During recrystallisation, substitution of a D–site ion different to the predominant ion occupying the D–site in the jarosite changes the chemistry of the jarosite, if only slightly. Jarosite recrystallisation over a longer time frame could therefore result in substantial uptake of different D–site ions, resulting in jarosite samples consisting of a solid solution due to differences in the amount of D–site uptake over time. The solid solution present in the jarosite samples analysed here is therefore likely a consequence of jarosite formation and on–going recrystallisation in acidic, sulfate rich conditions.

Synchrotron PXRD of the natural jarosite samples during this work also showed that one natrojarosite-bearing cobble contained natrojarosite with monoclinic symmetry. Prior studies have observed monoclinic symmetry in synthetic jarosites only. Thus, the discovery of monoclinic symmetry in a natural sample substantially changes our understanding of the crystal structure of natural jarosites. Synthetic monoclinic jarosites require slow growth conditions with low temperatures (80 to 120 °C) to form (Grey et al., 2011; Grey et al., 2013; Scarlett et al., 2010). Therefore, the presence of monoclinic natrojarosite at one of the coastal sites likely reflects slow jarosite precipitation at low temperature. The presence of silica in the natrojarosite cobble may also be acting as a physical barrier between the natrojarosite and the surrounding environment, inhibiting the transformation from monoclinic to rhombohedral symmetry. Thus, the presence of natural monoclinic natrojarosite likely reflects a unique interplay of conditions during the formation of the natrojarosite, and these formation conditions may be unique to low temperature, acidic and sulfate-rich coastal environments.

Examination of the thin section of monoclinic natrojarosite in Chapter 6 using BSE imaging shows that while the natrojarosite crystals has octahedral faces, the habits appear to be cubic. This pseudocubic habit may suggest that this jarosite is pseudomorphic after pyrite. This would support the notion in Chapter 4 that sulfides in the sediment are the source of the iron in jarosite. Electron backscatter diffraction of the thin section also shows that the natrojarosite cobble contains intermingled monoclinic and rhombohedral jarosite. This highlights the structural heterogeneity that can exist within samples of jarosites and highlights that the two jarosite symmetries can co-exist in a jarosite sample.

7.1.2 Comparison of jarosite and sediment $\delta^{56}\text{Fe}$ values with existing data

When the jarosite and sulfidic sediments $\delta^{56}\text{Fe}$ values are compared with iron isotope variations of other rocks and minerals (Figure 7.1), it can be seen that the jarosite and sulfidic sediment $\delta^{56}\text{Fe}$ values fall within the large ranges of $\delta^{56}\text{Fe}$ values recorded for (ancient and recent) pyrites, Precambrian oxides, and Precambrian carbonates. It is also evident that the range in jarosite and sulfidic sediment $\delta^{56}\text{Fe}$ values in this work are smaller than the very large ranges recorded for pyrites, Precambrian oxides, and Precambrian carbonates. As previously noted, jarosite likely inherits some of its isotopic composition from the precursor sulfides. Thus, the smaller range in $\delta^{56}\text{Fe}$ values for the jarosite compared to pyrites, Precambrian oxides, and Precambrian carbonates could be due to the smaller range in $\delta^{56}\text{Fe}$ values of the precursor sulfidic sediment analysed during this study. It is expected that supergene jarosites from other locations may have $\delta^{56}\text{Fe}$ values outside the range of $\delta^{56}\text{Fe}$ values recorded for the natural jarosites studied here given that pyrite has a very large $\delta^{56}\text{Fe}$ range, -4 to $\sim +4$ ‰ (Johnson et al., 2020; Mansor and Fantle, 2019).

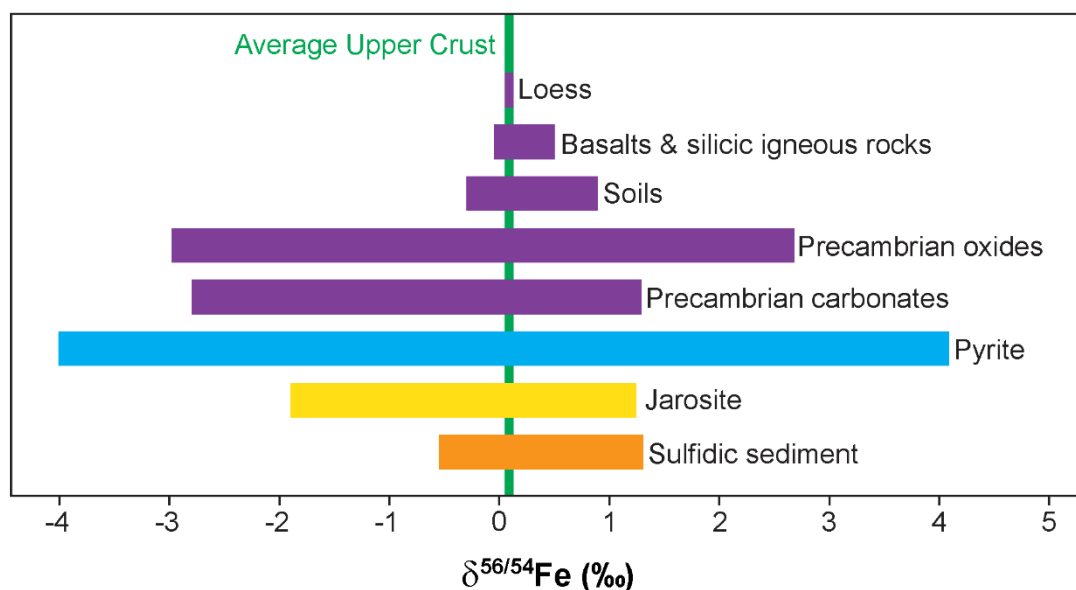


Figure 7.1. Plot of $\delta^{56}\text{Fe}$ values of jarosite and sediment samples from this work and various rocks and minerals. Average upper crust (green) and loess, basalts and silicic igneous rocks, soils, Precambrian oxides and Precambrian carbonates ranges (purple) from Johnson et al. (2020). Pyrite range (blue) based on Mansor and Fantle (2019) and Johnson et al. (2020). Jarosite range (yellow) based on this work (Whitworth et al., 2020b), Egal et al. (2008) and Dauphas and Morris (2008). Sulfidic sediment range (orange) based on this work (Whitworth et al., 2020b). Illustration modified after Johnson et al. (2020).

7.2 IMPLICATIONS OF FINDINGS FOR JAROSITE MANAGEMENT IN LOW TEMPERATURE, ACIDIC AND SULFATE-RICH ENVIRONMENTS

The research presented in this thesis highlights the geochemical and structural complexity of jarosites present in low temperature, acid-sulfate environments, that arise from mineral-fluid interactions and redox changes during jarosite formation and recrystallisation over time. Consequently, specific strategies need to be developed to manage jarosites in these environments successfully. These strategies should begin with a thorough characterisation of the jarosites requiring management. The PXRD results presented here show that the crystal chemistry and structure of jarosites in acidic, sulfate-rich environments can be variable. Substitution of different elements into the crystal structure of jarosite affects its reactivity, and substitution of metal(oids) can represent a store of toxic elements that can be mobilised into the environment (Chapter 5; Welch et al., 2007). Differences in the crystal structure of jarosites may also affect its behaviour in acid-sulfate environments (Chapter 6). It is therefore important to characterise jarosite geochemically and structurally before commencing management activities. In addition to this, the mineralogy of jarosite outcrops should also be investigated as accessory minerals present within jarosite outcrops may affect the behaviour of the jarosite. For example, the presence of silica in the cobbles and boulders analysed in this study may be slowing the transformation of jarosite into iron oxides (Chapter 4). This may be advantageous for management strategies aiming to prevent

jarosite decomposition, whereas for management strategies promoting jarosite decomposition to iron oxides, this presents an unwanted complication.

Another factor that needs to be considered during jarosite management in acidic, sulfate-rich conditions is jarosite's ability to recrystallise over time. The results from Chapter 5 show that despite limited Fe(II) sorption occurring, jarosite can substantially recrystallise in low temperature, acidic and sulfate-rich conditions. Further, D-site ions in the jarosite can be liberated during jarosite dissolution and ions present in the surrounding fluids can be incorporated into the jarosite structure during reprecipitation. Thus, toxic elements and H_3O^+ in the D-site of jarosite have the potential to be liberated during jarosite recrystallisation, with potentially devastating consequences. Keeping the jarosite in a closer equilibrium with surrounding fluids or creating a physical barrier between jarosite and surrounding fluids may be able to slow the rate of jarosite recrystallisation over time. However, this may not be practically achievable in natural environments. Nevertheless, it is important to recognise jarosite's ability to recrystallise over time when developing management strategies for jarosite's in acidic, sulfate-rich environments.

7.3 FUTURE RESEARCH

This research has provided valuable information on the chemical and structural complexities of jarosites in low temperature, acidic and sulfate-rich environments. It has also shed light on the various processes responsible for jarosite formation and recrystallisation and provided insight into the mineral-fluid interactions and redox changes that occur in these environments. Thus, iron isotope geochemistry and PXRD are valuable tools for not only developing a greater understanding of jarosite, but for better understanding the interplay of processes occurring in low temperature, acidic and sulfate-rich environments.

One avenue of future research would be to build on the iron isotope data set provided in this thesis, which is the first of its kind for jarosite, by investigating the iron isotope geochemistry of jarosites formed in other environments. Investigation of the iron isotope composition of jarosites in other low temperature, acidic and sulfate-rich environments such as acid mine drainage and acid sulfate soils would be able to provide insights into the processes effecting jarosite formation and recrystallisation in these environments, which is valuable given jarosite management is often required. This information would be valuable for understanding how mineral-fluid processes and redox changes vary in different acidic and sulfate-rich settings. Further, in these environments there may be the opportunity to measure dissolved Fe directly in contact with jarosite. This could further elucidate how jarosite recrystallises in iron-bearing fluids, and how iron isotopes are fractionated in this process.

Differences in the iron isotope geochemistry of supergene, hydrothermal and sedimentary jarosites could also exist, much like they do for sulfur isotopes (see Papike et al., 2006). If this is the case then iron isotope geochemistry could become a diagnostic tool for determining what processes formed a jarosite outcrop not only on Earth, but also on Mars. This would give planetary scientists another valuable tool to understanding the processes that acted on Mars in the past. Investigation of the iron isotope composition of hydrothermal and sedimentary jarosites would elucidate whether these differences exist.

The experiments conducted here examining iron isotope exchange and fractionation between jarosite and $\text{Fe(II)}_{\text{aq}}$ shows that discrepancies exist between experimentally derived fractionation factors and fractionation factors based on β -factors derived from spectroscopic techniques. These discrepancies may reflect surface exchange processes in this study versus bulk mineral iron exchange processes which are reflected by the β -factors. Given jarosite recrystallisation in acidic, sulfate-rich environments appears to be restricted to the surface of the jarosite, the use of β -factors to determine how iron isotopes partition between jarosite and other iron-bearing minerals and dissolved iron species may be inappropriate in these conditions given a bulk mineral iron exchange process does not occur. This could be resolved two ways. Firstly, as noted above, examination of coexisting jarosite and Fe(II) fluids may be able to provide insight on how iron isotopes are partitioned between the two phases.

Alternatively, additional experiments could be conducted that examine iron isotope fractionation between jarosite and dissolved Fe(II) (or Fe(III)) over longer timeframes (e.g. one year) and under different reactor conditions (e.g. in K_2SO_4 , with higher or lower Fe(II) concentrations) to determine whether recrystallisation is always restricted to the surface of the jarosite, and the impact these variable conditions have on the fractionation (and exchange) of iron isotope between jarosite and Fe(II) (or Fe(III)). This would have ramifications for the use of fractionation factors derived from spectroscopic techniques to describe not only iron isotope fractionation between jarosite and dissolved iron species, but any mineral reactions where a bulk mineral iron exchange process is unlikely to occur. Results from experiments conducted using different reactor fluids may also shed more light on conditions that promote or impede jarosite recrystallisation, which would inform the best strategies to manage jarosite recrystallisation in low temperature, acidic and sulfate-rich environments.

The identification of monoclinic symmetry in a natrojarosite-bearing cobble has changed our understanding on how jarosites crystallise in natural environments. However, it is currently unclear whether monoclinic symmetry in natural jarosites is rare, or whether the absence of monoclinic symmetry in past studies is due to the XRD data collected being insufficient in resolution to resolve the often subtle peak splitting associated with monoclinic symmetry. Continued investigation of the crystal structure of natural jarosites using high-resolution XRD data is needed to resolve this.

Further investigation of the formation and behaviour of natural monoclinic jarosites is also important. Synthetic monoclinic jarosites require specific conditions to form (see Grey et al., 2011; Grey et al., 2013; Scarlett et al., 2010) and this is likely true for natural monoclinic jarosites. Understanding the conditions resulting in the formation of natural monoclinic jarosite could have implications for minimising their formation in the environment, as well as understanding past conditions on Mars if monoclinic jarosite is identified. In terms of their behaviour, Brand et al. (2017) reported the thermal expansion of synthetic monoclinic natrojarosite. While the increase in the unit-cell volume with temperature here is similar to that observed by Brand et al. (2017), the evolution of the natrojarosite is subtly different to that reported by Grey et al. (2011). For example, Grey et al. (2011) observed an endotherm below 280 °C that was attributed to the formation of FeOHSO_4 due to the dehydration of domains of butlerite-like chains present in the synthetic jarosite. This endotherm was not present during heating of the natural monoclinic natrojarosite. Modelling of these data together with those earlier studies is required to confirm this, with the results having implications for understanding and predicting the behaviour of jarosites in low and high temperature environments.

References

- Alpers, C.N., Nordstrom, D.K., and Ball, J.W. (1989) Solubility of jarosite solid solutions precipitated from acid mine waters, Iron Mountain, California, U.S.A. Solubilité des solutions solides de jarosite précipitées à partir des eaux minières acides, Iron Mountain, Californie, U. S. A. Sciences Géologiques. Bulletin, 42(4), 281–298.
- Alpers, C.N., Rye, R.O., Nordstrom, D.K., White, L.D., and King, B.S. (1992) Chemical, crystallographic and stable isotopic properties of alunite and jarosite from acid–hypersaline Australian lakes. *Chemical Geology*, 96, 203–226.
- Anbar, A.D., Jarzecki, A.A., and Spiro, T.G. (2005) Theoretical investigation of iron isotope fractionation between $\text{Fe}(\text{H}_2\text{O})_6^{3+}$ and $\text{Fe}(\text{H}_2\text{O})_6^{2+}$: Implications for iron stable isotope geochemistry. *Geochimica et Cosmochimica Acta*, 69(4), 825–837.
- Anbar, A.D., and Rouxel, O. (2007) Metal Stable Isotopes in Paleooceanography. *Annual Review of Earth and Planetary Sciences*, 35(1), 717–746.
- Arregui, V., Gordon, A., and Steintveit, G. (1980) The jarosite process—past, present and future. In J.M. Cigan, T.S. Mackey, and T.J. O'Keefe, Eds. *Lead–Zinc–Tin'80*, p. 97–123. TMS–AIME, Warrendale, PA.
- Asta, M.P., Cama, J., Martínez, M., and Giménez, J. (2009) Arsenic removal by goethite and jarosite in acidic conditions and its environmental implications. *Journal of Hazardous Materials*, 171(1–3), 965–72.
- Balci, N., Bullen, T.D., Witte–Lien, K., Shanks, W.C., Motelica, M., and Mandernack, K.W. (2006) Iron isotope fractionation during microbially stimulated Fe(II) oxidation and Fe(III) precipitation. *Geochimica et Cosmochimica Acta*, 70(3), 622–639.
- Basciano, L.C., and Peterson, R.C. (2007) Jarosite hydronium jarosite solid–solution series with full iron site occupancy: Mineralogy and crystal chemistry. *American Mineralogist*, 92(8–9), 1464–1473.
- . (2008) Crystal chemistry of the natrojarosite–jarosite and natrojarosite–hydronium jarosite solid–solution series: A synthetic study with full Fe site occupancy. *American Mineralogist*, 93(5–6), 853–862.
- Bayliss, P., Kolitsch, U., Nickel, E.H., and Pring, A. (2010) Alunite supergroup: recommended nomenclature. *Mineralogical Magazine*, 74(05), 919–927.
- Beard, B.L., Handler, R.M., Scherer, M.M., Wu, L., Czaja, A.D., Heimann, A., and Johnson, C.M. (2010) Iron isotope fractionation between aqueous ferrous iron and goethite. *Earth and Planetary Science Letters*, 295(1–2), 241–250.
- Beard, B.L., and Johnson, C.M. (2004) Fe Isotope Variations in the Modern and Ancient Earth and Other Planetary Bodies. *Reviews in Mineralogy and Geochemistry*, 55, 319–357.
- Beard, B.L., Johnson, C.M., Cox, L., Sun, H., Nealson, K.H., and Aguilar, C. (1999) Iron Isotope Biosignatures. *Science*, 285(5435), 1889–1892.
- Beavis, S., Beavis, F., Somerville, P., and Welch, S. (2005) Spatial and temporal variability of acidity at a coastal acid sulfate soil site II: a time for change. CRC LEME.
- Bhattacharya, S., Mitra, S., Gupta, S., Jain, N., Chauhan, P., Parthasarathy, G., and Ajai. (2016) Jarosite occurrence in the Deccan Volcanic Province of Kachchh, western India: Spectroscopic studies on a Martian analog locality. *Journal of Geophysical Research: Planets*, 121(3), 402–431.
- Bigeleisen, J., and Mayer, M.G. (1947) Calculation of Equilibrium Constants for Isotopic Exchange Reactions. *The Journal of Chemical Physics*, 15(5), 261–267.
- Bird, M.I., Andrew, A.S., Chivas, A.R., and Lock, D.E. (1989) An isotopic study of surficial alunite in Australia: 1. Hydrogen and sulphur isotopes. *Geochimica et Cosmochimica Acta*, 53, 3223–3237.
- Bish, D.L., and Post, J.E. (1989) *Modern Powder Diffraction*. Mineralogical Society of America, Washington, DC.
- Bish, D.L., William Carey, J., Vaniman, D.T., and Chipera, S.J. (2003) Stability of hydrous minerals on the martian surface. *Icarus*, 164(1), 96–103.
- Blanchard, M., Balan, E., and Schauble, E.A. (2017) Equilibrium Fractionation of Non–traditional Isotopes: a Molecular Modeling Perspective. *Reviews in Mineralogy and Geochemistry*, 82(1), 27–63.

- Blanchard, M., Dauphas, N., Hu, M.Y., Roskosz, M., Alp, E.E., Golden, D.C., Sio, C.K., Tissot, F.L.H., Zhao, J., Gao, L., Morris, R.V., Fornace, M., Floris, A., Lazzeri, M., and Balan, E. (2015) Reduced partition function ratios of iron and oxygen in goethite. *Geochimica et Cosmochimica Acta*, 151, 19–33.
- Blanchard, M., Poitrasson, F., Méheut, M., Lazzeri, M., Mauri, F., and Balan, E. (2009) Iron isotope fractionation between pyrite (FeS₂), hematite (Fe₂O₃) and siderite (FeCO₃): A first-principles density functional theory study. *Geochimica et Cosmochimica Acta*, 73(21), 6565–6578.
- Bragg, W.H., and Bragg, W.L. (1913) The reflection of X-rays by crystals. *Proc. R. Soc. Lond. A.*, 88(605), 428–438.
- Brand, H.E.A., Scarlett, N.V.Y., and Grey, I.E. (2012) In situ studies into the formation kinetics of potassium jarosite. *Journal of Applied Crystallography*, 45(3), 535–545.
- Brand, H.E.A., Scarlett, N.V.Y., and Knight, K.S. (2017) Thermal expansion of deuterated monoclinic natrojarosite; a combined neutron–synchrotron powder diffraction study. *Journal of Applied Crystallography*, 50(2), 340–348.
- Brown, J.B. (1971) Jarosite–Goethite Stabilities at 25°C, 1 ATM. *Mineral. Deposita*, 6, 245–252.
- Burns, R.G. (1987) Ferric Sulfates on Mars. *Journal of Geophysical Research*, 92(B4), E570–E574.
- Busigny, V., and Dauphas, N. (2007) Tracing paleofluid circulations using iron isotopes: A study of hematite and goethite concretions from the Navajo Sandstone (Utah, USA). *Earth and Planetary Science Letters*, 254(3–4), 272–287.
- Busigny, V., Planavsky, N.J., Goldbaum, E., Lechte, M.A., Feng, L., and Lyons, T.W. (2018) Origin of the Neoproterozoic Fulu iron formation, South China: Insights from iron isotopes and rare earth element patterns. *Geochimica et Cosmochimica Acta*, 242, 123–142.
- Carson, C.D., Fanning, D.S., and Dixon, J.B. (1982) Alfisols and Ultisols with Acid Sulfate Weathering Features in Texas. *Acid Sulfate Weathering*, 127–146.
- Chen, L., Li, J.–W., Rye, R.O., Benzel, W.M., Lowers, H.A., and He, M.–Z. (2013) Mineralogical, chemical, and crystallographic properties of supergene jarosite–group minerals from the Xitieshan Pb–Zn sulfide deposit, northern Tibetan Plateau, China. *Mineralogy and Petrology*, 107(4), 487–499.
- Chen, L., and Li, J. (2014) ⁴⁰Ar/³⁹Ar ages and stable isotopes of supergene jarosite from the Baiyin VHMS ore field, NE Tibetan Plateau with paleoclimatic implications. *Chinese Science Bulletin*, 59(24), 2999–3009.
- Courtin–Nomade, A., Rakotoarisoa, O., Bril, H., Grybos, M., Forestier, L., Foucher, F., and Kunz, M. (2012) Weathering of Sb–rich mining and smelting residues: Insight in solid speciation and soil bacteria toxicity. *Geochemistry*, 72, 29–39.
- Craddock, P.R., and Dauphas, N. (2010) Iron Isotopic Compositions of Geological Reference Materials and Chondrites. *Geostandards and Geoanalytical Research*, 35(1), 101–123.
- . (2011) Iron and carbon isotope evidence for microbial iron respiration throughout the Archean. *Earth and Planetary Science Letters*, 303(1–2), 121–132.
- Crosby, H.A., Roden, E.E., Johnson, C.M., and Beard, B.L. (2007) The mechanisms of iron isotope fractionation produced during dissimilatory Fe(III) reduction by *Shewanella putrefaciens* and *Geobacter sulfurreducens*. *Geobiology*, 5(2), 169–189.
- Cullity, B.D. (1978) *Elements of X-ray Diffraction*. Addison–Wesley Publishing Company.
- Cunningham, C.G., Rye, R.O., Rockwell, B.W., Kunk, M.J., and Councell, T.B. (2005) Supergene destruction of a hydrothermal replacement alunite deposit at Big Rock Candy Mountain, Utah: mineralogy, spectroscopic remote sensing, stable–isotope, and argon–age evidences. *Chemical Geology*, 215(1–4), 317–337.
- Czaja, A.D., Johnson, C.M., Beard, B.L., Eigenbrode, J.L., Freeman, K.H., and Yamaguchi, K.E. (2010) Iron and carbon isotope evidence for ecosystem and environmental diversity in the ~2.7 to 2.5 Ga Hamersley Province, Western Australia. *Earth and Planetary Science Letters*, 292(1–2), 170–180.
- Dauphas, N., John, S.G., and Rouxel, O. (2017) Iron Isotope Systematics. *Reviews in Mineralogy and Geochemistry*, 82(1), 415–510.
- Dauphas, N., and Morris, R.V. (2008) Iron isotope in products of acid–sulphate basalt alteration: A prospective study for Mars. 71st Annual Meeting of the Meteoritical Society. July 28–August 1, 2008, 43, p. A35. *Meteoritics and Planetary Science Supplement*, Matsue, Japan.

- Dauphas, N., Roskosz, M., Alp, E.E., Golden, D.C., Sio, C.K., Tissot, F.L.H., Hu, M.Y., Zhao, J., Gao, L., and Morris, R.V. (2012) A general moment NRIXS approach to the determination of equilibrium Fe isotopic fractionation factors: Application to goethite and jarosite. *Geochimica et Cosmochimica Acta*, 94, 254–275.
- Dauphas, N., and Rouxel, O. (2006) Mass spectrometry and natural variations of iron isotopes. *Mass Spectrometry Reviews*, 25, 515–550.
- Dent, D. (1986) Acid sulphate soils : a baseline for research and development / David Dent. International Institute for Land Reclamation and Improvement/ILRI, Wageningen, Netherlands.
- Desborough, G.A., Smith, K.S., Lowers, H.A., Swayze, G.A., Hammarstrom, J.M., Diehl, S.F., Leinz, R.W., and Driscoll, R.L. (2010) Mineralogical and Chemical Characteristics of Some Natural Jarosites. *Geochimica et Cosmochimica Acta*, 74, 1041–1056.
- Dideriksen, K., Baker, J.A., and Stipp, S.L.S. (2006) Iron isotopes in natural carbonate minerals determined by MC–ICP–MS with a ^{58}Fe – ^{54}Fe double spike. *Geochimica et Cosmochimica Acta*, 70(1), 118–132.
- Dittrich, H., and Bieniok, A. (2009) Measurement Methods. Structural Properties: X–Ray and Neutron Diffraction. In J. Garche, Ed. *Encyclopedia of Electrochemical Power Sources*, p. 718–737. Elsevier, Amsterdam.
- Dollase, W. (1986) Correction of intensities for preferred orientation in powder diffractometry: application of the March model. *Journal of Applied Crystallography*, 19(4), 267–272.
- Domagal–Goldman, S.D., and Kubicki, J.D. (2008) Density functional theory predictions of equilibrium isotope fractionation of iron due to redox changes and organic complexation. *Geochimica et Cosmochimica Acta*, 72(21), 5201–5216.
- Doner, H.E., and Lynn, W.C. (1989) Carbonate, Halide, Sulfate, and Sulfide Minerals. *Minerals in Soil Environments*, 279–330.
- Douthitt, C.B. (2008) The evolution and applications of multicollector ICPMS (MC–ICPMS). *Analytical and Bioanalytical Chemistry*, 390(2), 437–40.
- Drouet, C., and Navrotsky, A. (2003) Synthesis, characterization, and thermochemistry of K–Na–H₃O jarosites. *Geochimica et Cosmochimica Acta*, 67(11), 2063–2076.
- Duan, Y., Severmann, S., Anbar, A.D., Lyons, T.W., Gordon, G.W., and Sageman, B.B. (2010) Isotopic evidence for Fe cycling and repartitioning in ancient oxygen–deficient settings: Examples from black shales of the mid–to–late Devonian Appalachian basin. *Earth and Planetary Science Letters*, 290(3–4), 244–253.
- Dutrizac, J.E. (1983) Factors affecting alkali jarosite precipitation. *Metallurgical Transactions B*, 14B, 531–539.
- Dutrizac, J.E., and Jambor, J.L. (2000) Jarosites and Their Application in Hydrometallurgy. *Reviews in Mineralogy and Geochemistry*, 40(1), 405–452.
- Dziony, W., Horn, I., Lattard, D., Koepke, J., Steinhöfel, G., Schuessler, J.A., and Holtz, F. (2014) In–situ Fe isotope ratio determination in Fe–Ti oxides and sulfides from drilled gabbros and basalt from the IODP Hole 1256D in the eastern equatorial Pacific. *Chemical Geology*, 363, 101–113.
- Ebert, S.W., and Rye, R.O. (1997) Secondary Precious Metal Enrichment by Steam–Heated Fluids in the Crofoot–Lewis Hot Spring Gold–Silver Deposit and Relation to Paleoclimate. *Economic Geology*, 92, 578–600.
- Egal, M., Elbaz–Poulichet, F., Casiot, C., Motelica–Heino, M., Négrel, P., Bruneel, O., Sarmiento, A.M., and Nieto, J.M. (2008) Iron isotopes in acid mine waters and iron–rich solids from the Tinto–Odiel Basin (Iberian Pyrite Belt, Southwest Spain). *Chemical Geology*, 253(3–4), 162–171.
- Ehlmann, B.L., and Mustard, J.F. (2012) An in–situ record of major environmental transitions on early Mars at Northeast Syrtis Major. *Geophysical Research Letters*, 39(L11202).
- Elardo, S.M., and Shahar, A. (2017) Non–chondritic iron isotope ratios in planetary mantles as a result of core formation. *Nature Geoscience*, 10(4), 317–321.
- Elwood Madden, M.E., Bodnar, R.J., and Rimstidt, J.D. (2004) Jarosite as an indicator of water–limited chemical weathering on Mars. *Nature*, 431, 821–823.

- Elwood Madden, M.E., Madden, A.S., Rimstidt, J.D., Zahrai, S., Kendall, M.R., and Miller, M.A. (2012) Jarosite dissolution rates and nanoscale mineralogy. *Geochimica et Cosmochimica Acta*, 91, 306–321.
- Epp, J. (2016) X-ray diffraction (XRD) techniques for materials characterization. In G. Hübschen, I. Altpeter, R. Tschuncky, and H.-G. Herrmann, Eds. *Materials Characterization Using Nondestructive Evaluation (NDE) Methods*, p. 81–124. Woodhead Publishing.
- Fanning, D.S., and Burch, S.N. (1997) Acid Sulphate Soils and Some Associated Environmental Problems. *Advances in GeoEcology*, 30, 145–158.
- Farrand, W.H., Glotch, T.D., Rice, J.W., Hurowitz, J.A., and Swayze, G.A. (2009) Discovery of jarosite within the Mawrth Vallis region of Mars: Implications for the geologic history of the region. *Icarus*, 204(2), 478–488.
- Fernandez, A., and Borrok, D.M. (2009) Fractionation of Cu, Fe, and Zn isotopes during the oxidative weathering of sulfide-rich rocks. *Chemical Geology*, 264(1–4), 1–12.
- Fitch, A.N. (2019) *Synchrotron Methods. Reference Module in Chemistry, Molecular Sciences and Chemical Engineering*. Elsevier.
- Friedrich, W., Knipping, P., and Laue, M. (1912) Sitzungsberichte der mathematisch-physikalischen klasse der koeniglich bayerischen akademie der wissenschaften zu muenchen. *Proc Bavarian Acad Sci*, 303–322.
- Friedrich, A.J., Beard, B.L., Reddy, T.R., Scherer, M.M., and Johnson, C.M. (2014a) Iron isotope fractionation between aqueous Fe(II) and goethite revisited: New insights based on a multi-direction approach to equilibrium and isotopic exchange rate modification. *Geochimica et Cosmochimica Acta*, 139, 383–398.
- Friedrich, A.J., Beard, B.L., Scherer, M.M., and Johnson, C.M. (2014b) Determination of the Fe(II)_{aq}-magnetite equilibrium iron isotope fractionation factor using the three-isotope method and a multi-direction approach to equilibrium. *Earth and Planetary Science Letters*, 391, 77–86.
- Friedrich, A.J., Helgeson, M., Liu, C., Wang, C., Rosso, K.M., and Scherer, M.M. (2015) Iron Atom Exchange between Hematite and Aqueous Fe(II). *Environmental Science & Technology*, 49(14), 8479–86.
- Friedrich, A.J., Nebel, O., Beard, B.L., and Johnson, C.M. (2019) Iron isotope exchange and fractionation between hematite (α -Fe₂O₃) and aqueous Fe(II): A combined three-isotope and reversal-approach to equilibrium study. *Geochimica et Cosmochimica Acta*, 245, 207–221.
- Frunzke, J., Hansen, T., Harrison, A., Lord, J.S., Oakley, G.S., Visser, D., and Wills, A.S. (2001) Magnetic ordering in diluted kagome antiferromagnets. *Journal of Materials Chemistry*, 11(1), 179–185.
- Gasharova, B. (2000) Jarosite AFe₃(SO₄)₂(OH)₆: Kristallchemische Charakterisierung und aquatische Reaktionen, p. 155. Ruprecht-Karls Universität, Heidelberg, Germany.
- Gasharova, B., Göttlicher, J., and Becker, U. (2005) Dissolution at the surface of jarosite: an in situ AFM study. *Chemical Geology*, 215(1–4), 499–516.
- Gault, A.G., Cooke, D.R., Townsend, A.T., Charnock, J.M., and Polya, D.A. (2005) Mechanisms of arsenic attenuation in acid mine drainage from Mount Bischoff, western Tasmania. *Science of the Total Environment*, 345(1–3), 219–28.
- Glaspie, C.N., Jenkinson, S.R., and Seitz, R.D. (2018) Effects of Estuarine Acidification on an Oyster-Associated Community in New South Wales, Australia. *Journal of Shellfish Research*, 37(1), 63–72.
- Glynn, P. (2000) Solid-Solution Solubilities and Thermodynamics: Sulfates, Carbonates and Halides. *Reviews in Mineralogy and Geochemistry*, 40(1), 481–511.
- Goldschmidt, V.M. (1937) The principles of distribution of chemical elements in minerals and rocks. The seventh Hugo Müller Lecture, delivered before the Chemical Society on March 17th, 1937. *Journal of the Chemical Society (Resumed)*(0), 655–673.
- Gong, H., Guo, P., Chen, S., Duan, M., Sun, P., Wang, X., and Niu, Y. (2020) A re-assessment of nickel-doping method in iron isotope analysis on rock samples using multi-collector inductively coupled plasma mass spectrometry. *Acta Geochimica*.
- Gorski, C.A., and Fantle, M.S. (2017) Stable mineral recrystallization in low temperature aqueous systems: A critical review. *Geochimica et Cosmochimica Acta*, 198, 439–465.

- Gostin, V.A. (1966) Tertiary stratigraphy of the Mornington district, Victoria. *Proceedings of the Royal Society of Victoria*, 79(2), 459–512.
- Graydon, J.W., and Kirk, D.W. (1987) The Mechanism of Ferrite Formation from Iron Sulfides during Zinc Roasting. *Metallurgical Transactions B*, 19B, 777–785.
- Grazulis, S., Chateigner, D., Downs, R.T., Yokochi, A.T., Quiros, M., Lutterotti, L., Manakova, E., Butkus, J., Moeck, P., and Le Bail, A. (2009) Crystallography Open Database– an open–access collection of crystal structure. *Journal of Applied Crystallography*, 42, 726–729.
- Grey, I.E., Scarlett, N.V.Y., Bordet, P., and Brand, H.E.A. (2011) Jarosite–butlerite intergrowths in non–stoichiometric jarosites: crystal chemistry of monoclinic natrojarosite–hydroniumjarosite phases. *Mineralogical Magazine*, 75(6), 2775–2791.
- Grey, I.E., Scarlett, N.V.Y., and Brand, H.E.A. (2013) Crystal chemistry and formation mechanism of non–stoichiometric monoclinic K–jarosites. *Mineralogical Magazine*, 77(3), 249–268.
- Grohol, D., Nocera, D.G., and Papoutsakis, D. (2003) Magnetism of pure iron jarosites. *Physical Review B*, 67(6), 064401.
- Guilbaud, R., Butler, I.B., and Ellam, R.M. (2011) Abiotic Pyrite Formation Produces a Large Fe Isotope Fractionation. *Science*, 332, 1548–1551.
- Hall, M.M., Jnr, Veeraraghavan, V.G., Rubin, H., and Winchell, P.G. (1977) The approximation of symmetric X–ray peaks by Pearson type VII distributions. *Journal of Applied Crystallography*, 10(1), 66–68.
- Handler, R.M., Friedrich, A.J., Johnson, C.M., Rosso, K.M., Beard, B.L., Wang, C., Latta, D.E., Neumann, A., Pasakarnis, T., Premaratne, W.A.P.J., and Scherer, M.M. (2014) Fe(II)–Catalyzed Recrystallization of Goethite Revisited. *Environmental Science & Technology*, 48(19), 11302–11311.
- Heimann, A., Johnson, C.M., Beard, B.L., Valley, J.W., Roden, E.E., Spicuzza, M.J., and Beukes, N.J. (2010) Fe, C, and O isotope compositions of banded iron formation carbonates demonstrate a major role for dissimilatory iron reduction in ~2.5Ga marine environments. *Earth and Planetary Science Letters*, 294(1–2), 8–18.
- Hohenberg, P., and Kohn, W. (1964) Inhomogeneous Electron Gas. *Physical Review*, 136(3B), B864–B871.
- Holdgate, G., and Gallagher, S. (2003) Tertiary. A period of transition to marine basin environments. 289–335 p. *Geological Society of Australia (Victoria Division)*.
- Holdgate, G.R., Smith, T.A.G., Gallagher, S.J., and Wallace, M.W. (2001) Geology of coal–bearing Palaeogene sediments, onshore Torquay Basin, Victoria. *Australian Journal of Earth Sciences*, 48(5), 657–679.
- Husson, O., Verburg, P.H., Phung, M.T., and Van Mensvoort, M.E.F. (2000) Spatial variability of acid sulphate soils in the Plain of Reeds, Mekong delta, Vietnam. *Geoderma*, 97, 1–19.
- Jamieson, H.E., Robinson, C., Alpers, C.N., Nordstrom, D.K., Poustovetov, A., and Lowers, H.A. (2005) The composition of coexisting jarosite–group minerals and water from the Richmond mine, Iron Mountain, California. *Canadian Mineralogist*, 43, 1225–1242.
- Jennings, D.S., and Driese, S.G. (2014) Understanding barite and gypsum precipitation in upland acid–sulfate soils: An example from a Lufkin Series toposequence, south–central Texas, USA. *Sedimentary Geology*, 299, 106–118.
- Johnson, C., Beard, B., and Weyer, S. (2020) *Iron Geochemistry: An Isotopic Perspective*. 360 p. Springer International Publishing.
- Johnson, C.M., Beard, B.L., Klein, C., Beukes, N.J., and Roden, E.E. (2008) Iron isotopes constrain biologic and abiologic processes in banded iron formation genesis. *Geochimica et Cosmochimica Acta*, 72(1), 151–169.
- Johnson, C.M., Skulan, J.L., Beard, B.L., Sun, H., Nealson, K.H., and Braterman, P.S. (2002) Isotopic fractionation between Fe(III) and Fe(II) in aqueous solutions. *Earth and Planetary Science Letters*, 195, 141–153.
- Johnston, S.G., Keene, A.F., Burton, E.D., Bush, R.T., Sullivan, L.A., McElnea, A.E., Ahern, C.R., Smith, C.D., Powell, B., and Hocking, R.K. (2010) Arsenic Mobilization in a Seawater Inundated Acid Sulfate Soil. *Environmental Science & Technology*, 44(6), 1968–1973.

- Jones, A.M., Collins, R.N., Rose, J., and Waite, T.D. (2009) The effect of silica and natural organic matter on the Fe(II)–catalysed transformation and reactivity of Fe(III) minerals. *Geochimica et Cosmochimica Acta*, 73(15), 4409–4422.
- Jones, A.M., Griffin, P.J., Collins, R.N., and Waite, T.D. (2014) Ferrous iron oxidation under acidic conditions – The effect of ferric oxide surfaces. *Geochimica et Cosmochimica Acta*, 145, 1–12.
- Jones, B., and Renaut, R.W. (2007) Selective mineralization of microbes in Fe–rich precipitates (jarosite, hydrous ferric oxides) from acid hot springs in the Waiotapu geothermal area, North Island, New Zealand. *Sedimentary Geology*, 194(1–2), 77–98.
- Jordan, M.K., Tang, H., Kohl, I.E., and Young, E.D. (2019) Iron isotope constraints on planetesimal core formation in the early solar system. *Geochimica et Cosmochimica Acta*, 246, 461–477.
- Karimian, N., Johnston, S.G., and Burton, E.D. (2017) Antimony and Arsenic Behavior during Fe(II)–Induced Transformation of Jarosite. *Environmental Science & Technology*, 51(8), 4259–4268.
- . (2018a) Antimony and arsenic partitioning during Fe²⁺–induced transformation of jarosite under acidic conditions. *Chemosphere*, 195, 515–523.
- . (2018b) Iron and sulfur cycling in acid sulfate soil wetlands under dynamic redox conditions: A review. *Chemosphere*, 197, 803–816.
- Kendall, M.R., Madden, A.S., Elwood Madden, M.E., and Hu, Q. (2013) Effects of arsenic incorporation on jarosite dissolution rates and reaction products. *Geochimica et Cosmochimica Acta*, 112, 192–207.
- Kita, N.T., Huberty, J.M., Kozdon, R., Beard, B.L., and Valley, J.W. (2011) High–precision SIMS oxygen, sulfur and iron stable isotope analyses of geological materials: accuracy, surface topography and crystal orientation. *Surface and Interface Analysis*, 43(1–2), 427–431.
- Klingelhöfer, G., Morris, R.V., Bernhardt, B., Schröder, C., Rodionov, D.S., de Souza, P.A., Jr., Yen, A., Gellert, R., Evlanov, E.N., Zubkov, B., Foh, J., Bonnes, U., Kankleit, E., Gütlich, P., Ming, D.W., Renz, F., Wdowiak, T., Squyres, S.W., and Arvidson, R.E. (2004) Jarosite and Hematite at Meridiani Planum from Opportunity's Mössbauer Spectrometer. *Science*, 306(5702), 1740–5.
- Kohn, W., and Sham, L.J. (1965) Self–Consistent Equations Including Exchange and Correlation Effects. *Physical Review*, 140(4A), A1133–A1138.
- Kubisz, J. (1970) Studies on synthetic alkali–hydronium jarosite. I. Synthesis of jarosite and natrojarosite. *Mineralogia Polonica*, 1, 47–57.
- . (1971) Studies of synthetic alkali–hydronium jarosites. II. Thermal investigations. *Mineralogia Polonica*, 2, 51–59.
- Kula, J., and Baldwin, S.L. (2011) Jarosite, argon diffusion, and dating aqueous mineralization on Earth and Mars. *Earth and Planetary Science Letters*, 310(3–4), 314–318.
- Lacelle, D., and Léveillé, R. (2010) Acid drainage generation and associated Ca–Fe–SO₄ minerals in a periglacial environment, Eagle Plains, Northern Yukon, Canada: A potential analogue for low–temperature sulfate formation on Mars. *Planetary and Space Science*, 58(4), 509–521.
- Langmuir, D. (1997) *Aqueous Environmental Geochemistry*. Prentice Hall, Upper Saddle River, New Jersey.
- Lavina, B., Dera, P., and Downs, R.T. (2014) Modern X–ray Diffraction Methods in Mineralogy and Geosciences. *Reviews in Mineralogy and Geochemistry*, 78(1), 1–31.
- Le Bail, A., Duroy, H., and Fourquet, J.L. (1988) Ab–initio structure determination of LiSbWO₆ by X–ray powder diffraction. *Materials Research Bulletin*, 23(3), 447–452.
- Leclerc, N., Meux, E., and Lecuire, J.–M. (2003) Hydrometallurgical extraction of zinc from zinc ferrites. *Hydrometallurgy*, 70(1–3), 175–183.
- Leineweber, A., and Mittemeijer, E.J. (2006) Anisotropic microstrain broadening due to compositional inhomogeneities and its parametrisation. *Z. Kristallogr. Suppl.*, 23, 177–122.
- Léveillé, D.Z., Oehler, A.G., Fairén, B.C., Clark, P.B., and Niles, J.G. (2015) Jarosite in Gale Crator, Mars: The importance of temporal and spatial variability and implications for habitability. *Astrobiology Science Conference*, p. P–7307.

- Li, W., Beard, B.L., and Johnson, C.M. (2015) Biologically recycled continental iron is a major component in banded iron formations. *Proceedings of the National Academy of Sciences of the United States of America*, 112(27), 8193–8.
- Li, Y., Kawashima, N., Li, J., Chandra, A.P., and Gerson, A.R. (2013) A review of the structure, and fundamental mechanisms and kinetics of the leaching of chalcopyrite. *Advances in Colloid and Interface Science*, 197–198, 1–32.
- Ling, Z., Cao, F., Ni, Y., Wu, Z., Zhang, J., and Li, B. (2016) Correlated analysis of chemical variations with spectroscopic features of the K–Na jarosite solid solutions relevant to Mars. *Icarus*, 271, 19–29.
- Liu, P.-P., Zhou, M.-F., Luais, B., Cividini, D., and Rollion-Bard, C. (2014) Disequilibrium iron isotopic fractionation during the high-temperature magmatic differentiation of the Baima Fe–Ti oxide-bearing mafic intrusion, SW China. *Earth and Planetary Science Letters*, 399, 21–29.
- Liu, Y., Goudge, T.A., Catalano, J.G., and Wang, A. (2018) Spectral and stratigraphic mapping of hydrated minerals associated with interior layered deposits near the southern wall of Melas Chasma, Mars. *Icarus*, 302, 62–79.
- Ljung, K., Maley, F., Cook, A., and Weinstein, P. (2009) Acid sulfate soils and human health—a Millennium Ecosystem Assessment. *Environ Int*, 35(8), 1234–42.
- Long, D.T., Fegan, N.E.M., J. D., Lyons, W.B., Hines, M.E., and Macumber, P.G. (1992) Formation of alunite, jarosite and hydrous iron oxides in a hypersaline system: Lake Tyrrell, Victoria, Australia. *Chemical Geology*, 96, 183–202.
- Lopes, D.d.V., Schaefer, C.E.G.R., Souza, J.J.L.L.d., Oliveira, F.S.d., Simas, F.N.B., Daher, M., and Gjorup, D.F. (2019) Concretionary horizons, unusual pedogenetic processes and features of sulfate affected soils from Antarctica. *Geoderma*, 347, 13–24.
- Louër, D. (2016) Powder X-Ray Diffraction, Applications, p. 723–731.
- Lueth, V.W. (2006) Textural and stable isotope discrimination of hypogene and supergene jarosite and environment of formation effects on $^{40}\text{Ar}/^{39}\text{Ar}$ geochronology (abstract). *Martian Sulfates as Records of Atmospheric–Fluid–Rock Interactions workshop*, LPI contribution XXX, Lunar and Planetary Institute, Houston, Texas.
- Lueth, V.W., Rye, R.O., and Peters, L. (2005) “Sour gas” hydrothermal jarosite: ancient to modern acid–sulfate mineralization in the southern Rio Grande Rift. *Chemical Geology*, 215(1–4), 339–360.
- Lyons, W.B., Welch, S., Long, D.T., Hines, M.E., Giblin, A.M., Carey, A.E., Macumber, P.G., Lent, R.M., and Herczeg, A.L. (1992) The trace-metal geochemistry of the Lake Tyrrell systems brines (Victoria, Australia). *Chemical Geology*, 96, 115–132.
- Majzlan, J., Glasnák, P., Fisher, R.A., White, M.A., Johnson, M.B., Woodfield, B., and Boerio-Goates, J. (2010) Heat capacity, entropy, and magnetic properties of jarosite-group compounds. *Physics and Chemistry of Minerals*, 37(9), 635–651.
- Mansor, M., and Fantle, M.S. (2019) A novel framework for interpreting pyrite-based Fe isotope records of the past. *Geochimica et Cosmochimica Acta*, 253, 39–62.
- March, A. (1932) Mathematische Theorie der Regelung nach der Korngestalt bei affiner Deformation. *Zeitschrift für Kristallographie – Crystalline Materials*, 81(1), 285.
- Marin-Carbonne, J., Rollion-Bard, C., and Luais, B. (2011) In-situ measurements of iron isotopes by SIMS: MC–ICP–MS intercalibration and application to a magnetite crystal from the Gunflint chert. *Chemical Geology*, 285(1–4), 50–61.
- Markl, G., von Blanckenburg, F., and Wagner, T. (2006) Iron isotope fractionation during hydrothermal ore deposition and alteration. *Geochimica et Cosmochimica Acta*, 70(12), 3011–3030.
- Martínez-Frías, J., Rodríguez-Losada, J.A., Delgado, A., and Rull, E. (2004) The volcanism-related multistage hydrothermal system of El Jaroso (SE Spain): Implications for the exploration of Mars. *Earth, Planets and Space*, 56(5–8).
- Matsuhisa, Y., Goldsmith, J.R., and Clayton, R.N. (1978) Mechanisms of hydrothermal crystallization of quartz at 250°C and 15 kbar. *Geochimica et Cosmochimica Acta*, 42, 173–182.
- McCusker, L.B., Von Dreele, R.B., Cox, D.E., Louër, D., and Scardi, P. (1999) Rietveld refinement guidelines. *Journal of Applied Crystallography*, 32, 36–50.

- Millet, M.-A., Baker, J.A., and Payne, C.E. (2012) Ultra-precise stable Fe isotope measurements by high resolution multiple-collector inductively coupled plasma mass spectrometry with a ^{57}Fe – ^{58}Fe double spike. *Chemical Geology*, 304–305, 18–25.
- Milliken, R.E., Swayze, G.A., Arvidson, R.E., Bishop, J.L., Clark, R.N., Ehlmann, B.L., Green, R.O., Grotzinger, J.P., Morris, R.V., Murchie, S.L., Mustard, J.F., and Weitz, C. (2008) Opaline silica in young deposits on Mars. *Geology*, 36(11).
- Mills, S.J., Nestola, F., Kahlenberg, V., Christy, A.G., Hejny, C., and Redhammer, G.J. (2013) Looking for jarosite on Mars: The low-temperature crystal structure of jarosite. *American Mineralogist*, 98(11–12), 1966–1971.
- Momma, K., and Izumi, F. (2011) Vesta 3 for three-dimensional visualization of crystals, volumetric and morphology data. *Journal of Applied Crystallography*, 44, 1272–1276.
- Mos, Y.M., Vermeulen, A.C., Buisman, C.J.N., and Weijma, J. (2018) X-Ray Diffraction of Iron Containing Samples: The Importance of a Suitable Configuration. *Geomicrobiology Journal*, 35(6), 511–517.
- Mosley, L.M., Fitzpatrick, R.W., Palmer, D., Leyden, E., and Shand, P. (2014a) Changes in acidity and metal geochemistry in soils, groundwater, drain and river water in the Lower Murray River after a severe drought. *Science of the Total Environment*, 485–486, 281–291.
- Mosley, L.M., Palmer, D., Leyden, E., Cook, F., Zammit, B., Shand, P., Baker, A., and R, W.F. (2014b) Acidification of floodplains due to river level decline during drought. *Journal of Contaminant Hydrology*, 161, 10–23.
- Murray, J., Kirschbaum, A., Dold, B., Guimaraes, E., and Miner, E. (2014) Jarosite versus Soluble Iron–Sulfate Formation and Their Role in Acid Mine Drainage Formation at the Pan de Azúcar Mine Tailings (Zn–Pb–Ag), NW Argentina. *Minerals*, 4(2), 477–502.
- Navrotsky, A., Forray, F., and Drouet, C. (2005) Jarosite stability on Mars. *Icarus*, 176(1), 250–253.
- Nielsen, U.G., Majzlan, J., and Grey, C.P. (2008) Determination and Quantification of the Local Environments in Stoichiometric and Defect Jarosite by Solid-State ^1H NMR Spectroscopy. *Chemistry of Materials*, 20(6), 2234–2241.
- Nishiyama, M., Maegawa, S., Inami, T., and Oka, Y. (2003) Magnetic ordering and spin dynamics in potassium jarosite: A Heisenberg kagomé lattice antiferromagnet. *Physical Review B*, 67.
- Nordstrom, D.K., Alpers, C.N., Ptacek, C.J., and Blowes, D.W. (2000) Negative pH and Extremely Acidic Mine Waters from Iron Mountain, California. *Environmental Science & Technology*, 34(2), 254–258.
- Öborn, I., and Berggren, D. (1995) Characterization of jarosite–natrojarosite in two northern Scandinavian soils. *Geoderma*, 66, 213–225.
- Paktunc, D., and Dutrizac, J.E. (2003) Characterization of arsenate–for–sulfate substitution in synthetic jarosite using x-ray diffraction and x-ray absorption spectroscopy. *The Canadian Mineralogist*, 41(4), 905–919.
- Papike, J.J., Burger, P.V., Karner, J.M., Shearer, C.K., and Lueth, V.W. (2007) Terrestrial analogs of martian jarosites: Major, minor element systematics and Na–K zoning in selected samples. *American Mineralogist*, 92(2–3), 444–447.
- Papike, J.J., Karner, J.M., and Shearer, C.K. (2006) Comparative planetary mineralogy: Implications of martian and terrestrial jarosite. A crystal chemical perspective. *Geochimica et Cosmochimica Acta*, 70(5), 1309–1321.
- Planavsky, N., Rouxel, O., Bekker, A., Shapiro, R., Fralick, P., and Knudsen, A. (2009) Iron-oxidizing microbial ecosystems thrived in late Paleoproterozoic redox-stratified oceans. *Earth and Planetary Science Letters*, 286(1–2), 230–242.
- Planavsky, N., Rouxel, O.J., Bekker, A., Hofmann, A., Little, C.T.S., and Lyons, T.W. (2012) Iron isotope composition of some Archean and Proterozoic iron formations. *Geochimica et Cosmochimica Acta*, 80, 158–169.
- Poitrasson, F., Roskosz, M., and Corgne, A. (2009) No iron isotope fractionation between molten alloys and silicate melt to 2000 °C and 7.7 GPa: Experimental evidence and implications for planetary differentiation and accretion. *Earth and Planetary Science Letters*, 278(3–4), 376–385.
- Polyakov, V.B. (1997) Equilibrium fraction of the iron isotopes: Estimation from Mössbauer spectroscopy data. *Geochimica et Cosmochimica Acta*, 61(19), 4213–4217.

- Polyakov, V.B. (2009) Equilibrium Iron Isotope Fractionation at Core–Mantle Boundary Conditions. *Science*, 323(5916), 912–914.
- Polyakov, V.B., Clayton, R.N., Horita, J., and Mineev, S.D. (2007) Equilibrium iron isotope fractionation factors of minerals: Reevaluation from the data of nuclear inelastic resonant X-ray scattering and Mössbauer spectroscopy. *Geochimica et Cosmochimica Acta*, 71(15), 3833–3846.
- Polyakov, V.B., and Mineev, S.D. (2000) The use of Mössbauer spectroscopy in stable isotope geochemistry. *Geochimica et Cosmochimica Acta*, 64(5), 849–865.
- Pritchett, B.N., Elwood Madden, M.E., and Madden, A.S. (2012) Jarosite dissolution rates and maximum lifetimes in high salinity brines: Implications for Earth and Mars. *Earth and Planetary Science Letters*, 357–358, 327–336.
- Putnis, A. (2009) Mineral Replacement Reactions. *Reviews in Mineralogy and Geochemistry*, 70(1), 87–124.
- Rampe, E.B., Ming, D.W., Blake, D.F., Bristow, T.F., Chipera, S.J., Grotzinger, J.P., Morris, R.V., Morrison, S.M., Vaniman, D.T., Yen, A.S., Achilles, C.N., Craig, P.I., Des Marais, D.J., Downs, R.T., Farmer, J.D., Fendrich, K.V., Gellert, R., Hazen, R.M., Kah, L.C., Morookian, J.M., Peretyazhko, T.S., Sarrazin, P., Treiman, A.H., Berger, J.A., Eigenbrode, J., Fairén, A.G., Forni, O., Gupta, S., Hurowitz, J.A., Lanza, N.L., Schmidt, M.E., Siebach, K., Sutter, B., and Thompson, L.M. (2017) Mineralogy of an ancient lacustrine mudstone succession from the Murray formation, Gale crater, Mars. *Earth and Planetary Science Letters*, 471, 172–185.
- Raymond, O.L., Liu, S., Gallagher, R., Highet, L.M., and Zhang, W. (2012) Surface Geology of Australia, 1:1 000 000 scale, 2012 edition [Digital Dataset]. In C.o.A. Geoscience Australia, Canberra, Ed.
- Reddy, T.R., Frierdich, A.J., Beard, B.L., and Johnson, C.M. (2015) The effect of pH on stable iron isotope exchange and fractionation between aqueous Fe(II) and goethite. *Chemical Geology*, 397, 118–127.
- Richter, F.M., Watson, E.B., Mendybaev, R., Dauphas, N., Georg, B., Watkins, J., and Valley, J. (2009) Isotopic fractionation of the major elements of molten basalt by chemical and thermal diffusion. *Geochimica et Cosmochimica Acta*, 73(14), 4250–4263.
- Rietveld, H.M. (1967) Line profiles of neutron powder–diffraction peaks for structural refinement. *Acta Crystallographica*, 22, 151–152.
- Rietveld, H.M. (1969) A Profile Refinement Method for Nuclear and Magnetic Structures. *Journal of Applied Crystallography*, 2, 65–71.
- Ripmeester, J.A., Ratcliffe, C.I., Dutrizac, J.E., and Jambor, J.L. (1986) Hydronium ion in the alunite–jarosite group. *Canadian Mineralogist*, 24, 435–447.
- Rodushkin, I., Stenberg, A., Andrén, H., Malinovsky, D., and Baxter, D.C. (2004) Isotopic Fractionation during Diffusion of Transition Metal Ions in Solution. *Analytical Chemistry*, 76(7), 2148–2151.
- Roskosz, M., Sio, C.K.I., Dauphas, N., Bi, W., Tissot, F.L.H., Hu, M.Y., Zhao, J., and Alp, E.E. (2015) Spinel–olivine–pyroxene equilibrium iron isotopic fractionation and applications to natural peridotites. *Geochimica et Cosmochimica Acta*, 169, 184–199.
- Rouxel, O.J., Bekker, A., and Edwards, K.J. (2005) Iron Isotope Constraints on the Archaean and Paleoproterozoic Ocean Redox State. *Science*, 307, 1088–1091.
- Rustad, J.R., Casey, W.H., Yin, Q.–Z., Bylaska, E.J., Felmy, A.R., Bogatko, S.A., Jackson, V.E., and Dixon, D.A. (2010) Isotopic fractionation of $\text{Mg}^{2+}(\text{aq})$, $\text{Ca}^{2+}(\text{aq})$, and $\text{Fe}^{2+}(\text{aq})$ with carbonate minerals. *Geochimica et Cosmochimica Acta*, 74(22), 6301–6323.
- Rustad, J.R., and Dixon, D.A. (2009) Prediction of Iron–Isotope Fractionation Between Hematite ($\alpha\text{-Fe}_2\text{O}_3$) and Ferric and Ferrous Iron in Aqueous Solution from Density Functional Theory. *The Journal of Physical Chemistry A*, 113(44), 12249–12255.
- Rye, R.O., and Alpers, C.N. (1997) The stable isotope geochemistry of jarosite. U.S. Geological Survey open–file report, 97–88.
- Rye, R.O., Bethke, P.M., Lanphere, M.A., and Steven, T.A. (2000) Neogene geomorphic and climatic evolution of the central San Juan Mountains, Colorado: K/Ar age and stable isotope data on supergene alunite and jarosite from the Creede mineral district. In P.M. Bethke, and R.L. Hay,

- Eds. Ancient Lake Creede: Its volcano–tectonic setting, history of sedimentation, and relation to mineralization in the Creede Mining District, Colorado, p. 95–104. Geol Soc Am Spec Paper 346.
- Rye, R.O., and Stoffregen, R.E. (1995) Jarosite–water oxygen and hydrogen isotopes fractionations: preliminary experimental data. *Economic Geology*, 90, 2336–2342.
- Samuels–Crow, K.E., Lueth, V.W., Peters, L., and McIntosh, W.C. (2012) $^{40}\text{Ar}/^{39}\text{Ar}$ geochronology of jarosite: The effectiveness of HF in removing silicate contaminants. *Chemical Geology*, 314–317, 23–32.
- Sandström, Å., Shchukarev, A., and Paul, J. (2005) XPS characterisation of chalcopyrite chemically and bio–leached at high and low redox potential. *Minerals Engineering*, 18(5), 505–515.
- Savage, K.S., Bird, D.K., and O'Day, P.A. (2005) Arsenic speciation in synthetic jarosite. *Chemical Geology*, 215(1–4), 473–498.
- Sayre, D. (2015) X–Ray Crystallography: The Past and Present of the Phase Problem. In I. Hargittai, and B. Hargittai, Eds. *Science of Crystal Structures: Highlights in Crystallography*, p. 3–18. Springer International Publishing, Cham.
- Scarlett, N.V., Grey, I.E., and Brand, H.E. (2013) In situ synchrotron diffraction studies on the formation kinetics of jarosites. *Journal of Synchrotron Radiation*, 20, 366–75.
- Scarlett, N.V.Y., Grey, I.E., and Brand, H.E.A. (2010) Ordering of iron vacancies in monoclinic jarosites. *American Mineralogist*, 95(10), 1590–1593.
- Schauble, E.A. (2004) Applying Stable Isotope Fractionation Theory to New Systems. *Reviews in Mineralogy and Geochemistry*, 55, 65–111.
- Schauble, E.A., Rossman, G.R., and Taylor, J., H. P. . (2001) Theoretical estimates of equilibrium Fe–isotope fractionation from vibrational spectroscopy. *Geochimica et Cosmochimica Acta*, 65(5), 2487–2497.
- Schmitt, B., Bronnimann, C., Eikenberry, E.F., Gozzo, F., Hoermann, C., Horisberger, R.P., and Patterson, B. (2003) Mythen detector system. *Nuclear Instruments and Methods in Physics Research Section A: Accelerators, Spectrometers, Detectors and Associated Equipment*, 501(1), 267–272.
- Schoenberg, R., Marks, M.A.W., Schuessler, J.A., von Blanckenburg, F., and Markl, G. (2009) Fe isotope systematics of coexisting amphibole and pyroxene in the alkaline igneous rock suite of the Ilímaussaq Complex, South Greenland. *Chemical Geology*, 258(1–2), 65–77.
- Schoenberg, R., and von Blanckenburg, F. (2005) An assessment of the accuracy of stable Fe isotope ratio measurements on samples with organic and inorganic matrices by high–resolution multicollector ICP–MS. *International Journal of Mass Spectrometry*, 242(2–3), 257–272.
- Schönbächler, M. (2016) Inductively Coupled Plasma Mass Spectrometry (ICP–MS). In W.M. White, Ed. *Encyclopedia of Geochemistry: A Comprehensive Reference Source on the Chemistry of the Earth*, p. 1–6. Springer International Publishing, Cham.
- Scott, K.M. (1987) Solid solution in, and classification of, gossan–derived members of the alunite–jarosite family, northwest Queensland, Australia. *American Mineralogist*, 72, 178–187.
- Shahar, A., Elardo, S.M., and Macris, C.A. (2017) Equilibrium Fractionation of Non–traditional Stable Isotopes: an Experimental Perspective. *Reviews in Mineralogy and Geochemistry*, 82, 65–83.
- Shahar, A., Young, E.D., and Manning, C.E. (2008) Equilibrium high–temperature Fe isotope fractionation between fayalite and magnetite: An experimental calibration. *Earth and Planetary Science Letters*, 268(3–4), 330–338.
- Sham, T.K., and Rivers, M.L. (2002) A Brief Overview of Synchrotron Radiation. *Reviews in Mineralogy and Geochemistry*, 49(1), 117–147.
- Simas, F.N.B., Schaefer, C.E.G.R., Melo, V.F., Guerra, M.B.B., Saunders, M., and Gilkes, R.J. (2006) Clay–sized Minerals in Permafrost–affected Soils (Cryosols) from King George Island, Antarctica. *Clays and Clay Minerals*, 54(6), 721–736.
- Smith, A.M.L., Dubbin, W.E., Wright, K., and Hudson–Edwards, K.A. (2006a) Dissolution of lead– and lead–arsenic–jarosites at pH 2 and 8 and 20 °C: Insights from batch experiments. *Chemical Geology*, 229(4), 344–361.

- Smith, A.M.L., Hudson–Edwards, K.A., Dubbin, W.E., and Wright, K. (2006b) Dissolution of jarosite $[\text{KFe}_3(\text{SO}_4)_2(\text{OH})_6]$ at pH 2 and 8: Insights from batch experiments and computational modelling. *Geochimica et Cosmochimica Acta*, 70(3), 608–621.
- Sossi, P.A., Halverson, G.P., Nebel, O., and Eggins, S.M. (2015) Combined Separation of Cu, Fe and Zn from Rock Matrices and Improved Analytical Protocols for Stable Isotope Determination. *Geostandards and Geoanalytical Research*, 39(2), 129–149.
- Sossi, P.A., and O'Neill, H.S.C. (2017) The effect of bonding environment on iron isotope fractionation between minerals at high temperature. *Geochimica et Cosmochimica Acta*, 196, 121–143.
- Spratt, H.J., Rintoul, L., Avdeev, M., and Martens, W.N. (2013) The crystal structure and vibrational spectroscopy of jarosite and alunite minerals. *American Mineralogist*, 98(10), 1633–1643.
- Squyres, S.W., Arvidson, R.E., Bell, J.F., 3rd, Bruckner, J., Cabrol, N.A., Calvin, W., Carr, M.H., Christensen, P.R., Clark, B.C., Crumpler, L., Marais, D.J., d'Uston, C., Economou, T., Farmer, J., Farrand, W., Folkner, W., Golombek, M., Gorevan, S., Grant, J.A., Greeley, R., Grotzinger, J., Haskin, L., Herkenhoff, K.E., Hviid, S., Johnson, J., Klingelhofer, G., Knoll, A.H., Landis, G., Lemmon, M., Li, R., Madsen, M.B., Malin, M.C., McLennan, S.M., McSween, H.Y., Ming, D.W., Moersch, J., Morris, R.V., Parker, T., Rice, J.W., Jr., Richter, L., Rieder, R., Sims, M., Smith, M., Smith, P., Soderblom, L.A., Sullivan, R., Wanke, H., Wdowiak, T., Wolff, M., and Yen, A. (2004) The Opportunity Rover's Athena science investigation at Meridiani Planum, Mars. *Science*, 306(5702), 1698–703.
- Stephens, P.W. (1999) Phenomenological model of anisotropic peak broadening in powder diffraction. *Journal of Applied Crystallography*, 32, 281–289.
- Stoffregen, R.E. (1993) Stability relations of jarosite and natrojarosite at 150–250°C. *Geochimica et Cosmochimica Acta*, 57, 2417–2429.
- Stoffregen, R.E., Alpers, C.N., and Jambor, J.L. (2000) Alunite–Jarosite Crystallography, Thermodynamics, and Geochronology. *Reviews in Mineralogy and Geochemistry*, 40(1), 453–479.
- Stookey, L.L. (1970) Ferrozine – A New Spectrophotometric Reagent for Iron. *Analytical Chemistry*, 42(7), 779–781.
- Stott, M.B., Watling, H.R., Franzmann, P.D., and Sutton, D. (2000) The role of iron–hydroxy precipitates in the passivation of chalcopyrite during bioleaching. *Minerals Engineering*, 13(10–1), 1117–1127.
- Strelow, F.W. (1980) Improved separation of iron from copper and other elements by anion–exchange chromatography on a 4% cross–linked resin with high concentrations of hydrochloric acid. *Talanta*, 27, 727–732.
- Sukitprapanon, T., Suddhiprakarn, A., Kheoruenromne, I., Anusontpornperm, S., and Gilkes, R.J. (2020) Nature of redox concentrations in a sequence of agriculturally developed acid sulfate soils in Thailand. *Pedosphere*, 30(3), 390–404.
- Suortti, P. (2003) X–Ray, Synchrotron Radiation, and Neutron Diffraction. In R.A. Meyers, Ed. *Encyclopedia of Physical Science and Technology* (Third Edition), p. 989–1023. Academic Press, New York.
- Swayze, G.A., Desborough, G.A., Smith, K.S., Lowers, H.A., Hammarstrom, J.M., Diehl, S.F., Leinz, R.W., and Driscoll, R.L. (2008) Understanding jarosite– from mine waste to Mars. In P.L. Verplant, Ed. *Understanding Contaminants Associated with Mineral Deposits*, p. 8–13.
- Tahata, M., Sawaki, Y., Yoshiya, K., Nishizawa, M., Komiya, T., Hirata, T., Yoshida, N., Maruyama, S., and Windley, B.F. (2015) The marine environments encompassing the Neoproterozoic glaciations: Evidence from C, Sr and Fe isotope ratios in the Hecla Hoek Supergroup in Svalbard. *Precambrian Research*, 263, 19–42.
- Taylor, S.D., Liu, J., Zhang, X., Arey, B.W., Kovarik, L., Schreiber, D.K., Perea, D.E., and Rosso, K.M. (2019) Visualizing the iron atom exchange front in the Fe(II)–catalyzed recrystallization of goethite by atom probe tomography. *Proceedings of the National Academy of Sciences of the United States of America*, 116(8), 2866–2874.
- Teng, F., Dauphas, N., and Watkins, J.M. (2017) Non–Traditional Stable Isotopes: Retrospective and Prospective. *Reviews in Mineralogy and Geochemistry*, 82(1), 1–26.

- Thollot, P., Mangold, N., Ansan, V., Le Mouélic, S., Milliken, R.E., Bishop, J.L., Weitz, C.M., Roach, L.H., Mustard, J.F., and Murchie, S.L. (2012) Most Mars minerals in a nutshell: Various alteration phases formed in a single environment in Noctis Labyrinthus. *Journal of Geophysical Research: Planets*, 117(E11).
- Thompson, A., Chadwick, O.A., Rancourt, D.G., and Chorover, J. (2006) Iron–oxide crystallinity increases during soil redox oscillations. *Geochimica et Cosmochimica Acta*, 70(7), 1710–1727.
- Thompson, P., Cox, D.E., and Hastings, J.B. (1987) Rietveld refinement of Debye–Scherrer synchrotron X–ray data from Al_2O_3 . *Journal of Applied Crystallography*, 20, 79–83.
- Trueman, A.M., McLaughlin, M.J., Mosley, L.M., and Fitzpatrick, R.W. (2020) Composition and dissolution kinetics of jarosite–rich segregations extracted from an acid sulfate soil with sulfuric material. *Chemical Geology*, 543, 119606.
- van Breemen, N. (1988) Redox Processes of Iron and Sulfur Involved in the Formation of Acid Sulfate Soils. In J.W. Stucki, B.A. Goodman, and U. Schwertmann, Eds. *Iron in Soils and Clay Minerals*, p. 825–841. Springer Netherlands, Dordrecht.
- VandenBerg, A.H.M. (2009) Rock unit names in the Bendigo Zone portion of central Victoria, Seamless Geology Project. Geological Survey of Victoria. Geoscience Victoria.
- Vasconcelos, P.M., Brimhall, G.H., Becker, T.A., and Renne, P.R. (1994) $^{40}\text{Ar}/^{39}\text{Ar}$ analysis of supergene jarosite and alunite: Implications to the paleoweathering history of the western USA and West Africa. *Geochimica et Cosmochimica Acta*, 58, 401–420.
- Von Dreele, R.B. (1997) Quantitative texture analysis by Rietveld refinement. *Journal of Applied Crystallography*, 30(4), 517–525.
- Wagner, D.P., Fanning, D.S., Foss, J.E., Patterson, M.S., and Snow, P.A. (1982) Morphological and Mineralogical Features Related to Sulfide Oxidation under Natural and Disturbed Land Surfaces in Maryland. *Acid Sulfate Weathering*, 109–125.
- Wallwork, K.S., Kennedy, B.J., and Wang, D. (2007) The High Resolution Powder Diffraction Beamline for the Australian Synchrotron. *AIP Conference Proceedings*, 879(1), 879–882.
- Wang, J., Davis, A.M., Clayton, R.N., and Mayeda, T.K. (1994) Kinetic isotopic fractionation during the evaporation of the iron oxide from liquid state. *Lunar and Planetary Science Conference*, 25, p. 1459–1460.
- Wawryk, C.M., and Foden, J.D. (2015) Fe–isotope fractionation in magmatic–hydrothermal mineral deposits: A case study from the Renison Sn–W deposit, Tasmania. *Geochimica et Cosmochimica Acta*, 150, 285–298.
- Weitz, C.M., Bishop, J.L., Thollot, P., Mangold, N., and Roach, L.H. (2011) Diverse mineralogies in two troughs of Noctis Labyrinthus, Mars. *Geology*, 39(10), 899–902.
- Welch, S.A., Beard, B.L., Johnson, C.M., and Braterman, P.S. (2003) Kinetic and equilibrium Fe isotope fractionation between aqueous Fe(II) and Fe(III). *Geochimica et Cosmochimica Acta*, 67(22), 4231–4250.
- Welch, S.A., Christy, A.G., Kirste, D., Beavis, S.G., and Beavis, F. (2007) Jarosite dissolution I — Trace cation flux in acid sulfate soils. *Chemical Geology*, 245(3–4), 183–197.
- Welch, S.A., Kirste, D., Christy, A.G., Beavis, F.R., and Beavis, S.G. (2008) Jarosite dissolution II — Reaction kinetics, stoichiometry and acid flux. *Chemical Geology*, 254(1–2), 73–86.
- Wendt, L., Gross, C., Kneissl, T., Sowe, M., Combe, J.–P., LeDeit, L., McGuire, P.C., and Neukum, G. (2011) Sulfates and iron oxides in Ophir Chasma, Mars, based on OMEGA and CRISM observations. *Icarus*, 213(1), 86–103.
- Wertheim, G.K., Butler, M.A., West, K.W., and Buchanan, D.N.E. (1974) Determination of the Gaussian and Lorentzian content of experimental line shapes. *Review of Scientific Instruments*, 45, 1369–1371.
- Wessa, P. (2017) Bagplot (v1.0.3) in Free Statistics Software (v1.2.1). Office for Research Development and Education.
- Wessel, B.M., Fiola, J.C., and Rabenhorst, M.C. (2017) Soil morphology, genesis, and monolith construction of an acid sulfate soil with silica–cementation in the US Mid–Atlantic Region. *Geoderma*, 308, 260–269.
- Weyer, S., and Schwieters, J.B. (2003) High precision Fe isotope measurements with high mass resolution MC–ICPMS. *International Journal of Mass Spectrometry*, 226(3), 355–368.

- White, I., Melville, M.D., Wilson, B.P., and Sammut, J. (1997) Reducing acidic discharge from coastal wetlands in eastern Australia. *Wetlands Ecology and Management*, 5, 55–72.
- White, W.M. (2018) Stable Isotope Geochemistry. In W.M. White, Ed. *Encyclopedia of Geochemistry: A Comprehensive Reference Source on the Chemistry of the Earth*, p. 1367–1374. Springer International Publishing, Cham.
- Whitworth, A.J., Brand, H.E.A., and Frierdich, A.J. (2020a) Iron isotope exchange and fractionation between jarosite and aqueous Fe(II). *Chemical Geology*, 554, 119802.
- Whitworth, A.J., Brand, H.E.A., Wilson, S.A., and Frierdich, A.J. (2020b) Iron isotope geochemistry and mineralogy of jarosite in sulfur-rich sediments. *Geochimica et Cosmochimica Acta*, 270, 282–295.
- Wiesli, R., Beard, B., and Johnson, C. (2004) Experimental determination of Fe isotope fractionation between aqueous Fe(II), siderite and "green rust" in abiotic systems. *Chemical Geology*, 211(3–4), 343–362.
- Will, G. (2006) *Powder Diffraction: The Rietveld Method and The Two Stage Method*. Springer, Berlin.
- Wills, A.S., Harrison, A., Ritter, C., and Smith, R.I. (2000) Magnetic properties of pure and diamagnetically doped jarosites: Model kagomé antiferromagnets with variable coverage of the magnetic lattice. *Physical Review B*, 61(9), 6156–6169.
- Wu, L., Percak-Dennett, E.M., Beard, B.L., Roden, E.E., and Johnson, C.M. (2012) Stable iron isotope fractionation between aqueous Fe(II) and model Archean ocean Fe–Si coprecipitates and implications for iron isotope variations in the ancient rock record. *Geochimica et Cosmochimica Acta*, 84, 14–28.
- Yanina, S.V., and Rosso, K.M. (2008) Linked reactivity at mineral–water interfaces through bulk crystal conduction. *Science*, 320(5873), 218–222.
- Yoshiya, K., Nishizawa, M., Sawaki, Y., Ueno, Y., Komiya, T., Yamada, K., Yoshida, N., Hirata, T., Wada, H., and Maruyama, S. (2012) In situ iron isotope analyses of pyrite and organic carbon isotope ratios in the Fortescue Group: Metabolic variations of a Late Archean ecosystem. *Precambrian Research*, 212–213, 169–193.
- Zahrai, S.K., Elwood Madden, M.E., Madden, A.S., and Rimstidt, J.D. (2013) Na–jarosite dissolution rates: The effect of mineral composition on jarosite lifetimes. *Icarus*, 223(1), 438–443.
- Zhu, Z.-Y., Jiang, S.-Y., Mathur, R., Cook, N.J., Yang, T., Wang, M., Ma, L., and Ciobanu, C.L. (2018) Iron isotope behavior during fluid/rock interaction in K–feldspar alteration zone – A model for pyrite in gold deposits from the Jiaodong Peninsula, East China. *Geochimica et Cosmochimica Acta*, 222, 94–116.
- Zimbelman, D.R., Rye, R.O., and Breit, G.N. (2005) Origin of secondary sulfate minerals on active andesitic stratovolcanoes. *Chemical Geology*, 215(1–4), 37–60.

Appendix 1

*Iron Isotope Geochemistry and
Mineralogy of Jarosite in Sulfur-Rich
Sediments: Supplementary Information*

TABLE OF CONTENTS

SI 1: Location details and physical description of the jarosite and sediment samples.....	III
SI 2: Photographs of the sediment (and jarosite) horizons at Fossil Beach and Southside Beach	VI
SI 3: Chemistry data for the jarosite and sediment samples	IX
SI 4: Iron isotope data for the jarosite and sediment samples	XXIV
SI 5: Mineralogy and crystallographic data for the jarosite and sediment samples	XXVI

SI 1. Location details and physical description of the jarosite and sediment samples

Table SI 1. Location, coordinates and description of the physical characteristics of the jarosite and sediment samples.

Sample ID	Location	Coordinates		Physical Description		
		Easting	Southing	Occurrence and morphology	Munsell Colour	
		WGS84	WGS84		Value	Description
<i>Jarosite</i>						
Js-FB-1	Fossil Beach	N/A	N/A	Cliff vein	5Y 8/6	Yellow
Js-FB-3A	Fossil Beach	145.0277	38.24183	Cliff nodule	2.5Y 8/4	Pale Brown
Js-FB-4	Fossil Beach	145.0278	38.24167	Cliff surface coating	2.5Y 8/6	Yellow
Js-FB-5	Fossil Beach	145.0278	38.24167	Cliff surface coating	5Y 8/6	Yellow
Js-FB-8A	Fossil Beach	145.0278	38.24167	Cliff surface coating	5Y 8/6	Yellow
Js-FB-9A	Fossil Beach	145.0277	38.24153	Cliff surface coating	5Y 8/3	Pale Yellow
Js-FB-11A	Fossil Beach	145.0277	38.24153	Cliff surface coating	10YR 5/6	Yellowish Brown
Js-FB-14	Fossil Beach	145.0278	38.24122	Cliff nodule	5Y 8/4	Pale Yellow
Js-FB-16	Fossil Beach	145.0278	38.241	Bedding in cliff	5Y 8/4	Pale Yellow
Js-FB-20A	Fossil Beach	145.0278	38.241	Cliff surface coating	5Y 8/3	Pale Yellow
Js-FB-21A	Fossil Beach	145.0278	38.241	Interior of boulder	2.5Y 7/8	Yellow
Js-FB-21B	Fossil Beach	145.0278	38.241	Exterior of boulder	2.5 6/8	Olive Yellow
Js-SB-1	Southside Beach	144.2759	38.3729	Cliff nodule	5Y 8/6	Yellow
Js-SB-2	Southside Beach	144.2759	38.3729	Cliff nodule	5Y 8/6	Yellow
Js-SB-4	Southside Beach	144.2759	38.3729	Cliff nodule	5Y 8/6	Yellow
Js-SB-5	Southside Beach	144.2759	38.3729	Cliff nodule	5Y 8/4	Pale Yellow
Js-SB-11	Southside Beach	144.2758	38.373	Interior of boulder	10YR 6/8	Bright Yellow Brown
Js-SB-12	Southside Beach	144.2758	38.373	Interior of boulder	10YR 8/4	Light Yellow Orange
Js-SB-15	Southside Beach	144.2756	38.37306	Cliff surface coating	5Y 8/6	Yellow
Js-SB-16	Southside Beach	144.2756	38.37306	Cliff vein	5Y 8/4	Pale Yellow
Js-SB-19	Southside Beach	144.2755	38.37309	Cliff surface coating	5Y 8/4	Pale Yellow
Js-SB-20A	Southside Beach	144.2755	38.37309	Cliff surface coating	5Y 7/4	Pale Yellow

Appendix 1

Js-SB-20B	Southside Beach	144.2755	38.37309	Cliff surface coating	5Y 8/4	Pale Yellow
Js-SB-24	Southside Beach	144.2734	38.37382	Cliff vein	5Y 8/3	Pale Yellow
Js-SB-26A	Southside Beach	144.2734	38.37382	Cliff surface coating	5Y 7/3	Pale Yellow
Js-SB-31	Southside Beach	144.2732	38.37397	Cliff surface coating	5Y 8/3	Pale Yellow
Js-SB-32A	Southside Beach	144.2732	38.37397	Exterior of cobble	5Y 8/4	Pale Yellow
Js-SB-32B	Southside Beach	144.2732	38.37397	Interior of cobble	5Y 8/8	Yellow
Js-SB-32D	Southside Beach	144.2732	38.37397	Exterior of cobble	5Y 8/6	Yellow
Js-SB-34A	Southside Beach	144.2732	38.37397	Interior of cobble	2.5Y 8/8	Yellow
Js-SB-34B	Southside Beach	144.2732	38.37397	Interior of cobble	2.5Y 7/8	Yellow
Js-SB-34C	Southside Beach	144.2732	38.37397	Exterior of cobble	10YR 6/8	Brownish Yellow
Js-SB-34D	Southside Beach	144.2732	38.37397	Exterior of cobble	5Y 8/6	Yellow
Js-SB-34F	Southside Beach	144.2732	144.2732	Interior of cobble	5Y 8/6	Yellow
Js-SB-34G	Southside Beach	144.2732	144.2732	Exterior of cobble	5Y 8/8	Yellow
Js-SB-34H	Southside Beach	144.2732	144.2732	Exterior of cobble	5Y 8/6	Yellow
Js-SB-34I	Southside Beach	144.2732	144.2732	Interior of cobble	5Y 8/8	Yellow
Js-SB-35A	Southside Beach	144.2732	38.37397	Interior of cobble	5Y 8/4	Pale Yellow
Js-SB-35B	Southside Beach	144.2732	38.37397	Interior of cobble	10YR 7/6	Bright Yellow Brown
Js-SB-35E	Southside Beach	144.2732	38.37397	Interior of cobble	5Y 8/8	Yellow
Js-SB-35F	Southside Beach	144.2732	38.37397	Interior of cobble	5Y 8/8	Yellow
Js-SB-38	Southside Beach	144.2685	38.37806	Pebble	5Y 8/4	Pale Yellow
Js-SB-39	Southside Beach	144.2685	38.37806	Cliff nodule	5Y 8/4	Pale Yellow
Js-SB-40A	Southside Beach	144.2685	38.37806	Cliff surface coating	5Y 8/3	Pale Yellow
Js-SB-42	Southside Beach	144.2702	38.37579	Cliff surface coating	5Y 8/4	Pale Yellow
Js-SB-47B	Southside Beach	144.2723	38.37441	Cliff nodule	2.5Y 9.5/2	Very Pale Yellow
Js-SB-59A	Southside Beach	144.269	38.37714	Exterior of boulder	2.5Y 7/6	Yellow
Js-SB-60	Southside Beach	144.269	38.37715	Exterior of cobble	5Y 8/8	Yellow
Js-SB-63	Southside Beach	144.2699	38.37672	Pebble	2.5Y 8/8	Yellow

Sediment

Appendix 1

Js-FB-8B	Fossil Beach	145.0278	38.24167	Cliff sediment	5Y 3/1	Very Dark Grey
Js-FB-9B	Fossil Beach	145.0277	38.24153	Cliff sediment	10YR 7/1	Light Grey
Js-FB-12	Fossil Beach	145.0277	38.24153	Cliff sediment	2.5Y 3/1	Very Dark Grey
Js-FB-20B	Fossil Beach	145.0278	38.241	Cliff sediment	10YR 5/1	Brownish Grey
Js-FB-27	Fossil Beach	145.0278	38.24133	Cliff sediment	5Y 8/1	Light Grey
Js-FB-31	Fossil Beach	145.0277	38.24153	Cliff sediment	2.5Y 5/2	Greyish Brown
Js-SB-28	Southside Beach	144.2734	38.37382	Cliff sediment	10YR 2/2	Brownish Black
Js-SB-40B	Southside Beach	144.2685	38.37806	Cliff sediment	10YR 2/1	Black
Js-SB-50	Southside Beach	144.2745	38.37443	Cliff sediment	2.5Y 4/2	Dark Greyish Brown
Js-SB-51	Southside Beach	144.2741	38.37458	Cliff sediment	10YR 4/1	Dark Grey
Js-SB-52	Southside Beach	144.2728	38.37503	Cliff sediment	7.5YR 4/3	Brown
Js-SB-55	Southside Beach	144.2723	38.37522	Cliff sediment	7.5YR 5/3	Brown
Js-SB-56	Southside Beach	144.2723	38.37522	Cliff sediment	10YR 4/2	Dark Greyish Brown
Js-SB-57	Southside Beach	144.2709	38.37594	Cliff sediment	7.5YR 3/2	Dark Brown
Js-SB-58	Southside Beach	144.2696	38.37669	Cliff sediment	7.5YR 6/4	Light Brown
Js-SB-59B	Southside Beach	144.269	38.37714	Sediment from boulder	10YR 7/2	Light Grey
Js-SB-62	Southside Beach	144.2677	38.3791	Sediment pebble	10YR 2/2	Very Dark Brown

SI 2. Photographs of the sediment (and jarosite) horizons at Fossil Beach and Southside Beach

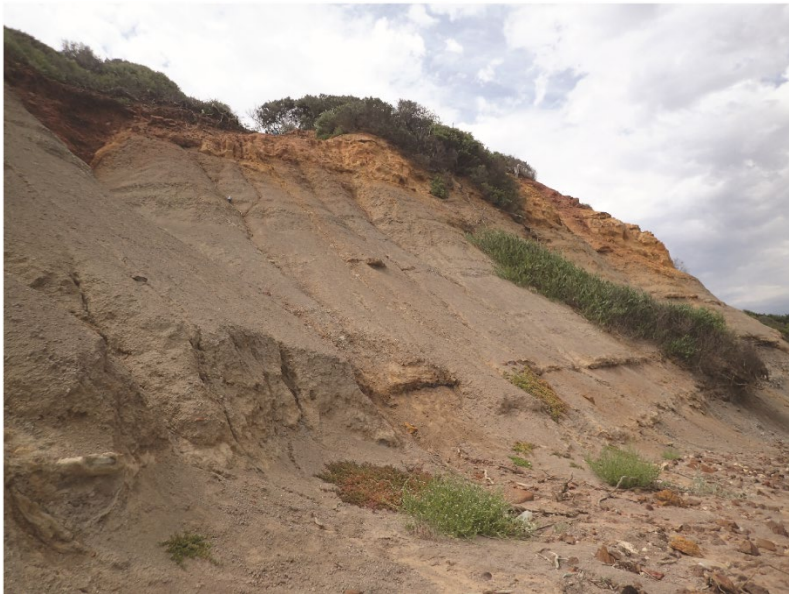


Figure SI 2A: Photograph of cliff sediment at Fossil Beach. Note the uniformity of the cliff sediment.



Figure SI 2B. Photograph of slip in cliff sediment at Fossil Beach. Note the light-yellow jarosite outcropping on the sediment.



Figure SI 2C. Photograph of cliff sediment at Southside Beach. Note that there are two different horizons: a lower dark brown horizon and an upper lighter, yellow horizon.



Figure SI 2D. Photograph of cliff sediment at Southside Beach. Note that there are two horizons: a lower dark black-brown horizon and an upper yellow-brown horizon that contact sub-vertically. Bright yellow jarosite mineralisation is visible at the contact of the two horizons.



Figure SI 2E. Photograph of a close-up of the contact between the lower, darker black-brown sediment horizon and upper light brown sediment horizon at Southside Beach. Note the sharpness of the contact, as well as the yellow jarosite mineralisation predominantly in the upper sediment horizon and at the contact.



Figure SI 2F. Photograph of a section of darker sediment with jarosite mineralisation at Southside Beach. Jarosite mineralisation does occur in darker cliff sediment at Southside Beach, but is more frequent in the lighter coloured sediment horizons.

SI 3. Chemistry data for the jarosite and sediment sample

Table SI 3A. Elemental composition of jarosite and sediment samples determined by inductively coupled plasma–mass spectrometry (ICP–MS).

<i>Jarosite</i>													
Sample ID	Js–FB– 1 ^a	Js–FB– 3A ^a	Js–FB– 4 ^a	Js–FB–5	Js–FB– 8A ^a	Js–FB– 9A ^a	Js–FB– 11A ^a	Js–FB– 14 ^a	Js–FB– 16 ^a	Js–FB– 20A ^a	Js–FB– 21A ^a	Js–FB– 21B ^a	Js–SB– 1 ^a
<i>Morphology</i>	Vein	Nodule	Coating	Coating	Coating	Coating	Coating	Nodule	Bedding	Coating	Boulder	Boulder	Nodule
<i>Major (wt%)</i>													
Na	4.28	1.22	2.13	2.88	2.10	2.03	0.37	4.00	2.49	2.39	1.53	2.13	3.45
Mg	0.05	0.25	0.06	0.05	0.06	0.06	0.17	0.05	0.05	0.05	0.04	0.05	0.17
Al	0.15	0.12	0.23	0.23	0.30	0.27	0.09	0.14	0.37	0.28	0.49	0.58	0.07
P	0.71	ND	0.03	0.04	ND	0.02	0.02	0.55	0.02	0.03	0.89	0.66	0.04
K	0.62	0.35	1.57	1.42	0.15	1.05	0.31	1.44	2.41	2.25	4.40	3.20	1.65
Ca	0.02	0.76	0.05	0.04	0.16	0.03	1.03	0.16	0.04	0.04	0.29	0.19	0.10
Fe	33.95	9.13	33.34	28.74	18.58	20.45	8.63	32.07	26.18	25.84	28.36	29.75	27.93
<i>Minor (ppm)</i>													
Li	ND	ND	ND	ND	ND	ND	ND	ND	ND	ND	ND	ND	ND
B	ND	213.682	ND	41.093	139.715	ND	41.093	ND	ND	ND	49.311	ND	ND
V	145.128	6.417	655.543	125.975	50.745	177.757	4.196	220.654	278.458	213.200	13.180	26.014	50.597
Cr	13.924	4.582	44.300	22.760	12.882	24.813	ND	30.495	90.236	49.625	30.079	46.233	9.818
Mn	8.427	13.197	57.479	34.901	75.287	44.441	98.580	32.675	75.128	42.294	173.549	225.462	7.235
Co	ND	ND	ND	ND	8.763	ND	12.446	ND	ND	ND	ND	4.027	ND
Ni	ND	ND	ND	ND	10.492	7.567	30.562	ND	ND	ND	9.176	21.752	ND
Cu	ND	ND	18.431	3.058	ND	7.073	10.388	ND	19.761	10.762	15.559	20.847	ND
Zn	80.013	17.491	54.707	26.423	35.913	44.286	75.548	13.118	62.801	43.728	41.309	47.171	26.795
Ge	ND	ND	0ND	ND	ND	ND	ND	ND	ND	ND	ND	ND	ND
As	85.923	25.508	54.709	37.591	51.353	44.975	730.013	80.553	68.135	63.436	23.495	30.543	138.283
Se	ND	ND	ND	ND	ND	ND	ND	7.025	ND	ND	ND	ND	ND
Rb	146.617	27.491	179.957	292.260	19.302	232.209	8.969	117.177	102.164	178.202	33.340	53.422	41.724
Sr	80.210	1144.196	387.683	323.240	357.747	216.179	372.829	1588.323	359.346	319.356	3007.770	1830.782	633.227
Y	ND	ND	ND	ND	ND	ND	ND	ND	ND	ND	ND	ND	ND

Appendix 1

Zr	ND	ND	ND	ND	ND	ND	ND	ND	ND	ND	5.205	4.861	ND
Mo	ND	ND	ND	ND	ND	ND	ND	ND	ND	ND	ND	ND	163.595
Cd	ND	ND	ND	ND	ND	ND	ND	ND	ND	ND	ND	ND	ND
Sn	ND	ND	ND	ND	ND	ND	ND	ND	ND	ND	ND	ND	ND
Sb	ND	ND	0.234	ND	ND	ND	ND	ND	ND	ND	ND	ND	ND
Cs	ND	ND	ND	ND	ND	ND	ND	ND	ND	ND	ND	ND	ND
Ba	158.523	26.102	104.557	68.152	9.079	238.860	13.798	79.023	43.245	193.615	158.942	95.747	15.649
La	302.876	2.745	5.822	24.521	4.751	13.353	ND	501.496	11.747	18.368	220.617	178.654	ND
Ce	688.225	8.761	13.466	27.838	18.325	27.498	3.727	799.779	11.459	18.200	413.698	365.788	ND
Pr	32.581	ND	ND	ND	ND	ND	ND	23.092	ND	ND	16.429	15.721	ND
Nd	62.382	4.122	5.802	4.092	5.893	8.733	ND	35.878	ND	ND	33.893	36.580	ND
Sm	4.952	ND	0.631	ND	ND	ND	ND	ND	ND	ND	ND	2.327	ND
Eu	ND	ND	ND	ND	ND	ND	ND	ND	ND	ND	ND	ND	ND
Gd	ND	ND	0.323	ND	ND	ND	ND	ND	ND	ND	ND	0.356	ND
Tb	ND	ND	ND	ND	ND	ND	ND	ND	ND	ND	ND	ND	ND
Dy	ND	ND	ND	ND	ND	ND	ND	ND	ND	ND	ND	ND	ND
Ho	ND	ND	ND	ND	ND	ND	ND	ND	ND	ND	ND	ND	ND
Er	ND	ND	ND	ND	ND	ND	ND	ND	ND	ND	ND	ND	ND
Tm	ND	ND	ND	ND	ND	ND	ND	ND	ND	ND	ND	ND	ND
Yb	ND	ND	ND	ND	ND	ND	ND	ND	ND	ND	ND	ND	ND
Lu	ND	ND	ND	ND	ND	ND	ND	ND	ND	ND	ND	ND	ND
Pb	23.772	6.609	26.945	43.633	6.987	126.782	24.689	29.669	30.020	192.860	ND	ND	6.966
Th	36.967	ND	20.197	18.851	7.699	14.747	5.366	90.628	15.964	15.614	43.142	47.884	3.914
U	ND	ND	ND	ND	ND	ND	ND	ND	ND	ND	ND	ND	ND

^a Analysed during run one

^b Analysed during run two

ND: Not detected as concentration below instrument detection limit. Detection limits for the two runs is provided in Table SI 2B. Note: each sample was diluted to one tenth or one hundredth of the original concentration for analysis. As such, ND reflects that the element of interest was not detected in the diluted sample.

Appendix 1

<i>Jarosite (cont)</i>													
Sample ID	Js-SB-2 ^a	Js-SB-4 ^a	Js-SB-5 ^a	Js-SB-11 ^a	Js-SB-12 ^a	Js-SB-15 ^a	Js-SB-16 ^a	Js-SB-19 ^a	Js-SB-20A ^a	Js-SB-20B ^a	Js-SB-24 ^a	Js-SB-26A ^a	Js-SB-31 ^a
<i>Morphology</i>	Nodule	Nodule	Nodule	Boulder	Boulder	Coating	Vein	Coating	Coating	Coating	Vein	Coating	Coating
<i>Major (wt%)</i>													
Na	4.06	4.02	2.51	2.40	0.14	2.65	4.12	2.95	0.60	4.03	2.43	9.94	3.17
Mg	0.16	0.15	0.12	0.18	0.23	0.08	0.10	0.05	0.06	0.11	0.09	0.29	0.06
Al	0.14	0.06	0.12	6.64	2.70	0.23	0.04	0.09	0.07	0.09	0.11	0.62	0.18
P	0.03	0.03	ND	0.08	ND	0.42	0.31	0.15	0.03	0.17	0.17	0.08	0.30
K	0.70	1.66	3.09	1.58	ND	3.03	0.88	0.57	0.11	0.44	1.97	0.04	2.29
Ca	0.08	0.11	0.12	0.14	2.00	0.10	0.05	0.49	0.01	0.18	0.11	0.09	0.09
Fe	29.89	31.81	27.98	26.19	1.74	29.11	32.00	24.49	3.71	29.56	24.60	12.12	31.40
<i>Minor (ppm)</i>													
Li	ND	ND	29.245	ND	ND	ND	ND	ND	ND	ND	ND	ND	ND
B	ND	ND	ND	90.404	41.093	41.093	ND	ND	57.530	57.530	ND	90.404	ND
V	115.905	56.027	197.107	208.757	16.734	231.810	218.432	249.926	39.441	61.753	702.340	49.314	539.392
Cr	27.074	10.234	14.965	343.895	30.049	22.373	10.175	15.768	ND	13.210	7.735	9.729	8.866
Mn	12.084	8.745	10.256	85.065	71.391	108.359	77.592	46.428	24.327	61.215	66.860	73.458	25.917
Co	ND	ND	ND	9.318	7.554	ND	ND	ND	ND	ND	ND	5.358	ND
Ni	ND	ND	4.021	23.543	49.207	ND	7.092	ND	ND	ND	ND	ND	4.241
Cu	ND	ND	3.315	25.131	2.218	ND	ND	ND	3.805	ND	24.500	ND	16.038
Zn	15.444	6.792	21.864	204.965	37.495	32.564	8.187	13.956	13.677	17.026	50.427	63.639	34.238
Ge	ND	ND	ND	ND	ND	ND	ND	ND	ND	ND	ND	ND	ND
As	73.505	134.926	266.161	303.417	38.263	588.038	207.424	217.493	36.249	107.404	130.228	29.201	42.290
Se	ND	ND	ND	ND	ND	ND	ND	ND	ND	ND	ND	7.025	ND
Rb	56.151	42.503	47.183	10.528	ND	42.113	53.227	18.717	ND	8.189	65.120	ND	139.988
Sr	651.165	711.037	858.204	1117.687	522.738	898.080	323.583	539.648	61.700	587.980	672.532	47.303	630.827
Y	ND	ND	ND	ND	ND	ND	ND	ND	ND	ND	ND	14.316	ND
Zr	ND	ND	ND	ND	ND	ND	ND	ND	ND	ND	ND	ND	ND

Appendix 1

Mo	96.086	56.718	36.525	29.677	23.783	23.907	24.571	ND	ND	ND	ND	ND	ND
Cd	ND	ND	ND	ND	ND	ND	ND	ND	ND	ND	ND	ND	ND
Sn	ND	ND	ND	ND	ND	ND	ND	ND	ND	ND	ND	ND	ND
Sb	ND	ND	ND	ND	ND	ND	ND	ND	ND	ND	ND	ND	ND
Cs	ND	ND	ND	ND	ND	ND	ND	ND	ND	ND	ND	ND	ND
Ba	10.274	15.530	49.845	53.100	27.715	31.717	11.289	53.817	9.855	81.382	18.666	9.437	56.385
La	ND	ND	ND	4.683	ND	46.808	39.999	22.473	7.063	24.980	15.588	ND	45.635
Ce	ND	ND	ND	10.695	7.155	194.921	120.932	76.263	24.473	67.083	28.720	30.513	133.103
Pr	ND	ND	ND	ND	ND	11.372	4.284	3.978	ND	ND	ND	ND	5.925
Nd	ND	ND	ND	ND	4.794	26.840	8.489	11.878	ND	7.908	5.069	29.618	19.176
Sm	ND	ND	ND	ND	ND	4.055	ND	ND	ND	ND	ND	6.381	1.462
Eu	ND	ND	ND	ND	ND	ND	ND	ND	ND	ND	ND	ND	ND
Gd	ND	ND	ND	ND	ND	ND	ND	ND	ND	ND	ND	ND	ND
Tb	ND	ND	ND	ND	ND	ND	ND	ND	ND	ND	ND	ND	ND
Dy	ND	ND	ND	ND	ND	ND	ND	ND	ND	ND	ND	ND	ND
Ho	ND	ND	ND	ND	ND	ND	ND	ND	ND	ND	ND	ND	ND
Er	ND	ND	ND	ND	ND	ND	ND	ND	ND	ND	ND	ND	ND
Tm	ND	ND	ND	ND	ND	ND	ND	ND	ND	ND	ND	ND	ND
Yb	ND	ND	ND	ND	ND	ND	ND	ND	ND	ND	ND	ND	ND
Lu	ND	ND	ND	ND	ND	ND	ND	ND	ND	ND	ND	ND	ND
Pb	17.659	ND	47.658	ND	ND	5.331	5.779	10.845	ND	ND	12.517	ND	20.292
Th	ND	5.932	5.804	243.138	41.872	158.159	40.920	43.709	13.268	24.429	12.666	19.612	18.479
U	ND	ND	ND	ND	ND	ND	ND	ND	ND	ND	ND	ND	ND

^a Analysed during run one

^b Analysed during run two

ND: Not detected as concentration below instrument detection limit. Detection limits for the two runs is provided in Table SI 2B. Note: each sample was diluted to one tenth or one hundredth of the original concentration for analysis. As such, ND reflects that the element of interest was not detected in the diluted sample.

Appendix 1

<i>Jarosite (cont)</i>													
Sample ID	Js-SB- 32A ^a	Js-SB- 32B ^a	Js-SB- 32D ^b	Js-SB- 34A ^a	Js-SB- 34B ^a	Js-SB- 34C ^a	Js-SB- 34D ^a	Js-SB- 34F ^b	Js-SB- 34G ^b	Js-SB- 34H ^b	Js-SB- 34I ^b	Js-SB- 35A ^a	Js-SB- 35B ^a
<i>Morphology</i>	Boulder	Boulder	Boulder	Boulder	Boulder	Boulder	Boulder	Boulder	Boulder	Boulder	Boulder	Boulder	Boulder
<i>Major (wt%)</i>													
Na	2.07	1.87	2.27	3.51	3.63	3.31	1.86	4.84	1.54	6.21	2.22	3.81	3.38
Mg	0.06	0.06	0.03	0.03	0.19	0.12	0.06	0.01	0.01	0.01	0.01	0.06	0.10
Al	0.06	0.06	ND	0.04	0.07	0.13	0.09	ND	ND	ND	ND	0.05	0.09
P	0.30	0.14	0.16	0.05	0.02	ND	0.19	0.03	0.14	0.05	0.02	0.02	0.04
K	4.78	5.42	4.83	1.57	0.86	0.91	4.08	2.66	4.46	3.96	2.69	0.27	0.22
Ca	0.18	0.10	0.11	0.02	0.18	0.05	0.18	0.03	0.08	0.02	0.01	0.21	0.12
Fe	31.98	32.45	31.79	32.15	29.71	34.65	28.36	31.75	27.61	28.70	25.23	26.83	30.90
<i>Minor (ppm)</i>													
Li	ND	ND	ND	ND	ND	ND	ND	ND	ND	ND	ND	ND	ND
B	ND	ND	ND	ND	ND	ND	ND	ND	ND	ND	ND	ND	ND
V	29.865	43.341	25.006	63.629	62.741	154.309	65.900	25.863	33.320	29.518	42.835	51.535	767.252
Cr	10.472	5.534	ND	ND	ND	8.122	5.236	20.032	ND	10.584	ND	30.079	83.750
Mn	23.373	12.720	13.842	27.825	28.223	29.813	43.964	13.207	19.057	14.702	ND	5.247	11.289
Co	ND	ND	ND	ND	ND	ND	ND	ND	ND	ND	ND	ND	ND
Ni	ND	37.947	ND	4.679	2496.783	6.946	29.758	ND	33.570	ND	ND	ND	ND
Cu	ND	ND	ND	ND	ND	ND	ND	ND	ND	ND	11.950	ND	15.758
Zn	8.373	11.723	23.435	24.004	24.376	224.317	32.657	23.448	10.372	ND	19.697	8.932	24.934
Ge	ND	ND	ND	ND	ND	ND	ND	ND	ND	ND	ND	ND	ND
As	14.097	20.810	11.326	8.055	10.405	6.041	21.816	ND	18.187	ND	41.133	502.450	2222.260
Se	ND	ND	ND	ND	ND	ND	ND	ND	ND	ND	ND	ND	ND
Rb	42.113	33.145	37.063	53.032	43.088	46.793	38.994	46.426	31.715	37.417	33.688	33.145	27.101
Sr	1773.195	953.839	958.457	203.953	201.782	181.444	1779.365	219.429	788.384	238.833	73.901	418.304	297.875
Y	ND	ND	ND	ND	ND	ND	ND	ND	ND	ND	ND	ND	ND
Zr	ND	ND	ND	ND	ND	ND	ND	ND	ND	ND	ND	ND	ND

Appendix 1

Mo	ND	ND	ND	ND	ND	ND	ND	ND	ND	ND	ND	19.549	28.016
Cd	ND	ND	ND	ND	ND	ND	ND	ND	ND	ND	ND	ND	ND
Sn	ND	ND	ND	ND	ND	ND	ND	ND	ND	ND	ND	ND	9.727
Sb	ND	ND	ND	ND	ND	ND	ND	ND	ND	ND	ND	ND	23.637
Cs	ND	ND	ND	ND	ND	ND	ND	ND	ND	ND	ND	ND	ND
Ba	170.499	36.853	67.154	29.566	20.219	17.381	171.843	ND	20.749	23.865	36.807	54.414	46.858
La	23.221	9.460	10.857	ND	ND	ND	15.546	ND	ND	ND	ND	ND	ND
Ce	21.000	7.483	9.017	ND	ND	ND	18.263	ND	ND	ND	ND	3.569	7.013
Pr	ND	ND	ND	ND	ND	ND	ND	ND	ND	ND	ND	ND	ND
Nd	ND	ND	ND	ND	ND	ND	ND	ND	ND	ND	ND	ND	4.519
Sm	ND	ND	ND	ND	ND	ND	ND	ND	ND	ND	ND	ND	ND
Eu	ND	ND	ND	ND	ND	ND	ND	ND	ND	ND	ND	ND	ND
Gd	ND	ND	ND	ND	ND	ND	ND	ND	ND	ND	ND	ND	ND
Tb	ND	ND	ND	ND	ND	ND	ND	ND	ND	ND	ND	ND	ND
Dy	ND	ND	ND	ND	ND	ND	ND	ND	ND	ND	ND	ND	ND
Ho	ND	ND	ND	ND	ND	ND	ND	ND	ND	ND	ND	ND	ND
Er	ND	ND	ND	ND	ND	ND	ND	ND	ND	ND	ND	ND	ND
Tm	ND	ND	ND	ND	ND	ND	ND	ND	ND	ND	ND	ND	ND
Yb	ND	ND	ND	ND	ND	ND	ND	ND	ND	ND	ND	ND	ND
Lu	ND	ND	ND	ND	ND	ND	ND	ND	ND	ND	ND	ND	ND
Pb	11.514	ND	ND	ND	ND	ND	10.715	ND	ND	ND	ND	4.208	4.462
Th	3.958	ND	ND	ND	ND	ND	7.384	ND	ND	ND	ND	7.075	49.159
U	ND	ND	ND	ND	ND	ND	ND	ND	ND	ND	ND	ND	ND

^a Analysed during run one

^b Analysed during run two

ND: Not detected as concentration below instrument detection limit. Detection limits for the two runs is provided in Table SI 2B. Note: each sample was diluted to one tenth or one hundredth of the original concentration for analysis. As such, ND reflects that the element of interest was not detected in the diluted sample.

Appendix 1

<i>Jarosite (cont)</i>											<i>Sediment</i>		
Sample ID	Js-SB- 35E ^b	Js-SB- 35F ^b	Js-SB- 38 ^a	Js-SB- 39 ^a	Js-SB- 40A ^a	Js-SB- 42 ^a	Js-SB- 47B ^a	Js-SB- 59A ^a	Js-SB- 60 ^a	Js-SB- 63 ^a	Js-FB- 8B ^b	Js-FB- 9B ^b	Js-FB- 12 ^b
<i>Morphology</i>	Boulder	Boulder	Pebble	Nodule	Coating	Coating	Nodule	Boulder	Boulder	Pebble	Cliff Sediment	Cliff Sediment	Cliff Sediment
<i>Major (wt%)</i>													
Na	3.48	3.50	4.49	3.97	10.77	4.67	0.85	3.89	3.85	3.96	0.08	0.23	0.13
Mg	0.02	0.02	0.06	0.06	0.18	0.11	0.08	0.13	0.16	0.07	0.02	0.49	0.06
Al	ND	ND	0.11	0.08	0.67	1.24	3.15	0.16	0.15	0.04	0.22	7.03	0.61
P	0.03	0.04	0.18	0.12	0.06	0.07	0.05	ND	0.19	0.38	ND	0.02	ND
K	0.39	0.40	0.83	0.38	0.05	0.89	1.06	0.40	0.29	1.48	0.06	1.29	0.18
Ca	0.20	0.06	0.03	0.01	0.02	0.01	0.01	0.01	0.08	0.07	0.11	0.01	0.15
Fe	22.54	23.83	33.70	30.02	11.69	27.39	2.07	24.29	23.56	31.64	37.07	2.09	36.18
<i>Minor (ppm)</i>													
Li	ND	ND	ND	ND	ND	ND	ND	ND	ND	ND	ND	35.014	ND
B	ND	ND	ND	73.967	41.093	ND	ND	ND	ND	ND	29.943	80.326	23.434
V	67.778	139.959	282.901	372.347	54.744	590.433	37.615	106.822	149.965	83.671	ND	235.077	11.354
Cr	42.834	29.151	101.571	12.734	13.864	89.105	ND	64.858	116.804	110.437	ND	92.600	ND
Mn	12.336	16.891	9.779	ND	38.558	20.352	12.402	5.088	6.201	5.565	64.975	72.180	267.797
Co	ND	ND	ND	ND	10.849	ND	ND	ND	ND	ND	ND	9.703	ND
Ni	10.132	ND	ND	4.899	22.446	3.948	5.557	19.120	14.842	24.786	12.995	22.341	44.168
Cu	ND	ND	ND	ND	ND	3.525	ND	ND	ND	ND	ND	12.088	11.090
Zn	16.720	ND	13.956	19.352	49.590	26.237	49.125	64.755	30.703	32.191	49.235	86.010	37.572
Ge	ND	ND	ND	ND	ND	ND	ND	ND	ND	ND	ND	ND	ND
As	421.312	512.934	365.174	72.833	60.415	47.661	ND	67.463	402.766	329.597	ND	30.914	91.228
Se	ND	ND	ND	ND	ND	7.025	ND	ND	ND	ND	ND	1.761	ND
Rb	ND	42.275	44.258	76.818	2.535	52.642	17.352	35.290	28.856	47.963	ND	71.330	8.507
Sr	308.597	467.571	228.748	14.854	34.963	45.590	20.795	61.586	689.442	490.631	39.096	40.537	100.442
Y	ND	ND	ND	ND	ND	ND	ND	ND	61.551	ND	ND	15.015	ND

Appendix 1

Zr	ND	ND	ND	ND	ND	9.584	ND	ND	11.583	ND	ND	195.093	14.520
Mo	ND	ND	ND	ND	ND	63.815	25.983	ND	ND	ND	87.869	5.995	35.789
Cd	ND	ND	ND	ND	ND	ND	ND	ND	ND	ND	ND	ND	ND
Sn	ND	ND	ND	ND	ND	ND	ND	ND	ND	ND	ND	3.552	ND
Sb	ND	ND	ND	ND	ND	ND	ND	ND	ND	ND	ND	ND	ND
Cs	ND	ND	ND	ND	ND	ND	ND	ND	ND	ND	ND	6.550	ND
Ba	25.918	64.695	20.607	4.181	5.854	84.488	5.943	64.927	121.401	31.597	58.613	308.812	35.239
La	ND	ND	42.005	ND	ND	3.476	ND	ND	40.841	29.468	ND	26.420	ND
Ce	ND	ND	77.558	9.773	7.166	6.985	4.666	ND	83.496	79.249	ND	52.818	ND
Pr	ND	ND	ND	ND	ND	ND	ND	ND	ND	ND	ND	5.927	ND
Nd	ND	ND	4.092	ND	7.878	5.649	13.344	ND	16.458	ND	ND	24.323	ND
Sm	ND	ND	ND	ND	ND	ND	ND	ND	ND	ND	ND	4.457	ND
Eu	ND	ND	ND	ND	ND	ND	ND	ND	ND	ND	ND	ND	ND
Gd	ND	ND	ND	ND	ND	ND	ND	ND	5.481	ND	ND	3.545	ND
Tb	ND	ND	ND	ND	ND	ND	ND	ND	ND	ND	ND	ND	ND
Dy	ND	ND	ND	ND	ND	ND	ND	ND	7.442	ND	ND	2.796	ND
Ho	ND	ND	ND	ND	ND	ND	ND	ND	ND	ND	ND	ND	ND
Er	ND	ND	ND	ND	ND	ND	ND	ND	4.738	ND	ND	1.544	ND
Tm	ND	ND	ND	ND	ND	ND	ND	ND	ND	ND	ND	ND	ND
Yb	ND	ND	ND	ND	ND	ND	ND	ND	3.719	ND	ND	1.598	ND
Lu	ND	ND	ND	ND	ND	ND	ND	ND	ND	ND	ND	ND	ND
Pb	ND	ND	9.161	5.439	ND	11.287	ND	ND	12.647	ND	24.944	11.638	ND
Th	ND	9.019	21.516	15.128	24.460	9.359	ND	7.739	69.891	113.175	ND	38.959	ND
U	ND	ND	ND	ND	ND	ND	ND	ND	ND	ND	107.376	2.602	ND

^a Analysed during run one

^b Analysed during run two

ND: Not detected as concentration below instrument detection limit. Detection limits for the two runs is provided in Table SI 2B. Note: each sample was diluted to one tenth or one hundredth of the original concentration for analysis. As such, ND reflects that the element of interest was not detected in the diluted sample.

<i>Sediment (cont)</i>											
Sample ID	Js-FB- 20B ^b	Js-FB- 27 ^b	Js-FB- 31 ^b	Js-SB- 28 ^b	Js-SB- 40B ^b	Js-SB- 50 ^b	Js-SB- 51 ^b	Js-SB- 52 ^b	Js-SB- 55 ^b	Js-SB- 56 ^b	Js-SB- 57 ^b
<i>Morphology</i>	Cliff Sediment	Cliff Sediment	Cliff Sediment	Cliff Sediment	Cliff Sediment	Cliff Sediment	Cliff Sediment	Cliff Sediment	Cliff Sediment	Cliff Sediment	Cliff Sediment
<i>Major (wt%)</i>											
Na	0.58	0.12	0.66	1.80	0.80	0.78	0.40	0.47	3.83	0.71	1.43
Mg	0.50	0.77	0.84	0.91	0.23	1.02	0.36	0.27	1.00	0.21	0.54
Al	7.19	1.25	4.21	14.98	4.05	4.52	6.36	4.92	23.87	5.55	10.34
P	0.01	0.06	0.01	0.10	0.02	0.02	0.02	0.02	0.07	0.01	0.06
K	1.18	0.26	0.71	3.72	0.87	0.96	0.97	1.04	8.00	1.53	2.34
Ca	0.01	2.85	0.80	0.11	0.01	0.30	0.02	0.02	0.09	0.02	0.03
Fe	1.71	1.32	3.02	3.97	1.42	8.54	1.68	1.27	3.17	1.54	3.36
<i>Minor (ppm)</i>											
Li	32.644	7.027	21.776	112.184	17.160	22.471	27.660	36.975	85.308	20.837	53.481
B	185.778	17.575	64.703	273.525	50.513	74.207	53.117	85.273	187.080	43.353	144.435
V	192.283	38.764	116.387	335.674	82.256	420.151	235.848	106.412	449.292	117.769	153.669
Cr	133.736	19.475	51.790	179.179	45.685	101.953	76.934	53.765	217.347	57.453	96.259
Mn	64.472	587.614	343.570	537.956	101.702	526.084	222.572	139.187	362.974	82.305	151.042
Co	6.656	3.737	9.084	10.108	7.853	10.557	16.916	3.060	15.231	11.011	13.303
Ni	40.186	17.242	27.400	29.534	14.388	32.461	42.021	9.618	54.697	23.208	19.036
Cu	12.379	2.032	7.071	21.449	5.266	7.459	8.395	7.338	35.348	7.630	12.925
Zn	62.996	21.948	43.293	83.395	38.511	118.071	144.329	29.107	92.794	31.819	53.540
Ge	ND	ND	ND	ND	ND	ND	ND	ND	ND	ND	ND
As	25.773	10.682	34.587	79.282	17.415	58.959	37.342	22.996	111.976	25.812	24.654
Se	1.700	0.820	ND	4.160	ND	ND	2.824	1.032	3.097	1.275	3.037
Rb	63.059	15.958	45.170	114.834	33.437	44.795	46.824	41.136	183.551	52.528	82.860
Sr	37.613	404.201	833.467	165.745	41.877	287.729	50.636	47.028	379.3374	70.239	168.82
Y	15.230	16.242	10.611	43.036	15.443	13.219	20.545	13.831	33.709	12.494	23.144

Appendix 1

Zr	194.919	49.101	134.269	1095.664	287.850	219.310	262.685	288.291	645.823	169.133	366.962
Mo	3.672	2.125	ND	3.544	2.103	ND	ND	ND	4.035	5.511	3.095
Cd	ND	ND	ND	ND	ND	ND	ND	ND	ND	ND	ND
Sn	3.551	ND	1.723	7.012	1.434	ND	1.804	2.000	7.865	1.539	3.626
Sb	ND	ND	ND	1.836	ND	ND	ND	ND	2.985	ND	1.102
Cs	6.126	1.121	3.691	10.452	3.264	ND	4.421	4.398	12.876	4.056	7.306
Ba	245.294	67.192	179.022	846.677	199.137	159.887	217.161	471.544	1427.867	290.815	1341.431
La	28.700	10.679	15.680	44.601	25.884	16.849	32.599	19.300	43.580	17.889	44.068
Ce	54.166	26.204	36.580	87.381	52.018	50.440	79.416	38.785	103.448	37.511	101.389
Pr	6.186	2.514	3.850	10.053	5.454	ND	8.611	4.161	9.037	3.758	9.119
Nd	25.180	11.944	16.667	40.729	22.377	20.106	36.989	17.206	36.484	15.582	34.227
Sm	4.578	2.273	3.131	7.748	4.051	ND	7.230	2.909	7.460	3.187	6.463
Eu	ND	ND	ND	1.351	ND	ND	1.121	ND	1.645	ND	1.056
Gd	3.617	2.639	2.505	6.709	3.175	ND	5.738	2.323	6.363	2.550	5.180
Tb	ND	ND	ND	0.919	0.304	ND	ND	ND	0.865	ND	ND
Dy	2.852	2.033	2.133	6.925	2.746	ND	4.330	2.175	6.862	2.262	4.116
Ho	ND	ND	ND	1.371	0.412	ND	ND	ND	1.312	ND	0.877
Er	1.534	1.076	1.081	4.901	1.696	ND	2.139	1.387	4.622	1.352	2.576
Tm	ND	ND	ND	ND	0.113	ND	ND	ND	ND	ND	ND
Yb	1.605	0.790	1.052	5.974	2.017	ND	2.267	1.621	5.132	1.490	2.724
Lu	ND	ND	ND	0.805	ND	ND	ND	ND	ND	ND	ND
Pb	11.346	3.464	12.293	28.626	9.265	16.086	13.403	12.095	37.484	12.751	36.096
Th	43.561	9.242	30.569	83.531	28.312	41.810	64.992	41.012	98.648	31.091	52.577
U	3.075	1.396	1.815	8.334	2.024	11.035	2.665	2.420	7.323	3.599	3.649

^a Analysed during run one

^b Analysed during run two

ND: Not detected as concentration below instrument detection limit. Detection limits for the two runs is provided in Table SI 2B. Note: each sample was diluted to one tenth or one hundredth of the original concentration for analysis. As such, ND reflects that the element of interest was not detected in the diluted sample.

<i>Sediment (cont)</i>			
Sample ID	Js-SB- 58 ^b	Js-SB- 59B ^b	Js-SB- 62 ^b
<i>Morphology</i>	Cliff Sediment	Boulder Sediment	Sediment Pebble
<i>Major (wt%)</i>			
Na	3.59	6.16	0.58
Mg	1.21	1.09	0.28
Al	18.08	7.78	6.20
P	0.05	0.05	0.03
K	5.25	2.39	1.06
Ca	0.06	0.07	0.01
Fe	3.30	1.79	1.95
<i>Minor (ppm)</i>			
Li	58.425	34.074	30.601
B	223.793	195.412	81.628
V	364.478	554.806	110.312
Cr	178.151	215.031	73.933
Mn	228.953	385.880	82.954
Co	5.145	7.066	7.066
Ni	24.140	10.493	26.261
Cu	31.160	23.792	7.414
Zn	50.336	28.807	38.043
Ge	ND	ND	ND
As	50.745	79.755	29.502
Se	2.004	5.596	ND
Rb	105.749	106.155	45.994
Sr	205.806	264.075	45.017
Y	27.304	62.708	16.621

Zr	797.638	1136.103	239.887
Mo	7.133	48.878	ND
Cd	ND	ND	ND
Sn	8.098	17.613	ND
Sb	2.253	52.594	ND
Cs	10.647	11.051	ND
Ba	1009.793	557.321	388.068
La	22.327	85.301	18.343
Ce	47.870	174.782	36.169
Pr	5.775	19.326	3.671
Nd	24.634	80.459	15.973
Sm	5.167	16.930	3.324
Eu	0.908	2.634	ND
Gd	4.416	13.214	3.113
Tb	ND	1.764	ND
Dy	5.470	12.024	2.759
Ho	1.026	2.146	ND
Er	4.004	7.177	1.574
Tm	ND	0.906	ND
Yb	5.014	8.204	1.624
Lu	ND	1.055	ND
Pb	31.336	29.875	12.018
Th	74.188	190.079	31.825
U	7.898	20.317	2.093

^a Analysed during run one^b Analysed during run two

ND: Not detected as concentration below instrument detection limit. Detection limits for the two runs is provided in Table SI 2B. Note: each sample was diluted to one tenth or one hundredth of the original concentration for analysis. As such, ND reflects that the element of interest was not detected in the diluted sample.

Table SI 3B. Detection limits for the ICP–MS data.

<i>Run #</i>	1	2
<i>Major (ppm)</i>		
Na	0.0014	0.0046
Mg	0.0007	0.0009
Al	0.0042	0.0146
P	0.0033	0.0014
K	0.0067	0.0124
Ca	0.0001	0.0004
Fe	0.0057	0.0041
<i>Minor (ppb)</i>		
Li	0.5849	0.1880
B	0.8219	0.4692
V	0.0740	0.2160
Cr	0.0881	0.1966
Mn	0.0747	0.2109
Co	0.0737	0.1761
Ni	0.0768	0.1754
Cu	0.0439	0.1017
Zn	0.0875	0.1686
Ge	0.8866	0.1610
As	0.0806	0.1943
Se	0.1054	0.1640
Rb	0.1170	0.1690
Sr	0.0846	0.1876
Y	0.0818	0.1645
Zr	0.0869	0.2007
Mo	0.2851	0.4193
Cd	0.0974	0.1632
Sn	0.0961	0.1568
Sb	0.0725	0.1624
Cs	0.0949	0.1560
Ba	0.0585	0.2462
La	0.0694	0.1548
Ce	0.0678	0.1547
Pr	0.0715	0.1471
Nd	0.0788	0.1578
Sm	0.0771	0.1543
Eu	0.0691	0.1491
Gd	0.0820	0.1522
Tb	0.0735	0.1489
Dy	0.0833	0.1488
Ho	0.0682	0.1481
Er	0.0666	0.1492

Appendix 1

Tm	0.0686	0.1473
Yb	0.0732	0.1506
Lu	0.0672	0.1469
Pb	0.0774	0.1504
Th	0.0716	0.1422
U	0.0781	0.1478

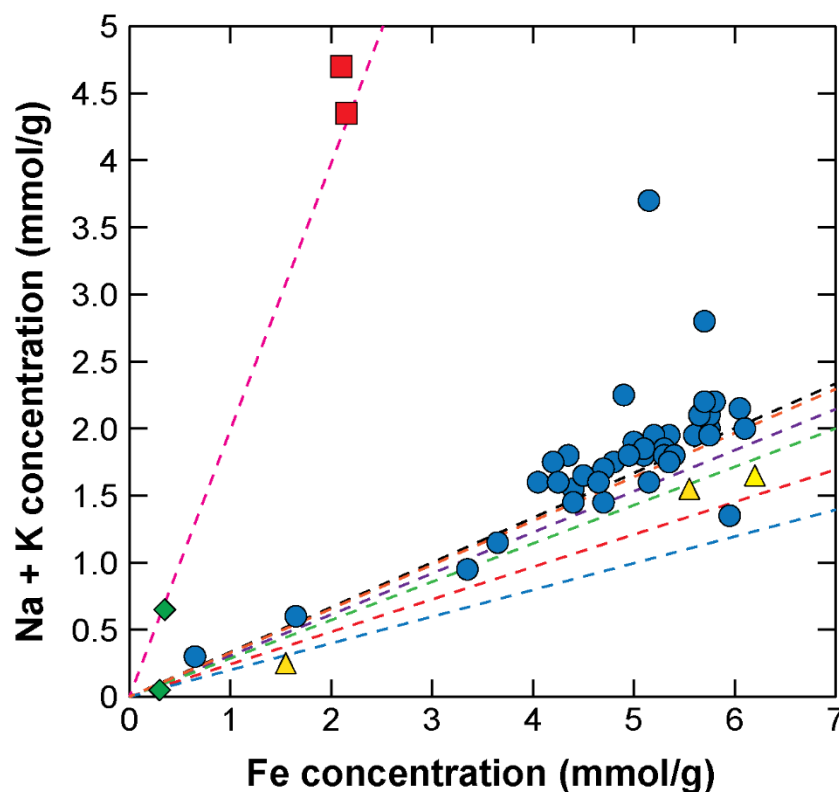


Figure SI 3. Plot of Fe concentration vs Na + K concentration for the jarosite samples after dissolution of ~20 mg of dry sample in 10 mL of 1 M HCl. Samples containing sideronatrite (and no jarosite) are shown as red squares. Samples containing jarosite and other iron-bearing minerals (goethite, pyrite) are shown as yellow triangles. Samples containing no jarosite (or other primary iron-bearing minerals) are shown as green diamonds. The dashed black line represents the stoichiometric ratio of (Na+K):Fe in the jarosite–natrojarosite solid solution $[(K,Na)Fe_3(SO_4)_2(OH)]$. The dashed orange line represents the stoichiometric ratio of 99 % jarosite $[(K,Na)Fe_3(SO_4)_2(OH)]$ and 1 % iron oxyhydroxide $[FeO(OH)]$. The dashed purple line represents the stoichiometric ratio of 95 % jarosite $[(K,Na)Fe_3(SO_4)_2(OH)]$ and 5 % iron oxyhydroxide $[FeO(OH)]$. The dashed green line represents the stoichiometric ratio of 90 % jarosite $[(K,Na)Fe_3(SO_4)_2(OH)]$ and 10 % iron oxyhydroxide $[FeO(OH)]$. The red dashed line represents the stoichiometric ratio of 80 % jarosite $[(K,Na)Fe_3(SO_4)_2(OH)]$ and 20 % iron oxyhydroxide $[FeO(OH)]$. The dashed blue line represents the stoichiometric ratio of 70 % jarosite $[(K,Na)Fe_3(SO_4)_2(OH)]$ and 30% iron oxyhydroxide $[FeO(OH)]$. The dashed pink line represents the stoichiometric ratio of Na:Fe in sideronatrite $[Na_2Fe(SO_4)_2(OH) \cdot 3H_2O]$.

SI 4. Iron isotope data for the jarosite and sediment samples

Table SI 4. Iron isotope composition of the jarosite and sediment samples determined by multi-collector inductively coupled plasma–mass spectrometry (MC–ICP–MS).

Sample ID	$\delta^{56}\text{Fe}$ (‰)	$\delta^{57}\text{Fe}$ (‰)
<i>Jarosite</i>		
Js–FB–1	-0.69 ± 0.03	-1.02 ± 0.05
Js–FB–3A	-0.43 ± 0.03	-0.62 ± 0.05
Js–FB–4	-0.4 ± 0.02	-0.57 ± 0.04
Js–FB–5	-0.23 ± 0.02	-0.32 ± 0.03
Js–FB–8A	0.77 ± 0.09	1.13 ± 0.07
Js–FB–9A	-0.72 ± 0.03	-1.08 ± 0.04
Js–FB–11A	-0.48 ± 0.16	-0.67 ± 0.13
Js–FB–14	-0.45 ± 0.03	-0.63 ± 0.08
Js–FB–16	0.1 ± 0.03	0.2 ± 0.05
Js–FB–20A	0.03 ± 0.03	0.06 ± 0.04
Js–FB–21A	-1.38 ± 0.03	-2.01 ± 0.08
Js–FB–21B	-1.91 ± 0.03	-2.81 ± 0.05
Js–SB–1	-0.39 ± 0.03	-0.60 ± 0.08
Js–SB–2	-0.12 ± 0.07	-0.22 ± 0.05
Js–SB–4	-0.45 ± 0.02	-0.69 ± 0.04
Js–SB–5	-0.20 ± 0.00	-0.30 ± 0.10
Js–SB–11	0.09 ± 0.03	0.05 ± 0.04
Js–SB–12	-0.14 ± 0.04	-0.20 ± 0.07
Js–SB–15	0.23 ± 0.06	0.34 ± 0.09
Js–SB–16	-0.06 ± 0.03	-0.06 ± 0.04
Js–SB–19	-0.24 ± 0.06	-0.38 ± 0.11
Js–SB–20A	-0.09 ± 0.02	-0.15 ± 0.04
Js–SB–20B	0.11 ± 0.03	0.19 ± 0.06
Js–SB–24	-0.12 ± 0.00	-0.16 ± 0.04
Js–SB–26A	0.28 ± 0.02	0.45 ± 0.05
Js–SB–31	0.00 ± 0.00	0.02 ± 0.08
Js–SB–32A	1.08 ± 0.13	1.57 ± 0.26
Js–SB–32B	1.24 ± 0.02	1.81 ± 0.03
Js–SB–32D	1.05 ± 0.21	1.54 ± 0.20
Js–SB–34A	-1.56 ± 0.02	-2.27 ± 0.03
Js–SB–34B	-0.97 ± 0.02	-1.44 ± 0.04
Js–SB–34C	-1.52 ± 0.02	-2.28 ± 0.04
Js–SB–34D	0.64 ± 0.02	0.96 ± 0.03
Js–SB–34F	0.70 ± 0.03	0.98 ± 0.05
Js–SB–34G	1.02 ± 0.14	1.52 ± 0.16
Js–SB–34H	0.64 ± 0.03	1.01 ± 0.05
Js–SB–34I	1.02 ± 0.00	1.52 ± 0.01
Js–SB–35A	0.16 ± 0.03	0.27 ± 0.03

Js-SB-35B	0.38 ± 0.03	0.59 ± 0.03
Js-SB-35E	0.05 ± 0.04	0.07 ± 0.06
Js-SB-35F	-0.22 ± 0.05	-0.34 ± 0.07
Js-SB-38	0.12 ± 0.03	0.16 ± 0.03
Js-SB-39	-0.45 ± 0.03	-0.70 ± 0.03
Js-SB-40A	0.73 ± 0.03	1.06 ± 0.04
Js-SB-42	-1.44 ± 0.03	-2.11 ± 0.04
Js-SB-47B	-0.36 ± 0.03	-0.52 ± 0.06
Js-SB-59A	-1.53 ± 0.02	-2.24 ± 0.04
Js-SB-60	-0.36 ± 0.04	-0.51 ± 0.03
Js-SB-63	0.47 ± 0.02	0.72 ± 0.07
<i>Sediment</i>		
Js-FB-8B	-0.45 ± 0.03	-0.71 ± 0.04
Js-FB-9B	0.43 ± 0.01	0.65 ± 0.03
Js-FB-12	-0.81 ± 0.03	-1.19 ± 0.04
Js-FB-20B	0.56 ± 0.02	0.80 ± 0.04
Js-FB-27	-0.54 ± 0.05	-0.76 ± 0.05
Js-FB-31	-0.53 ± 0.02	-0.85 ± 0.04
Js-SB-28	0.33 ± 0.02	0.44 ± 0.04
Js-SB-40B	0.06 ± 0.02	0.11 ± 0.04
Js-SB-50	0.05 ± 0.03	0.11 ± 0.05
Js-SB-51	-0.27 ± 0.04	-0.40 ± 0.05
Js-SB-52	0.34 ± 0.03	0.52 ± 0.04
Js-SB-55	1.30 ± 0.03	1.95 ± 0.03
Js-SB-56	-0.10 ± 0.02	0.13 ± 0.05
Js-SB-57	-0.03 ± 0.03	0.07 ± 0.04
Js-SB-58	0.58 ± 0.03	0.90 ± 0.06
Js-SB-59B	-0.24 ± 0.22	0.33 ± 0.24
Js-SB-62	0.02 ± 0.03	0.08 ± 0.05

Statistical uncertainties are based on two standard error in-run statistics (45 2-s on peak integration) if only one analysis; for samples analysed in replication, the error is 2σ and the reported iron isotope composition is the mean of the replicate analyses.

SI 5. Mineralogy and crystallographic data for the jarosite and sediment samples

Dry, hand ground jarosite and sediment samples were loaded into 0.3-mm diameter borosilicate glass capillaries then mounted onto the PD beamline (Wallwork et al., 2007) at the Australian Synchrotron. Capillaries were rotated at ~1 Hz during data collection to increase powder averaging. Diffraction patterns were collected over several beamtimes with the MYTHEN-II microstrip detector (Schmitt et al., 2003) at a wavelength of 0.77448(1) Å, 0.7754319(3) Å, 0.776979(1) Å, or 0.590726(6) Å as determined from refinement of NIST SRM LaB₆ 660b. To cover the gaps between detector modules, two datasets, each with a of collection time of 300 s, were collected with the detector set 5° apart and then merged to a single dataset. Paired 300 s datasets were merged using PDViPeR software available at the PD beamline. Additionally, six of the jarosite samples were analysed using a Bruker D8 Advance ECO XRD equipped with a cobalt source and a LYNXEYE XE linear position sensitive detector. These samples were hand-ground and mounted dry on a zero-background holder [Si single crystal (911)].

Bruker DIFFRAC.EVA was used to identify the minerals present in the samples using the Crystallography Open Database. Rietveld refinements were done using Bruker DIFFRAC.TOPAS software to investigate the structures of the jarosite subgroup minerals in the samples and to determine their unit cell parameters.

Although the jarosite samples represent a continuous solid solution, as a simple means of classification for descriptive purposes, the jarosite samples were classified according to subgroups determined by refining the lattice parameters using synchrotron-based XRD data. Literature lattice parameters for endmember jarosite (a : 7.3029, c : 17.2043) and endmember natrojarosite (a : 7.3153, c : 16.5868) from Basciano and Peterson (2007) and (2008), respectively, were used as an indicative guides to the relative amount of K and Na in the D site. Figure 3 illustrates how the samples were classified. Samples with a c -lattice parameter >16.8956 Å (half way between the literature c parameters for endmember jarosite and natrojarosite) are denoted as jarosite. Those with a c -lattice parameter < 16.8956 Å are denoted as natrojarosite. Within these two categories, we then describe the level of substitution of K or Na in the D site. Samples with more than a 10% relative deviation from the literature value for pure natrojarosite (>16.6486 Å) are described as “K–natrojarosite”. Similarly, samples with more than a 10% relative deviation from the literature value for pure jarosite (<17.1426 Å) are described as “Na–jarosite”. No attempt is made to account for hydronium substitution. It can be seen in Figure 3 that the majority of samples are K–natrojarosite, with a smaller number being natrojarosite and Na–jarosite. No samples were classified as endmember jarosite. As such, the name ‘jarosite’ is used herein to refer to all members of the subgroup and (K)jarosite is used to refer to endmember jarosite.

Note that errors associated with refinement of the c parameter are generally an order of magnitude larger than those for the a parameter. This is due in part to a solid solution between potassium and sodium which manifests as asymmetric peak broadening along [001].

Table SI 4 Mineralogy of the jarosite and sediment samples and jarosite unit cell parameters by Rietveld refinement using synchrotron XRD patterns.

Sample ID	Morphology	Minerals present	Crystal System (Jarosite Subgroup)	Lattice Parameters (Jarosite Subgroup)			
				<i>a</i> (Å)	<i>b</i> (Å)	<i>c</i> (Å)	β (°)
<i>Jarosite</i>							
Js-FB-1	Cliff vein	Natrojarosite, quartz	Rhombohedral	7.31477(3)		16.6260(1)	
Js-FB-3A	Cliff nodule	Quartz, (K)natrojarosite, halite, gypsum, illite	Rhombohedral	7.3146(1)		16.7198(9)	
Js-FB-4	Cliff surface coating	(K)Natrojarosite, quartz	Rhombohedral	7.30670(5)		16.766(1)	
Js-FB-5	Cliff surface coating	(K)Natrojarosite, quartz, illite	Rhombohedral	7.31727(8)		16.8627(8)	
Js-FB-8A	Cliff surface coating	Quartz, (K)natrojarosite, gypsum, kaolinite, illite	Rhombohedral	7.3165(1)		16.6647(6)	
Js-FB-9A	Cliff surface coating	Quartz, (K)natrojarosite, illite, kaolinite	Rhombohedral	7.30829(9)		16.703(1)	
Js-FB-11A	Cliff surface coating	Quartz, pyrite, gypsum, (K)natrojarosite ^a , smectite	Rhombohedral	N/A		N/A	
Js-FB-14	Cliff nodule	(K)Natrojarosite, quartz, halite	Rhombohedral	7.3094(1)		16.676(1)	
Js-FB-16	Bedding in cliff	Quartz, (K)natrojarosite, illite	Rhombohedral	7.30133(7)		16.806(1)	
Js-FB-20A	Cliff surface coating	(K)Natrojarosite, quartz, illite	Rhombohedral	7.30662(5) ^b		16.7324(3) ^b	
Js-FB-21A	Interior of boulder	Quartz, (Na)jarosite, illite	Rhombohedral	7.28764(9) ^b		17.093(1) ^b	
Js-FB-21B	Exterior of boulder	(Na)Jarosite, quartz	Rhombohedral	7.2882(1) ^b		17.084(1) ^b	
Js-SB-1	Cliff nodule	(K)Natrojarosite, halite, quartz	Rhombohedral	7.32295(5)		16.707(1)	
Js-SB-2	Cliff nodule	(K)Natrojarosite, halite	Rhombohedral	7.32111(4)		16.6566(2)	
Js-SB-4	Cliff nodule	(K)Natrojarosite, gypsum, halite	Rhombohedral	7.32210(6)		16.6876(3)	
Js-SB-5	Cliff nodule	(K)Natrojarosite, quartz	Rhombohedral	7.31727(8)		16.863(1)	
Js-SB-11	Interior of boulder	(K)Natrojarosite, alunite	Rhombohedral	7.32817(8)		16.7078(3)	
Js-SB-12	Interior of boulder	Gypsum, quartz	Rhombohedral	N/A		N/A	
Js-SB-15	Cliff surface coating	(K)Natrojarosite, quartz	Rhombohedral	7.32163(5)		16.814(1)	
Js-SB-16	Cliff vein	(K)Natrojarosite, quartz, halite	Rhombohedral	7.32663(4)		16.6676(2)	
Js-SB-19	Cliff surface coating	(K)Natrojarosite, gypsum, quartz	Rhombohedral	7.3275(1)		16.6679(5)	
Js-SB-20A	Cliff surface coating	Natrojarosite ^a , quartz, illite, kaolinite	Rhombohedral	N/A		N/A	
Js-SB-20B	Cliff surface coating	Natrojarosite, quartz, halite, gypsum	Rhombohedral	7.31282(6)		16.6315(3)	
Js-SB-24	Cliff vein	(K)Natrojarosite, quartz	Rhombohedral	7.3212(1)		16.7784(6)	

Js-SB-26A	Cliff surface coating	Sideronatrite, quartz, gypsum, kaolinite, smectite	Rhombohedral	N/A		N/A	
Js-SB-31	Cliff surface coating	(K)Natrojarosite, quartz	Rhombohedral	7.32137(7)		16.714(1)	
Js-SB-32A	Exterior of boulder	(Na)Jarosite, quartz	Rhombohedral	7.30932(6)		17.023(1)	
Js-SB-32B	Interior of boulder	(Na)Jarosite, quartz, halite	Rhombohedral	7.29505(7)		17.050(1)	
Js-SB-32D	Exterior of boulder	(Na)Jarosite, quartz	Rhombohedral	7.30862(8)		17.025(1)	
Js-SB-34A	Interior of boulder	Natrojarosite, quartz, smectite	Rhombohedral	7.30705(5) ^b		16.601(1) ^b	
Js-SB-34B	Interior of boulder	Natrojarosite, quartz, smectite	Rhombohedral	7.30570(7)		16.5796(3)	
Js-SB-34C	Exterior of boulder	Natrojarosite, quartz, goethite, smectite	Rhombohedral	7.30703(6) ^b		16.5817(3) ^b	
Js-SB-34D	Exterior of boulder	(Na)Jarosite, quartz, halite	Rhombohedral	7.29511(9) ^b		17.066(1) ^b	
Js-SB-34F	Interior of boulder	Natrojarosite, quartz	Rhombohedral	7.3188(2) ^b		16.6269(6) ^b	
Js-SB-34G	Exterior of boulder	(Na)Jarosite, quartz,	Rhombohedral	7.30763(7) ^b		17.075(1) ^b	
Js-SB-34H	Exterior of boulder	(Na)Jarosite, quartz	Rhombohedral	7.30668(8) ^b		17.080(1) ^b	
Js-SB-34I	Interior of boulder	(Na)Jarosite, quartz, halite	Rhombohedral	7.3112(1) ^b		16.949(1) ^b	
Js-SB-35A	Interior of boulder	Natrojarosite, quartz, gypsum	Monoclinic	12.7025(2)	7.32182(7)	6.96583(8)	127.187(1)
Js-SB-35B	Interior of boulder	Natrojarosite, goethite, quartz, gypsum, halite	Monoclinic	12.6909(3)	7.3188(2)	6.9799(1)	127.425(2)
Js-SB-35E	Interior of boulder	Natrojarosite, quartz, gypsum	Monoclinic	12.7000(3)	7.3230(1)	6.9688(1)	127.164(2)
Js-SB-35F	Interior of boulder	Natrojarosite, quartz	Rhombohedral	7.32448(6)		16.6462(3)	
Js-SB-38	Pebble	Natrojarosite, quartz, halite	Rhombohedral	7.31942(3)		16.6320(2)	
Js-SB-39	Cliff nodule	Natrojarosite, quartz	Rhombohedral	7.3250(1)		16.6431(6)	
Js-SB-40A	Cliff surface coating	Quartz, sideronatrite, halite, smectite	Rhombohedral	N/A		N/A	
Js-SB-42	Cliff surface coating	Natrojarosite, quartz	Rhombohedral	7.3013(1)		16.6434(5)	
Js-SB-47B	Cliff nodule	Alunite	Rhombohedral	N/A		N/A	
Js-SB-59A	Exterior of boulder	Natrojarosite, quartz, halite, smectite	Rhombohedral	N/A		N/A	
Js-SB-60	Exterior of boulder	Natrojarosite, quartz, halite, illite, smectite	Rhombohedral	7.29522(4)		16.5627(2)	
Js-SB-63	Pebble	Natrojarosite, quartz, halite	Rhombohedral	7.29472(5)		16.5919(3)	
<i>Sediment</i>							
Js-FB-8B	Cliff sediment	Pyrite, quartz, gypsum, smectite					
Js-FB-9B	Cliff sediment	Quartz, illite, kaolinite					

Js-FB-12	Cliff sediment	Pyrite, quartz, gypsum, jarosite	N/A
Js-FB-20B	Cliff sediment	Quartz, kaolinite, illite	
Js-FB-27	Cliff sediment	Quartz, calcite, illite	
Js-FB-31	Cliff sediment	Quartz, illite, kaolinite, pyrite	
Js-SB-28	Cliff sediment	Quartz, kaolinite, illite	
Js-SB-40B	Cliff sediment	Quartz, halite, illite, sideronatriite	
Js-SB-50	Cliff sediment	Quartz, pyrite, calcite, kaolinite, illite	
Js-SB-51	Cliff sediment	Quartz, pyrite, illite, kaolinite	
Js-SB-52	Cliff sediment	Quartz, illite, kaolinite, gypsum	
Js-SB-55	Cliff sediment	Quartz, kaolinite, illite, smectite	
Js-SB-56	Cliff sediment	Quartz, pyrite, kaolinite, illite, smectite	
Js-SB-57	Cliff sediment	Quartz, kaolinite, illite, halite	
Js-SB-58	Cliff sediment	Quartz, kaolinite, illite, halite	
Js-SB-59B	Sediment from boulder	Quartz, halite, kaolinite, illite	
Js-SB-62	Sediment pebble	Quartz, pyrite, kaolinite, illite	

^a Chemistry has been used to classify the species within the jarosite subgroup present in the sample.

^b Unit cell parameters are from most abundant jarosite subgroup species in the sample.

Appendix 2

Iron Isotope Exchange and Fractionation

between Jarosite and Aqueous Fe(II):

Supplementary Information

TABLE OF CONTENTS

SI 1: Jarosite and natrojarosite reactor pH data	XXXIII
SI 2: Jarosite and natrojarosite reactor K data	XXXIV
SI 3: Jarosite and natrojarosite reactor Fe(II) and Total Fe concentration data	XXXV
SI 4: Jarosite and natrojarosite reactor Fe isotope data.....	XXXVI
SI 5: Jarosite and natrojarosite reactor XRD data	XXXVII
SI 6: Jarosite and natrojarosite dissolution–reprecipitation calculations	XL
SI 7: Jarosite and natrojarosite K release calculations	XLII
SI 8: Jarosite and natrojarosite decomposition calculations	XLIV
SI 9: Jarosite and natrojarosite Fe atom exchange calculations	XLVI
SI 10: Jarosite and natrojarosite ICP–OES results	XLVII

SI 1: Jarosite and natrojarosite reactor pH data

Table SI 1. pH results for the jarosite and natrojarosite reactors. Data represent the mean of duplicate reactions.

Time (hours)	pH		
	SS-1	SS-2	No Fe(II) _{aq}
<i>Jarosite</i>			
0 ^a	7.905 (±0.007) ^b	7.895 (±0.049)	
0.08	4.520 (±0.014)	4.480 (±0.014)	
4	4.315 (±0.035)	4.295 (±0.035)	
24	4.175 (±0.007)	4.195 (±0.035)	
168	4.050 (±0.000)	4.050 (±0.000)	
336	3.920 (±0.028)	3.905 (±0.007)	
672	3.845 (±0.007)	3.865 (±0.007)	
1680	3.705 (±0.007)	3.705 (±0.007)	3.725 (±0.007)
<i>Natrojarosite</i>			
0 ^a	4.220 (±0.000)	4.225 (±0.035)	
0.08	4.450 (±0.014)	4.405 (±0.021)	
4	4.490 (±0.014)	4.460 (±0.028)	
24	4.445 (±0.078)	4.405 (±0.035)	
168	4.365 (±0.078)	4.245 (±0.021)	
336	4.105 (±0.035)	4.085 (±0.092)	
672	4.030 (±0.212)	4.010 (±0.071)	
1680	3.610 (±0.014)	3.630 (±0.014)	4.130 (±0.099)

^a Time zero reactors have the same composition as the other reactors except there is no jarosite present. See section 2.3 in the main manuscript for full details.

^b Errors reported at the 1 σ level

SI 2. Jarosite and natrojarosite reactor K data

Table SI 2. Potassium results for the jarosite and natrojarosite reactor solutions determined by inductively coupled plasma–mass spectrometry (ICP–MS) and inductively coupled plasma–optical emission spectroscopy (ICP–OES). Samples were diluted to one tenth of the original concentration for analysis. All sample concentrations were above the ICP–MS and ICP–OES instrument detection limits of 0.40 μM and 7.86 μM , respectively.

Time (hours)	K (μM)		
	SS–1	SS–2	No Fe(II) _{aq}
<i>Jarosite</i>			
0 ^a	2.66 (± 3.34) ^b	1.10 (± 0.52)	
0.08	21.44 (± 1.01)	19.35 (± 0.99)	
4	22.67 (± 1.73)	22.33 (± 0.55)	
24	23.30 (± 2.64)	21.85 (± 1.66)	
168	27.48 (± 0.92)	26.47 (± 3.86)	
336	25.08 (± 1.80)	24.93 (± 1.12)	
672	26.97 (± 1.48)	27.16 (± 1.04)	
1680	30.18 (± 0.46)	28.74 (± 0.61)	58.96 (± 13.90) ^c
<i>Natrojarosite</i>			
0	2.66 (± 3.34)	1.10 (± 0.52)	
0.08	4.79 (± 0.24)	4.72 (± 0.35)	
4	6.79 (± 1.25)	6.71 (± 0.55)	
24	8.40 (± 1.77)	7.37 (± 1.19)	
168	9.60 (± 0.52)	10.16 (± 0.59)	
336	13.48 (± 3.51)	10.71 (± 0.58)	
672	12.00 (± 1.19)	11.98 (± 0.35)	
1680	15.50 (± 0.79)	15.02 (± 0.42)	16.38 (± 5.56) ^c

^a Time zero reactors have the same composition as the other reactors except there is no jarosite present. See section 2.3 in the main manuscript for full details.

^b Errors reported at the 1σ level

^c K concentration measured using ICP–OES

SI 3: Jarosite and natrojarosite reactor Fe(II) and Total Fe concentration data

Table SI 3. Fe(II) and Total Fe concentrations results for the jarosite and natrojarosite reactor solutions. Data represent the mean of duplicate reactions.

Time (hours)	Fe(II) concentration (mM)			Total Fe concentration (mM)		
	SS-1	SS-2	No Fe(II) _{aq}	SS-1	SS-2	No Fe(II) _{aq}
<i>Jarosite</i>						
0 ^a	0.213 (±0.013) ^b	0.215 (±0.013)		0.240 (±0.034)	0.235 (±0.017)	
0.08	0.233 (±0.008)	0.226 (±0.000)		0.252 (±0.006)	0.246 (±0.008)	
4	0.233 (±0.008)	0.234 (±0.001)		0.247 (±0.004)	0.246 (±0.000)	
24	0.226 (±0.001)	0.215 (±0.002)		0.251 (±0.010)	0.239 (±0.000)	
168	0.233 (±0.001)	0.236 (±0.004)		0.251 (±0.008)	0.254 (±0.002)	
336	0.226 (±0.006)	0.226 (±0.001)		0.253 (±0.008)	0.246 (±0.001)	
672	0.224 (±0.013)	0.222 (±0.006)		0.244 (±0.001)	0.252 (±0.008)	
1680	0.221 (±0.001)	0.223 (±0.003)	0.007 (0.006)	0.232 (±0.001)	0.243 (±0.001)	0.003 (0.002)
<i>Natrojarosite</i>						
0 ^a	0.213 (±0.013)	0.215 (±0.013)		0.240 (±0.034)	0.235 (±0.017)	
0.08	0.221 (±0.001)	0.219 (±0.004)		0.239 (±0.001)	0.237 (±0.008)	
4	0.222 (±0.005)	0.222 (±0.003)		0.248 (±0.001)	0.243 (±0.003)	
24	0.223 (±0.003)	0.227 (±0.002)		0.249 (±0.004)	0.241 (±0.004)	
168	0.222 (±0.001)	0.233 (±0.003)		0.252 (±0.001)	0.259 (±0.002)	
336	0.244 (±0.004)	0.247 (±0.001)		0.251 (±0.008)	0.257 (±0.017)	
672	0.256 (±0.013)	0.244 (±0.001)		0.239 (±0.003)	0.251 (±0.000)	
1680	0.239 (±0.004)	0.237 (±0.001)	0.006 (0.004)	0.246 (±0.005)	0.238 (±0.005)	0.007 (0.006)

^a Time zero reactors have the same composition as the other reactors except there is no jarosite present. See section 2.3 in the main manuscript for full details.

^b Errors reported at the 1σ level

SI 4. Jarosite and natrojarosite reactor Fe isotope dataTable SI 4. Fe(II)_{aq} $\delta^{56}\text{Fe}$ and $\delta^{57/56}\text{Fe}$ results for the jarosite and natrojarosite reactors. Data represent the mean of duplicate reactors.

Time (hours)	$\delta^{56}\text{Fe}$ (‰)		$\delta^{57/56}\text{Fe}$ (‰)	
	SS-1	SS-2	SS-1	SS-2
<i>Jarosite</i>				
0 ^a	1.03 (± 0.08) ^b	-3.49 (± 0.04)	884.80 (± 1.57)	891.72 (± 1.14)
0.08	0.82 (± 0.02)	-3.40 (± 0.03)	812.70 (± 13.98)	830.35 (± 4.60)
4	0.52 (± 0.01)	-3.15 (± 0.00)	707.00 (± 0.14)	706.84 (± 0.03)
24	0.29 (± 0.00)	-3.06 (± 0.05)	645.88 (± 0.54)	655.58 (± 15.13)
168	-0.15 (± 0.06)	-2.90 (± 0.01)	526.13 (± 12.73)	528.07 (± 2.74)
336	-0.23 (± 0.08)	-2.85 (± 0.04)	521.25 (± 42.65)	511.32 (± 15.84)
672	-0.49 (± 0.03)	-2.71 (± 0.01)	437.33 (± 5.45)	434.37 (± 4.15)
1680	-0.71 (± 0.04)	-2.61 (± 0.03)	370.76 (± 14.85)	396.31 (± 17.52)
<i>Natrojarosite</i>				
0	1.03 (± 0.08)	-3.49 (± 0.04)	884.80 (± 1.57)	891.72 (± 1.14)
0.08	0.93 (± 0.01)	-3.47 (± 0.03)	860.67 (± 0.05)	866.15 (± 2.41)
4	0.77 (± 0.02)	-3.42 (± 0.00)	829.63 (± 9.67)	826.57 (± 0.55)
24	0.68 (± 0.03)	-3.42 (± 0.02)	805.48 (± 16.81)	799.21 (± 0.79)
168	0.51 (± 0.16)	-3.24 (± 0.00)	734.21 (± 53.36)	707.39 (± 1.80)
336	0.21 (± 0.10)	-3.22 (± 0.08)	668.21 (± 33.33)	686.99 (± 40.15)
672	0.10 (± 0.28)	-3.13 (± 0.01)	634.86 (± 87.31)	658.89 (± 26.14)
1680	-0.66 (± 0.08)	-2.72 (± 0.02)	407.50 (± 25.88)	422.44 (± 4.88)

^a Time zero reactors have the same composition as the other reactors except there is no jarosite present. See section 2.3 in the main manuscript for full details.

^b Errors reported at the 1 σ level

SI 5. Jarosite and natrojarosite XRD data

Table SI 5. Mineralogy and jarosite unit cell parameters data for the selected 70-day reactor sediment. Rietveld refinement of the synchrotron XRD patterns collected for the selected sediment was completed to produce the data. Mineralogy and jarosite unit cell parameters for unreacted jarosite (Js–Syn–01) and natrojarosite (Js–SB–38) are provided for comparison.

Reactor ID	Spike Solution	Minerals present	Crystal System	Lattice Parameters	
				<i>a</i> (Å)	<i>c</i> (Å)
<i>Jarosite</i>					
J30G–1	1	Jarosite	Rhombohedral	7.30503(2)	17.21401(6)
J30G–2	2	Jarosite	Rhombohedral	7.30495(2)	17.21242(6)
J30H	–	Jarosite	Rhombohedral	7.30499(3)	17.21366(6)
Js–Syn–01	–	Jarosite	Rhombohedral	7.30439(2)	17.21554(5)
<i>Natrojarosite</i>					
J31G–1	1	Natrojarosite, quartz,	Rhombohedral	7.31879(2)	16.6233(2)
J31G–2	2	Natrojarosite, quartz	Rhombohedral	7.31880(2)	16.6232(1)
J31H	–	Natrojarosite ^a , quartz, jarosite	Rhombohedral	7.31857(2)	16.6229(1)
Js–SB–38	–	Natrojarosite, quartz, halite	Rhombohedral	7.31896(2)	16.6228(1)

^a Main jarosite phase in the sample. Unit cell parameters are provided for this jarosite phase.

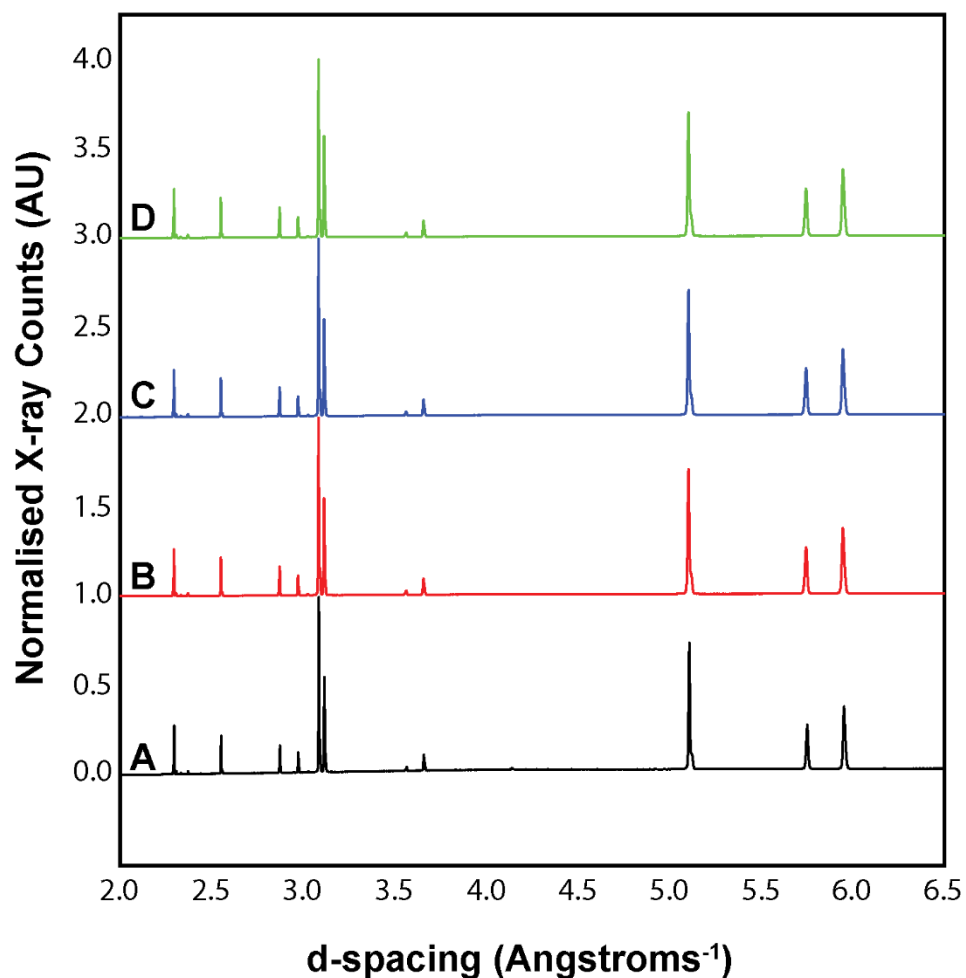


Figure SI 5A. Powder X-ray diffraction (XRD) patterns for jarosite samples showing that (A) unreacted Js-Syn-01, (B) J30H, Js-Syn-01 reacted in a solution containing no Fe(II)_{aq} over 70 days, (C) J30G-1, Js-Syn-01 reacted in a solution containing spike solution 1 for 70 days, and (D) J30G-2, Js-Syn-01 reacted in a solution containing spike solution 2 for 70 days, have identical (within error) XRD patterns. Spike solution details can be found in the main manuscript (section 2.3).

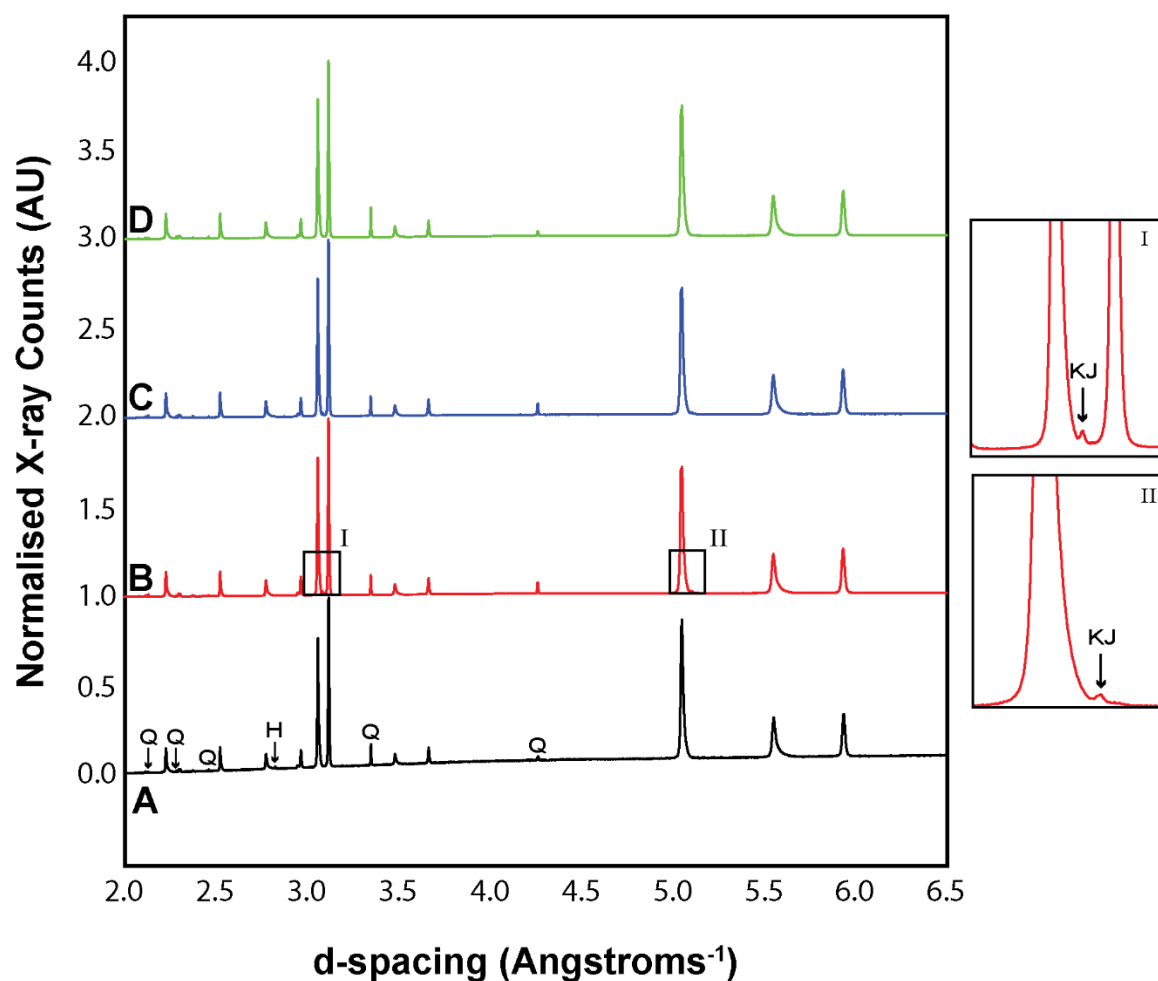


Figure SI 5B. Powder X-ray diffraction (XRD) patterns for natrojarosite samples showing that (A) unreacted Js-SB-38, (B) J31H, Js-SB-38 reacted in a solution containing no $\text{Fe(II)}_{\text{aq}}$ over 70 days, (C) J31G-1, Js-SB-38 reacted in a solution containing spike solution 1 for 70 days, and (D) J31G-2, Js-SB-38 reacted in a solution containing spike solution 2 for 70 days, have identical (within error) XRD patterns. Characteristic peaks of accessory phases quartz (Q), halite (H) and jarosite (KJ) are highlighted for reference. In sample J31H, a minor amount of jarosite is present, and is likely due to chemical heterogeneity in the natrojarosite pebble the sample was prepared from. Spike solution details can be found in the main manuscript (section 2.3).

SI 6. Jarosite and natrojarosite dissolution–reprecipitation calculations

The following steps were used to calculate the approximate amount of jarosite and natrojarosite dissolution–recrystallisation required to liberate enough H_3O^+ to cause the ~ 0.8 pH drop observed in the reactors:

Jarosite

Starting pH: 4.5; End pH: 3.71

Step 1: Determine the amount of H^+ added to the reactors

$$(10^{-4.50}) * 1000 = 0.032 \text{ mM } H^+$$

$$(10^{-3.71}) * 1000 = 0.195 \text{ mM } H^+$$

$$\rightarrow H^+ \text{ added: } 0.195 - 0.032 = 0.163 \text{ mM } H^+ \text{ added to the reactors}$$

Step 2: Determine the amount (mg) of hydronium jarosite dissolution–recrystallisation required to add 0.163 mM H^+

Stoichiometry of the sample: $(K_{0.941}H_3O_{0.059})Fe_{3.040}(SO_4)_2(OH)_6$

Amount of H_3O^+ jarosite in the sample: $20.0 \text{ mg} * 0.059 = 1.180 \text{ mg } H_3O \text{ jarosite}$

As 1.180 mg of jarosite with H_3O^+ occupancy was added to the reactor, the concentration of hydronium jarosite, if all dissolved and recrystallised, would be:

$$\left(\frac{1.180 \text{ mg } H_3O \text{ Js}}{0.01 \text{ L}} \right) * \left(\frac{1 \text{ mmol } H^3O \text{ Js}}{480.74 \text{ mg } H^3O \text{ Js}} \right) = \frac{0.245 \text{ mmol}}{L} = 0.245 \text{ mM}$$

Thus, as jarosite contains one H_3O^+ in its structure, complete dissolution–recrystallisation of 1.180 mg hydronium–rich jarosite would add 0.245mM H_3O^+ into the reactor solution

$$\rightarrow x \text{ mg } H_3O \text{ Js} = 0.163 \text{ mM } H^+$$

$$\rightarrow 1.180 \text{ mg } H_3O \text{ Js} = 0.245 \text{ mM } H_3O^+$$

$$\frac{0.163 \text{ mM} * 1.180 \text{ mg } H_3O \text{ Js}}{0.245 \text{ mM}} = x \text{ mg } H_3O \text{ Js} = 0.785 \text{ mg } H_3O \text{ Js}$$

Step 3: Determine the percentage of hydronium jarosite dissolution–recrystallisation

$$\frac{0.785 \text{ mg } H_3O \text{ Js}}{1.180 \text{ mg } H_3O \text{ Js}} * 100 = 66.53\% \text{ dissolution} - \text{recrystallisation}$$

Step 4: Determine the overall percentage of jarosite dissolution–recrystallisation

There is 5.9% hydronium jarosite in the sample

$$\rightarrow 5.9\% * 0.665 = 3.92\%$$

Therefore approximately 4% jarosite containing H_3O would need to undergo dissolution–reprecipitation to account for the 0.79 pH drop.

Natrojarosite

Starting pH: 4.43; End pH: 3.62

Step 1: Determine the amount of H⁺ added to the reactors

$$(10^{-4.43}) * 1000 = 0.037 \text{ mM H}^+$$

$$(10^{-3.62}) * 1000 = 0.240 \text{ mM H}^+$$

→ H⁺ added: 0.240 – 0.037 = 0.203 mM H⁺ added to the reactors

Step 2: Determine the amount (mg) of hydronium jarosite dissolution–recrystallisation required to add 0.203 mM H⁺

Stoichiometry of the sample: (Na_{0.852}K_{0.097}H₃O_{0.051})Fe_{3.195}(SO₄)₂(OH)₆

Amount of H₃O⁺ jarosite in the sample: 20.0 mg * 0.051 = 1.020 mg H₃O jarosite

As 1.020 mg of natrojarosite with H₃O⁺ occupancy was added to the reactor, the concentration of hydronium jarosite, if all dissolved and recrystallised, would be:

$$\left(\frac{1.020 \text{ mg H}_3\text{O Js}}{0.01 \text{ L}} \right) * \left(\frac{1 \text{ mmol H}^+ \text{ Js}}{480.74 \text{ mg H}_3\text{O Js}} \right) = \frac{0.212 \text{ mmol}}{\text{L}} = 0.212 \text{ mM}$$

Thus, as natrojarosite contains one H₃O⁺ in its structure, complete dissolution–recrystallisation of 1.020 mg hydronium–rich natrojarosite would add 0.203 mM H₃O⁺ into the reactor solution

→ x mg H₃O Js = 0.203 mM H⁺

→ 1.020 mg H₃O Js = 0.212 mM H₃O⁺

$$\frac{0.203 \text{ mM} * 1.020 \text{ mg Js}}{0.212 \text{ mM}} = x \text{ mg H}_3\text{O Js} = 0.977 \text{ mg H}_3\text{O Js}$$

Step 3: Determine the percentage of hydronium jarosite dissolution–recrystallisation

$$\frac{0.977 \text{ mg H}_3\text{O Js}}{1.020 \text{ mg H}_3\text{O Js}} * 100 = 95.78\% \text{ dissolution – recrystallisation}$$

Step 4: Determine the overall percentage of natrojarosite dissolution–recrystallisation

There is 5.1% hydronium jarosite in the sample

→ 5.1% * 0.958 = 4.89%

Therefore approximately 5% of natrojarosite containing hydronium would need to undergo dissolution–reprecipitation to account for the 0.81 pH drop.

SI 7. Jarosite and natrojarosite K release calculations

The following steps were used to calculate the approximate amount of K-rich regions in the jarosite and natrojarosite solid that dissolved to liberate enough K⁺ to account for the amount of K⁺ in solution after 70 days:

*Jarosite*Step 1: Determine the amount of K⁺ added to the reactors

Initial Concentration: 1.88 μM

Final Concentration: 29.46 μM

→ K⁺ added: 29.46 – 1.88 = 27.58 μM or 0.028 mM K⁺ added to the reactors

Step 2: Determine the amount of jarosite that dissolved to release 0.028 mM K⁺ into solution

Stoichiometry of the sample: (K_{0.941}H₃O_{0.059})Fe_{3.040}(SO₄)₂(OH)₆

Amount of K-jarosite in the sample: 20.0 mg * 0.941 = 18.82 mg K-jarosite

As 18.82 mg of jarosite with K occupancy was added to the reactor, the concentration of K-rich jarosite if all reacted would be:

$$\left(\frac{18.82 \text{ mg Js}}{0.01 \text{ L}}\right) * \left(\frac{1 \text{ mmol Js}}{500.8 \text{ mg Js}}\right) = \frac{3.76 \text{ mmol}}{\text{L}} = 3.76 \text{ mM}$$

Thus, as jarosite contains one K in its structure, complete reaction of 18.82 mg synthetic K jarosite would add 3.76 mM K⁺ into the reactor solution

→ x mg Js = 0.028 mM H⁺

→ 18.82 mg Js = 3.76 mM H₃O⁺

$$\frac{0.028 \text{ mM} * 18.82 \text{ mg Js}}{3.76 \text{ mM}} = x \text{ mg Js} = 0.140 \text{ mg K Js}$$

Step 3: Determine the percentage of K-rich jarosite dissolution

$$\frac{0.138 \text{ mg Js}}{18.82 \text{ mg Js}} * 100 = 0.74\% \text{ dissolution}$$

Therefore approximately 0.73% of the jarosite containing K would need to undergo dissolution to account for the 0.028 mM addition to the reactor solution after 70 days.

Natrojarosite

Step 1: Determine the amount of K⁺ added to the reactors

Initial Concentration: 1.88 μM

Final Concentration: 15.26 μM

→ K⁺ added: 15.26 – 1.88 = 13.38 μM or 0.013 mM K⁺ added to the reactors

Step 2: Determine the amount of K-rich natrojarosite that dissolved to release 0.0279 mM K⁺ into solution

Stoichiometry of the sample: (Na_{0.852}K_{0.097}H₃O_{0.051})Fe_{3.195}(SO₄)₂(OH)₆

Amount of K-rich jarosite in the sample: 20.0 mg * 0.097 = 1.94 mg K jarosite

As 1.94 mg of natrojarosite with K occupancy was added to the reactor, the concentration of K-rich natrojarosite if all reacted would be:

$$\left(\frac{1.94 \text{ mg Js}}{0.01 \text{ L}} \right) * \left(\frac{1 \text{ mmol Js}}{500.8 \text{ mg Js}} \right) = \frac{0.39 \text{ mmol}}{\text{L}} = 0.39 \text{ mM}$$

Thus, as jarosite contains one K in its structure, complete reaction of 1.94 mg K-rich natrojarosite would add 0.39 mM K⁺ into the reactor solution

→ x mg Js = 0.013 mM H⁺

→ 1.94 mg Js = 0.39 mM H₃O⁺

$$\frac{0.013 \text{ mM} * 1.94 \text{ mg Js}}{0.39 \text{ mM}} = x \text{ mg Js} = 0.065 \text{ mg K Js}$$

Step 3: Determine the percentage of K-rich natrojarosite dissolution

$$\frac{0.065 \text{ mg Js}}{1.94 \text{ mg Js}} * 100 = 3.35\% \text{ dissolution}$$

Therefore approximately 3.35% of the natrojarosite containing K would need to undergo dissolution to account for the 0.013 mM addition to the reactor solution after 70 days.

SI 8. Jarosite and natrojarosite decomposition calculations

The following steps were used to calculate the approximate amount of jarosite and natrojarosite decomposition required to liberate enough H^+ to cause the ~0.8 pH drop observed in the reactors:

Jarosite

Starting pH: 4.5; End pH: 3.71

Step 1: Determine the amount of H^+ added to the reactors

$$(10^{-4.50}) * 1000 = 0.032 \text{ mM } H^+$$

$$(10^{-3.71}) * 1000 = 0.195 \text{ mM } H^+$$

→ H^+ added: $0.195 - 0.032 = 0.163 \text{ mM } H^+$ added to the reactors

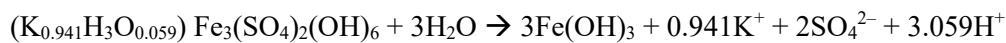
Step 2: Determine the amount of H^+ liberated during jarosite decomposition

Stoichiometry of the sample: $(K_{0.941}H_3O_{0.059})Fe_{3.040}(SO_4)_2(OH)_6$

Stoichiometry of the sample with max Fe occupancy: $(K_{0.941}H_3O_{0.059})Fe_3(SO_4)_2(OH)_6$

Molar Mass based of stoichiometry: 499.613 g/mol

Decomposition equation (modified from Eq. 1 in main body):



Amount of jarosite added to the reactor: 20.0 mg

Concentration of jarosite if all decomposed:

$$\left(\frac{20.00 \text{ mg Js}}{0.01 \text{ L}} \right) * \left(\frac{1 \text{ mmol Js}}{499.613 \text{ mg Js}} \right) = \frac{4.003 \text{ mmol}}{L} = 4.003 \text{ mM}$$

The decomposition of jarosite results in $3.059H^+$ (in the form of H^+ and H_3O^+) being liberated. Thus, 12.245 mM H^+ is liberated from jarosite during decomposition.

Step 3: Determine the percentage of jarosite decomposition required to liberate 0.163 mM H^+

20.0 mg of jarosite decomposition = 12.245 mM H^+ liberated

→ x mg = 0.163 mM

→ 20.0 mg = 12.245 mM

$$\frac{0.163 \text{ mM} * 20.0 \text{ mg Js}}{12.245 \text{ mM}} = x \text{ mg Js} = 0.266 \text{ mg Js}$$

→ $(0.266 \text{ mg} / 20.0 \text{ mg}) * 100 = 1.33 \%$ jarosite would need to decompose to produce a 0.79 pH decrease.

Natrojarosite

Starting pH: 4.43; End pH: 3.62

Step 1: Determine the amount of H⁺ added to the reactors

$$(10^{-4.43}) * 1000 = 0.037 \text{ mM H}^+$$

$$(10^{-3.62}) * 1000 = 0.240 \text{ mM H}^+$$

→ H⁺ added: 0.240 – 0.037 = 0.203 mM H⁺ added to the reactors

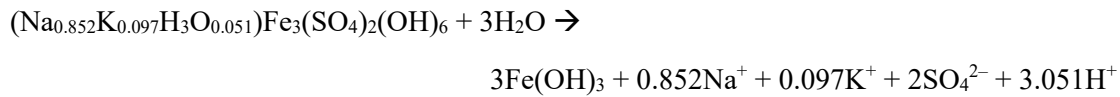
Step 2: Determine the amount (mg) of natrojarosite decomposition required to add 0.203 mM H⁺

Stoichiometry of the sample: (Na_{0.852}K_{0.097}H₃O_{0.051})Fe_{3.195}(SO₄)₂(OH)₆

Stoichiometry of the sample with max Fe occupancy: (Na_{0.852}K_{0.097}H₃O_{0.051})Fe₃(SO₄)₂(OH)₆

Molar Mass based of stoichiometry: 486.049 g/mol

Decomposition equation (modified from Eq. 1 in main body):



Amount of natrojarosite added to the reactor: 20.0 mg

Concentration of natrojarosite if all decomposed:

$$\left(\frac{20.00 \text{ mg Na Js}}{0.01 \text{ L}} \right) * \left(\frac{1 \text{ mmol Na Js}}{486.049 \text{ mg Na Js}} \right) = \frac{4.115 \text{ mmol}}{\text{L}} = 4.115 \text{ mM}$$

The decomposition of natrojarosite results in 3.051H⁺ (in the form of H⁺ and H₃O⁺) being liberated. Thus, 12.555 mM H⁺ is liberated from natrojarosite during decomposition.

Step 3: Determine the percentage of natrojarosite decomposition required to liberate 0.203 mM H⁺

20.0 mg of natrojarosite decomposition = 12.555 mM H⁺ liberated

→ x mg = 0.203 mM

→ 20.0 mg = 12.555 mM

$$\frac{0.203 \text{ mM} * 20.0 \text{ mg Js}}{12.555 \text{ mM}} = x \text{ mg Na Js} = 0.323 \text{ mg Na Js}$$

→ (0.323 mg / 20.0 mg) * 100 = 1.62 % natrojarosite would need to decompose to produce a 0.81 pH decrease.

SI 9. Jarosite and natrojarosite Fe atom exchange equations and calculations

There are two endmember models that can be used to calculate the percentage of Fe atoms in a solid that exchange with a fluid: the homogeneous recrystallisation model and the heterogeneous recrystallisation model. Descriptions of these models are provided in the main manuscript (see Section 4.1).

Homogeneous exchange of Fe atoms in jarosite can be quantified using Equation SI 9A (modified from Handler et al., 2014):

$$\% \text{ Js Fe Exchange} = \frac{N_{\text{Fe(II)}} \times (\delta_{\text{Fe(II)}}^i - \delta_{\text{Fe(II)}}^t)}{N_{\text{Js}} \times (\delta_{\text{Fe(II)}}^t - \delta_{\text{Js}}^i)} \times 100 \quad (\text{Eq. SI 9A})$$

where $\delta_{\text{Fe(II)}}^i$ and δ_{Js}^i are the initial $\delta^{57/56}\text{Fe}$ for $\text{Fe(II)}_{\text{aq}}$ and jarosite, $\delta_{\text{Fe(II)}}^t$ is the $\delta^{57/56}\text{Fe}$ value of $\text{Fe(II)}_{\text{aq}}$ at time t , and $N_{\text{Fe(II)}}$ and N_{Js} are the total moles of $\text{Fe(II)}_{\text{aq}}$ and moles of Fe(III) in jarosite in the system, respectively.

Applied to our results, the percentage of Fe atoms exchanged with jarosite after 70 days based on homogeneous recrystallisation is:

$$\text{SS-1: } \frac{0.25 \text{ mM} \times (884.8 - 370.76)}{11.92 \text{ mM} \times (370.76 - 0.12)} \times 100 = 2.91 \%$$

$$\text{SS-2: } \frac{0.25 \text{ mM} \times (891.71 - 396.31)}{11.92 \text{ mM} \times (396.31 - 0.12)} \times 100 = 2.62 \%$$

The percentage of Fe atoms exchanged with natrojarosite after 70 days based on homogeneous recrystallisation is:

$$\text{SS-1: } \frac{0.25 \text{ mM} \times (884.8 - 407.50)}{12.04 \text{ mM} \times (407.50 - 0.05)} \times 100 = 2.43 \%$$

$$\text{SS-2: } \frac{0.25 \text{ mM} \times (891.71 - 422.44)}{12.04 \text{ mM} \times (422.44 - 0.05)} \times 100 = 2.31 \%$$

Heterogeneous exchange of Fe atoms in jarosite can be quantified using Equation SI 9B (modified from Friedrich et al., 2019):

$$\% \text{ Js Fe Exchange} = \frac{N_{\text{Fe(II)}}}{N_{\text{Js}}} \times \ln \left(\frac{\delta_{\text{Js}}^i - \delta_{\text{Fe(II)}}^i}{\delta_{\text{Js}}^i - \delta_{\text{Fe(II)}}^t} \right) \quad (\text{Eq SI 9B})$$

Applied to our results, the percentage of Fe atoms exchanged with jarosite after 70 days based on heterogeneous recrystallisation is:

$$\text{SS-1: } \frac{0.25 \text{ mM}}{11.92 \text{ mM}} \times \ln \left(\frac{0.12 - 884.8}{0.12 - 370.76} \right) = 1.82 \%$$

$$\text{SS-2: } \frac{0.25 \text{ mM}}{11.92 \text{ mM}} \times \ln \left(\frac{0.12 - 891.71}{0.12 - 396.31} \right) = 1.70 \%$$

The percentage of Fe atoms exchanged with natrojarosite after 70 days based on heterogeneous recrystallisation is:

$$\text{SS-1: } \frac{0.25 \text{ mM}}{12.04 \text{ mM}} \times \ln \left(\frac{0.05 - 884.8}{0.05 - 370.76} \right) = 1.61 \%$$

$$\text{SS-2: } \frac{0.25 \text{ mM}}{12.04 \text{ mM}} \times \ln \left(\frac{0.05 - 884.8}{0.05 - 370.76} \right) = 1.55 \%$$

SI 10. Jarosite and natrojarosite ICP–OES results

Table SI 10A. Elemental composition of jarosite and natrojarosite samples determined by inductively coupled plasma–optical emission spectrometry (ICP–OES).

Sample ID	Element Concentration (wt%)			
	Na	S	K	Fe
Js–SB–38	3.50	11.46	0.68	31.82
Js–Syn–01	ND	11.71	6.71	30.94

ND. Not detected as element concentration is below the instrument detection limit (see Table SI 10B for details). Samples were diluted to one tenth of the original concentration for analysis; ND reflects that the element was not detected in the diluted sample.

Table SI 10B. Detection Limits for ICP–OES Data

Element	Concentration (ppm)
Na	0.0045
S	0.0853
K	0.0727
Fe	0.0061

Appendix 3

*The First Occurrence of Monoclinic
Jarosite in a Natural Environment*

TABLE OF CONTENTS

SI 1. Partial powder X-ray diffraction patterns of the Js-SB-35 subsamples analysed at room temperature	LI
SI 2. Additional EBSD images of the Js-SB-35 thin section	LII

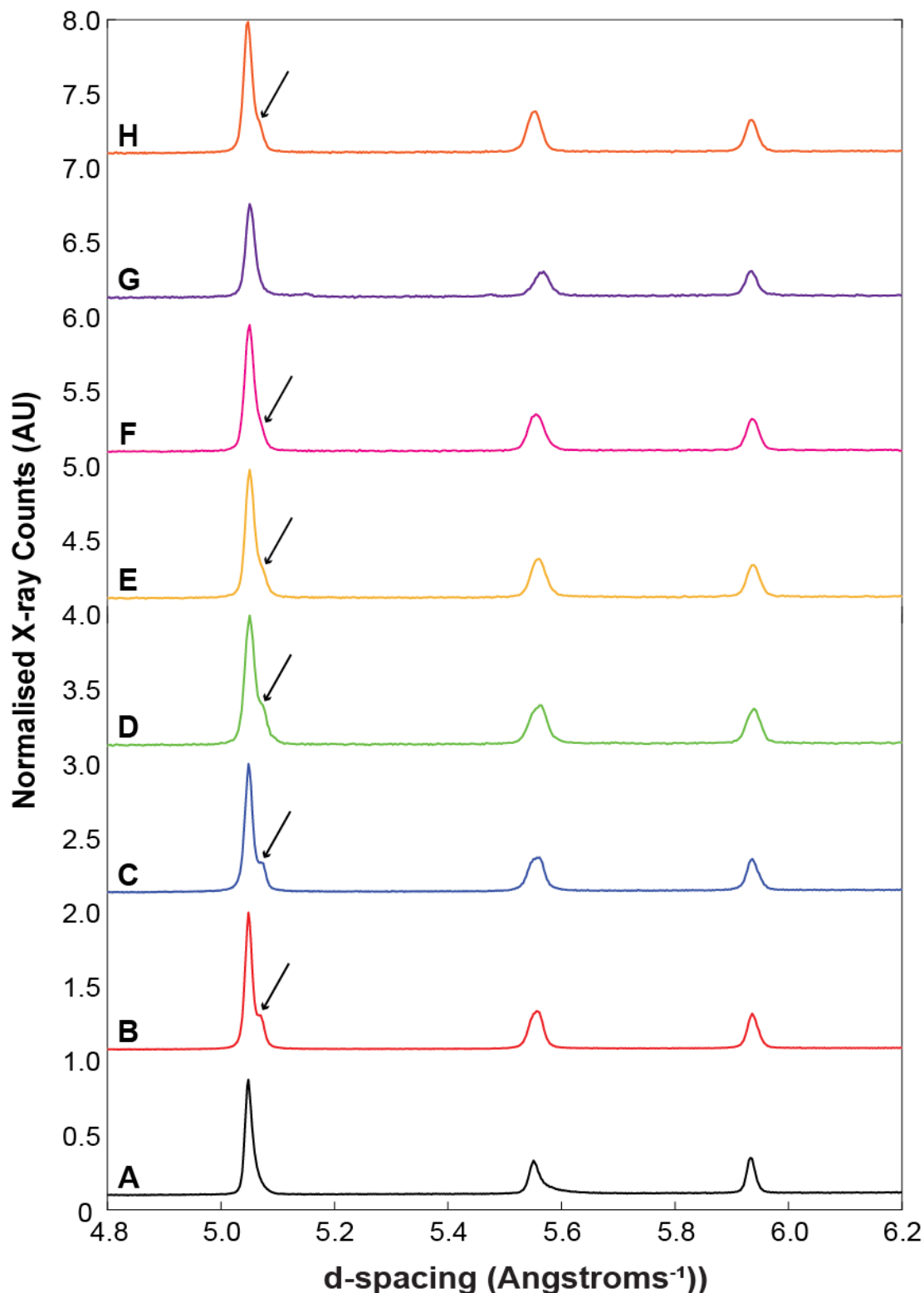
SI 1. Partial powder X-ray diffraction patterns of the Js-SB-35 subsamples analysed at room temperature

Figure SI 1. Partial powder X-ray diffraction patterns of the Js-SB-35 subsamples (B-H) measured at room temperature and a rhombohedral natrojarosite, Js-SB-38 (A), from Whitworth et al. 2020b, for comparison. (B) Js-SB-35A. (C) Js-SB-35B. (D) Js-SB-35E. (E) Js-SB-35F. (F) Js-SB-35G. (G) Js-SB-35H. (H) Js-SB-35I. The black arrows show peak shouldering associated with monoclinic symmetry.

SI 2. Additional EBSD images of the Js-SB-35 thin section

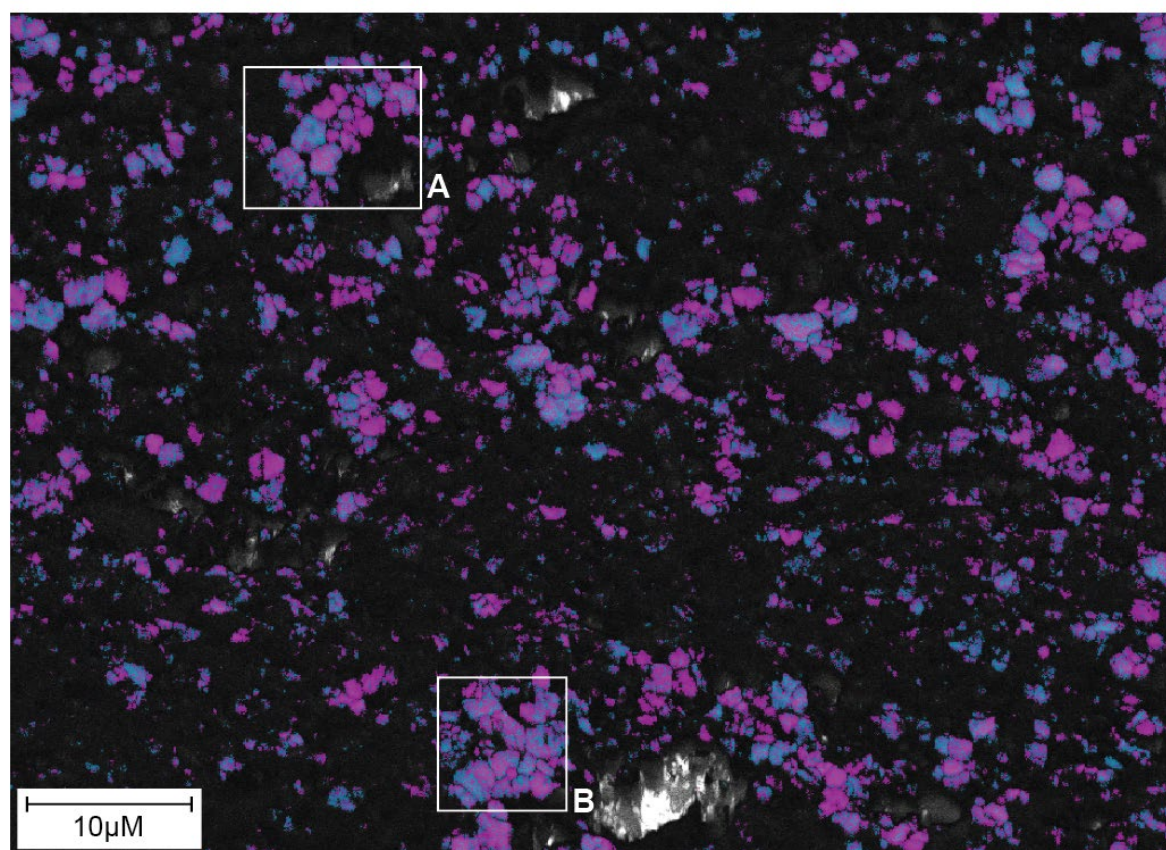


Figure SI 2.1. EBSD image of the region enclosed by the larger white box in Figure 6.8. The regions that index as monoclinic and/or rhombohedral natrojarosite are coloured. The regions that do not index as monoclinic and/or rhombohedral natrojarosite (so are accessory phases) are black. Quantitative analysis of the phases present in this region show that 11.5% of the phases index as monoclinic natrojarosite, 6.1% index as rhombohedral natrojarosite, and 82.4% do not index as monoclinic or rhombohedral natrojarosite. White boxes enclose regions examined at a higher magnification. Details on the methodology can be found in Chapter 6 (section 6.2.3).

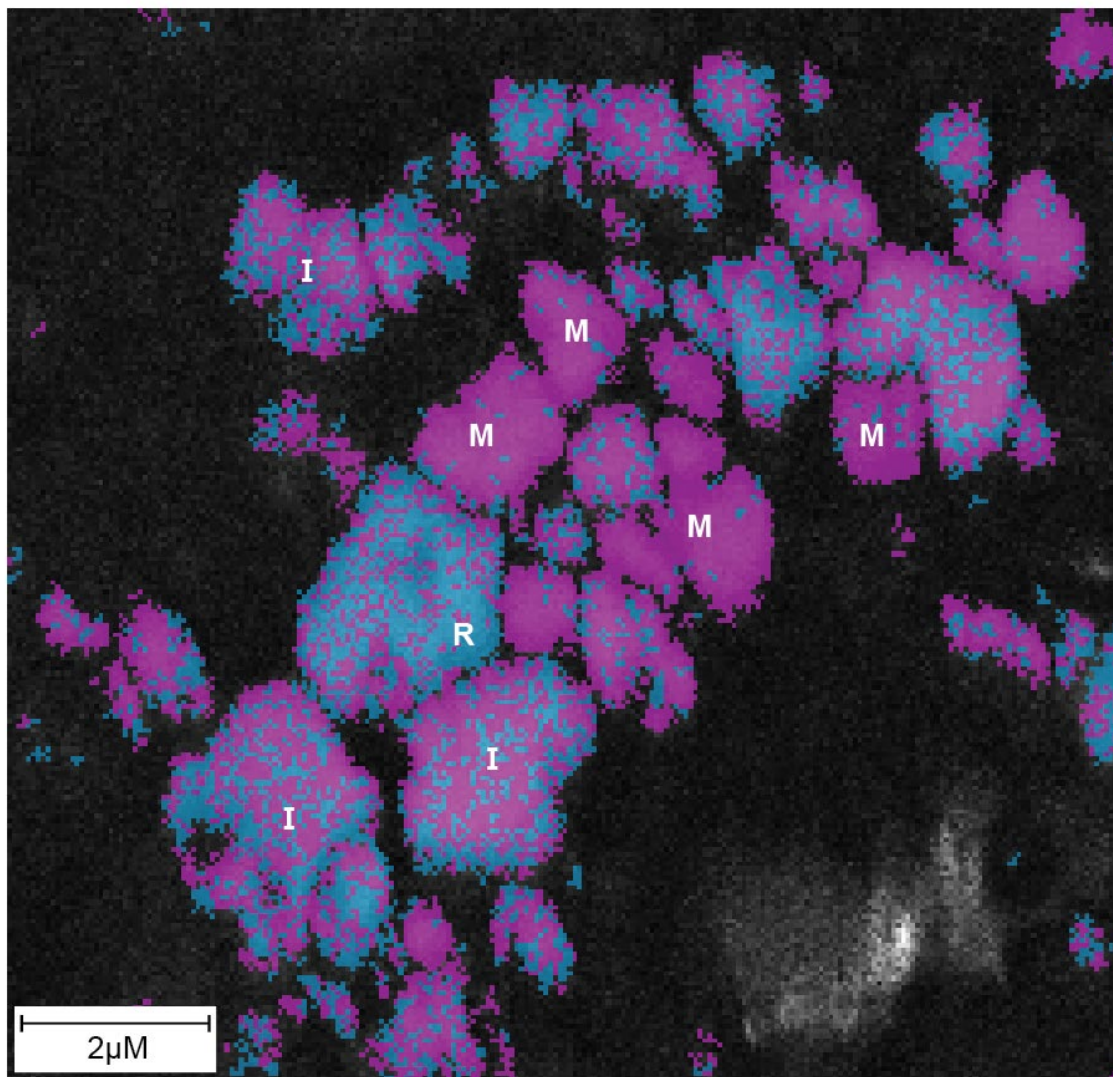


Figure SI 2.2. EBSD image of region A in Figure SI 2.1 highlighting regions that index as monoclinic natrojarosite (M; purple), rhombohedral natrojarosite (R; blue), or can be indexed using either a monoclinic or rhombohedral model (I; mottled blue and purple). Black regions correspond to accessory phases. Quantitative analysis of the phases present in this region show that 21.2% of the phases index as monoclinic natrojarosite, 10.7% index as rhombohedral natrojarosite, and 68.1% do not index as monoclinic or rhombohedral natrojarosite.

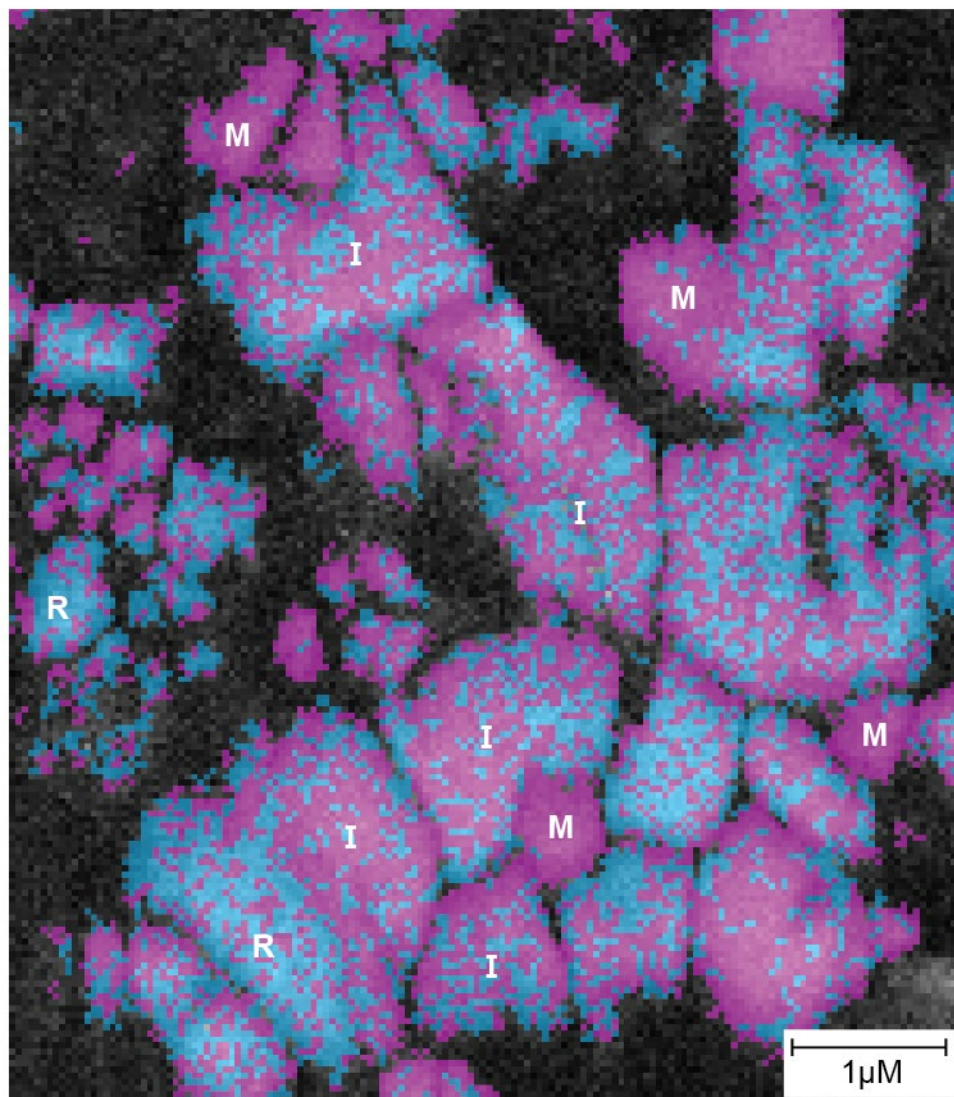


Figure SI 2.3. BSD image of region B in Figure SI 2.1 highlighting regions that index as monoclinic natrojarosite (M; purple), rhombohedral natrojarosite (R; blue), or can be indexed using either a monoclinic or rhombohedral model (I; mottled blue and purple). Black regions correspond to accessory phases. Quantitative analysis of the phases present in this region show that 36.3% of the phases index as monoclinic natrojarosite, 22.7% index as rhombohedral natrojarosite, and 41.0% do not index as monoclinic or rhombohedral natrojarosite.